# GYRORESONANT WAVE-PARTICLE INTERACTIONS IN A DYNAMIC MAGNETOSPHERE

A DISSERTATION
SUBMITTED TO THE DEPARTMENT OF ELECTRICAL ENGINEERING
AND THE COMMITTEE ON GRADUATE STUDIES
OF STANFORD UNIVERSITY
IN PARTIAL FULFILLMENT OF THE REQUIREMENTS
FOR THE DEGREE OF
DOCTOR OF PHILOSOPHY

By
William Baugh Gail
June 1987

I certify that I have read this thesis and that in my opinion it is fully adequate, in scope and in quality, as a dissertation for the degree of Doctor of Philosophy.

Robert A. Helliwell
(Principal Advisor)

I certify that I have read this thesis and that in my opinion it is fully adequate, in scope and in quality, as a dissertation for the degree of Doctor of Philosophy.

Umran S. Inan

I certify that I have read this thesis and that in my opinion it is fully adequate, in scope and in quality, as a dissertation for the degree of Doctor of Philosophy.

James Young

Approved for the University Committee on Graduate Studies:

Dean of Graduate Studies & Research

# ABSTRACT

Gyroresonant wave-particle interactions are a fundamental mechanism for coupling electromagnetic waves and energetic (1 keV-10 MeV) particles in magnetoplasmas. Such interactions play an important role in controlling the structure of the earth's radiation belts and the corresponding transfer of energy between the magnetosphere and ionosphere. Traditional experimental methods for studying gyroresonance interactions assume that the magnetosphere is static over the time scale of the observations. While the assumption may be valid in many situations, the magnetosphere is ultimately a dynamic medium and an understanding of magnetospheric processes necessarily requires knowledge of the response of the interaction mechanism to changes in the magnetic field and plasma properties.

This thesis presents a new method for studying gyroresonance interactions in a dynamic environment. In this approach, rapid global compressions of the magnetosphere, known as Sudden Commencements, are utilized as "natural experiments" since they cause step-like perturbations in the magnetic field and plasma parameters. The response of the interaction mechanism to the perturbations is monitored with satellite and ground-based wave and particle instruments. The method was applied through development of an extensive observational data set. Wave data for several hundred Sudden Commencements were analysed for amplitude and spectral modifications and correlated with magnetic field and particle observations. Characteristic, well-defined changes in both coherent and incoherent wave emissions were observed, including wave growth on the order of 20 dB, increases in the upper frequency limit of the waves, and enhanced triggering of discrete emissions. The growth rate for the incoherent wave emissions (0.3-2.7 dB/sec) was found to be two orders of magnitude

less than known growth rates for coherent waves. Measurable particle precipitation was commonly associated with the wave growth.

In order to determine the applicability of current static models of gyroresonance interactions to dynamic magnetospheres, both nonlinear and quasi-linear models were modified to provide predictions of wave characteristics applicable to Sudden Commencements. The quasi-linear models were found to accurately predict many of the observed features of incoherent emissions; the nonlinear models correctly predicted the enhanced occurrence of discrete emissions. The results emphasize the potential value of carefully developed gyroresonance interaction models which incorporate dynamic effects.

This dissertation is dedicated to my mother and father

**Ann** and **Bill Gail**

and to my wife

**Elke Meier**

# ACKNOWLEDGEMENTS

I am forever grateful to Dr. Martin Pomerantz for introducing me to the field of space physics and inspiring me with his dedication to discovering the workings of the earth and the sun.

This research was supervised by Prof. Robert Helliwell and Prof. Umran Inan, whose advice and guidance greatly influenced the direction of my work. I would like to thank them both for many stimulating discussions as well as their unending support. It has been a priviledge to work with them and gain from their experience.

My association with the Stanford VLF group has been extremely rewarding. I am especially grateful to Prof. Don Carpenter for his insight, wisdom, and personal friendship and to Prof. John Katsufrakis and Dr. Tim Bell for their encouragement and advice. I have greatly enjoyed sharing the learning curve with my fellow students, particularly Curt Carlson and my office mates Hoc Ngo and Bill Armstrong. I would also like to thank my third reader, Prof. James Young, for his careful review of the thesis.

The thesis could not have been completed without the generous advice and assistance of a number of people outside Stanford. I owe a special thank you to Dr. Sumant Krishnaswamy and Prof. Ted Rosenberg of University of Maryland for many helpful discussions and a great deal of help in acquiring the necessary digital data. Dr. Lou Lanzerotti of Bell Laboratories provided the magnetometer data that were recorded

on the University of Maryland data systems. Dr. David Knecht of Air Force Geophysics Laboratories kindly sent the published volumes of magnetometer data from the AFGL chain. The GOES magnetometer data and copies of the hard to find *IAGA Bulletin* were obtained with the help of Dan Wilkinson and Viola Miller at NOAA. Data from the DE-1 spacecraft, which were not included in this thesis but were used extensively in preliminary studies, were provided by Dr. Ann Persoon and Prof. Dan Gurnett at University of Iowa (wave data) and by Dr. Brian Ledley and Jim Burns at Goddard Space Flight Center (magnetometer data). Computer source code for the Tsygnanenko-Usmanov magnetic field model was obtained through Dr. Ray Walker and Harlan Spence at UCLA. The three-dimensional raytracing analysis and helpful comments on longitudinal wave propagation were provided by Dr. Iwane Kimura of Kyoto University. Finally, I would like to thank the field scientists who spent a year or more of their lives in Antarctica collecting the data upon which my research was based.

Most of all, I am grateful for the generous support of my family. My wife Elke, who I met during the last half of my graduate studies, inspired me with her continuous encouragement and with the example of her own Ph.D. work.

This research was supported in part by the National Aeronautics and Space Administration under grant NAS5-25744 and in part by the National Science Foundation Department of Polar Programs under grants DPP-82-17820, DPP-79-23171, DPP-83-17092, and DPP-83-18508.

# TABLE OF CONTENTS

# LIST OF FIGURES AND TABLES

| Table | | Page |
|---|---|---|

# Chapter 1

# INTRODUCTION

## 1.1 DESCRIPTION OF THE PROBLEM

Gyroresonance interactions between waves and particles are of general interest in plasma physics. Significant amounts of energy and momentum may be transfered through such interactions, resulting in both wave growth and particle scattering. Gyroresonance processes provide a useful method for heating ions and electrons in laboratory plasmas, but can also result in instabilities which disrupt the plasma. In space plasmas, gyroresonance processes couple wave and particle distributions and thus play a major role in the dynamics of the plasma environment.

The earth's magnetosphere is a readily accessible space plasma which provides an excellent laboratory for studying the gyroresonance interaction mechanism. Energetic particles are magnetically confined to circulate in the radiation belts by the dipole structure of the inner magnetosphere. The particles interact with waves generated through plasma processes within the magnetosphere as well as waves injected by ground-based sources. The interactions modify the structure of the radiation belts and cause ionospheric disturbances which disrupt terrestrial radio communications.

The large scale morphology of the magnetosphere results from the interaction of the dipolar magnetic field of the earth with the solar wind, as depicted in Figure 1.1.

The boundary between the magnetosphere and solar wind, known as the magnetopause, is formed where the pressure of the solar wind balances the pressure within the magnetosphere. On the nightside, field lines extend to large distances, forming the magnetotail. The inner magnetosphere, defined here to be the region consisting of field lines which close at the earth, extends to the magnetopause on the dayside and to a roughly similar distance on the nightside.

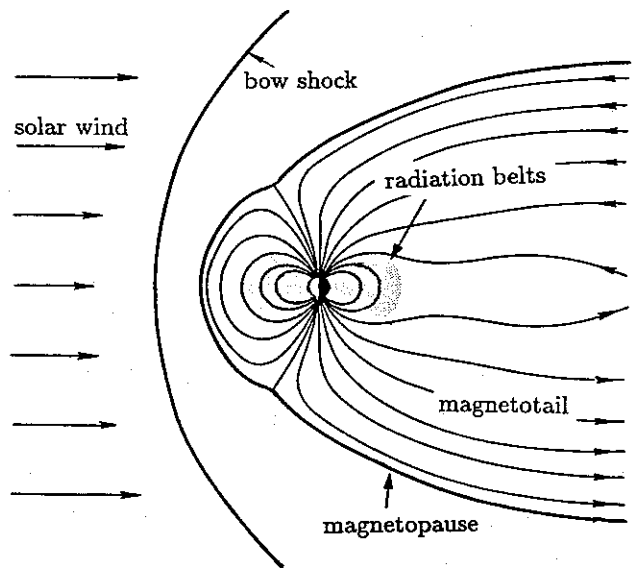


**Figure 1.1.** The structure of the earth's magnetosphere and the interaction with the solar wind.

Wave-particle interactions in the inner magnetosphere involve resonance between the energetic radiation belt particles and electromagnetic waves. The resonance interactions are believed to be most effective in the vicinity of the geomagnetic equator, as shown in Figure 1.2(a). The characteristics of the interactions are determined by the properties of the local environment, in particular the magnetic field and particle population, as well as the wave spectrum. The interaction mechanism may be thought of in a simple sense as a wave amplifier with gain characteristics which are

functions of the environmental parameters within the interaction region. A schematic representation of such an amplifier is shown in Figure 1.2(b).

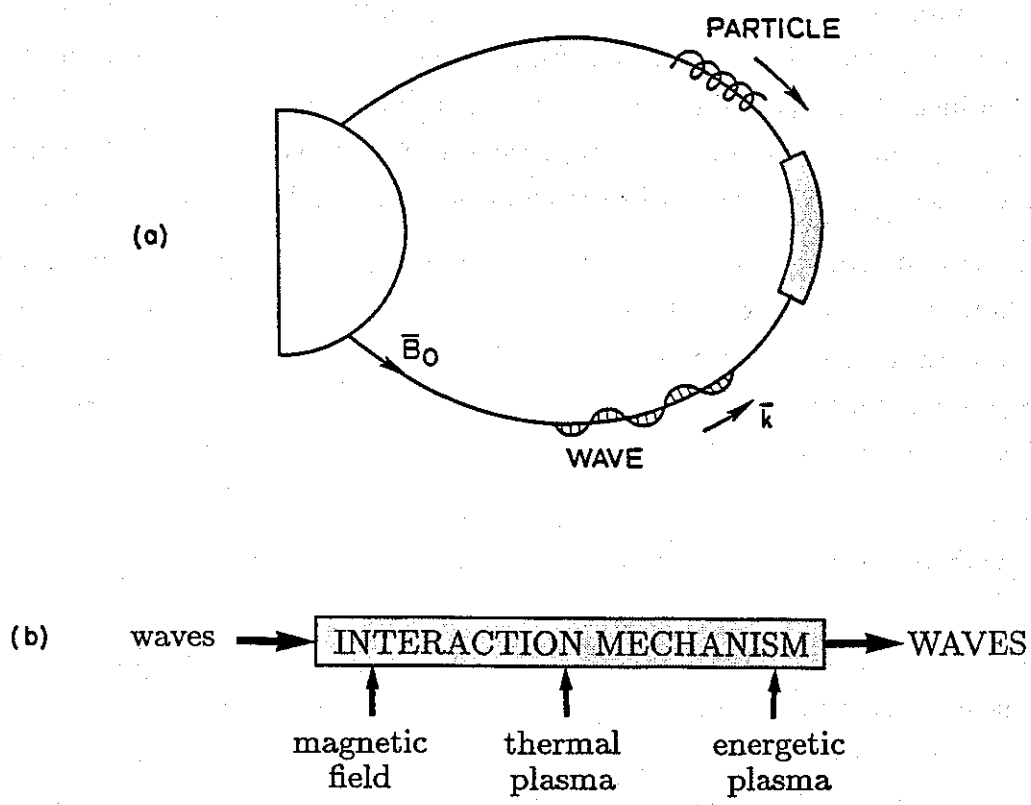


**Figure 1.2.** The gyroresonance interaction mechanism in the earth's magnetosphere. (a) The configuration of the interaction showing the interaction region. (b) A schematic representation of the interaction illustrating the role of the environmental parameters.

Experimental studies of gyroresonance interactions typically take one of two approaches. In the first, wave spectra and particle distributions are measured *in situ* using spacecraft and compared with theoretical predictions [e.g., *Kennel and Petschek*, 1966; *Lyons et al.*, 1972; *Etcheto et al.*, 1973; *Maeda and Lin*, 1981; *Church and Thorne*, 1983; *Huang et al.*, 1983; *Kimura et al.*, 1983; *Cornilleau-Wehrlin et al.*,

1985]. The second approach involves injection of coherent signals into the magnetosphere from ground-based transmitters. The signals are recorded after traversing the interaction region and analyzed for amplitude and spectral changes which result from the interaction with energetic particles [e.g., *Helliwell and Katsufrakis*, 1974; *Kimura et al.*, 1983; *Helliwell et al.*, 1986]. The first approach is often used for studies of incoherent gyroresonance processes associated with wave emissions such as plasmaspheric and mid-latitude hiss; the second is more typically applied to coherent processes associated with ELF/VLF transmitter signals and discrete emissions.

In most experimental studies, the magnetic field and plasma properties are assumed to be static over the time scale of the observation. While this assumption may be valid in many situations, the magnetosphere is ultimately a dynamic medium. A complete understanding of magnetospheric wave-particle interactions requires an assessment of the effect of dynamic changes in the environment on the interaction process.

## 1.2 METHOD OF SOLUTION

The ideal experiment for studying the role of the environmental parameters in gyroresonance interactions would involve selectively perturbing the various parameters and observing the resulting change in the wave spectrum. Since we are limited in our ability to directly manipulate the magnetosphere, a controlled experiment of this type is not currently feasible.

Similar natural perturbations do exist, however, which provide the opportunity to study the effects of environmental changes. The perturbations, known as Sudden Commencements (SC), correspond to rapid compressions (or decompressions) of the entire magnetosphere caused by changes in solar wind properties. The magnetopause can move inward as much as 2-3 $R_e$ within 2-6 minutes during a SC. The disturbance is transmitted throughout the magnetosphere in the form of hydromagnetic waves and is observed both at spacecraft altitudes and on the ground as a sudden increase or decrease in the magnetic field strength. Corresponding to the changes in magnetic field strength are changes in the magnetic field geometry, the electric field configuration, and the thermal and energetic particle distributions.

SC thus provide a natural step-like perturbation of the environmental parameters which govern the gyroresonance interaction mechanism. By measuring the wave spectrum during such an event and comparing it with the pre-event spectrum, the response of the wave generation mechanism to temporal perturbations in the environment may be inferred. The characteristics of the wave response provide the basic observational constraints necessary for development of dynamic models of gyroresonance interactions.

## 1.3 OVERVIEW AND OUTLINE OF THE THESIS

This thesis presents a new method for investigating gyroresonant wave-particle interactions in a dynamic magnetosphere based on the analysis of observed changes in wave properties associated with Sudden Commencements (SC). Changes in wave properties during SC were quantitatively characterized using an extensive data set from spacecraft and ground-based observatories. Particular emphasis was placed on observations made during the first several tens of seconds of the SC, when the changes in the magnetic field and plasma associated with the magnetospheric compression can be most accurately modeled. Measurements of both amplitude and spectral characteristics of the waves were obtained and correlated with observations of magnetic field and particle precipitation.

The observational results were then compared with predictions of gyroresonance interaction models based on both nonlinear and quasi-linear theories. Gyroresonance models have been developed primarily for a static magnetosphere, so both the theoretical basis and the model concepts were modified where necessary to apply to a dynamic magnetosphere. While the investigation is limited to the specific class of magnetospheric perturbations known as SC, the method should be applicable to a variety of other magnetospheric perturbations, particularly those which occur over similar time scales.

The remainder of the thesis is organized as follows:

Chapter 2 describes the basic background knowledge on magnetospheric physics, wave-particle interactions, and SC.

Chapter 3 contains a description of data from satellite and ground-based instruments illustrating a variety of features of wave and particle activity associated with SC. This chapter represents the primary contribution of the thesis work and provides the basic observational constraints for dynamic models of gyroresonance interactions.

In Chapter 4, the potential applications and limitations of the data are discussed and a general characterization of the data is presented.

In Chapter 5, the observations are compared with predictions of gyroresonance interaction models and implications for dynamic gyroresonance models are discussed.

Chapter 6 includes a summary of the work and suggestions for future research.

## 1.4 CONTRIBUTIONS

1) A new observational method was developed to investigate the effect of dynamic changes in the earth's magnetosphere on gyroresonant wave-particle interactions. This method is based on analysis of wave characteristics during Sudden Commencements (SC).

2) The method was used to quantitatively characterize the effect of dynamic changes in the magnetosphere on observed wave amplitudes and spectra. A data set of several hundred SC was developed for this purpose using observations from both spacecraft and ground-based observatories. The results provide the constraints necessary to modify current static models of gyroresonance interactions to apply to a dynamic magnetosphere. The observations include the first measurement of a growth rate for incoherent whistler-mode waves in the magnetosphere (0.3-2.7 dB/sec), which was found to be lower by approximately two orders of magnitude than the measured growth rate for coherent waves.

3) The theoretical wave growth rate obtained in quasi-linear models for a static magnetosphere [e.g., *Kennel and Petschek*, 1966] was modified to include for the first time the effect of a general time-dependent magnetic field perturbation. The derivation indicates that in particular cases the quasi-linear growth rate may be strongly controlled by the magnetic field perturbation.

4) Time-dependent changes in the interaction parameters which are used to characterize nonlinear models (the interaction length, the wave trapping threshold, and the bunching efficiency) were explicitly calculated for a dynamic environment using a magnetospheric model which was developed to simulate SC-induced changes in magnetic field strength and geometry.

5) The observational results were compared with predictions of both nonlinear and quasi-linear models of gyroresonance interactions. The observed increase in the occurrence rate of discrete emissions is consistent with predictions of our interaction parameter model. The observed characteristics of diffuse emissions were shown to be quantitatively comparable to predictions made using a simple quasi-linear model of wave growth during SC developed by *Perona* [1972] and provide the first experimental verification of the Perona model. The results suggest that current static models of gyroresonance interactions, when properly modified, may be used to predict properties of gyroresonance interactions in a dynamic magnetosphere.

# Chapter 2
# BACKGROUND

In this chapter, the important background concepts relevant to the work discussed in the remainder of the thesis are presented. The basic plasma and magnetospheric concepts are readily available in many textbooks and are thus reviewed only briefly here. The theories of gyroresonance interactions and relevant knowledge on SC, which are probably less familiar to the reader, are presented in greater detail.

## 2.1 THE MAGNETOSPHERE

*Magnetic field.* The earth's magnetosphere and corresponding plasma environment are shown schematically in Figure 2.1. The geometry of the magnetosphere and the location of the magnetopause are determined by the interaction of the earth's dipole magnetic field with the solar wind. The interaction compresses the field on the dayside and creates a tail-like structure on the nightside which extends in the anti-sunward direction to several tens of earth radii. The region of closed field lines extends to the magnetopause on the dayside. At high latitudes (above approximately 75° geomagnetic latitude), the field lines extending into the magnetotail do not close back onto the earth. Only wave-particle interactions associated with the closed field line region are addressed in this thesis.

The nominal magnetopause standoff distance is usually taken to be 10-11 $R_e$ at the subsolar point, but it can range from 6 $R_e$ to 14 $R_e$ [*Fairfield*, 1971] depending on

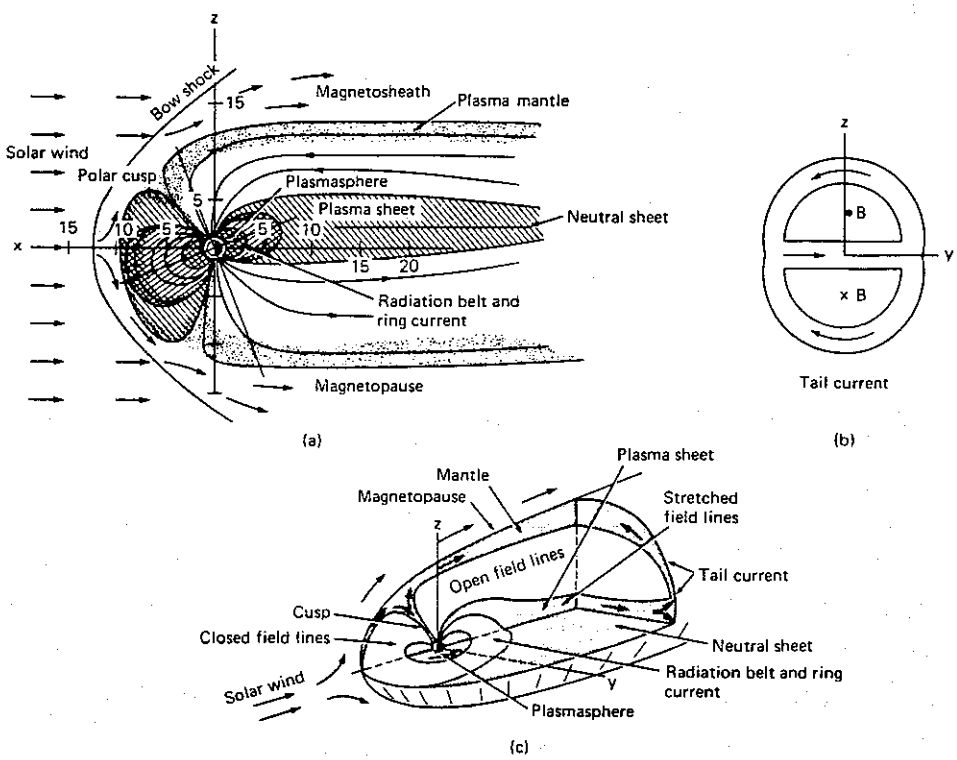


**Figure 2.1.** The geometry of the magnetosphere and plasma environment. (a) noon-midnight meridian projection. (b) tail current system as viewed from the sun. (c) three-dimensional perspective of (a) [*Lyons and Williams*, 1984].

solar wind conditions. A plot illustrating the observed variation is shown in Figure 2.2. Simple models describing the equilibrium configuration as a dynamic pressure balance between magnetic and plasma forces within the magnetosphere and similar forces in the solar wind [*Mead and Beard*, 1964; *Olson*, 1969] predict the observed magnetopause position quite accurately on the dayside and somewhat less so in the tail region [*Fairfield*, 1971].

The magnetospheric geometry corresponding to the pressure balance configuration is a direct result of currents (the Chapman-Ferraro currents) which flow on the magnetopause surface. In addition to the surface currents, a number of other current systems are known to exist throughout the interior of the magnetosphere. The most important of these are the ring current, which flows in a circular pattern in the equatorial plane in the vicinity of 6 $R_e$, and the tail current, which flows across the tail

in the equatorial plane. A number of field models have been developed which reproduce spacecraft measurements of field strength quite well throughout much of the magnetosphere (see Appendix C for a discussion of field models).

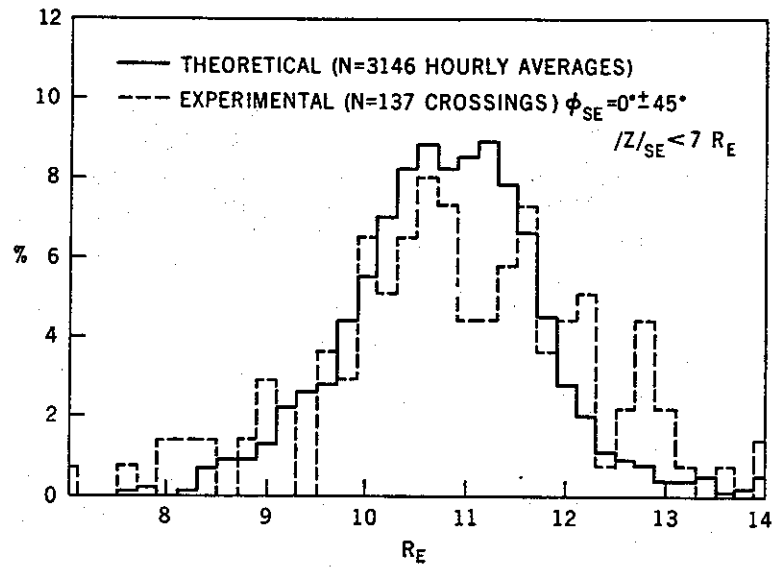


**Figure 2.2.** The distribution of the subsolar magnetopause position. The plot shows both direct measurements from spacecraft crossings and predicted values based on solar wind data [*Fairfield*, 1971].

*Thermal plasma.* The thermal plasma density in the inner magnetosphere decreases with radial distance above the ionosphere, including a steep gradient known as the plasmapause where the density drops by as much as two orders of magnitude in a distance of <2 $R_e$ [*Carpenter*, 1963]. The plasmapause location varies between equatorial distances of 2 and 7 $R_e$, depending on geomagnetic activity [*Carpenter and Park*, 1973]. A typical density profile is shown in Figure 2.3. The thermal plasma consists primarily of electrons and protons in the energy range 0.1-1 eV which originate as upward flowing particles from the ionosphere [*Lyons and Williams*, 1984].

*Energetic plasma.* In addition to thermal particles, the magnetospheric plasma includes a population of high energy (100 eV - 100 MeV) electrons and protons. The particles are trapped within the inner magnetosphere by magnetic field gradients,

forming the earth's radiation belts. Particle fluxes maximize in two regions known as the inner and outer radiation belts [*Lyons and Williams*, 1984]. Inner belt fluxes peak inside an equatorial distance of 2 $R_e$ and are quite stable. Outer belt fluxes peak near the plasmapause during geomagnetically quiet conditions and move inward during magnetic storms [*Lyons and Thorne*, 1973].

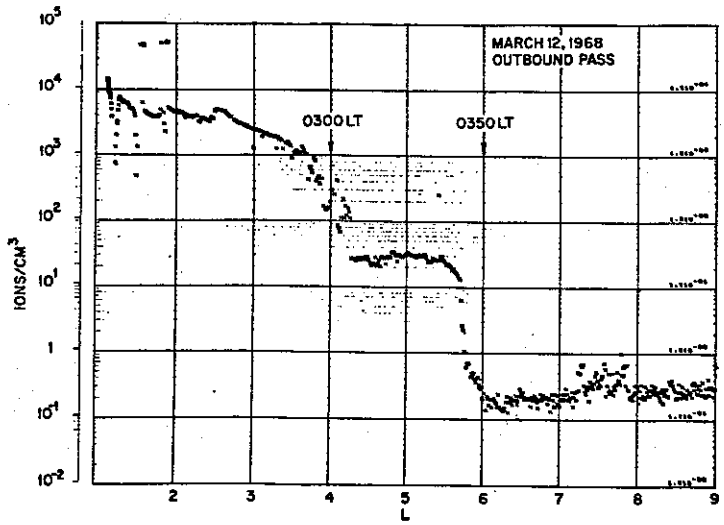


**Figure 2.3.** Typical radial profile of the thermal plasma. The steep gradient at L=4-6 is the plasmapause [*Chappel et al.*, 1971].

The trajectory of a given energetic particle in the magnetosphere can be described as a superposition of three simple motions: a gyromotion of the particle around the field line, a bounce motion along the field line between hemispheres, and a drift motion around the earth. The theory of particle motion in a magnetosphere is quite well developed and is described in many textbooks [e.g., *Schulz and Lanzerotti*, 1974]. Particle-particle collisions are rare in the radiation belts; particles would remain trapped indefinitely in the absence of other scattering processes. Interactions with plasma waves thus provide an important mechanism for scattering and loss of radiation belt particles.

*Plasma waves.* The magnetosphere supports a variety of plasma wave modes. Due to the spatial variations in magnetic field strength and plasma density, the observed

modes and the characteristic spectrum vary considerably with location. In the inner magnetosphere, wave activity is a function of radial position, local time, and latitude. The plasmapause tends to be an important boundary dividing regions of distinctly different wave activity [*Carpenter et al.*, 1968].

Within the plasmasphere, the wave spectrum consists primarily of plasmaspheric hiss, whistlers, and discrete emissions. Plasmaspheric hiss is an incoherent whistler-mode wave emission with a typical bandwidth of a few hundred Hz and a peak spectral power density near several hundred Hz. It is believed to be generated through gyroresonance interactions with radiation belt electrons [*Thorne et al.*, 1973]. Interactions between plasmaspheric hiss and radiation belt particles are thought to be an effective mechanism for continuous scattering and loss of energetic electrons from the plasmasphere into the ionosphere [*Lyons and Thorne*, 1973]. Whistlers, signals from ground-based VLF transmitters, and emissions triggered by interactions of these waves with energetic particles are are all known to cause significant particle scattering and loss [*Rosenberg et al.*, 1971; *Imhof et al.*, 1983; *Voss et al.*, 1985].

Outside the plasmapause, plasmaspheric hiss is generally not observed and whistlers are less common. A detailed spacecraft study [*Burtis and Helliwell*, 1976] showed that bandlimited discrete emissions, known collectively as magnetospheric chorus, and broadband hiss are the prevalent forms of whistler-mode emission outside the plasmapause in the region 0300-1500 MLT. The frequency of emissions appears to be more closely related to the equatorial electron gyrofrequency along the field line of observation than to the local electron gyrofrequency, suggesting an equatorial generation region [*Dunckel et al.*, 1969; *Burtis and Helliwell*, 1976]. Since the region of maximum chorus occurrence corresponds quite closely to the zone of hard electron precipitation reported by *Hartz and Brice* [1967], it is believed that chorus emissions play an important role in controlling the structure and dynamics of the outer radiation belt. *Park et al.* [1981] found that the occurrence of chorus emissions at ground stations was correlated with spacecraft measurements of energetic particle flux. Associations between chorus and energetic particles have also been observed on satellites and balloons [*Oliven and Gurnett*, 1968; *Rosenberg et al.*, 1981; *Rosenberg et al.*, 1987].

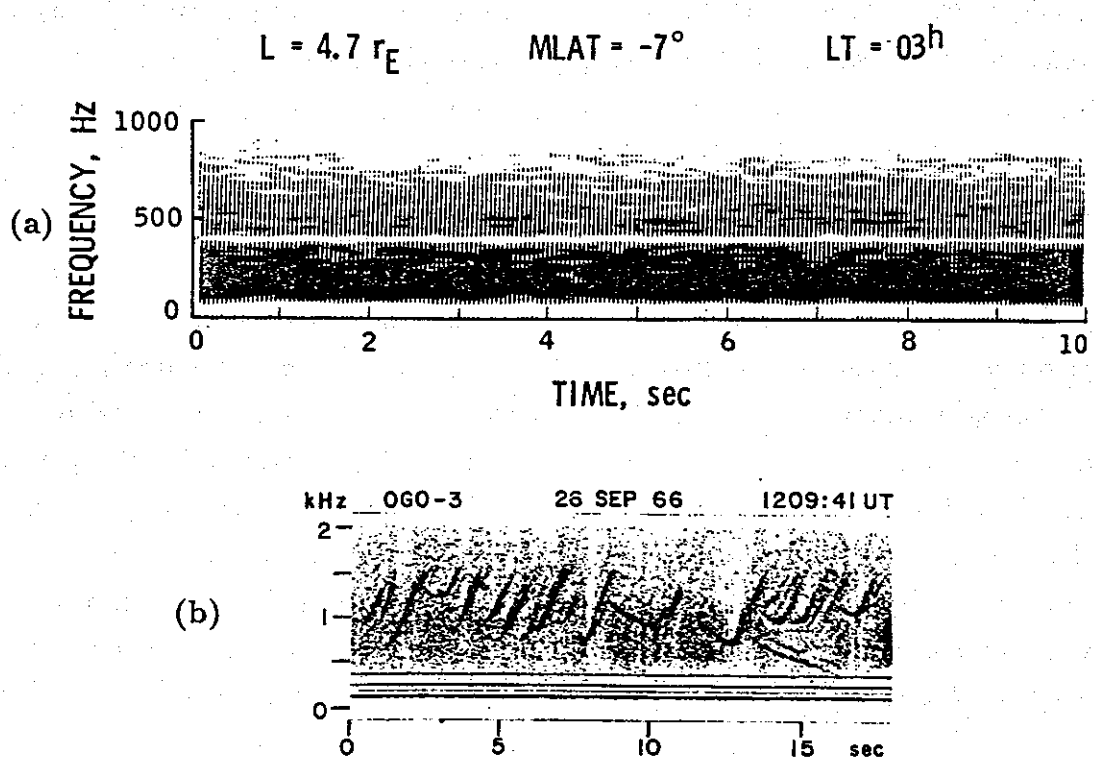


**Figure 2.4.** Examples of dynamic spectra for wave phenomena observed in the inner magnetosphere. (a) Plasmaspheric hiss (lack of data at 400 Hz results from an interference filter on the spacecraft) [*Thorne et al.*, 1973]. (b) Magnetospheric chorus showing discrete emissions and background hiss measured by the OGO-3 satellite at L=7.8, geomagnetic latitude 40°, and 1210 LT [*Burtis and Helliwell*,1976].

Examples of spectra for wave phenomena observed at satellite altitudes both inside and outside the plasmapause are shown in Figure 2.4. The wave spectra may be classified as *diffuse* and *discrete*. Diffuse emissions are relatively broadband and incoherent while discrete emissions are narrowband and coherent. The classification will be used loosely in this thesis. The emissions in Figure 2.4(a) are primarily diffuse while Figure 2.4(b) shows evidence of both diffuse and discrete emissions.

Waves which propagate within field-aligned electron density enhancements or *ducts* in the magnetosphere are of particular interest. The refractive index variation within a duct confines the wave normal to small angles, effectively guiding the wave along the magnetic field direction in a manner similar to the guiding of light by optical

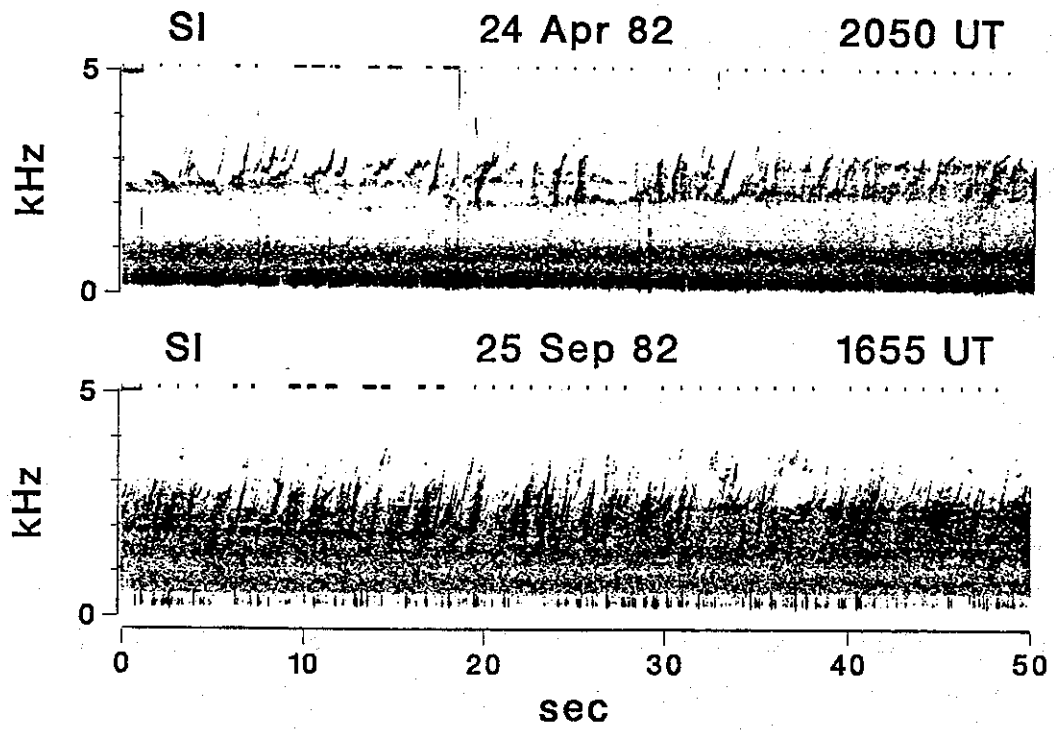


**Figure 2.5.** Examples of dynamic spectra for wave phenomena observed at high-latitude ground stations. Both examples show evidence of diffuse and discrete emissions.

fibers. The limitation of the wave normal to small angles facilitates transmission through the ionosphere [*Helliwell*, 1965]. It is generally believed that ELF/VLF waves observed with ground-based receivers propagate through the magnetosphere in ducts. Figure 2.5 shows typical spectra for wave phenomena observed at high-latitude ground stations. In both examples, diffuse and discrete emissions are evident. Waves spectra observed at ground stations are similar in many ways to wave spectra observed at satellite altitudes (as can be seen by comparing Figures 2.4 and 2.5) although distinct differences do exist [*Carpenter et al.*, 1968; *Edgar*, 1972; *Bell et al.*, 1981].

## 2.2 GYRORESONANCE INTERACTIONS

### 2.2.1 *THE WHISTLER MODE*

The dispersion relation for electromagnetic waves in a cold, collisionless, homogeneous, infinite plasma with a homogeneous static magnetic field $\mathbf{B_0}$ is given by [*Ratcliffe*, 1959]

$$n^2 = 1 - \frac{\frac{{\omega_p}^2}{\omega^2}}{1 + \frac{{\omega_H}^2 \sin^2\theta}{2({\omega_p}^2 - \omega^2)} \mp \left[ \left( \frac{{\omega_H}^2 \sin^2\theta}{2({\omega_p}^2 - \omega^2)} \right)^2 + \frac{{\omega_H}^2}{\omega^2} \cos^2\theta \right]^{\frac{1}{2}}} , \tag{2.2.1}$$

where $n$ is the refractive index, $\omega_p$ is the plasma frequency, $\omega_H$ is the electron gyrofrequency, $\omega$ is the wave frequency, and $\theta$ is the angle between the wave normal and the magnetic field vector. The two characteristic waves, corresponding to the two signs before the square root, are elliptically polarized. The characteristic wave corresponding to the minus sign is known as the *whistler mode.* Both the phase and group velocities of whistler-mode waves in the magnetosphere are less than the vacuum velocity of light. Equation 2.2.1 simplifies considerably when it is assumed that $\mathbf{k} \| \mathbf{B_0}$, which is approximately true for ducted propagation. Under this assumption, the whistler-mode waves are right-hand circularly polarized and the wave field vectors rotate in the same sense as the electrons.

### 2.2.2 *THE BASIC INTERACTION*

Wave-particle interactions in the inner magnetosphere involve resonance between energetic charged particles and waves. Resonance occurs when the Doppler-shifted wave frequency seen by the particles is an integer multiple of the particle gyrofrequency [e.g., *Helliwell*, 1965]. For electrons, the resonance condition is given by

$$\omega - \mathbf{k} \cdot \mathbf{v}_{\|} = \mathrm{m}\omega_H \qquad \mathrm{m} = 0, \pm 1, \pm 2, \pm 3, \ldots \ , \tag{2.2.2}$$

where $\omega$ is the wave frequency, $\mathbf{k}$ is the wave vector, $\mathbf{v}_{\|}$ is the parallel component of the electron velocity, and $\omega_H$ is the electron gyrofrequency. The interactions of primary interest in magnetospheric physics are the m=0 longitudinal (Landau) and m=1 cyclotron resonances. In longitudinal resonance, the wave phase velocity is nearly equal to the particle parallel velocity and the waves and particles travel in the same direction. In cyclotron resonance with whistler-mode waves ($\omega < \omega_H$), the Doppler-shifted frequency of the wave (in the reference frame of the particle) is equal to the particle gyrofrequency and the waves and particles travel in opposite directions. Longitudinal resonance has been proposed as a mechanism for the generation of auroral hiss [e.g., *Maggs*, 1976] and invoked to explain the observed lower-frequency cutoff of plasmaspheric hiss [*Thorne et al.*, 1973], but was shown by *Tkalcevic et al.* [1984] to play a relatively minor role in wave-particle interactions associated with ducted waves.

Boundary conditions imposed by the ionosphere as well as spatial variations in the magnetic field and thermal plasma add considerable complexity to the resonance phenomenon. In particular, magnetic field inhomogeneity and the corresponding gyrofrequency variation imply that the resonance condition for a given wave frequency can be satisfied only locally. Since the inhomogeneity is minimum at the magnetic equator, the spatial extent of the resonance region is largest near the equator. Most theories of gyroresonance interactions and wave growth in the magnetosphere exploit this fact by assuming that the interaction is limited to an *interaction region* in the vicinity of the magnetic equator and that interactions outside this region are less important.

Two classes of theories have been developed to describe magnetospheric gyroresonance interactions. The first class, known as nonlinear theories, are generally applied to discrete emissions. The second class, known as quasi-linear theories, are mostly applied to diffuse emissions (see Figures 2.4-2.5 for examples of discrete and diffuse emissions). The purpose of this thesis is to study the applicability of the theories to natural wave activity throughout the magnetosphere and in particular to investigate the effectiveness of the theories in describing wave generation in a dynamic environment. The theories are described in more detail in the following sections.

### 2.2.3 *NONLINEAR THEORIES*

*General description.* Nonlinear theories are based on explicit calculations of particle trajectories under the influence of wave fields and may be used to study both wave growth and particle scattering. The approach generally requires use of numerical simulations to provide solutions to the nonlinear equations of motion. It is particularly well suited to studies of interactions with coherent monochromatic waves (e.g., signals from ground-based transmitters), but has only recently been applied to more complicated spectral forms [*Chang et al.*, 1983; *Inan*, 1987] due to the complexity of the simulation. The advantage of this approach has been the ability to include the effects of coherent phase bunching of the electrons, which are believed to play a primary role in generation of coherent wave forms such as chorus and discrete emissions [*Helliwell and Inan*, 1982].

*Basic theory.* Nonlinear theories start with the equations of motion for an individual electron in a magnetic field subject to a wave perturbation. The force applied on the electron by the wave field is given by the Lorentz equation

$$\mathbf{F} = -e(\mathbf{E}_w + \mathbf{v} \times \mathbf{B}_w) \ , \tag{2.2.3}$$

where $\mathbf{E}_w$ and $\mathbf{B}_w$ are the wave electric and magnetic fields and $\mathbf{v}$ is the electron velocity. Under the condition of a magnetic field which is inhomogenous in the z-direction, the equations of motion for an electron subject to a longitudinal whistler-mode wave are [*Inan*, 1977]

$$\frac{dv_\parallel}{dt} = (\frac{eB_w}{m})v_\perp \sin\phi - \frac{v_\perp}{2\omega_H}\frac{d\omega_H}{dz} \tag{2.2.4}$$

$$\frac{dv_\perp}{dt} = -(\frac{eB_w}{m})(v_\parallel + \frac{\omega}{k})\sin\phi + \frac{v_\perp v_\parallel}{2\omega_H}\frac{d\omega_H}{dz} \tag{2.2.5}$$

$$\frac{d\phi}{dt} = \omega_H - \omega - kv_{\parallel} - (\frac{eB_w}{m})(v_{\parallel} + \frac{\omega}{k})\frac{\cos\phi}{v_{\perp}} \,. \tag{2.2.6}$$

where $v_{\parallel}$ and $v_{\perp}$ are the magnitudes of the parallel and perpendicular components of the electron velocity along $-\mathbf{B_0}$, $\phi$ is the angle between $v_{\perp}$ and $-\mathbf{B}_w$, and $z$ is distance along $-\mathbf{B_0}$. The terms involving $B_w$ describe the Lorentz force on the electron due to the wave field. The terms involving $\frac{d\omega_H}{dz}$ describe the adiabatic forces on the electron due to the magnetic field inhomogeneity.

*Simulations.* According to the hypothesized mechanism, an initially uniform phase distribution of electrons in resonance with a coherent wave of sufficient amplitude is phase bunched by the potential well of the wave to produce a phase coherent distribution. The phase bunched electrons constitute a current which radiates coherently and provides a positive feedback for the waves. If the feedback gain is large enough, the system is unstable and the wave amplitude grows in time until a saturation limit is reached, as shown in Figure 2.6. Falling or rising emissions result from the changing resonance condition as the resonant electrons move respectively toward or away from the equator [*Helliwell*, 1967].

The Lorentz force equation represents the starting point for numerical simulations. A number of nonlinear particle simulations have been developed in an effort to understand the coherent gyroresonance interaction. *Omura and Matsumoto* [1982] discussed a completely self-consistent model for nonlinear interactions in a homogeneous magnetic field. Other models [e.g., *Helliwell*, 1967; *Dysthe*, 1972; *Nunn*, 1974; *Vomvoridis et al.*, 1982; *Helliwell and Inan*, 1982], while not self-consistent, assume an inhomogeneous field and are thus more applicable to the magnetosphere. Recent simulation work by *Carlson* [1987] indicates that wave growth is largely produced by electrons having a narrow but varying range of parallel velocities that are selected by the wave as it is amplified and progresses through the equatorial interaction region. Carlson's simulations provide quantitative predictions that are similar to observed characteristics of coherent wave growth associated with signals injected from ground-based transmitters.

*Interaction parameters.* The importance of coherent and nonlinear effects in gyroresonance phenomena can be described by three parameters which characterize the physics of the interaction [*Helliwell*, 1967; *Inan et al.*, 1978; *Inan et al.*, 1983]. The parameters are the interaction length ($L_I$), the trapping threshold ($B_T$), and the bunching efficiency ($\Gamma_B$).

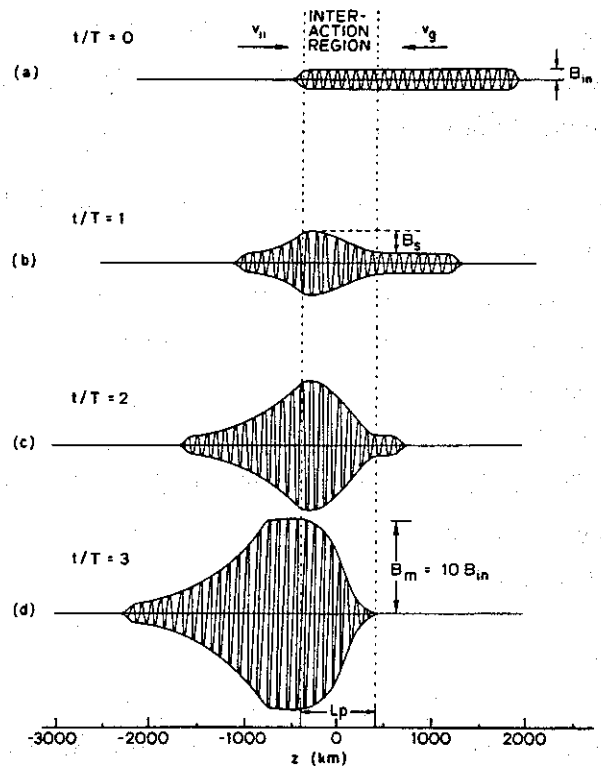


**Figure 2.6.** Schematic diagram of wave growth resulting from the coherent gyroresonance interaction. The wave pulse travels to the left with velocity $v_g$ and electrons travel to the right with velocity $v_\parallel$. The envelope of the wave packet represents the wave amplitude and the x-axis scale refers to distance in km from the geomagnetic equator. Growth is approximately exponential in time until saturation is reached and is self-sustaining after that point [*Helliwell and Inan*, 1982].

The interaction length $L_I$ is defined as the length of the region over which the phase $\phi$ for an unperturbed particle varies by $\pi$ radians. Using the resonance condition (Equation 2.2.2), the interaction length is given by the integral

$$\int_{-L_I/2}^{+L_I/2} \left(\omega_H - \omega - kv_\parallel^u\right) \frac{dz}{v_\parallel^u} \simeq \pi \,, \tag{2.2.7}$$

where $v_\parallel^u$ is the electron parallel velocity in the absence of the wave field and $z$ represents arc length along the field line.

The trapping threshold $B_T$ describes the wave amplitude necessary to trap particles in the potential well of the wave. For wave amplitudes larger than $B_T$, the wave field term in the equations of motion dominates and particle trajectories are significantly perturbed; for wave amplitudes less than $B_T$, the inhomogeneity term dominates and particle trajectories are approximately adiabatic. The threshold level corresponds to the transition from linearity to nonlinearity in the equations of motion. The threshold field is given by [*Inan et al.*, 1983]

$$B_T = \frac{m}{e}\left(\frac{1}{kv_\perp}\right)|\Pi(z)|\,, \tag{2.2.8}$$

where

$$\Pi(z) = -\frac{v_\parallel}{2N_e}\left(\omega_H - \omega\right)\frac{dN_e}{dz} + \left(\frac{3}{2} + \frac{\omega_H - \omega}{2\omega_H}\tan^2\alpha\right) v_\parallel \frac{d\omega_H}{dz} \tag{2.2.9}$$

describes the inhomogeneity of the magnetic field. $N_e$ is the electron density and $\alpha$ is the pitch angle.

The bunching efficiency $\Gamma_B$ provides an indication of the effectiveness of the phase bunching process and is given by $\Gamma_B = \frac{T_R}{T_B}$, where

$$T_B = \frac{\pi}{2}\left(\frac{e}{m}B_w k v_\perp\right)^{-\frac{1}{2}} \tag{2.2.10}$$

characterizes the time over which phase bunching occurs [*Helliwell and Inan*, 1982] and

$$T_R = \int_{-L_I/2}^{+L_I/2} \frac{dz}{v_{\parallel}{}^{u}} \tag{2.2.11}$$

is the transit time through the resonance region with length $L_I$. For $\Gamma_B << 1$, the particles are only partially phase bunched within the resonance period. The importance of phase bunching in determining the radiation characteristics of the interaction increases with $\Gamma_B$.

### 2.2.4 *QUASI-LINEAR THEORIES*

*General description.* Quasi-linear theories involve a stochastic treatment of the wave-particle interaction and describe the corresponding perturbation of electron trajectories as a diffusion process. This approach allows for a primarily analytic description of the interaction and is applicable only to incoherent wave distributions. It has been applied to describe the equilibrium wave and particle distributions throughout the magnetosphere [*Kennel and Petschek*; 1966; *Lyons et al.*, 1972; *Etcheto et al.*, 1973; *Huang et al.*, 1983; *Church and Thorne*, 1983; *Cornilleau-Wehrlin et al.*, 1985; *Korth et al.*, 1985; *Silevitch and Rothwell*, 1986]. However, as coherent effects are not included, the theory cannot describe the many important effects associated with discrete emissions and artificial transmitter signals.

*Basic theory.* The common starting point for quasi-linear theories is the collisionless Boltzmann or Vlasov equation applied to an infinite plasma [*Chen*, 1974],

$$\frac{\partial f(\mathbf{v})}{\partial t} + \mathbf{v} \cdot \nabla f(\mathbf{v}) - \frac{e}{m}\left[\mathbf{E} + \frac{\mathbf{v} \times \mathbf{B}}{c}\right] \cdot \frac{\partial f(\mathbf{v})}{\partial \mathbf{v}} = 0 \,, \tag{2.2.12}$$

where $f(\mathbf{v})$ is the electron distribution function, $e$ is the electron charge, $m$ is the electron mass, and $\mathbf{E}$ and $\mathbf{B}$ are the electric and magnetic fields. The equation describes the dynamics of the particle distribution under the influence of arbitrary electric and magnetic fields, which are governed by the Maxwell equations. A particular solution

to the set of equations is obtained by introducing periodic perturbations in the particle distribution and fields everywhere in space and keeping only the linear terms. With the assumption that only particles satisfying the gyroresonance condition contribute to the interaction, a solution for the temporal wave growth rate is obtained, given by [*Kennel and Petschek*, 1966]

$$\gamma = \pi\omega_H\left(1 - \frac{\omega}{\omega_H}\right)^2 \eta(E_R)\left[A(E_R) - A_c\right], \tag{2.2.13}$$

where

$$\eta(E_R) = 2\pi {v_R}^3 \int_0^{\frac{\pi}{2}} \frac{\sin\alpha}{\cos^3\alpha} F(\alpha, E) d\alpha \tag{2.2.14}$$

is the fraction of the total particle distribution which satisfies the resonance condition,

$$A(E_R) = \frac{\int_0^{\frac{\pi}{2}} \frac{\sin^2\alpha}{\cos^4\alpha} \frac{\partial F(\alpha,E)}{\partial\alpha} d\alpha}{2\int_0^{\frac{\pi}{2}} \frac{\sin\alpha}{\cos^3\alpha} F(\alpha, E) d\alpha} \tag{2.2.15}$$

is a function that describes the anisotropy in the distribution of particle pitch angles, and

$$A_c = \frac{\omega}{\omega_H - \omega} \tag{2.2.16}$$

is called the critical anisotropy. The distribution function terms $F$ and $\frac{\partial F}{\partial \alpha}$ are evaluated subject to $E_\parallel = E_R$, where $E_R$ is the electron resonant energy, prior to integration. The plasma is unstable when the anisotropy $A$ is greater than the critical anisotropy $A_c$, leading to wave growth [*Kennel and Petschek*, 1966].

The particle distribution $F$ obeys a Fokker-Planck equation, which may be written as a diffusion equation of the form

$$\frac{\partial F}{\partial t} = \frac{1}{\sin\alpha}\frac{\partial}{\partial \alpha}\left(D_{\alpha\alpha}\sin\alpha\frac{\partial F}{\partial \alpha}\right), \tag{2.2.17}$$

where $D_{\alpha\alpha}(\alpha)$ is the diffusion coefficient. Note that only the coefficient for pure pitch angle diffusion is included since pitch angle diffusion dominates velocity space diffusion for wave frequencies much less than the electron gyrofrequency [*Lyons and Williams*, 1984]. The diffusion coefficient is directly proportional to the power spectral density of the waves [*Inan*, 1987].

When quasi-linear theory is used to model wave-particle interactions in the magnetosphere, a number of assumptions and approximations based on empirical constraints must be introduced. In particular, particle loss in the ionosphere must be balanced by a source, wave growth and particle scattering must be properly integrated along the wave propagation path, and wave loss through the ionosphere should be included. *Kennel and Petschek* [1966] averaged spatially-dependent quantities over a bounce period in their classic theory describing the limit of stably trapped particle fluxes in the radiation belts. They found that development of an anisotropic distribution as a result of particle precipitation losses results in wave growth that in turn scatters particles and reduces the anisotropy. This feedback process results in the establishment of a stable equilibrium flux.

*Etcheto et al.* [1973] refined the theory of *Kennel and Petschek* [1966] and used it to obtain a better agreement with observations. More recently, *Maeda and Lin* [1981] and *Cornilleau-Wehrlin et al.* [1985] have used the Kennel-Petschek theory to calculate predicted wave spectra in specific cases and found that they agree well with observations. *Davidson and Chiu* [1986] developed a set of three coupled differential equations which describe the temporal evolution of the particle flux, diffusion rate, and wave growth rate and calculated the characteristic oscillations about the equilibrium values. However, a satisfactory application of quasi-linear theory to the generation of plasmaspheric hiss, for example, has yet to be obtained [*Huang et al.*, 1983; *Church and Thorne*, 1983], despite a widespread belief that the basic method is valid [*Lyons and Williams*, 1984]. Moreover, recent work by *Helliwell et al.* [1986] suggests the possibility that diffuse emissions such as hiss may be generated entirely

through coherent interactions. Such problems illustrate the complexity of the interaction process and underscore the need for experimental verification of the many assumptions within the theory.

A few attempts have been made at applying the Kennel-Petschek quasi-linear theory to situations in which the ambient magnetic field has a time varying component. *Coroniti and Kennel* [1972] addressed the role of hydromagnetic waves in controlling electron precipitation by introducing a small sinusoidal magnetic field fluctuation into the Kennel-Petschek theory. They found that such fluctuations can strongly modulate the whistler-mode wave amplitudes, leading to observable precipitation pulsations. *Perona* [1972], using a similar approach, added a perturbation which was linear in time in an effort to explain observed precipitation enhancements during SC. The results obtained by *Perona* [1972] will be discussed at length in Chapter 5.

## 2.3 SUDDEN COMMENCEMENTS

### 2.3.1 *INTRODUCTION*

Impulsive or steplike changes in the magnitude of the geomagnetic field which are observed on a global scale are known as Sudden Impulses (SI). These changes may be either positive or negative and represent a rapid expansion or compression of the entire geomagnetic field. In many cases, sudden impulses are followed by geomagnetic storms and are then designated sudden storm commencements (SSC or SC). The distinction between SI and SC is somewhat arbitrary and many authors have suggested that there is no difference between the initial disturbance associated with SI and SC [*Matsushita*, 1962]. We will use the term SI unless the more specific term SC is warranted.

Impulsive global magnetic events were of great interest to the pioneers of magnetospheric research. *Chapman and Ferraro* [1931] suggested early on that they could result from disturbances of the geomagnetic field by interplanetary phenomena. It is now well accepted that sudden changes in the momentum of the solar wind associated

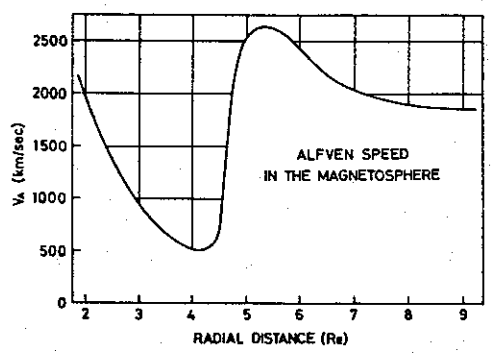


**Figure 2.7.** Alfvén wave speed in the magnetosphere for relatively undisturbed daytime conditions [*Nishida*, 1978].

with shocks and discontinuities can produce the compression of the magnetosphere that is manifested as a sudden impulse [*Nishida*, 1978]. Observations have shown that such solar wind disturbances are indeed associated with SI [*Burlaga and Ogilvie*, 1969; *Patel and Coleman*, 1970]. Early workers studied the magnetic signatures of SC in great detail and much is known about the response of the geomagnetic field to these disturbances, although many other aspects are still poorly understood. Interest in SC has been revived recently, due in part to the need to understand solar wind-magnetosphere coupling processes.

### 2.3.2 *MORPHOLOGY*

The pressure equilibrium condition which determines the magnetopause standoff distance may be upset by changes in the solar wind momentum associated with shocks and discontinuities, and the magnetopause position must be adjusted to maintain the dynamic pressure balance. Satellite observations show that the geocentric distance of the magnetopause at the subsolar point can change as much as 2-3 $R_e$ from an initial radius of 8-12 $R_e$ [*Nishida and Cahill*, 1964; *Kaufmann and Walker*, 1974; *Knott et al.*, 1982] in a period of 2-6 min. The adjustment is thought to occur adiabatically [*Baumjohann et al.*, 1983]. *Burlaga and Ogilvie* [1969] found that SI were associated with a variety of shock and discontinuity structures but found no relation between the shock speed, thickness, or type and the rise time of the SI.

The response of the geomagnetic field to such disturbances is complex but reasonably well understood (see *Nishida* [1978] for an overview or *Wilken et al.* [1982] for a brief discussion). Compressional hydromagnetic waves are generated along the magnetopause as a result of the solar wind disturbance and propagate isotropically inward [*Tamao*, 1975]. These are fast magnetosonic waves with a propagation speed slightly higher than the local Alfvén speed. Near the magnetopause, the magnitude of the disturbance may be comparable to the ambient magnetic field so that a nonlinear wave would be expected which, for a positive SI, would propagate as a shock [*Nishida and Cahill*, 1964]. Both field line curvature and nonuniformities couple the magnetosonic mode to the transverse Alfvén mode [*Tamao*, 1969; *Chen and Hasegawa*, 1974a], generating field-aligned hydromagnetic waves that propagate at the local Alfvén speed. Typical Alfvén speeds at the equator are shown plotted as a function of geocentric distance in Figure 2.7. The large decrease in Alfvén speed near 5 $R_e$ results from the sudden increase in mass density moving inward across the plasmapause. Consequently, the propagation speed for the magnetosonic wave is quite small within the plasmasphere compared to that of the field-aligned Alfvén wave outside the plasmapause and the Alfvén wave generally reaches the ionosphere at polar latitudes several tens of seconds before the magnetosonic wave arrives at the equatorial ionosphere [*Ondoh*, 1971; *Araki*, 1977].

The initial magnetic signal observed on the ground is generated from currents in the ionosphere driven by the electric field of the hydromagnetic wave [*Nishida*, 1964; *Schutz et al.*, 1974; *Newton et al.*, 1978]. Observations of a well-defined minimum in the amplitude of SI magnetic perturbations at magnetic latitudes near 20°-30° [*Wilson and Sugiura*, 1961] are in general agreement with the fact that the Hall conductivity at high latitudes and the Cowling conductivity near the equator are much larger than conductivities at middle latitudes [*Araki*, 1977]. The electric field generated in the ionosphere couples to the earth-ionosphere waveguide where it propagates at nearly the free-space speed of light [*Kikuchi et al.*, 1978; *Kikuchi and Araki*, 1979a; *Kikuchi and Araki*, 1979b; *Kikuchi*, 1986], explaining the observed nearly simultaneous onset of the initial magnetic perturbation at all latitudes and local times [*Matsushita*, 1962]. These currents decay with the disappearance of the original hydromagnetic

bance, but longer term modifications to the geomagnetic field may continue as a result of enhanced convection in the outer magnetosphere and modification of the Chapman-Ferraro current on the magnetopause as well as subsequent development of the ring and tail currents [*Araki*, 1977].

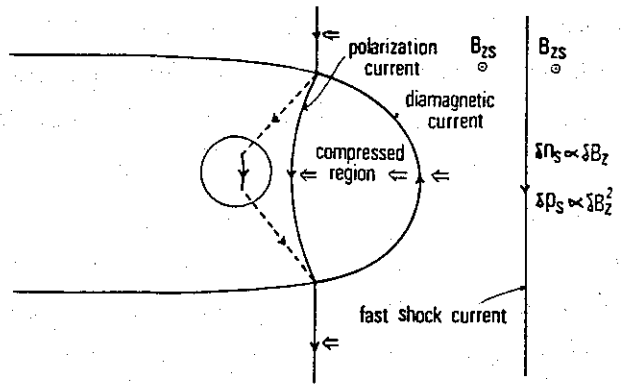


**Figure 2.8.** Transient electric currents and plasma drifts during SC. Open arrows illustrate plasma drifts and dashed lines indicate field aligned current systems. Ionospheric Hall currents are not shown [*Tamao*, 1975].

Associated with the inwardly propagating magnetosonic wave front is a dusk to dawn polarization electric field [*Tamao*, 1975] which, when coupled to the transverse Alfvén wave, determines the polarization of the electric field that is impressed on the ionosphere. This field generates a dusk to dawn Pederson current and associated Hall current systems which connect back to the currents on the magnetosonic wavefront and the magnetopause through field-aligned currents associated with the Alfvén wave [*Tamao*, 1975]. These field and current systems and the corresponding plasma drifts are shown in Figure 2.8. As the magnetosonic wave passes the earth, the electric field in the outer magnetopause returns to the dawn-dusk configuration, though typically at an enhanced level [*Araki*, 1977].

### 2.3.3 *OBSERVATIONAL CHARACTERISTICS*

*Magnetic field.* The response of the magnetic field to SI both on the ground and at satellite altitudes has been well documented and forms the basis for most of the current knowledge of SI mechanisms.

SI are usually identified in ground magnetograms by a sudden change in the H component (horizontal, geomagnetic north) of the magnetic field [e.g., *Wilson and Sugiura*, 1961; *Matsushita*, 1962]. Positive changes are observed about twice as often as negative changes [*Nishida and Cahill*, 1964]. Linear polarization of the disturbance vector predominates near the equator [*Wilson and Sugiura*, 1961] while elliptic polarization is common at high latitudes [*Wilson and Sugiura*, 1961; *Patel and Cahill*, 1974], although there is some disagreement about the latter conclusion [*Matshushita*, 1962; *Araki and Allen*, 1982]. In most events, a negative impulse known as a preliminary reverse impulse (PRI) precedes the main impulse (MI) at high and low latitudes, but is not observed at middle latitudes [*Araki*, 1977]. The combination of this delay with the polarization relations led early workers to conclude that the PRI is the signature of the Alfvén wave arriving in the auroral region, as discussed in the previous section. The onset of SC is nearly simultaneous around the world, but the amplitude varies with latitude and local time. A statistical study of SC [*Mayaud*, 1975] showed a mean rise time, defined as the time interval between the onset of the disturbance and the first extreme in the H component, of 4 min and a typical H component amplitude of 10-30 $\gamma$. Histograms of rise time and amplitude are shown in Figures 2.9 and 2.10.

The magnetic signature observed at satellite altitudes is distinctly different from that seen on the ground, due in large part to the absence of ionospheric current effects. The nearly simultaneous onset of the initial magnetic perturbation seen at ground stations is not observed at satellite altitudes. *Wilken et al.* [1982] and *Kuwashima and Fukunishi* [1985] measured the relative onset time of SC using geostationary satellites separated in local time and found differences of up to 3 min between the onset time at local noon and midnight. The observed distribution for a number of such measurements is shown in Figure 2.11. *Wilken et al.* [1982] calculated the azimuthal propagation velocity of the disturbance in one case to be 910 km/sec, consistent with

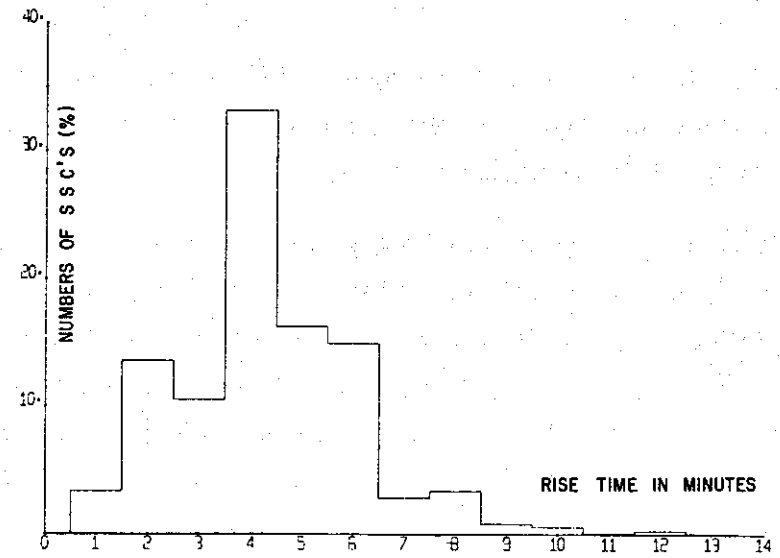


**Figure 2.9.** Rise time of SC observed at ground stations. The study was based on 2462 events from the period 1868-1967 [*Mayaud*, 1975].

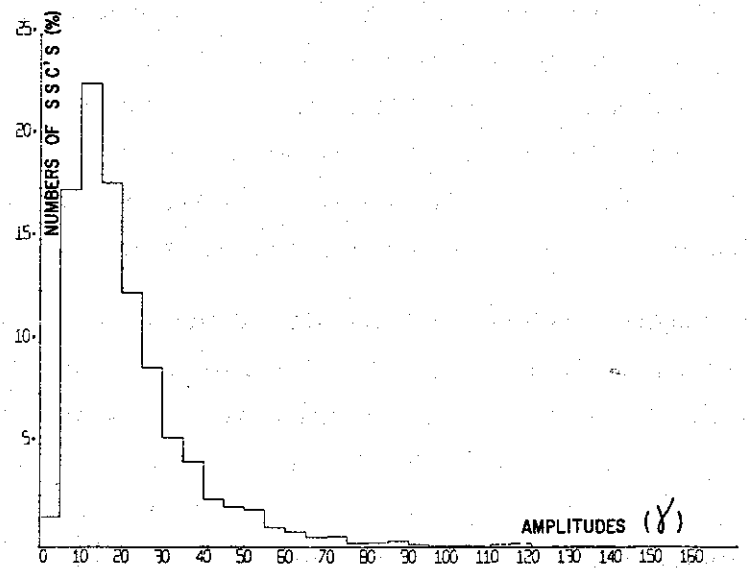


**Figure 2.10.** Amplitude of SC observed at ground stations. The study was based on 2462 events from the period 1868-1967 [*Mayaud*, 1975].

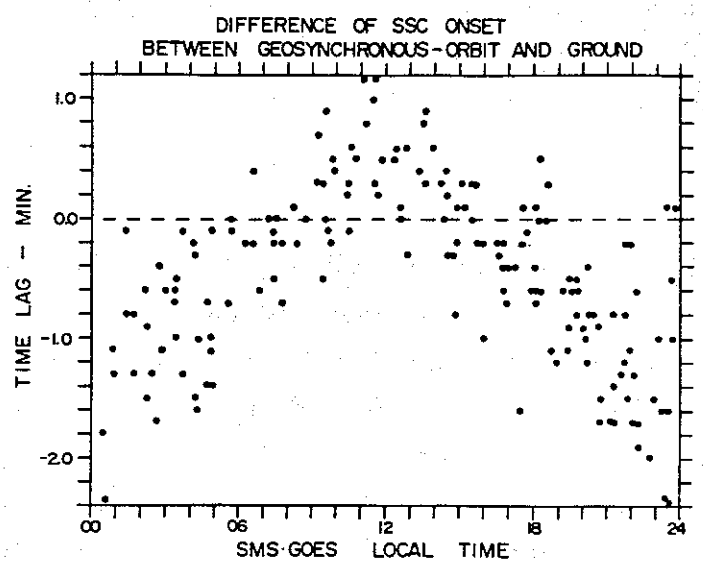


**Figure 2.11.** Onset time of SC observed at geosynchronous alititude. Points are plotted as a function of spacecraft local time and the time lag is referenced to the onset of the ground perturbation [*Kuwashima and Fukunishi*, 1985].

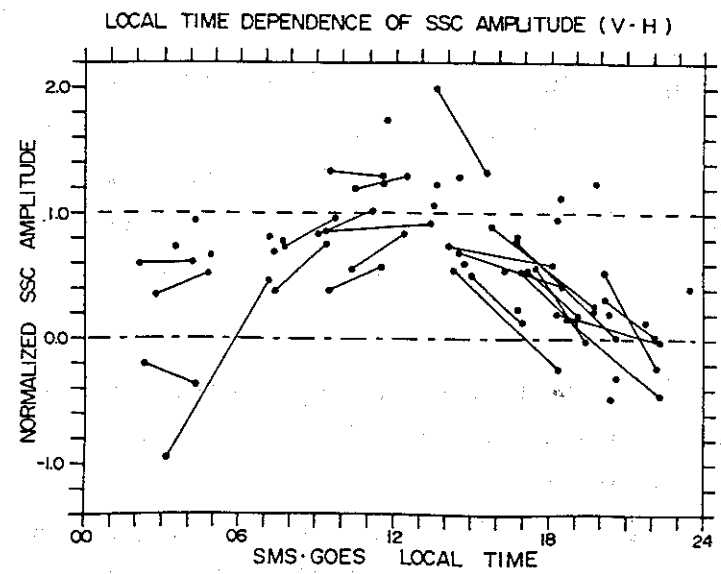


**Figure 2.12.** Amplitude of SC observed at geosynchronous altitude. Points are plotted as a function of spacecraft local time, normalized by the ground amplitude. The lines identify multiple-spacecraft observations for a given event [*Kuwashima and Fukunishi*, 1985].

the expected value for a magnetosonic wave. *Kokubun* [1983] and *Kuwashima and Fukunishi* [1985] showed that SC amplitude is also highly dependent on local time at geostationary altitude, the maximum amplitude occurring near local noon and very small amplitudes occurring near midnight. The observed amplitude distribution is shown in Figure 2.12.

Following the initial impulse, damped oscillations (denoted Psc) are often observed both on the ground and at satellite altitudes. *Wilson and Sugiura* [1961] found that oscillations were observed more often at high latitudes, that the oscillation period for a given event was independent of latitude, and that the mean oscillation period was 4-5 min. At spacecraft altitudes, damped oscillations with periods similar to ground observations are often observed [*Nopper et al.*, 1982] and are, in many cases, accompanied by similar particle flux oscillations [*Barfield and Coleman*, 1970; *Baumjohann et al.*, 1984]. Oscillations with periods from 40-330 sec have been noted [*Fukunishi*, 1979; *Sakurai et al.*, 1984; *Wedeken et al.*, 1986], the shorter period oscillations possibly representing harmonics of the typical 4-5 min oscillations. *Baumjohann et al.* [1984] explained the observed damped transverse oscillations as a field line resonance driven by a tailward travelling wavelet generated on the magnetopause by the solar wind disturbance. Their analysis was based on theoretical work by *Chen and Hasagewa* [1974b] which showed that damped oscillations should accompany such a wavelet on the magnetopause. *Baumjohann et al.* [1983] suggested that observed compressional oscillations (shown in Figure 2.13) with a 2 min period could result from overshoot and oscillation of the magnetopause around the expected velocity associated with the earthward motion.

*Thermal plasma.* Plasma drifts at geosynchronous altitude have been measured by *Lin et al.* [1973] and *Baumjohann et al.* [1983] during SI. *Baumjohann et al.* [1983] found evidence of plasma motion associated with the arrival of the initial magnetosonic wave as well as the inward motion of the nearby magnetopause. Their results are shown in Figure 2.13. Using measurements of whistlers received on the ground, *Park* [1975] was able to measure the inward displacement of an ionization duct and make a rough calculation of the drift velocity and electric field in the region near the plasmapause. *McNeill* [1970] reported sudden changes in the phase path of VLF transmitter signals

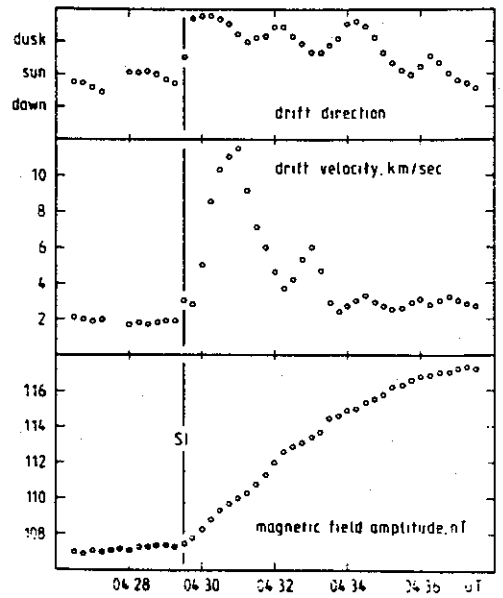


**Figure 2.13.** Magnetic field strength and energetic plasma drift observed during a SI. The measurements were made by the GEOS 2 spacecraft located at L=6.6 near 0700 LT. Drift measurements correspond to 1.2 keV electrons [*Baumjohann et al.*, 1983].

propagating near $L$=2.8 on the night side associated with SI, indicating that SI can produce significant plasma drifts even within the nightside plasmasphere.

*Energetic plasma.* Measurements of energetic particles during SI have recently been discussed by several authors. In all cases, simultaneous flux changes were observed at all energies for both ions and electrons at the time of the magnetic perturbation [*Arnoldy et al.*, 1982; *Wilken et al.*, 1982; *Tsunomura and Kuwashima*, 1984; *Korth et al.*, 1985; *Wilken et al.*, 1986]. *Arnoldy et al.* [1982] found that plasma injections associated with SI were similar to those observed during substorms with the exception that SI plasma injection occurs at all local times. Two competing mechanisms are thought to account for the initial flux variations observed by spacecraft [*Paulikas and Blake*, 1970; *Wilken et al*, 1982; *Tsunomura and Kuwashima*, 1984]. Betatron acceleration due to the increased magnetic field causes a flux enhancement for any given energy. The earthward plasma drift behind the wave front causes a flux decrease for any given radial position, since particle flux generally decreases with radial

distance. Following the initial effects, plasma convected from the tail may account for additional flux variations [*Arnoldy et al.*, 1982]. When discussing wave-particle interactions, energetic particle measurements made by spacecraft may be somewhat misleading. Spacecraft remain essentially stationary during a SC, while the region of wave-particle interactions may drift inward with a given field line or otherwise change location.

*Plasma waves.* Observations have shown that sudden changes in wave activity in the ULF, ELF, and VLF bands occur during SI. The changes indicate that wave-particle interaction properties are significantly affected by the magnetic perturbation and associated plasma variations. It is commonly believed that the interactions leading to the observed wave activity involve ion gyroresonance in the ULF band and electron gyroresonance in the ELF and VLF bands.

*Morozumi* [1965] was the first to recognize that changes in ELF/VLF wave activity in the inner magnetosphere are associated with SC. In a study of a small number of events, *Morozumi* [unpublished report] found that VLF enhancements accompanied SC in the afternoon sector, decreases accompanied SC in the morning sector, and no change was observed near midnight. *Hayashi et al.* [1968] examined SI in more detail and concluded that SI were usually accompanied by abrupt changes in VLF chorus activity in the daytime and that positive/negative magnetic impulses were associated with increases/decreases in VLF noise. This conclusion conflicts with the results obtained by Morozumi (our work indicates that neither is completely correct). *Hayashi et al.* [1968] also noted that the VLF noise was always seen about 30 sec prior to the magnetic perturbation at high latitudes and that the center frequency of chorus bands increased during positive SI. The results led them to suggest that VLF wave growth rates along the dayside equator increase/decrease as a result of the magnetic compression/expansion. In their model, based on the theory of *Kennel and Petschek* [1966], the magnetic field change preferentially affects the perpendicular energy of the gyrating electrons through betatron acceleration, changing the pitch angle anisotropy and thus modifying the growth rate. *Kokubun* [1983] invoked the model of betatron acceleration to qualitatively explain observations of VLF intensity enhancements simultaneous with magnetic field changes over one several hour period. *Korth et al.*

[1985] used a recent refinement of the Kennel-Petschek theory by *Cornilleau-Wehrlin et al.* [1985] to explain wave activity observed during a SC. In their theory, wave growth is only possible when betatron acceleration increases the anisotropy beyond a level which will support path-integrated amplitude gain.

Correlations between ULF emissions and SC were noted by *Tepley and Wentworth* [1962] who found that SC were sometimes accompanied by a "single train" of ULF emissions starting about 1 min after the magnetic perturbation and lasting 2-5 min. The emissions had a rising frequency structure and were most commonly observed at stations located near noon and midnight. *Kokubun and Oguti* [1968] and *Oguti and Kokubun* [1969] analyzed ULF emissions during SC in more detail. Their results showed that emissions were observed first at auroral latitudes, with increasing delay moving equatorward (up to 6 min at latitudes near 60°),and lasted up to several hours after the SC. *Hirasawa* [1981] showed that increases/decreases in ULF amplitude were correlated with positive/negative variations in the magnetic H component and that the frequency of emissions observed at auroral stations increased by factors of 1.5-10 following SI, similar to the observations of *Hayashi et al.* [1968] with VLF chorus. He suggested that changes in the ion cyclotron growth rate due to ion betatron acceleration would cause such effects. *Olson and Lee* [1983] explicitly calculated the growth rate change that would result from the betatron process and concluded that it adequately explained similar observations that they had made.

*Particle precipitation.* Trapped electrons may be precipitated from the magnetosphere as a result of interactions with waves. Observations of electron precipitation thus provide information on the wave-particle interaction process. *Brown et al.* [1961] first described ionospheric absorption and X-ray production during a SC and suggested that they could result from either precipitation of trapped particles or injection of particles from the solar wind. *Ortner et al.* [1962] and *Hartz* [1963] reported that ionospheric absorption during SC was localized around the maximum of the auroral zone and rarely observed at geomagnetic latitudes below 57° or above 75° and was most probable near local noon. They also noted that absorption was generally limited to less than 15 min duration. Observations of X-ray fluxes from balloon measurements near L$\simeq$6 during a SC [*Ullaland et al.*, 1970] indicated periodicities of 1.8 sec and 50

sec in the observed particle precipitation. *Leinbach et al.* [1970] found in a case study that absorption effects were similar at conjugate stations but that the time profile of absorption depended on latitude. They concluded that precipitation of trapped electrons resulting from interactions with waves was the most probable cause.

# Chapter 3

# OBSERVATIONS

Due to the complexity of magnetospheric phenomena, progress in magnetospheric physics has been driven by observational results. The observations presented in this chapter are intended to provide empirical constraints necessary for the development of models of gyroresonance interactions applicable to a dynamic magnetosphere.

The first section includes a discussion of the methodology that was used to select data sets for analysis, a description of the receiving and recording equipment used for data collection, and a characterization of the data sets that were chosen. The remainder of the chapter is divided into sections describing occurrence statistics for wave activity associated with SC, amplitude and spectral properties of the waves, characteristics of the wave growth process, the onset time of the wave growth with respect to the magnetic disturbance, and particle precipitation observations.

## 3.1 DESCRIPTION OF DATA SETS

### 3.1.1 *METHODOLOGY*

Ground-based and spacecraft observations provide significantly different information about wave-particle interactions. Waves observed at ground stations are generally believed to propagate throughout the magnetosphere in ducts, while spacecraft normally observe primarily nonducted waves. Ducted waves have small wave normal

angles and propagate along field-aligned paths to their ionospheric exit points; non-ducted waves have unrestricted wave normal angles and can propagate across field lines. Ground-based and spacecraft observations each have particular characteristics which determine their usefulness for any given study.

Ground-based observations have the distinct advantage that ducts are relatively stable over periods as long as several hours [*Carpenter et al.*, 1972]. Wave activity observed before and after a SI can be associated with a particular set of ducts and thus provides information on how the wave-particle interactions occurring within those ducts are modified. Ground stations observe waves exiting the ionosphere within a radius of 500 km or more [*Walker*, 1974; *Tsuruda et al.*, 1982] meaning that a single ground-based receiver can monitor wave activity from a fairly large region of the magnetosphere. The disadvantage of the large viewing area is that it is difficult to precisely identify a wave source region and to distinguish wave sources associated with more than one duct. Propagation effects associated with ducts also generally limit observations to waves with frequencies below the minimum half-gyrofrequency along the propagation path.

**Table 3.1.** Geophysical and data set parameters for ground stations.

| Station | Geographic latitude (deg) | Geographic longitude (deg) | Geomagnetic latitude (deg) | Geomagnetic noon (UT) | Data set |
|---|---|---|---|---|---|
| Byrd | 80.0 S | 120.0 W | 67.9 S | 1800 | 1963-5, 67-8 |
| Eights | 75.2 S | 77.2 W | 59.5 S | 1700 | 1963, 65 |
| Palmer | 64.8 S | 64.1 W | 48.5 S | 1630 | 1982-3 |
| Roberval | 48.4 N | 72.3 W | 61.3 N | 1700 | - |
| Siple | 75.9 S | 84.3 W | 61.1 S | 1700 | 1977-8, 82-3 |
| South Pole | 90.0 S | - | 73.8 S | 1530 | 1981-5 |

Spacecraft are not limited to observations of waves with small wave normal angles or frequencies below the half-gyrofrequency and thus provide observations of waves,

such as plasmasheric hiss and Auroral Kilometric Radiation (AKR), which are not seen on the ground. However, spacecraft monitor only waves with raypaths that reach the spacecraft directly and thus view a very limited region of the magnetosphere at any given time. In addition, spacecraft are subject to data collection limitations far more strict than ground stations, and broadband wave data are particularly difficult to obtain. During a SI, both magnetic field lines and the particle distribution convect past a spacecraft and it is probably unreasonable to assume that waves observed by a spacecraft are coming from the same source region before and after a SI.

Due mostly to the data limitations, ground observations were chosen as the primary data source for this study. Spacecraft observations were studied for a number of events, but a lack of adequate wave data (broadband wave data with sufficient time resolution were not available for any SC) precluded development of significant conclusions from the spacecraft observations.

Both SC and the more general class of magnetic perturbations known as SI were examined for this study. SC were identified using published lists which provide a concensus identification of SC from an established global network of ground magnetic observatories. SI were in most cases identified using magnetograms from the small set of ground stations for which complete data sets were available (see Table 3.1). A complete list of all SC and SI examined is given in Appendix E. In order to develop an objective data set, only those events identified in published lists as SC were analyzed in detail for this study.

Use of relative rather than absolute measurements of wave amplitude and spectral characteristics was emphasized in the observational work. Relative measurements eliminate the uncertainties involved in instrument calibration and minimize the number of assumptions required in interpreting quantitative results. Studies involving SC are particularly well adapted to use of relative measurements.

### 3.1.2 *DATA SETS*

Lists of worldwide magnetic variations identified as SC (and SI when available) were

obtained from *J. Geophys. Res.*, *IAGA Bulletin No. 12* (to 1969) and *No. 32* (1970-80), and *NOAA Solar-Geophysical Data* (1981-85).

Ground data for the study were obtained from several stations. The stations, along with geophysical and data set parameters, are listed in Table 3.1. The stations at Palmer, Siple, and South Pole, which form a roughly meridional chain (colocated within ±1 hour geomagnetic local time with geomagnetic latitudes of 48.5°, 61.1°, and 73.8° respectively), were used to provide latitudinal comparisons.

ELF/VLF wave data were obtained with Stanford University receivers which have a bandwidth of 300 Hz - 20 kHz. Broadband data recorded on analog tape were generally available only for periods of 1 min out of every 5 or 15 min, although longer recordings were obtained for some events. Signals from the wave receivers as well as magnetometers and riometers were recorded in analog form on paper charts or in digital form with 1 sec resolution on University of Maryland digital data systems (depending on the station and year). Wave data were recorded as narrowband amplitudes in the channels 0.5-1 kHz, 1-2 kHz, 2-4 kHz, 11-13 kHz, and 31-38 kHz. Magnetometer data were obtained with the Bell Laboratories tri-axial fluxgate magnetometers which measure the magnetic field in the geomagnetic North-South (H), East-West (D), and vertical (Z) directions. The magnetomenters have a passband cutoff of 0.25 Hz and a noise level of 0.25 nT [*S. Krishnaswamy*, personal communication]. Riometer data were obtained with the University of Maryland riometers at frequencies of 20.5 MHz, 30.0 MHz, and 51.4 MHz. The riometers have bandwidths of 200 kHz, time constants of 0.25 sec, noise levels of 0.02 dB, and a half-power beamwidth of 30° [*S. Krishnaswamy*, personal communication].

Additional ground magnetometer data from published plots of tri-axial magnetometer data recorded by the Air Force Geophysical Laboratories magnetometer chain [*Knecht*, 1985] and the Japanese Antarctic station Syowa [*Fujii et al.*, 1985] were used for identification of SI.

Spacecraft magnetic field data were obtained with the NOAA GOES satellites located in geostationary orbit. The GOES magnetometers are twin fluxgate spinning sensors which sample the field every 0.75 sec and are capable of measuring field strength

changes of 0.2 nT [*D. Wilkinson*, private communication]. The data used for this work were in the form of 3 sec averages for each of the 3 components.

**Table 3.2.** The limited set of SC events used for detailed analysis.

| Year | Date | UT | Day No. |
|---|---|---|---|
| 1982 | Jan 29 | 1744 | 029 |
| | Feb 5 | 1611 | 036 |
| | Mar 1 | 1138 | 060 |
| | Apr 1 | 1305 | 091 |
| | Apr 16 | 1702 | 106 |
| | Jun 12 | 1443 | 163 |
| | Jul 16 | 1519 | 197 |
| | Sep 25 | 1703 | 268 |
| | Oct 31 | 1338 | 304 |
| | Nov 23 | 0917 | 327 |
| | Nov 24 | 0923 | 328 |
| 1983 | Jan 9 | 1544 | 009 |
| | Feb 4 | 1614 | 035 |
| | Apr 12 | 1055 | 102 |
| | Apr 13 | 1100 | 103 |
| | Oct 21 | 1324 | 294 |

Several hundred SI were examined using the analog chart data during the preliminary portion of the study. A list of the events is included in Appendix E. Based on the results of the preliminary study, a limited data set of 16 SC from the period 1982-83 was chosen for detailed analysis in this thesis. A list of the limited set events is given in Table 3.2. The limited set is not intended to be an objective sample of the entire data set but rather to best demonstrate those characteristics of the events which can be applied to understanding the wave generation process. Analysis of other events is included when useful.

## 3.2 OCCURRENCE STATISTICS

Statistical data on the occurrence of changes in wave activity associated with SC were compiled for South Pole, Siple, and Palmer covering the periods 1981-85 at

South Pole, 1977-78 and 1982-83 at Siple, and 1982-83 at Palmer. Histograms of the observed occurrence rates plotted versus Universal Time are shown in Figure 3.1.

The number of reported SC during periods when data were available was 132 at South Pole, 104 at Siple, and 62 at Palmer. Distinct changes in wave amplitude in the narrowband chart channels were observed in 67 of the cases at South Pole, 62 of the cases at Siple, and 22 of the cases at Palmer, corresponding to overall observation probabilities of 0.5, 0.6, and 0.3 respectively. The maximum occurrence rate of about 0.8 measured at both South Pole and Siple represents a lower limit for the global occurrence of changes in ELF/VLF emissions at ground stations, indicating that changes in wave activity are associated with at least 80% of reported SC.

A broad maximum in occurrence rate near geomagnetic noon was noted at South Pole with a corresponding minimum near geomagnetic midnight. Occurrence rates as high as 0.8-1.0 were noted within several hours of local noon. A similar minimum near geomagnetic midnight was observed at Siple, but the distribution near noon was less peaked. Occurrence rates of 0.6-0.9 were observed at all local times except near midnight. At both stations, the occurrence rates near midnight were in the range 0.0-0.3. At Palmer, maxima were observed 2-4 hours prior to local noon and local midnight, with occurrence rates of roughly 0.3-0.6. The occurrence statistics from Palmer are somewhat less reliable than the statistics for South Pole and Siple due to the smaller sample size.

## 3.3 WAVE AMPLITUDE CHARACTERISTICS

### 3.3.1 *BASIC OBSERVATIONS*

*South Pole observations.* Amplitude plots from South Pole for the limited data set of 16 SC are shown in Figures 3.2-3.5. Each panel shows the magnetic field H-, D-, and Z- components as well as ELF/VLF wave amplitude in the bands 0.5-1 kHz, 1-2 kHz, and 2-4 kHz for a period of one hour with marked times in UT. The impulsive noise at 5 min intervals in the ELF/VLF channels (e.g., Figure 3.2(c)) is due to

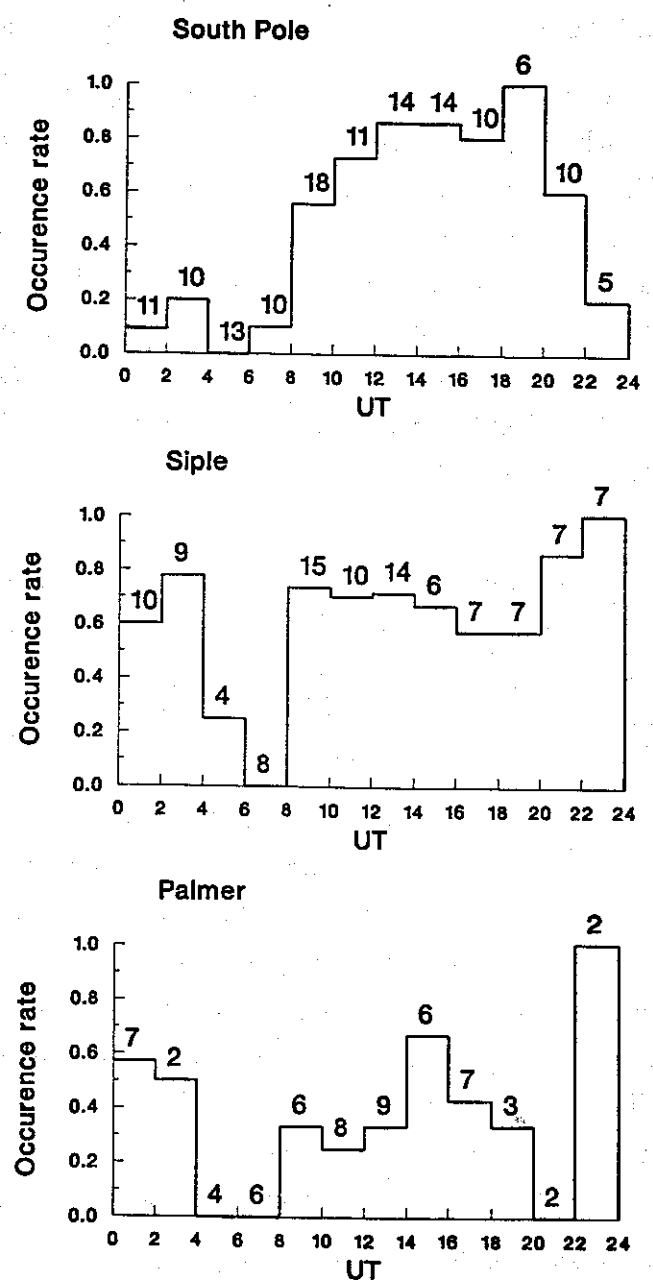


**Figure 3.1.** Normalized occurrence rate of wave activity associated with SC at South Pole, Siple, and Palmer. Events are binned in 2 hour intervals and normalized by the total number of reported SC for which data were available (shown at the top of each bin).

artificial calibration tones injected into the receiving system. The ELF/VLF channel amplitudes are not calibrated and thus do not refer to absolute field strengths.

In each example, the onset of the SC was indicated by a sudden increase or decrease in the amplitude of the magnetic field components and was accompanied by distinct changes in the ELF/VLF amplitude in all three channels. Though both the 11-13 kHz and 31-38 kHz channels were also recorded during the 1982-83 period, they rarely indicated amplitude changes associated with SC and thus are not included in the figures. The limitation of noise to the lower frequency channels is consistent with the noise being primarily mid-latitude hiss, chorus, or polar chorus [*Helliwell*, 1965] rather than auroral hiss, similar to the observations of *Morozumi* [1965] and *Hayashi et al.* [1968]. Dynamic spectra for these events, which will be presented in the next section, confirm this conclusion.

Figure 3.2 shows four examples of SC observations at South Pole in which transient enhancements of wave activity lasting several minutes were observed (in Figure 3.2(a), the amplitude of the 2-4 kHz channel does not accurately reflect the natural activity amplitude as it was dominated by modulated or CW signals from the Siple transmitter at 3.8 kHz propagating sub-ionospherically to South Pole). Each example shows that wave amplitude increased for a period of 1-8 min at the time of the SC and subsequently returned to a steady level which differed from the original amplitude. The duration of the enhancement was dependent on frequency. The amplitude increase preceded the arrival of the magnetic perturbation by up to 1 min. The growth time, defined loosely as the amount of time for the wave amplitude to increase from the pre-event level to the first significant peak level, was 15-60 sec for each channel in these events. The growth onset occurred first in the 0.5-1 kHz channel and with increasing delay in the 1-2 kHz and 2-4 kHz channels. A more reliable analysis of the growth period using broadband data for several events is discussed in Section 3.5.

Figure 3.3 shows four examples in which a transient increase was observed and in which the amplitude following the increase was significantly different from prior activity. In all four examples, a noise band with relatively steady amplitude was observed prior to the SC. Following the enhancement a significant decrease in noise amplitude occurred in all channels, taking 4-10 min to reach a minimum level. In Figure 3.3(a),

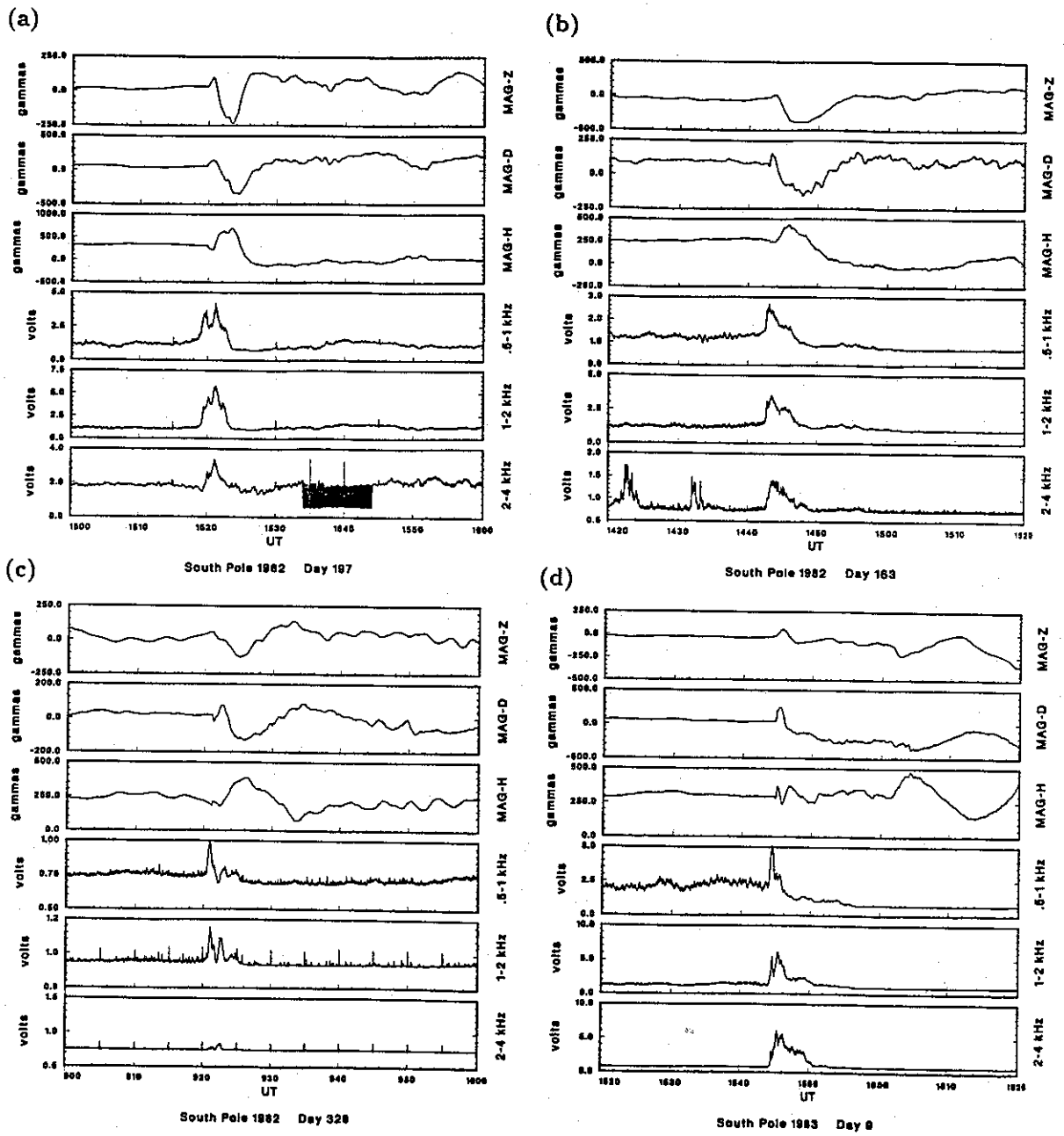


**Figure 3.2.** Magnetic field and wave amplitude recorded at South Pole for four SC. Each panel shows the H-, D-, and Z- components of the magnetic field and the ELF/VLF amplitude in the 0.5-1, 1-2, and 2-4 kHz channels. The periodic "spikes" in the ELF/VLF are calibration tones. The 2-4 kHz channel in panel (a) does not accurately reflect the natural activity during this period as it was dominated by a sub-ionospheric signal from the Siple transmitter.

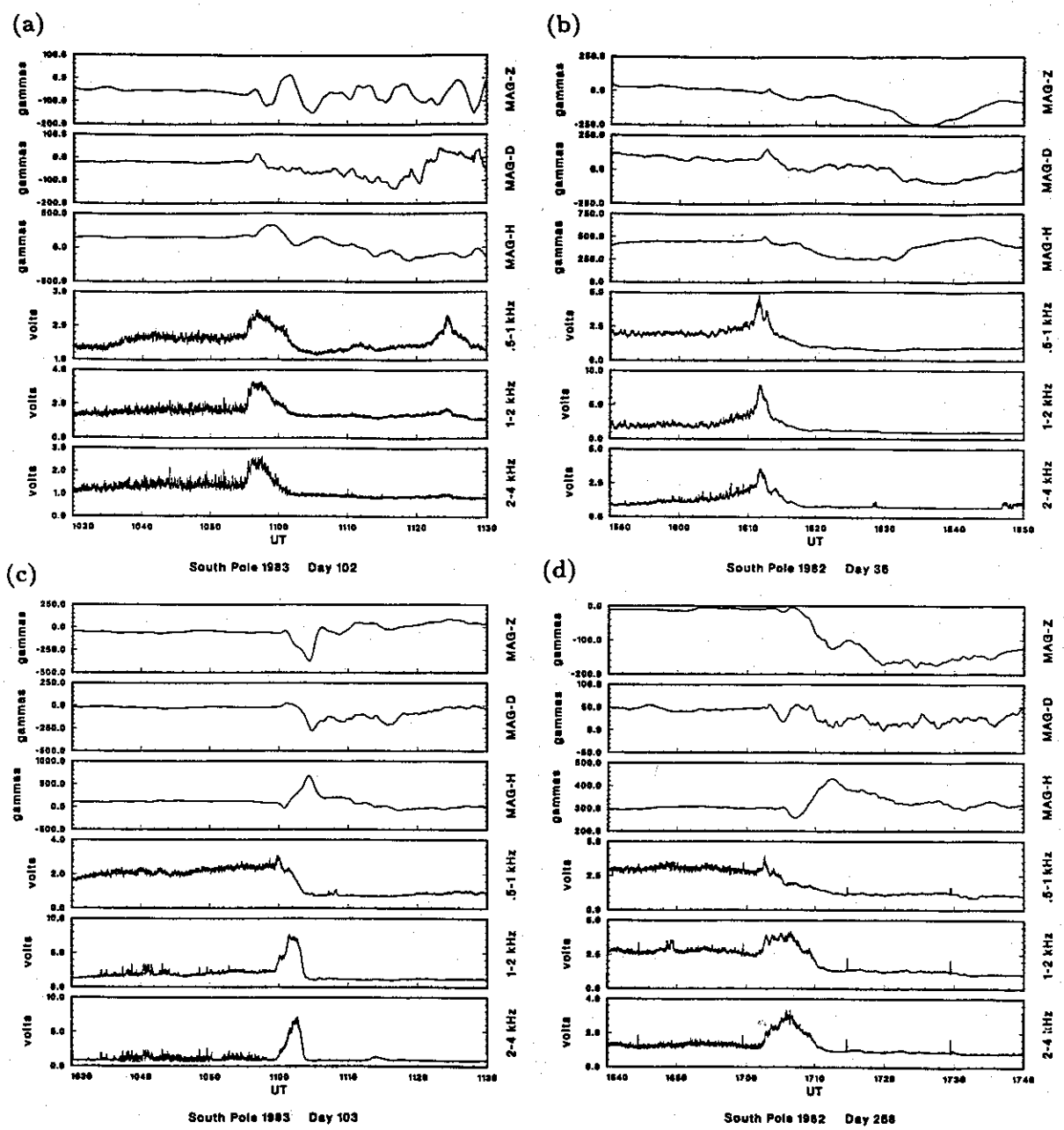


**Figure 3.3.** Magnetic field and wave amplitude recorded at South Pole for four SC. Each panel shows the H-, D-, and Z- components of the magnetic field and the ELF/VLF amplitude in the 0.5-1, 1-2, and 2-4 kHz channels. The periodic "spikes" in the ELF/VLF are calibration tones.

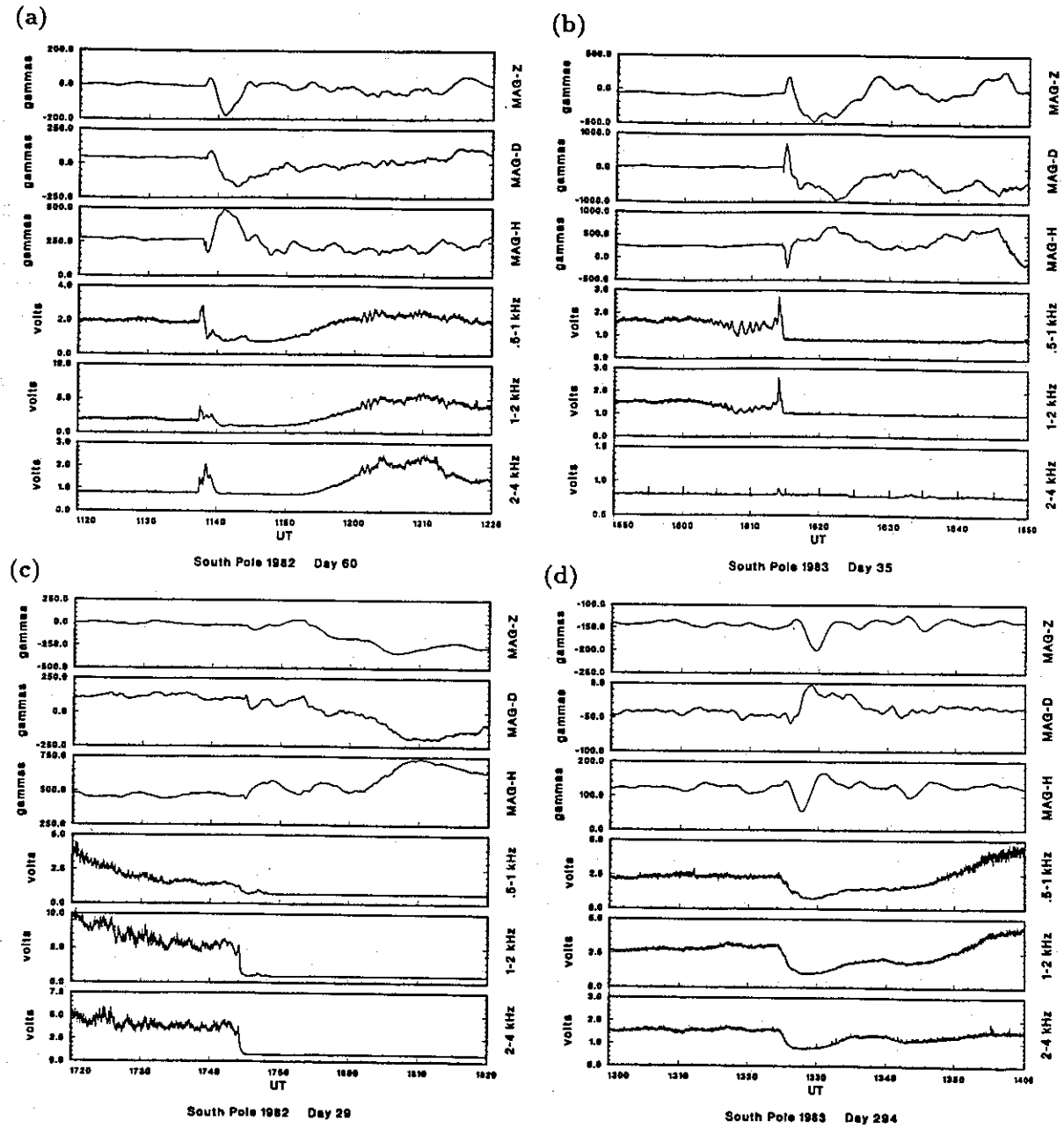


**Figure 3.4.** Magnetic field and wave amplitude recorded at South Pole for four SC. Each panel shows the H-, D-, and Z- components of the magnetic field and the ELF/VLF amplitude in the 0.5-1, 1-2, and 2-4 kHz channels. The periodic "spikes" in the ELF/VLF are calibration tones.

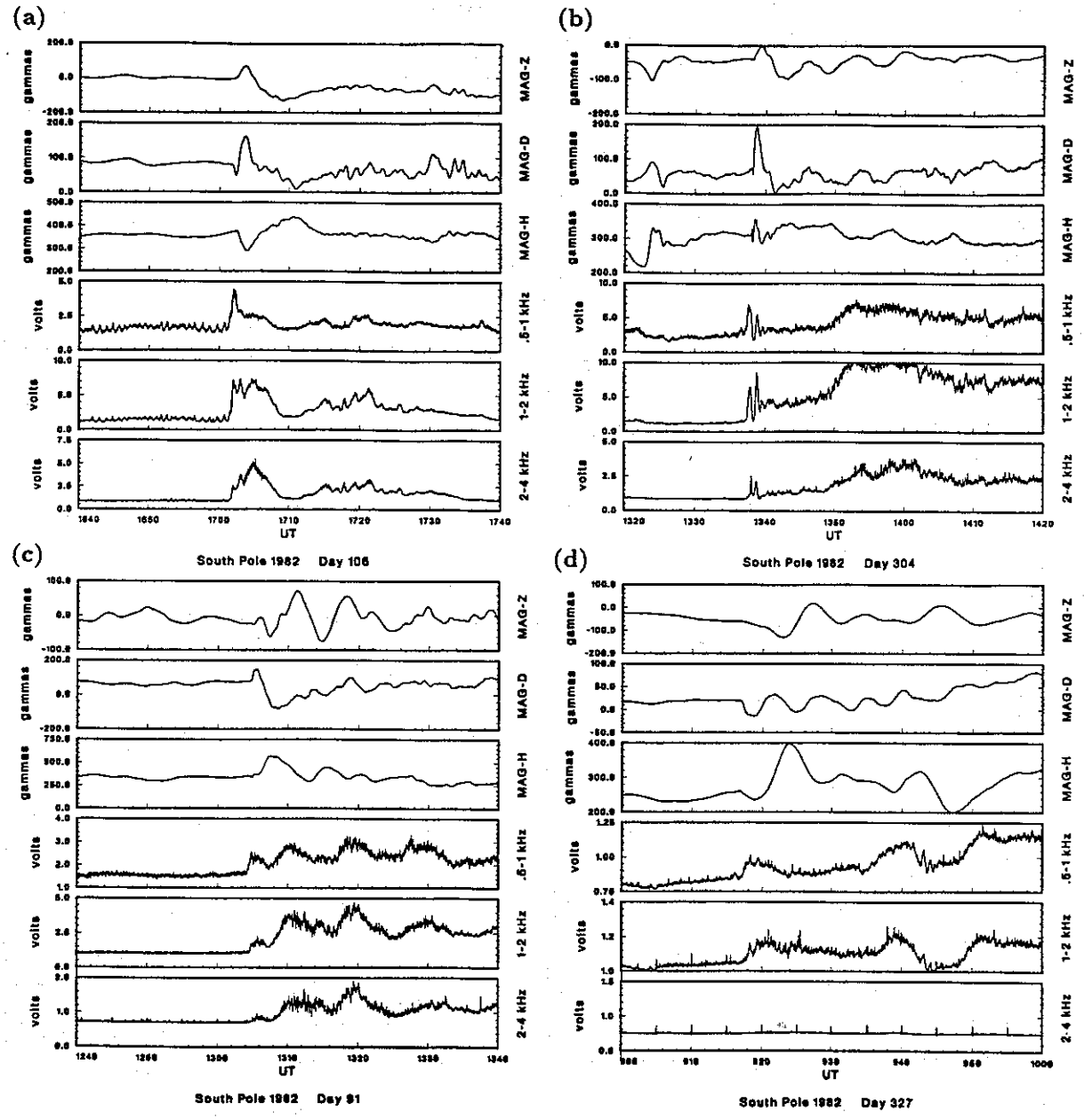


**Figure 3.5.** Magnetic field and wave amplitude recorded at South Pole for four SC. Each panel shows the H-, D-, and Z- components of the magnetic field and the ELF/VLF amplitude in the 0.5-1, 1-2, and 2-4 kHz channels. The periodic "spikes" in the ELF/VLF are calibration tones.

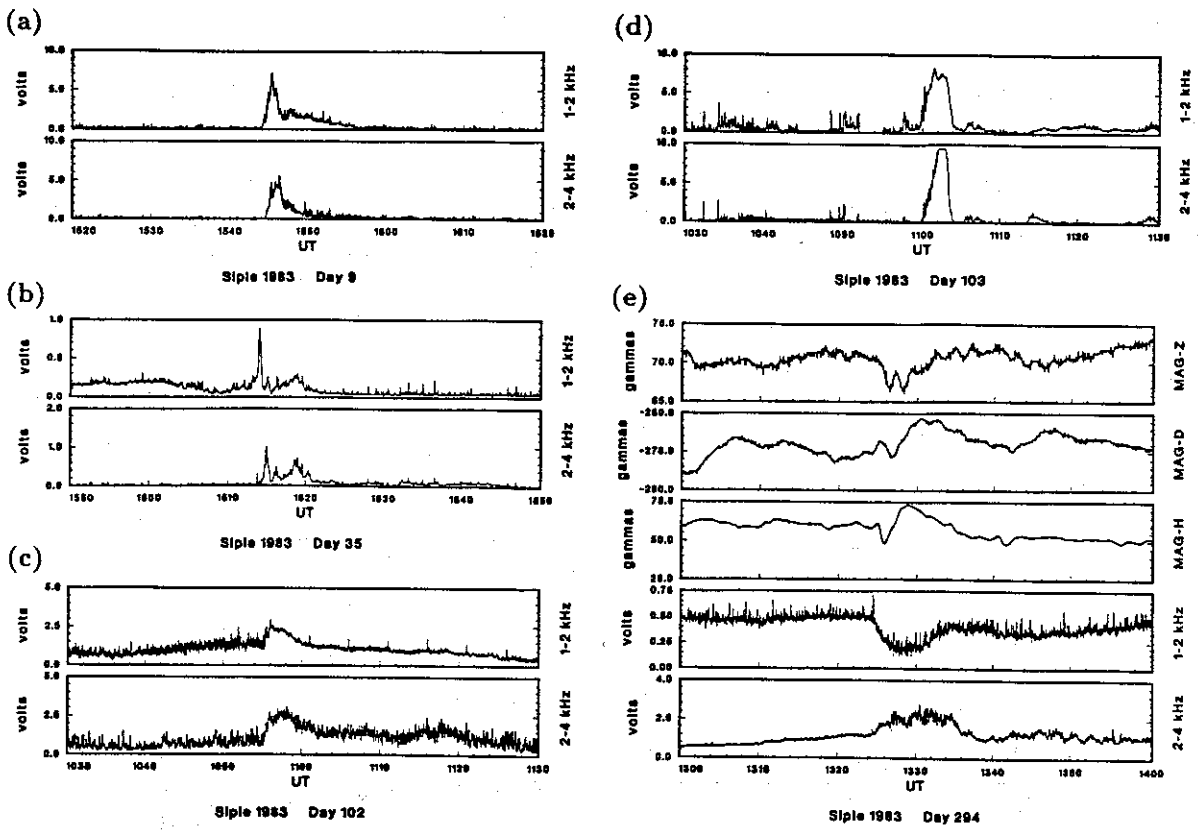


**Figure 3.6.** Magnetic field and wave amplitude recorded at Siple for four SC. Each panel shows the ELF/VLF amplitude in the 1-2 and 2-4 kHz bands. The periodic "spikes" in the ELF/VLF are calibration tones.

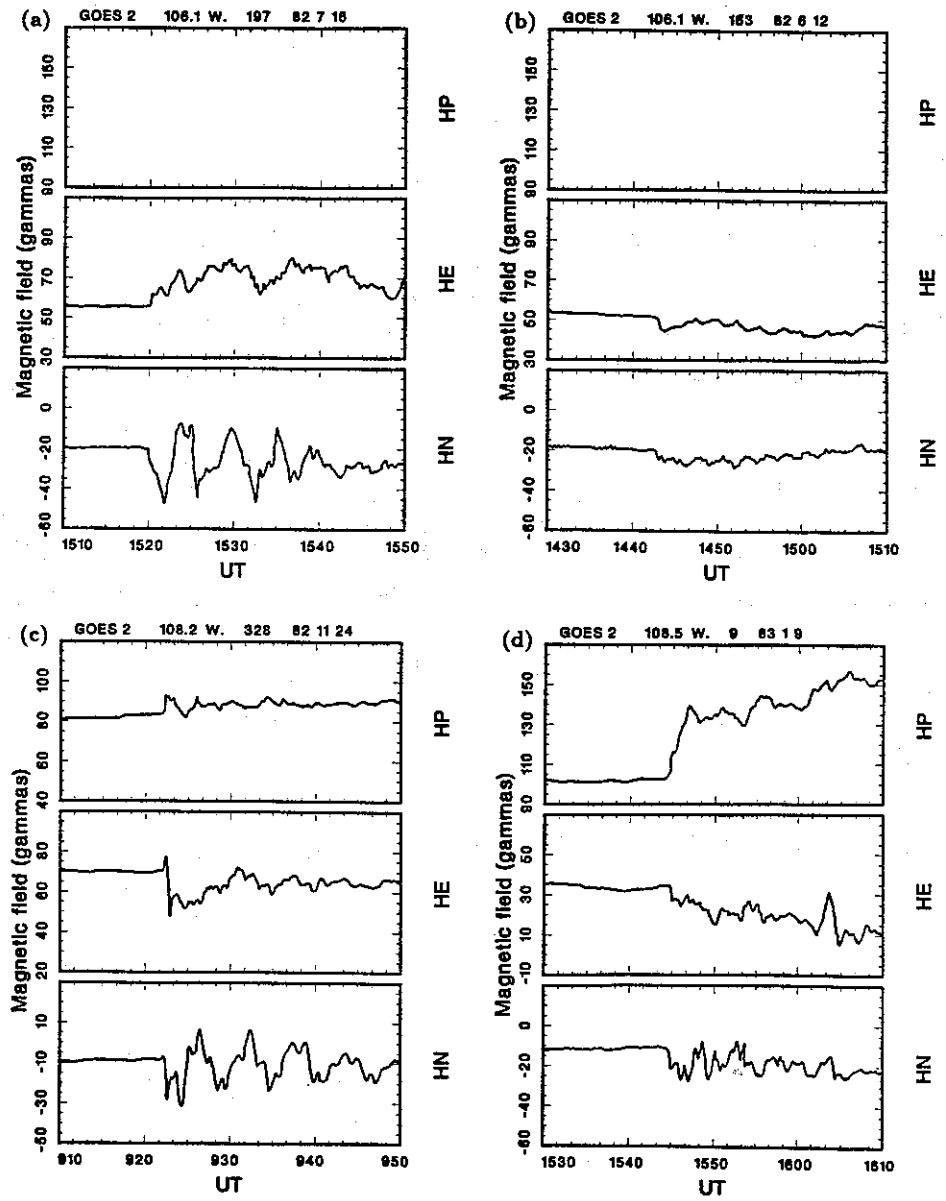


**Figure 3.7.** Magnetic field at geostationary altitude for four SC. Each panel shows the HP-, HE-, and HN- components of the magnetic field measured by the GOES-2 spacecraft.

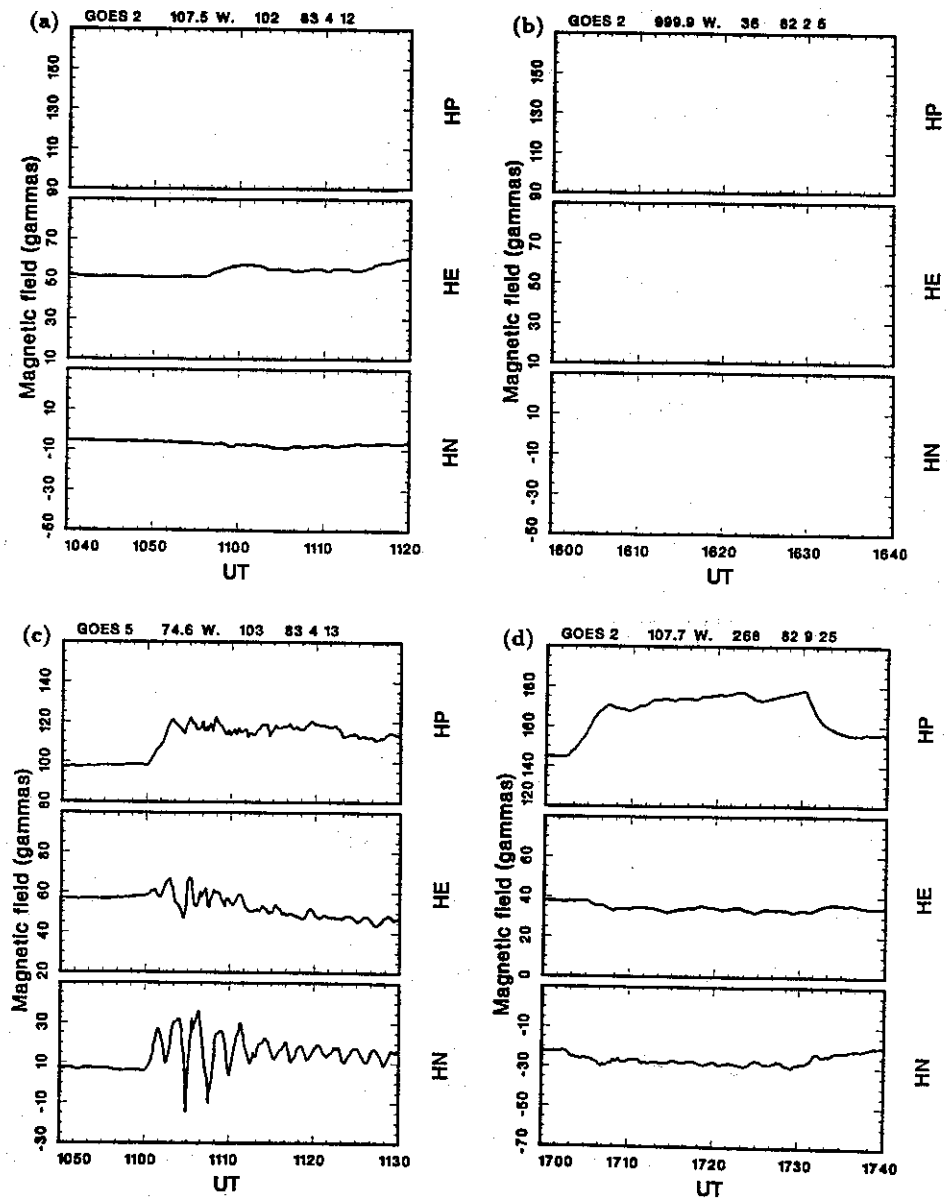


**Figure 3.8.** Magnetic field at geostationary altitude for four SC. Each panel shows the HP-, HE-, and HN- components of the magnetic field measured by the GOES-2 or GOES-5 spacecraft.

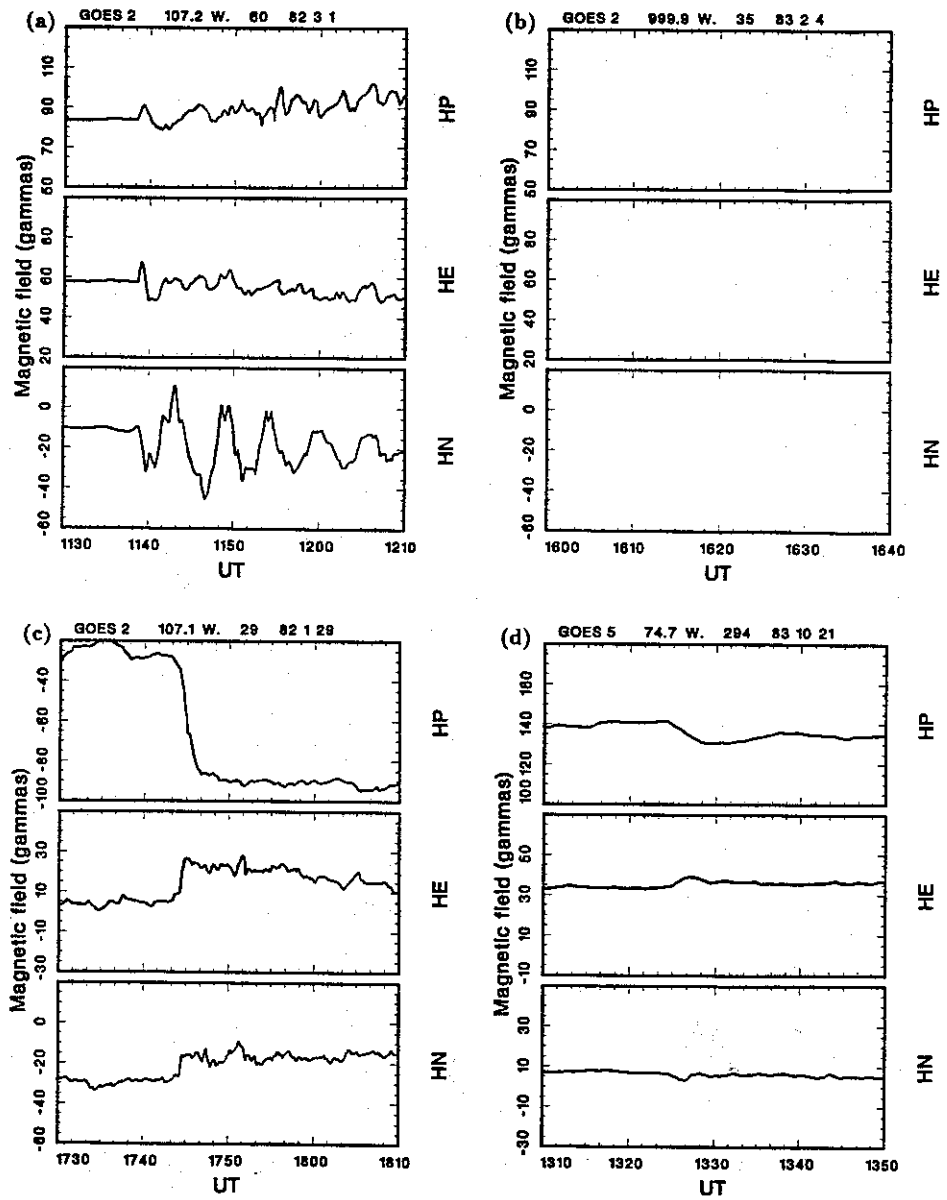


**Figure 3.9.** Magnetic field at geostationary altitude for four SC. Each panel shows the HP-, HE-, and HN- components of the magnetic field measured by the GOES-2 or GOES-5 spacecraft.

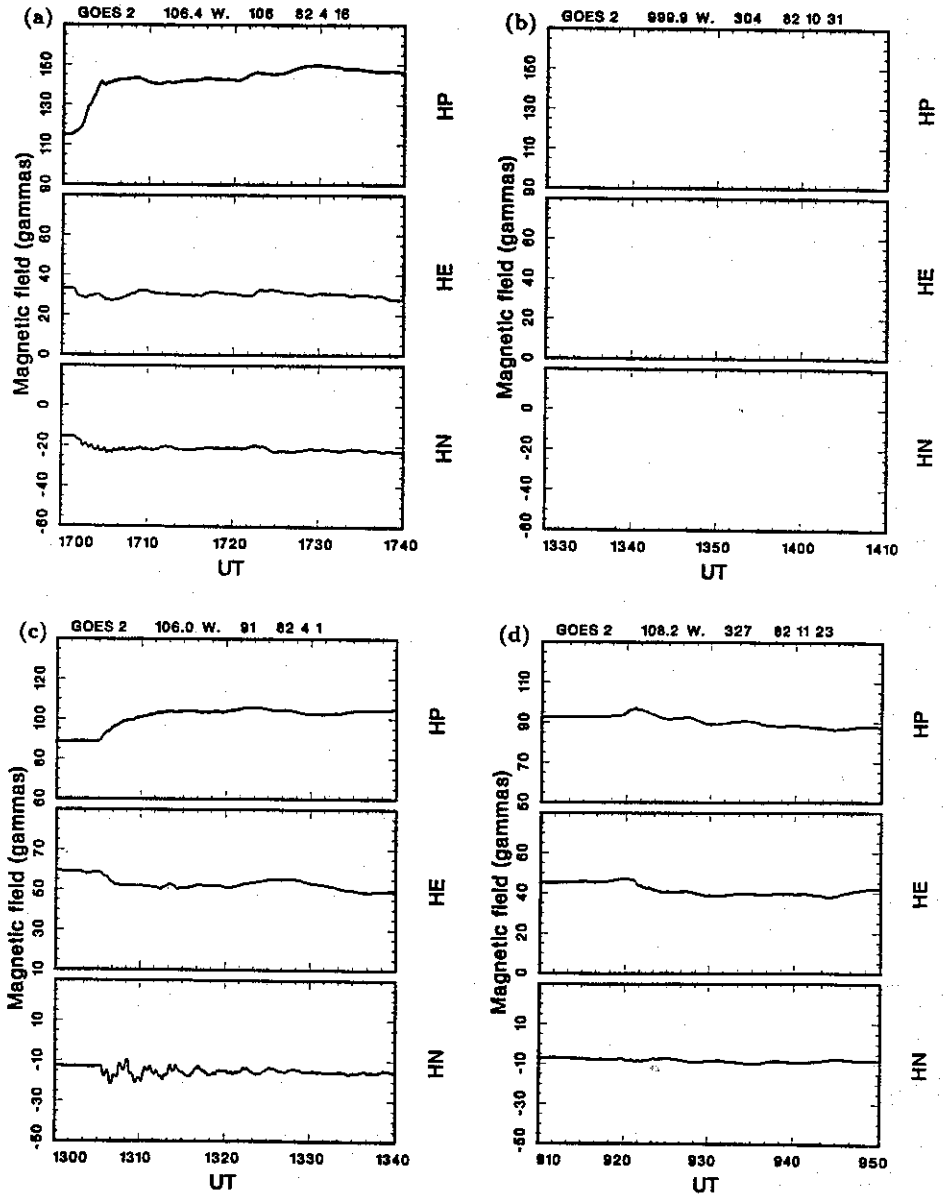


**Figure 3.10.** Magnetic field at geostationary altitude for four SC. Each panel shows the HP-, HE-, and HN- components of the magnetic field measured by the GOES-2 spacecraft.

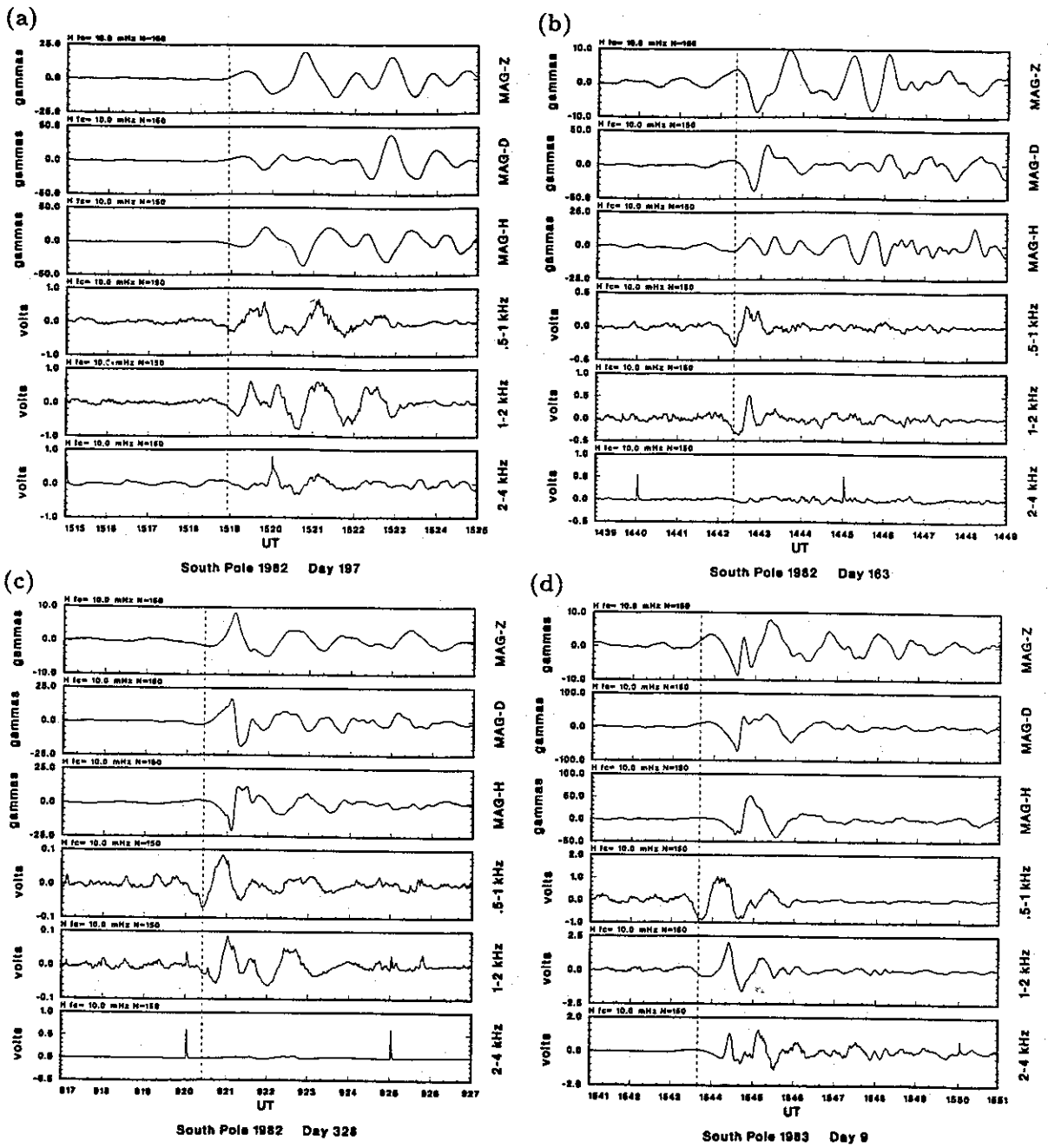


**Figure 3.11.** Oscillations in the magnetic field and wave amplitude recorded at South Pole for four SC. The dashed lines indicate the wave growth onset.

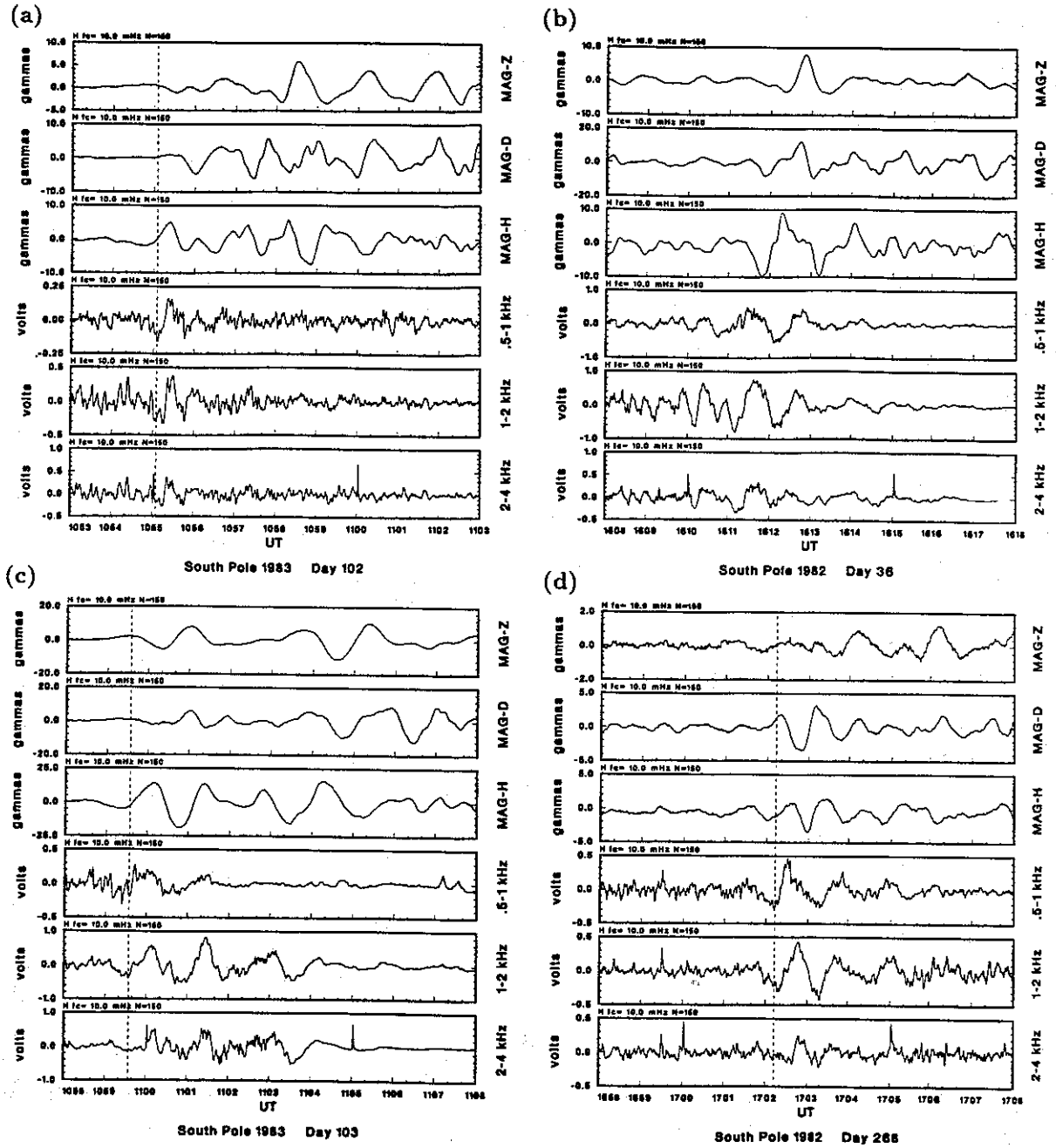


**Figure 3.12.** Oscillations in the magnetic field and wave amplitude recorded at South Pole for four SC. The dashed lines indicate the wave growth onset.

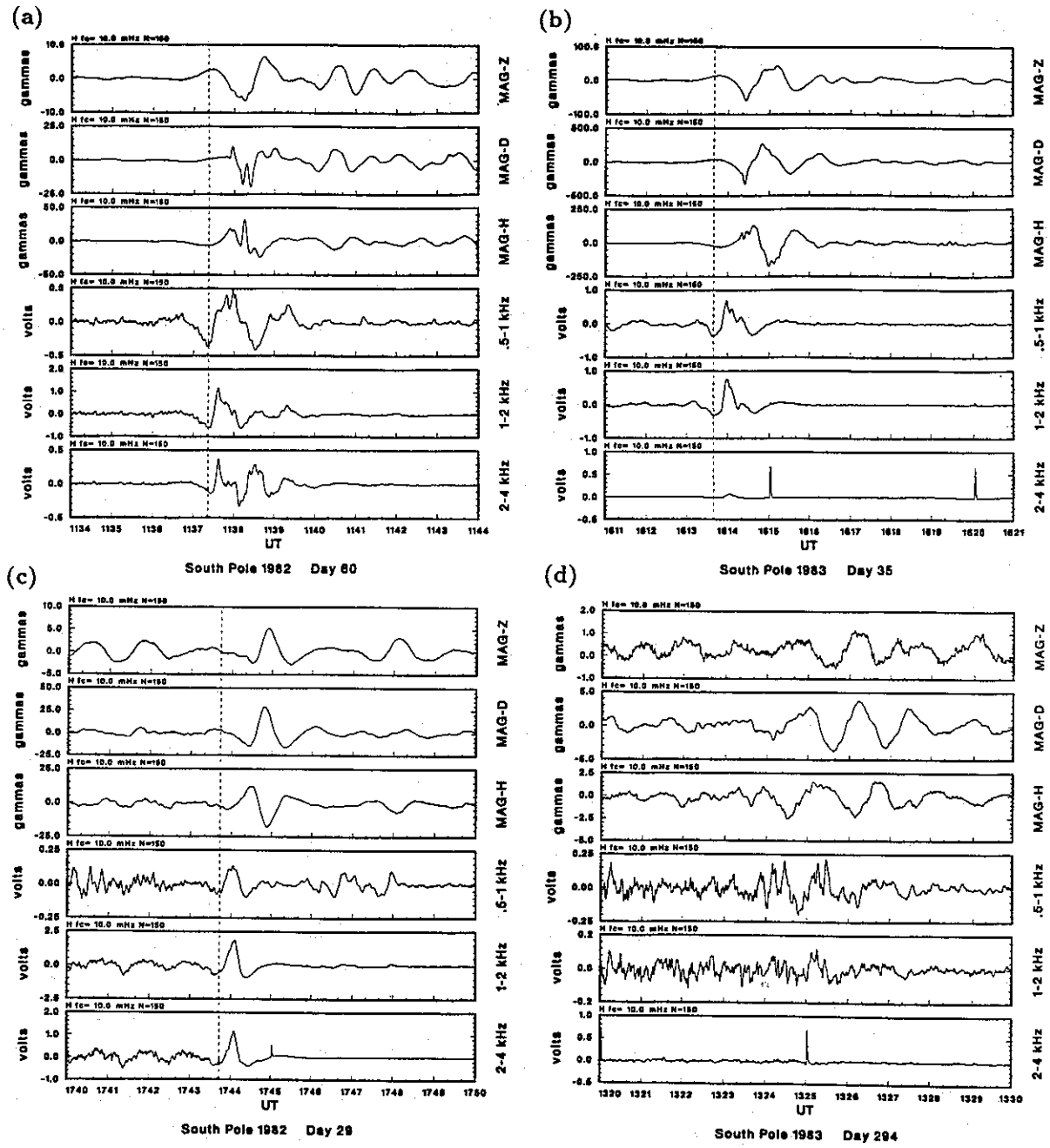


**Figure 3.13.** Oscillations in the magnetic field and wave amplitude recorded at South Pole for four SC. The dashed lines indicate the wave growth onset.

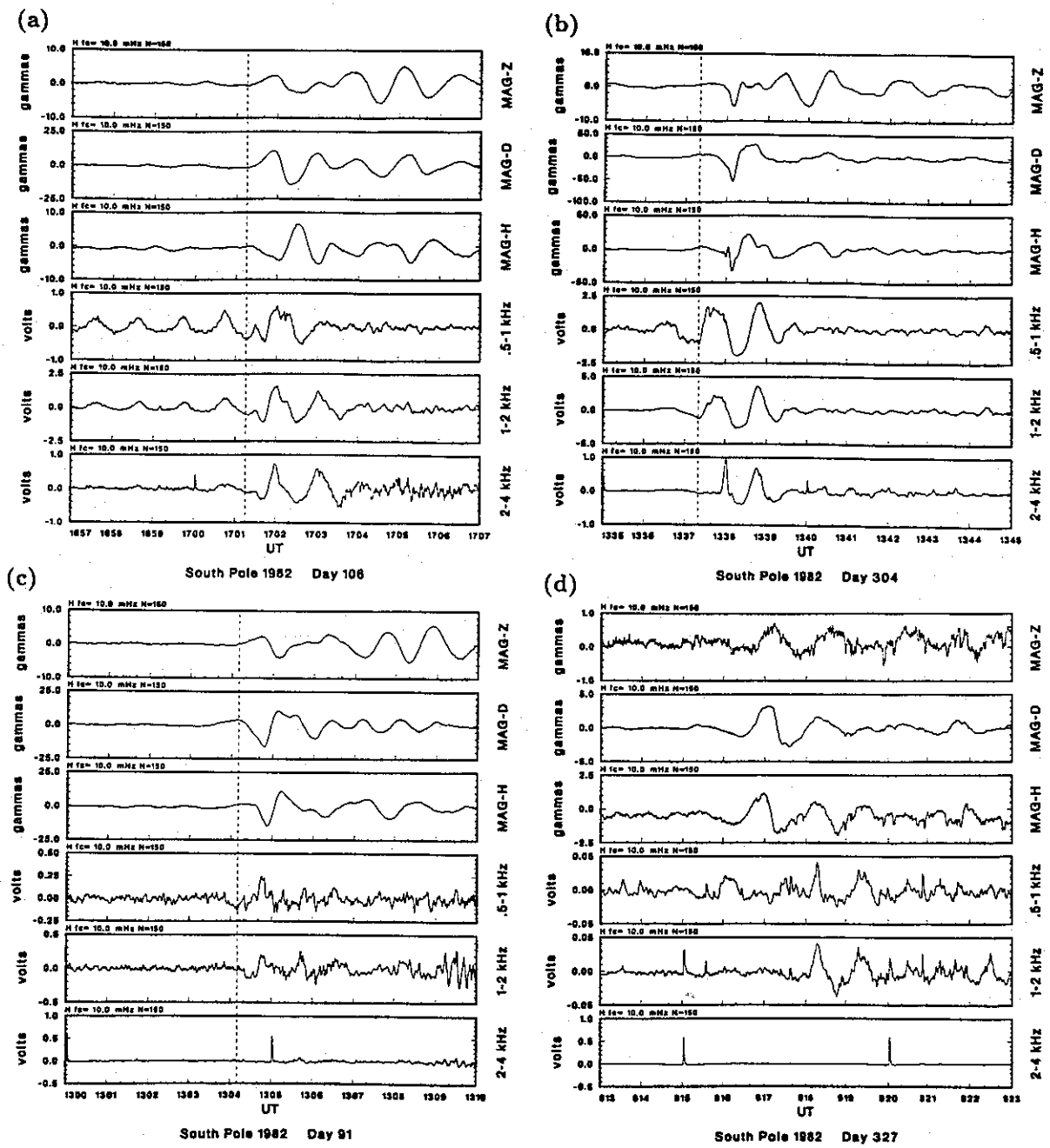


**Figure 3.14.** Oscillations in the magnetic field and wave amplitude recorded at South Pole for four SC. The dashed lines indicate the wave growth onset.

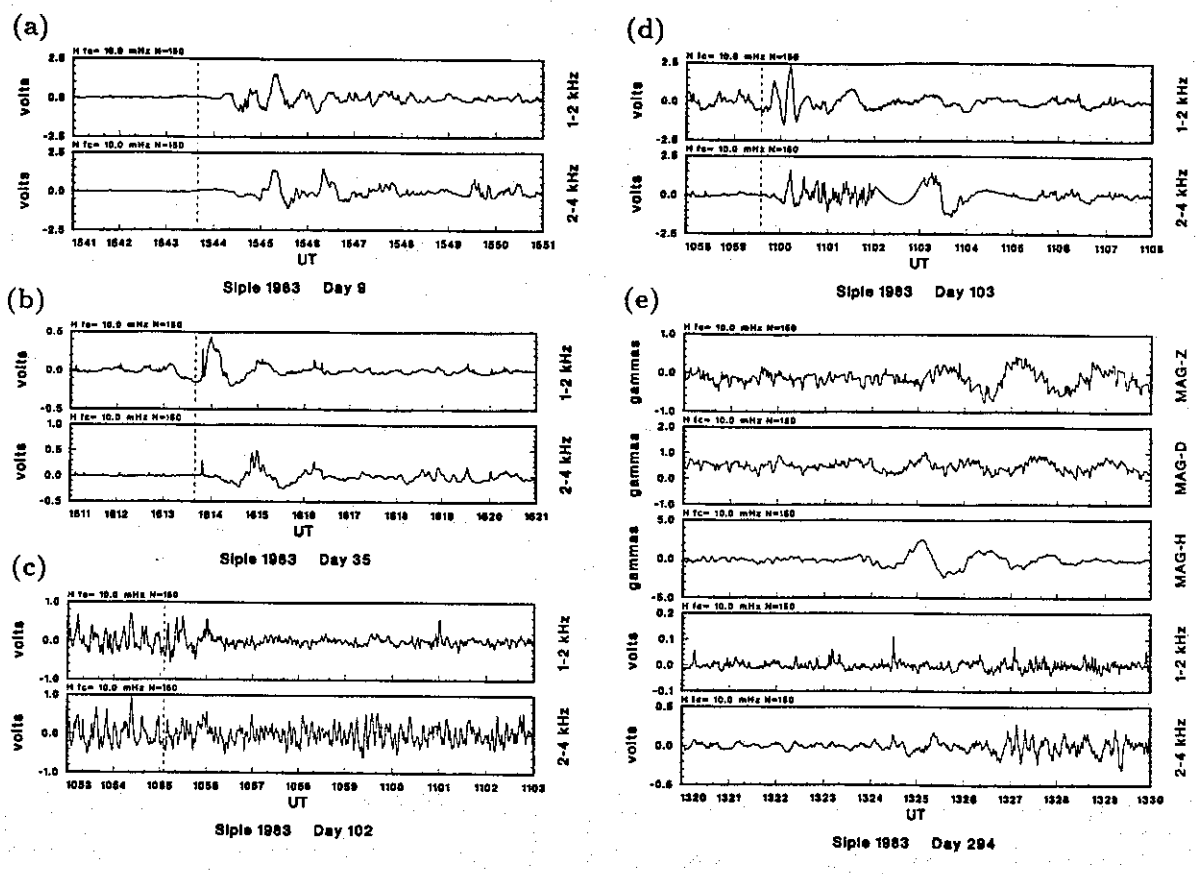


**Figure 3.15.** Oscillations in the magnetic field and wave amplitude recorded at Siple for five SC. The dashed lines indicate the wave growth onset at South Pole.

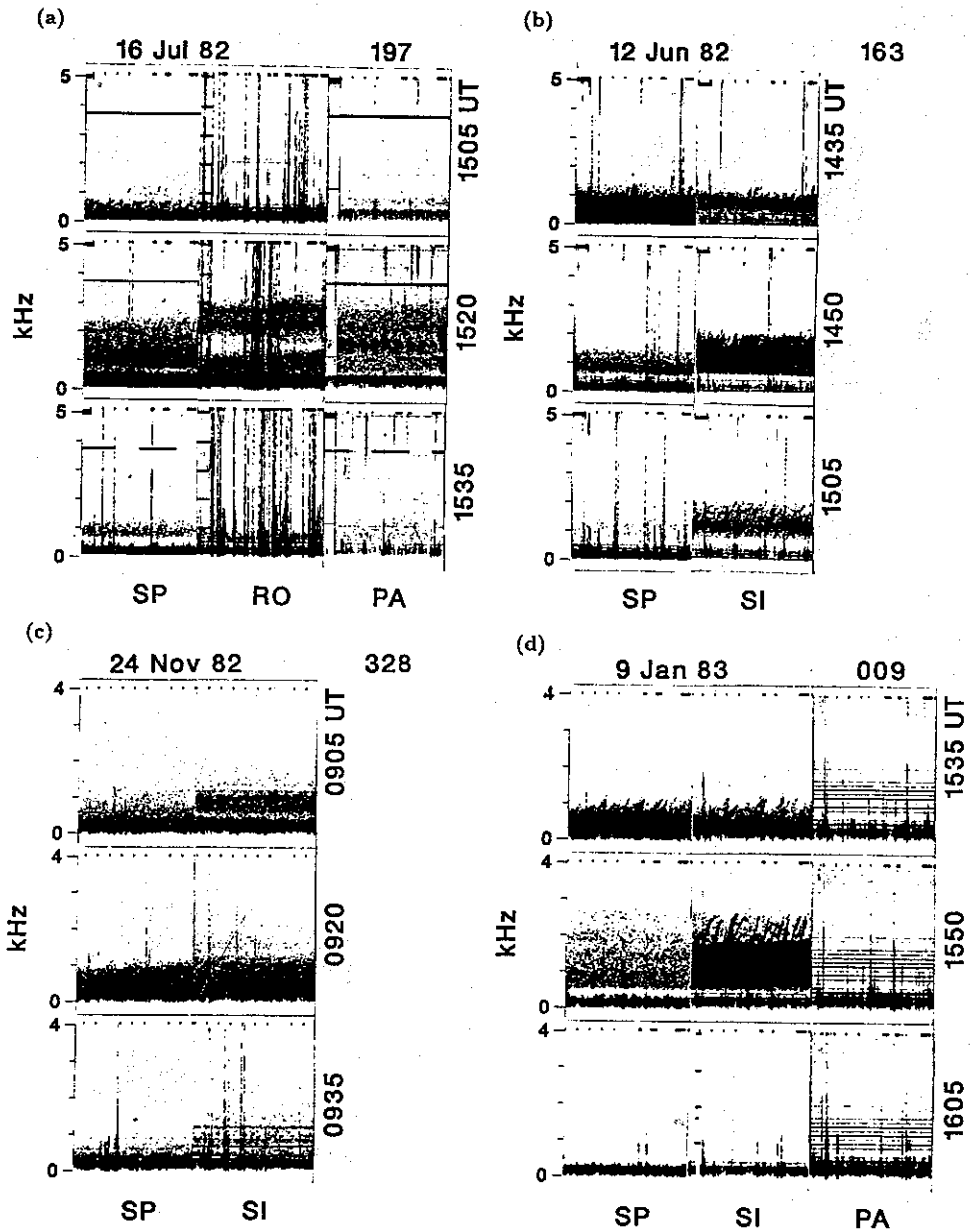


**Figure 3.16.** Synoptic dynamic spectra recorded at South Pole, Siple, and Palmer for four SC. Each panel shows dynamic spectra in the band 0-4 or 0-5 kHz for three 10 sec periods separated in time by 15 min. The periods were chosen to illustrate the spectra prior to, during, and after the SC whenever possible.

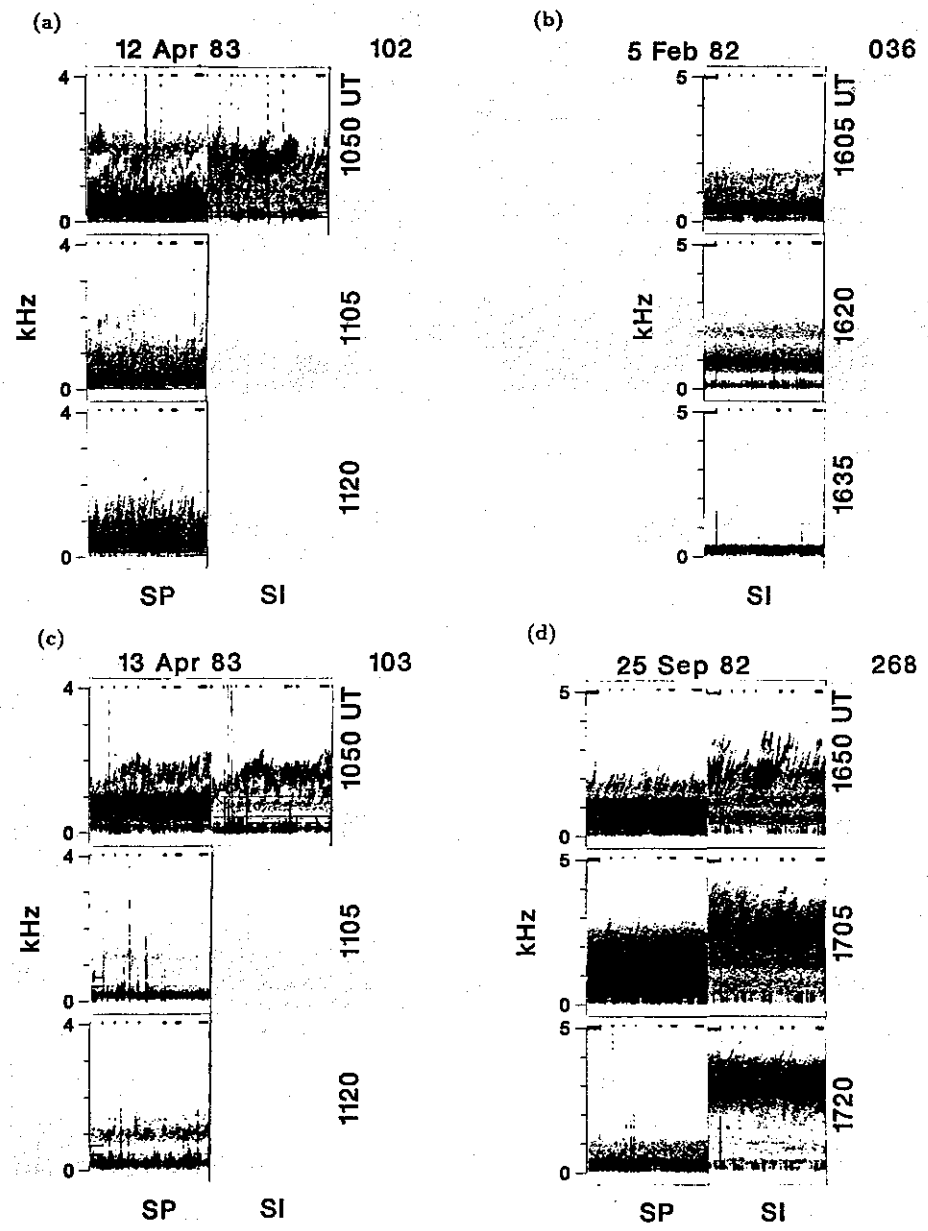


**Figure 3.17.** Synoptic dynamic spectra recorded at South Pole, Siple, and Palmer for four SC. Each panel shows dynamic spectra in the band 0-4 or 0-5 kHz for three 10 sec periods separated in time by 15 min. The periods were chosen to illustrate the spectra prior to, during, and after the SC whenever possible.

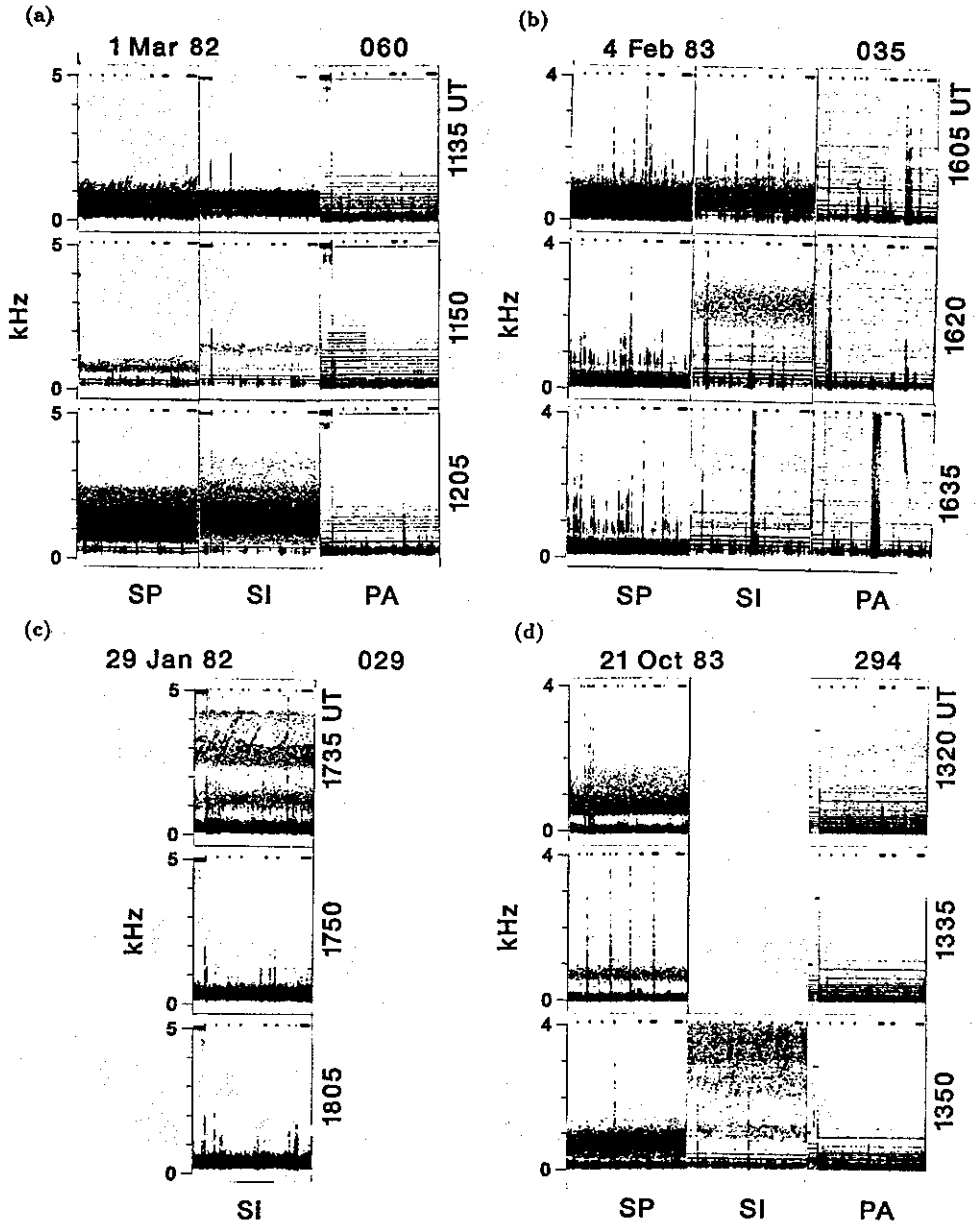


**Figure 3.18.** Synoptic dynamic spectra recorded at South Pole, Siple, and Palmer for four SC. Each panel shows dynamic spectra in the band 0-4 or 0-5 kHz for three 10 sec periods separated in time by 15 min. The periods were chosen to illustrate the spectra prior to, during, and after the SC whenever possible.

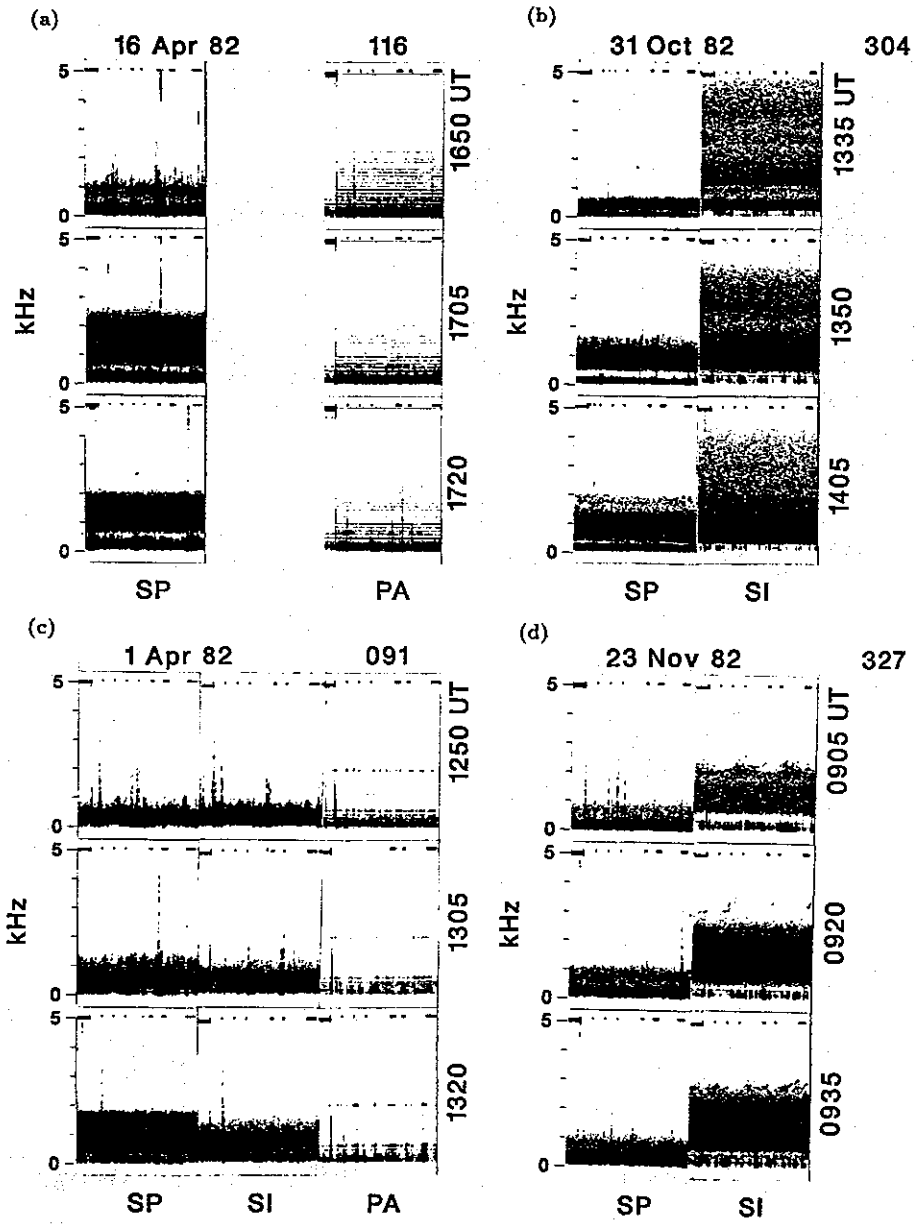


**Figure 3.19.** Synoptic dynamic spectra recorded at South Pole, Siple, and Palmer for four SC. Each panel shows dynamic spectra in the band 0-5 kHz for three 10 sec periods separated in time by 15 min. The periods were chosen to illustrate the spectra prior to, during, and after the SC whenever possible.

the amplitude remained below the pre-SC amplitude for a period of 20-25 min. In Figures 3.3(b-d), the amplitude remained at a reduced level for over 60 min.

Four events with wave amplitude reductions are shown in Figure 3.4. In Figures 3.4(b,c), very short transient enhancements were followed by amplitude reductions that reached minimum levels within 1 min. In Figures 3.4(a,d), an amplitude reduction lasting 20-25 min was followed by an amplitude increase in all channels to greater than pre-event levels. Note that in Figure 3.4(d) no transient enhancement occurred prior to the amplitude reduction.

Four events with long-lasting wave amplitude increases are shown in Figure 3.5. Amplitude increases following SC were observed to persist for several hours in many of the events examined. In Figures 3.5(a,b), the long-lasting increases were preceded by transient amplitude enhancements similar to those shown in Figures 3.2-3.4. No transient enhancement is evident in Figures 3.5(c,d), although an enhancement may be obscured by the ensuing activity.

*Siple observations.* Figure 3.6 shows amplitude plots of the 1-2 kHz and 2-4 kHz channels recorded at Siple station corresponding to five of the events illustrated in Figures 3.2-3.5. In each case, distinct changes in wave activity at Siple were associated with the SC. While the wave amplitude changes at Siple were generally similar to those at South Pole, some distinct differences can be noted. In Figure 3.6(c), the wave amplitude in the 2-4 kHz channel following the transient enhancement was greater than that prior to the SC. At South Pole, a similar transient enhancement was observed, but the subsequent wave amplitude was less than prior to the SC. In Figure 3.6(e), the 1-2 kHz channel showed a transient decrease while the 2-4 kHz channel showed a transient increase. At South Pole, both channels showed transient decreases. The comparison between wave activity at South Pole and Siple will be discussed in more detail in Section 3.4.

### 3.3.2 *PARTICULAR RESULTS*

*Magnetic field - ELF/VLF correlation.* Several authors [*Hayashi et al.*, 1968; *Korth et al.*, 1985] have suggested that wave amplitude increases/decreases are correlated

with compression/decompression of the magnetic field. As indicated by Figures 3.2-3.6, the wave response to a SC is more complex than a simple increase or decrease of the wave amplitude. In order to examine the assertion in more detail, however, the events in the limited data set have been compared with the magnetic field at geostationary altitude recorded by the GOES satellites.

Plots of the vector magnetic field from the GOES 2 or GOES 5 satellite for each of the events in the limited data set are shown in Figures 3.7-3.10. Each plot covers a period of 40 min and shows the amplitude of the HP (geographic North), HE (radially inward), and HN (westward) components of the magnetic field. GOES 2 and GOES 5 were located at the geographic equator near 107° W and 75° W (equivalent to local times of UT-7 hours and UT-5 hours) during the period covered by these events, with magnetic latitudes of approximately 9° and 11° respectively. The HP component was not available for three events (Figures 3.7(a,b) and 3.8(a)); no data were available for the three events in Figures 3.8(b), 3.9(b), and 3.10(b). Clear field strength increases were associated with the SC for the six events shown in Figures 3.7(c,d), 3.8(c,d), and 3.10(a,c). Decreases were observed for the two events in Figures 3.9(c,d). The response for the events in Figures 3.9(a) and 3.10(d) was uncertain, possibly due to the fact that the satellite was close to local midnight where the magnetic field response to a SC may be poorly defined [*Kuwashima and Fukunishi*, 1985].

In five of the six cases where field strength increases were observed at GOES, the wave amplitude at South Pole was characterized by a transient increase followed by a long-duration decrease. In the sixth case (Figure 3.10(c)), the wave amplitude was characterized by a long-duration increase. In both cases where field strength decreases were observed at GOES, long-duration wave amplitude decreases were observed at South Pole, although for the event shown in Figure 3.9(c) the decrease was preceded by a very short transient increase (note: the event in Figure 3.9(b) had a similar amplitude response and ground magnetograms indicate that this event was associated with a field strength decrease). In one of the two GOES decrease cases (Figure 3.9(d)), an amplitude increase occurred in the 2-4 kHz channel at Siple. The duration of the transient enhancement, although clearly frequency dependent, was in most cases roughly comparable to the rise time of the magnetic disturbance at GOES.

Despite the clear correlation between the onset of the magnetic perturbation and changes in the wave activity, the correlation between the subsequent ground/satellite magnetic field signatures and further wave activity is not obvious. The clearest correlations are shown in Figure 3.5(c). In this event, oscillations with a period of about 10 min lasting for a few cycles can be seen in both the ELF/VLF and magnetometer channels. Similar oscillations occurred in the magnetic signatures for the events in Figures 3.3(a) and 3.5(b,d) without counterparts in the ELF/VLF signatures. Correlations seem to be highly variable with characteristics that are not clear.

*Wave amplitude oscillations.* Well-defined oscillations in the wave amplitude were observed during the transient wave enhancement during several events. Figures 3.11-3.15 show amplitude plots for the limited event set which have been high pass filtered to emphasize oscillations with periods shorter than 100 sec. The filter techniques are described in Appendix B. Each panel shows the H-, D-, and Z-components of the magnetometer along with the wave amplitude in the 0.5-1, 1-2, and 2-4 kHz bands. The plots cover a time period of 10 min centered around the transient enhancement. Measured values for the oscillation period and the number of observed cycles for each of the events are given in Table 3.3.

In 12 of the 16 events, 3-4 cycles of a damped oscillation with period 60-90 sec were observed in the ELF/VLF channels. For example, in Figure 3.11(a) 3 cycles of an oscillation with period 80-90 sec appeared in each of the ELF/VLF channels following the SC onset near 1519 UT. Beginning at 1520 UT, what appears to be a 120 sec oscillation with two different phases present is evident in both the magnetometer H- and Z-components. Starting near 1523 UT, an oscillation with period about 60 sec began in the D-component.

The extent of the correlation between the oscillations in the magnetic field and the wave amplitude is not clear. Oscillations with periods in the range 60-90 sec are apparent in the magnetic field as well as the wave amplitude in at least 8 of the cases. However, the magnetic field oscillations do not have the damped structure observed in the wave amplitude and in most of the 8 cases there is a measurable difference between the magnetic field and wave periods.

Of particular interest is the case shown in Figure 3.14(a). In this example, 3 cycles of a 60 sec oscillation were observed in the ELF/VLF following the SC. Prior to the SC, the 0.5-1 and 1-2 kHz channels also showed a clear periodicity of approximately the same period, suggesting the possibility that oscillations associated with the SC represent a fundamental periodicity of the system independent of the SC-induced perturbation. A similar effect may also be noted in Figure 3.14(b).

Similar plots showing data recorded at Siple for five of the events are shown in Figure 3.15. Each plot shows the high-pass filtered wave amplitude in the 1-2 and 2-4 kHz channels covering a period of 10 min. In two of examples (Figures 3.15(a,b)), 3-4 cycles of an oscillation with period 60-70 sec are evident, only one of which (Figure 3.15(a)) had similar oscillations at South Pole. Of the three events with no apparent oscillations at Siple, two exhibited oscillations at South Pole.

There are two potential explanations for such oscillations. The first is that the oscillations are due to an oscillatory modulation of the environmental parameters superimposed on the SC compression. *Baumjohann et al.* [1983] found 2 min oscillations in both the plasma drift and the magnetic field at the GEOS 2 spacecraft during a SC (see Figure 2.13) and attributed them to an overshoot and subsequent oscillation of the magnetopause velocity about the expected value. A number of investigators have reported damped magnetic oscillations (Psc) with fundamental periods typically 4-5 min both on the ground [e.g. *Wilson and Sugiura*, 1961] and at spacecraft altitudes [*Barfield and Coleman*, 1970; *Baumjohann et al.*, 1984] as well as apparent harmonics starting near 40 sec [*Fukunishi*, 1979; *Sakurai et al.*, 1984; *Wedeken et al.*, 1986]. Such oscillations are often attributed to field line resonance. The fundamental periods tend to be somewhat longer than the observed ELF/VLF periods of 60-90 sec but the harmonic periods are in the correct range. The similarity of the ELF/VLF and magnetic field oscillation periods at South Pole supports the relation between magnetic field and wave activity, although the lack of one-to-one correlations weakens the argument. The second explanation is that the transient response of the wave growth rate to the step-like magnetic perturbation results in an overshoot and subsequent oscillation of the wave amplitude about the equilibrium level. This explanation will be discussed further in Chapter 5.

**Table 3.3.** Measured values for oscillations in the magnetic field and wave amplitude.

| | | Magnetometer | | ELF/VLF | | |
|---|---|---|---|---|---|---|
| Year | Day | Period (sec) | Cycles | Period (sec) | Cycles | Notes |
| 1982 | 029 | - | - | - | - | |
| | 036 | - | - | 80 | 3 | |
| | 060 | - | - | 80-90 | 2 | 0.5-1 kHz |
| | | - | - | 50 | 3 | 2-4 kHz |
| | 091 | - | - | - | - | |
| | 106 | 70 | 5+ | 60 | 3 | |
| | 163 | - | - | - | - | |
| | 197 | - | - | 80-90 | 3 | |
| | 268 | 60 | 5+ | 70 | 3-4 | |
| | 304 | - | - | 60-70 | 3 | |
| | 327 | 80 | 3+ | - | - | |
| | 328 | 90 | 4+ | 90 | 3 | |
| 1983 | 009 | 80 | 2-3 | 80 | 2-3 | 0.5-1 kHz |
| | | - | - | 50 | 5 | 2-4 kHz |
| | 035 | - | - | - | - | |
| | 102 | 60 | 5 | - | - | |
| | 103 | 80 | 5+ | 80-90 | 4-5 | |
| | 294 | 70-90 | 5+ | 70-80 | 3 | |

*Local time dependence.* Twice during the 1982-83 period, two SC were observed exactly one day apart to within 5 min. Such event pairs provide a unique opportunity to study the characteristics of SC wave emissions under conditions where local time, dipole tilt, and seasonal effects are held constant. The events of interest are the pair in Figures 3.2(c) and 3.5(d) (Pair 1) and the pair in Figures 3.3(a) and 3.3(c) (Pair 2). Data from Siple for Pair 2 are shown in Figures 3.6(c,d)). In Pair 2, the amplitude response in the 1-2 kHz and 2-4 kHz channels was somewhat similar, both events showing transient enhancements of approximately 5 min duration followed by amplitude reductions, but the response in the 0.5-1 kHz channels was considerably different for the two events. The significantly different magnetometer signatures for the two events should be noted as well. Pair 1 was even less consistent. The amplitude for the first event in Pair 1 was primarily transient with little long-duration amplitude

modification, while the response for the second event showed no transient effect but rather a long-enduring amplitude increase. Again, the magnetic signatures for the two events were considerably different. Indeed, the events in Figures 3.2(a) and 3.2(b) showed a much more similar response in both the magnetic field and wave amplitude even though these events were observed roughly one month apart and differ by one hour in local time.

The results suggest that the wave response to SC is more sensitive to the configuration of the particular event than to the magnetic local time of the receiver. Moreover, factors which determine the characteristics of the wave response are significantly different over time scales as short as one day.

## 3.4 WAVE SPECTRAL CHARACTERISTICS

The relative rarity of SC makes it difficult to obtain continuous broadband data for the full duration of a SC. For most cases studied here, broadband data were available only at the synoptic intervals of 1 min in every 5 or 15. In this section, both continuous and synoptic broadband data are used to discuss spectral characteristics of the waves. The synoptic data illustrate the observed long-term spectral modifications and the comparison of spectra recorded at different stations. The continuous data are used primarily to show the spectral modifications associated with the transient wave enhancement.

### 3.4.1 *SYNOPTIC DYNAMIC SPECTRA*

Figures 3.16-3.19 show dynamic spectra from synoptic recordings for each of the events in the limited data set. The figures illustrate a number of long term changes in ELF/VLF spectra commonly observed during SC. For each event, sample spectrograms covering the band 0-4 kHz or 0-5 kHz for three 10 sec periods are shown. The samples are separated in time by 15 min and thus cover a total period of 30 min. For each event, spectrograms from South Pole, Siple, and Palmer are shown

(when available; spectrograms from Roberval are substituted for Siple for one event). The three samples were chosen to cover intervals prior to, during, and after the SC whenever possible. The samples can be compared with the corresponding amplitude records to determine the extent to which each sample represents typical wave activity for the corresponding period. In the following discussion, the approximate upper and lower cutoff frequencies of the observed wave activity will be referred to as the UCF and LCF respectively.

Some of the features of the spectrograms result from terrestrial interference effects which are not of interest to us. The vertical lines are due to atmospherics (sferics) from lightning. The noise band below 400 Hz which appears to consist of impulsive emissions (see Figure 3.19(a) for a clear example) is also due to sferics. The nearly monochromatic lines seen mostly at lower frequencies are power line harmonics from the station power grid.

In each of the examples, the first sample shows that polar chorus consisting of diffuse and discrete emissions with a UCF in the range 0.5-2.5 kHz was observed prior to the event at South Pole. In eight of the examples (Figures 3.16(a,b,d), 3.17(a,c), 3.18(a,b), and 3.19(c)), data from Siple (or Roberval) were available and showed similar polar chorus activity with a UCF within a few hundred Hz of that observed at South Pole, although differences in band structure and LCF were apparent. In three of the eight cases (Figures 3.16(b,d), 3.17(c)), similar discrete emissions are identifiable in the spectrograms from South Pole and Siple, indicating that both stations were observing wave activity from the same source region. In Figure 3.16(b), despite the clear correlation between discrete emissions, the LCF at Siple was significantly higher than that at South Pole. Differences in the sub-ionospheric propagation losses between the ionospheric exit point of the wave activity and the two receivers may account for such discrepancies or South Pole may have been observing an additional source region not observed at Siple.

In four of the examples (Figures 3.16(c), 3.17(d), 3.19(b,d)), wave activity observed at Siple prior to the SC was distinctly different from that observed at South Pole. In Figures 3.19(b,d), a band of diffuse emissions with UCF greater than 2 kHz is evident at Siple while South Pole data show wave activity only below 1 kHz. In Figure

3.17(d), strong wave activity consisting of diffuse and discrete emissions occurred at both stations. However, at Siple activity extended up to about 3.5 kHz while South Pole data show emissions only up to 2.0 kHz; there is no clear correlation between emissions observed at the two stations.

The second sample in each example shows the change in the wave spectrum during or immediately after the SC. In Figures 3.16(a,c,d), 3.17(d), and 3.19(a,c,d), the second sample includes some portion of the transient wave enhancement associated with the first few minutes after the onset of the SC. These seven examples best represent the initial wave changes resulting from the SC. In each case, an increase in the UCF was observed at both South Pole and Siple/Roberval (when available), in several cases by as much as 1 kHz or more. Five of the cases (Figures 3.16(a,b,d), 3.17(b), 3.18(b), and 3.19(b)) showed an increase in the LCF as well. In general, both the diffuse and discrete emissions components of the observed wave spectrum were modified following the SC. In Figure 3.16(d), well-defined discrete emissions are evident near the new UCF at Siple with no comparable emissions apparent in the South Pole data despite the fact that similar emissions occurred at both stations prior to the SC.

The third sample (as well as the second sample for some events) represents the long-term modification of the wave spectrum associated with each event. In each case, the spectrum in the third sample was distinctly different from that in the first sample, suggesting that modifications of the wave source were not simply transient. The long term modifications varied considerably between events. In Figures 3.16(a-d), 3.17(a-d), and 3.18(b,c), decreases in the amplitude of the diffuse emissions and the occurrence rate of discrete emissions were observed, whereas Figures 3.18(a,d) and 3.19(a-d) showed distinct amplitude increases and corresponding modifications of the bandwidth and spectral structure.

In only one of the 16 events (Figure 3.16(a)) did Palmer record a change in wave activity associated with the SC. In this event, Palmer was observing very little wave activity prior to the SC. During the transient enhancement, diffuse emissions in the band 0-3 kHz with some evidence of discrete (and periodic) structure were observed. Following the transient enhancement, the wave activity was similar to that prior to the SC.

### 3.4.2 *CONTINUOUS DYNAMIC SPECTRA*

For the limited data set, only one event (shown in Figure 3.2(a)) had continuous data available. A dynamic spectrogram for the event is shown in Figure 3.20(a). This event provides a good illustration of the initial amplitude enhancement as well as the long term spectral modification. Prior to the onset of noise growth near 1519 UT, the spectrum consisted of a diffuse noise band with LCF below 100 Hz, UCF at approximately 0.8 kHz, and a band of discrete emissions from the UCF of the diffuse emissions to about 1.4 kHz (spectral features such as discrete emissions may be more apparent in the higher resolution spectrograms for these events shown in Figures 3.22-3.28). At the time of the SC, the UCF of the diffuse noise began to increase, reaching 2.2 kHz after 30 sec and remaining near this frequency for about 3 min. No similar increase in the UCF of the discrete emissions was observed. During this period, an increase in the LCF to about 300 Hz was also observed. The UCF of the diffuse noise subsequently decreased to 300 Hz and the discrete emissions became sporadic. The growth onset period will be discussed in more detail in Section 3.5.

Figures 3.20(b-d) and 3.21 show dynamic spectra for seven other events for which continuous broadband data were available. In each case, a transient enhancement of the wave activity was observed together with an increase in the UCF. The length of the transient amplitude increase varied from 1 to 6 min and the corresponding rise time of the UCF varied from less than 1 min to several minutes. In all examples except Figure 3.20(c) the wave activity consisted primarily of a diffuse component with some discrete emissions. In Figure 3.20(c), only discrete emissions were observed and a clear increase in both the frequency range and the UCF of the emissions was observed following the SC.

It should be noted that in these examples the observed wave growth generally appeared to consist of amplitude and spectral modification of previously existing wave activity. This was particularly evident in the example in Figure 3.20(d) in which the triggered emissions associated with the SC perturbation appeared to have a lower (triggering) frequency closely associated with the UCF of the diffuse emissions band even as the UCF increased throughout the event.

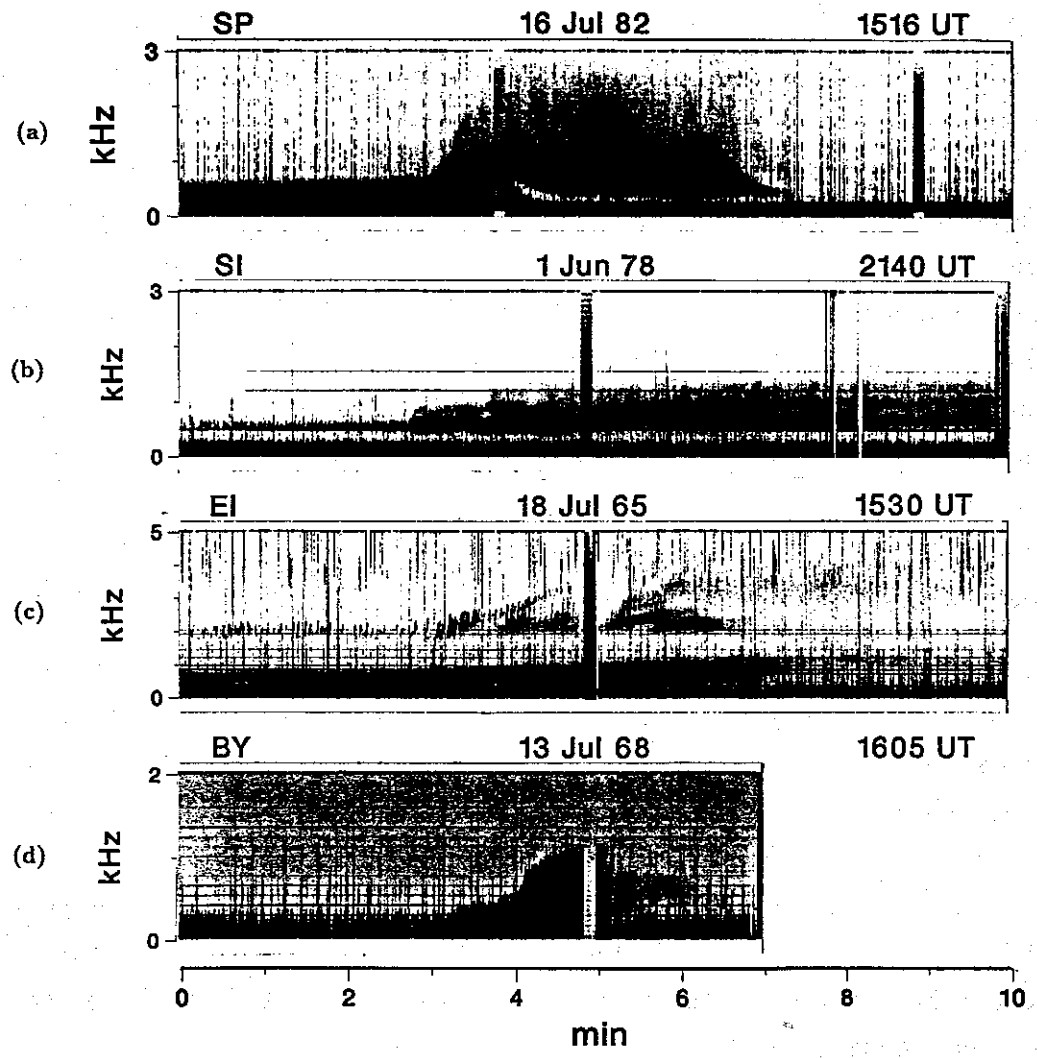


**Figure 3.20.** Continuous dynamic spectra for four SC. The figure illustrates the transient wave enhancement commonly observed during SC.

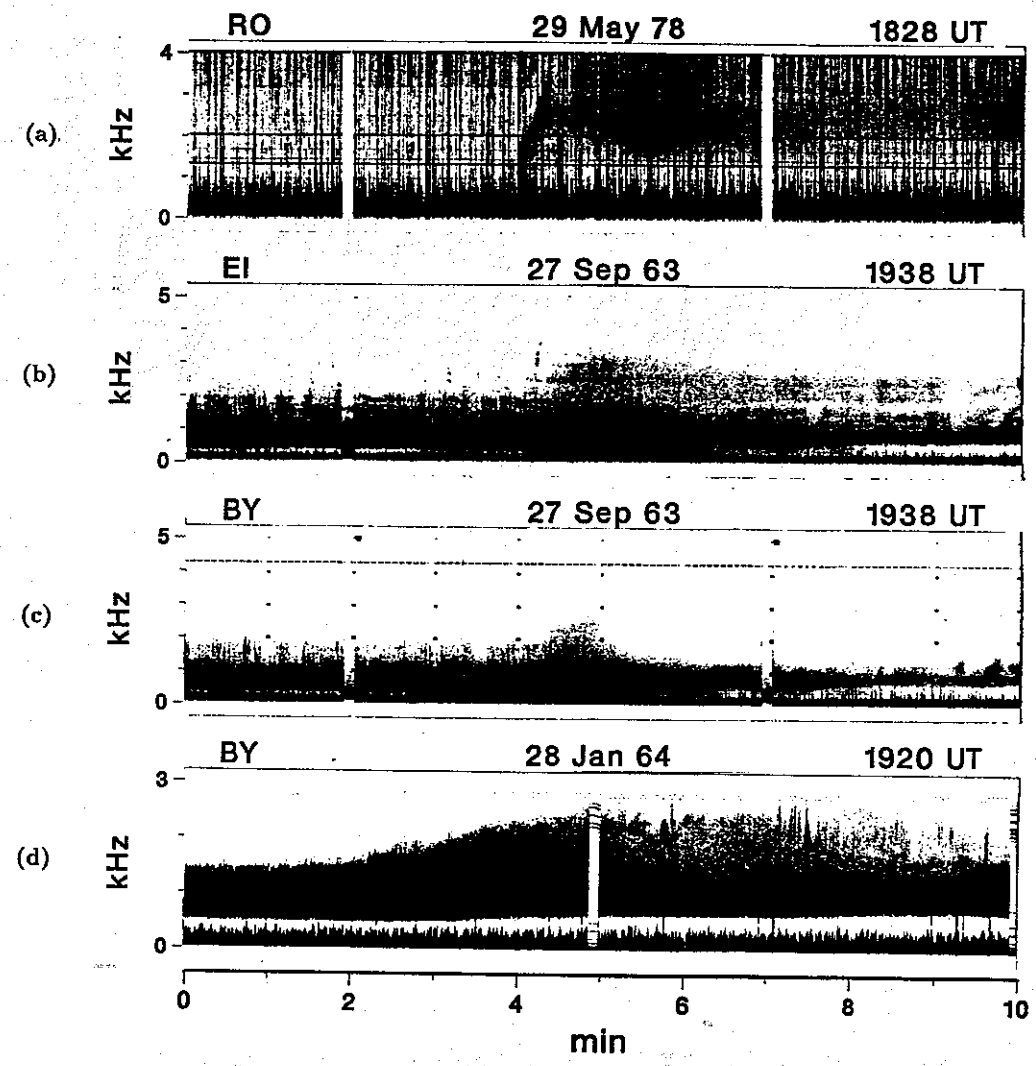


**Figure 3.21.** Continuous dynamic spectra for four SC. The figure illustrates the transient wave enhancement commonly observed during SC.

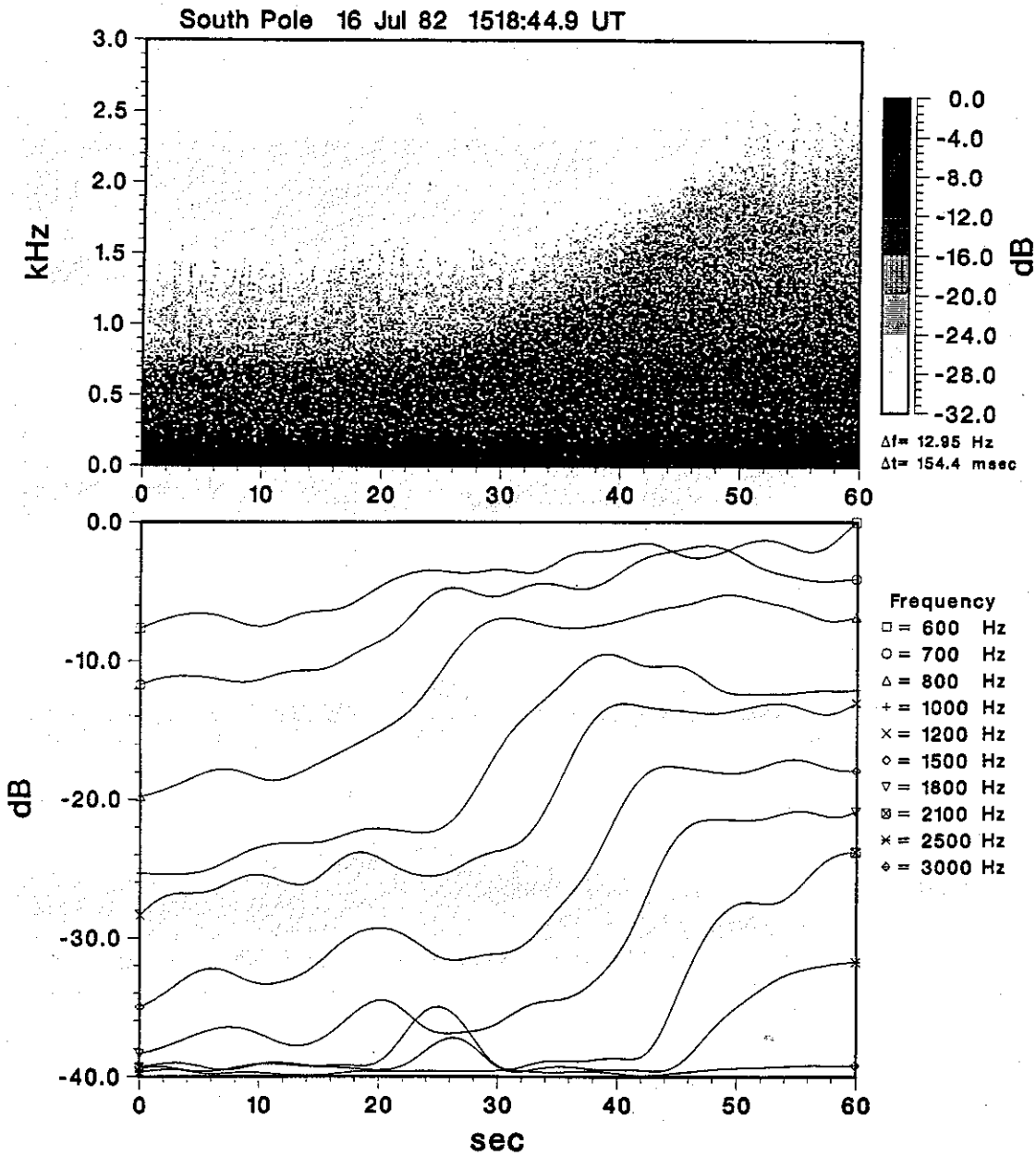


**Figure 3.22.** Dynamic spectra and narrowband amplitude plots for the wave growth period. The top panel shows dynamic spectra for the period during which wave growth was observed. The bottom panel shows amplitude in a number of narrowband channels for the same period.

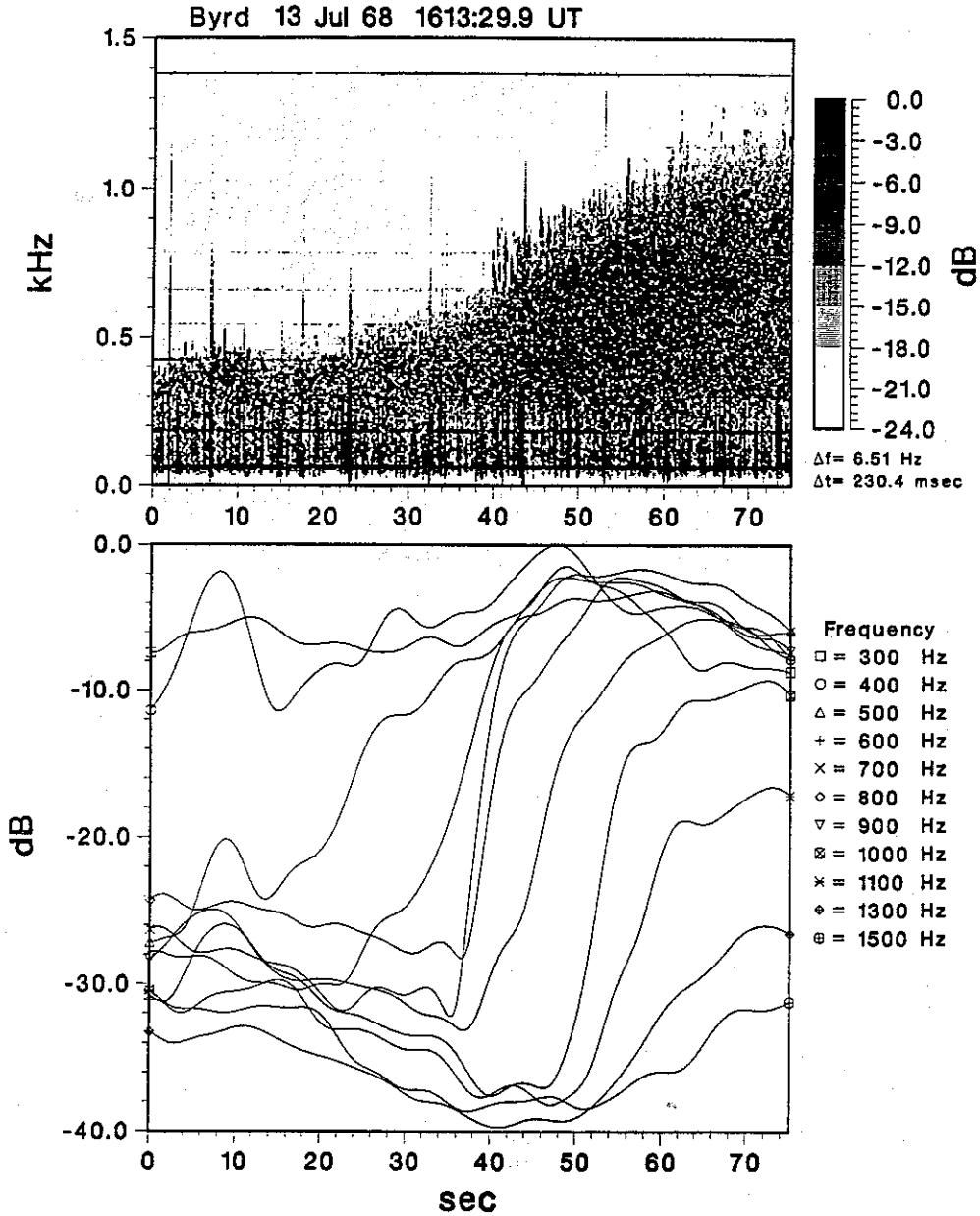


**Figure 3.23.** Dynamic spectra and narrowband amplitude plots for the wave growth period. The top panel shows dynamic spectra for the period during which wave growth was observed. The bottom panel shows amplitude in a number of narrowband channels for the same period.

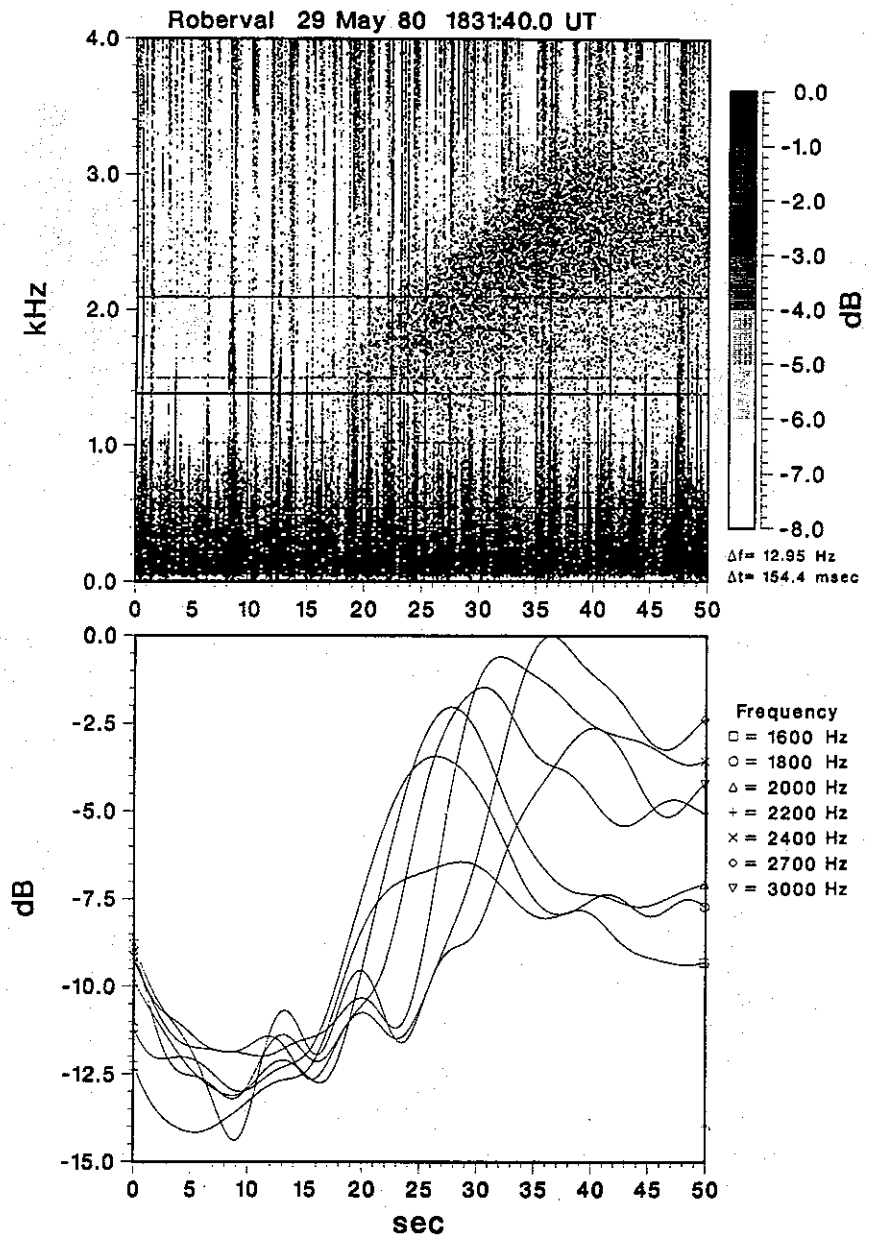


**Figure 3.24.** Dynamic spectra and narrowband amplitude plots for the wave growth period. The top panel shows dynamic spectra for the period during which wave growth was observed. The bottom panel shows amplitude in a number of narrowband channels for the same period.

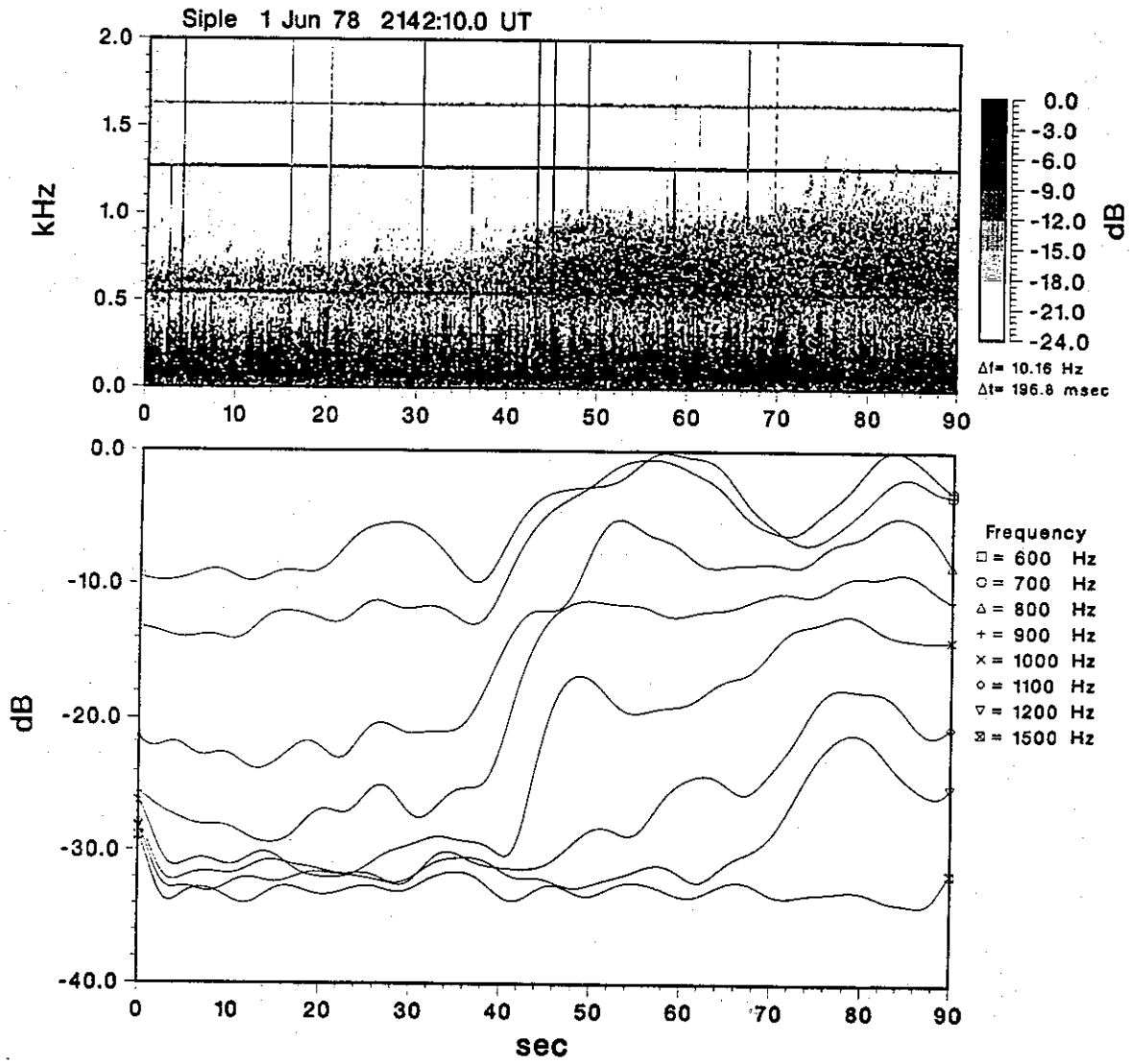


**Figure 3.25.** Dynamic spectra and narrowband amplitude plots for the wave growth period. The top panel shows dynamic spectra for the period during which wave growth was observed. The bottom panel shows amplitude in a number of narrowband channels for the same period.

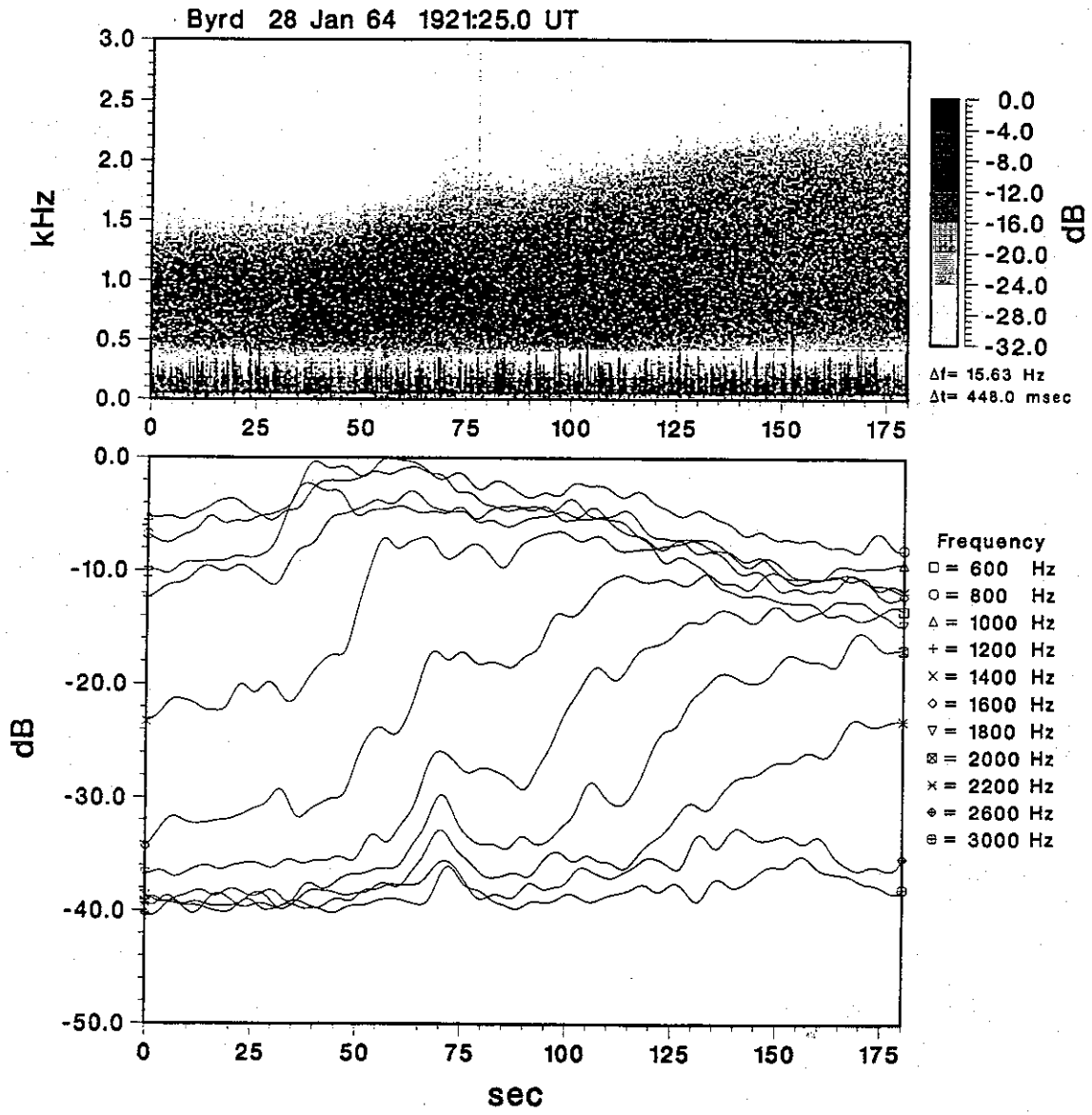


**Figure 3.26.** Dynamic spectra and narrowband amplitude plots for the wave growth period. The top panel shows dynamic spectra for the period during which wave growth was observed. The bottom panel shows amplitude in a number of narrowband channels for the same period.

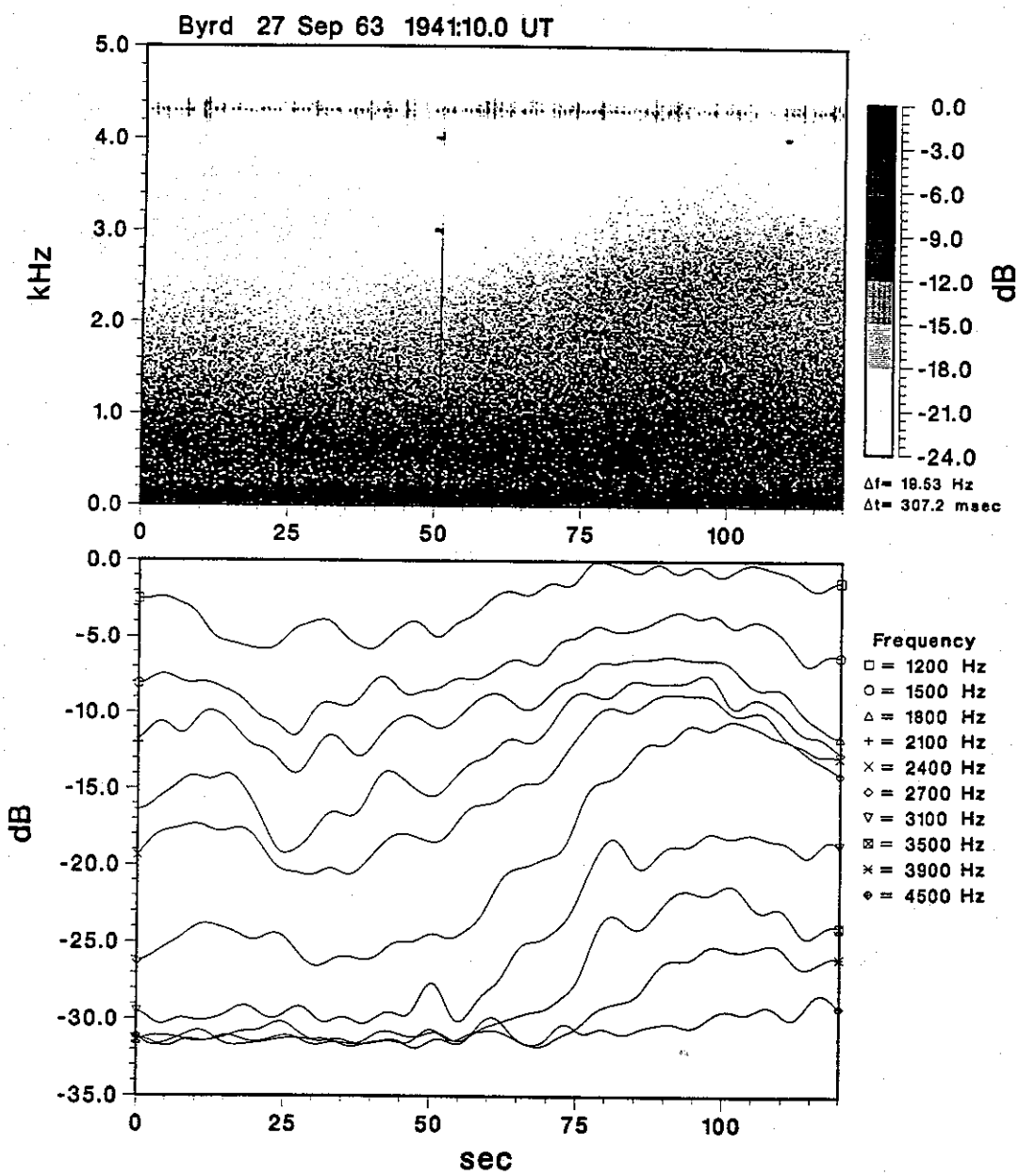


**Figure 3.27.** Dynamic spectra and narrowband amplitude plots for the wave growth period. The top panel shows dynamic spectra for the period during which wave growth was observed. The bottom panel shows amplitude in a number of narrowband channels for the same period.

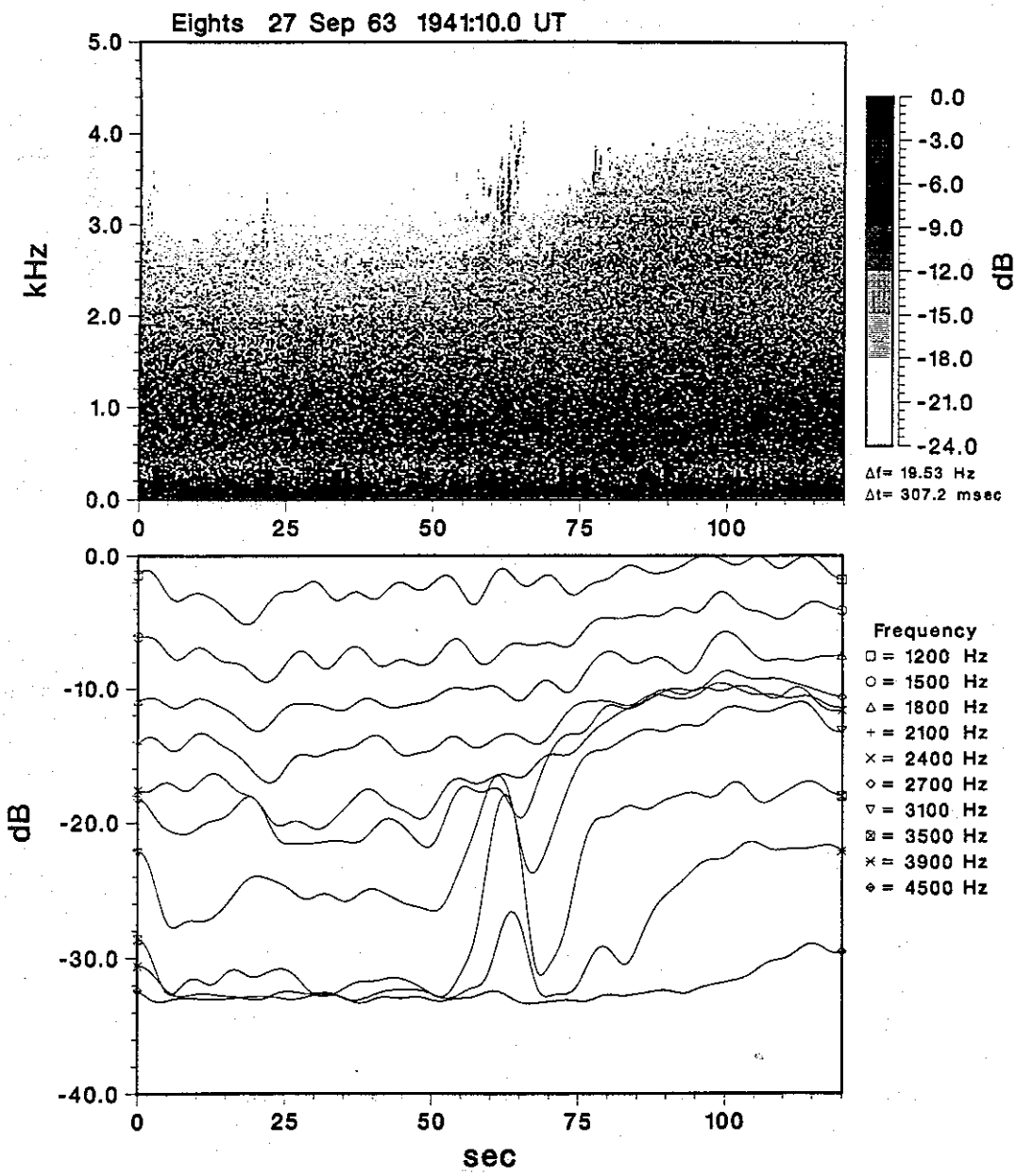


**Figure 3.28.** Dynamic spectra and narrowband amplitude plots for the wave growth period. The top panel shows dynamic spectra for the period during which wave growth was observed. The bottom panel shows amplitude in a number of narrowband channels for the same period.

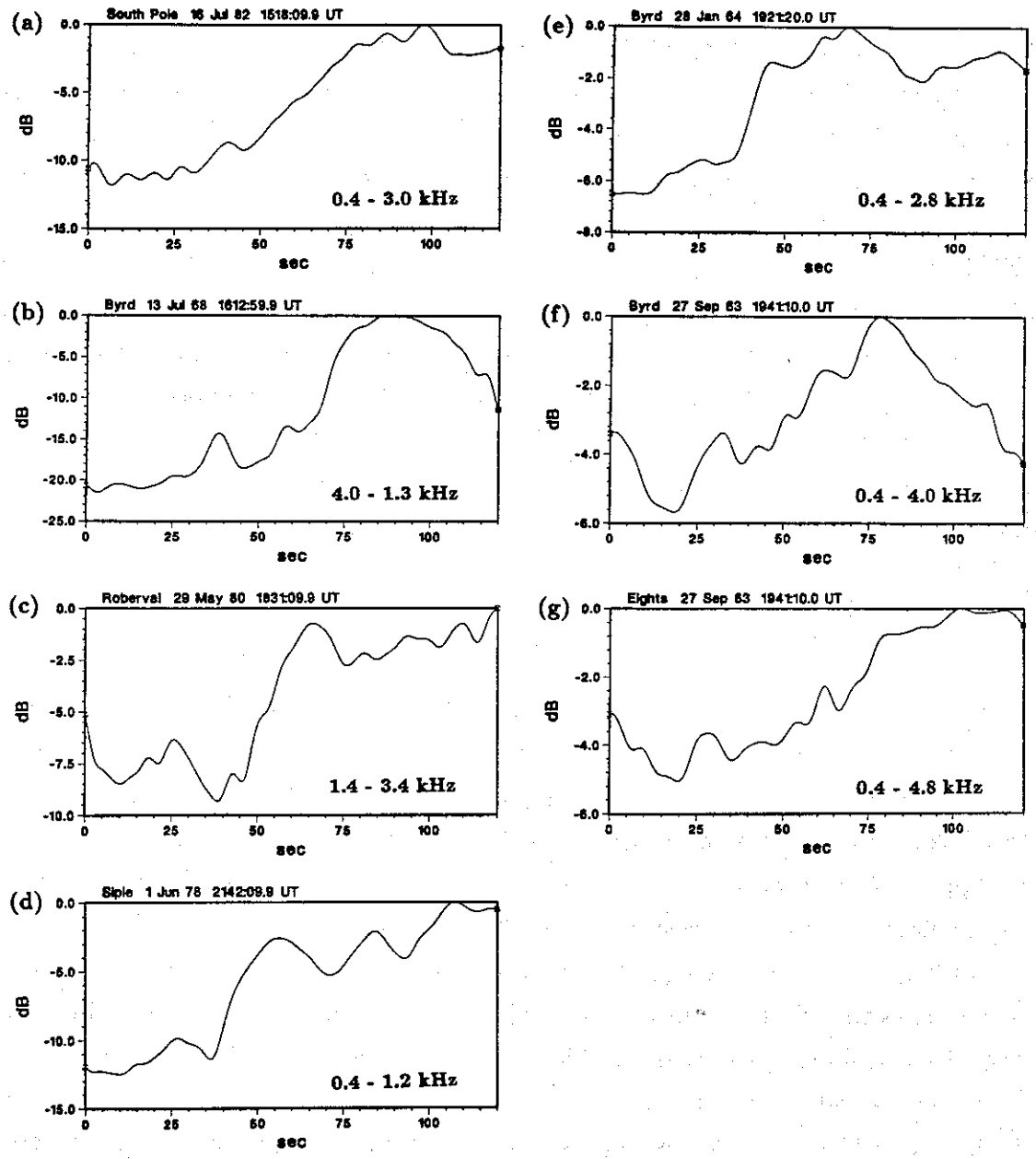


**Figure 3.29.** Wideband amplitude plots for the wave growth period. The filter pass bands were chosen to include all magnetospheric wave energy and exclude the sferic wave energy at lower frequencies.

## 3.5 WAVE GROWTH CHARACTERISTICS

The wave growth period, in most cases the first several tens of seconds of the event, provides what is probably the best opportunity for making measurements which can be compared with theoretical predictions. This is so for two main reasons. First, the observed spectral modifications result from only those changes in the source mechanism which act within this short time period. Thus, for example, enhanced electron distributions injected from the magnetotail cannot play a role in the wave growth observed on the dayside during the growth period. Second, the magnetic field and plasma changes associated with the SC can be easily modeled during the early part of the disturbance and thus allow for reliable modeling of the expected changes in wave properties. In this section, we examine in detail the growth onset period for several events, including measurements of the growth period, growth rate, and UCF modifications.

### 3.5.1 *DESCRIPTION OF DATA FORMAT*

Figures 3.22-3.28 illustrate seven examples of wave activity during the wave growth onset period of the SC. Longer period dynamic spectra for each of the events are also shown in Figures 3.20-3.21. The data for the figures were digitized from the original broadband analog tapes and processed in digital form using computer codes discussed in Appendix D. In each example, the top panel is a dynamic spectrogram showing the changes in the wave spectrum observed during the growth period. The time scale shows elapsed seconds starting from the time shown at the top of the plot. The bottom panel shows the amplitude in a number of narrowband channels corresponding to the period shown in the spectrogram. The 0 dB reference level is the same for both the spectrogram and the amplitude plot. The bandwidth of the narrowband filters was 50 Hz. The filter output was low passed, in order to distinguish the growth trend from higher frequency fluctuations in the wave amplitude, and processed to remove the impulses caused by sferics. The details of the filter procedure are discussed in Appendix B. The filter center frequencies are indicated by the legend on the right hand side of the plot. In each of the figures, however, amplitude generally decreases

with frequency so that the figure can be viewed in a simple manner by recognizing that the center frequency of the filter channels increases as the plot is scanned downward. Measured values for a number of features of the seven events are listed in Table 3.4.

In most of the events (e.g., Figure 3.22), the start and end of the growth phase (as indicated by the saturation of the amplitude) are readily apparent in the figures. In Figure 3.28, it is not clear whether the discrete emissions (readily seen near 60 sec but observed sporadically throughout the record) or the subsequent growth beginning near 65-75 sec indicates the start of the growth period. Analysis of data prior to this period shows that similar emissions occurred over a number of minutes before the SC, suggesting that the occurrence of the emissions near the growth onset was probably coincidental. For this discussion, it will be assumed that the emissions were not part of the SC triggered growth process.

In Figures 3.25 and 3.26 there is some ambiguity in determining the saturation point. In Figure 3.25, it appears that the initial growth was confined to the period 35-50 sec. The growth at higher frequencies in the period 65-85 sec was due to the appearance of discrete emissions at these frequencies. The growth analysis for this event will thus be restricted to the period 35-50 sec. Figure 3.26 presents a more difficult problem. It is not clear whether the initial growth period should terminate at the first amplitude peak level (near 70 sec at the higher frequencies) or extend to the final peak level near 150 sec. The earlier value is consistent with the saturation of the wideband amplitude shown in Figure 3.29(e) and will thus be used for the following discussion.

### 3.5.2 *PARTICULAR RESULTS*

*The upper cutoff frequency.* As noted previously, the UCF increases during the growth phase with growth observed first at lower frequencies and with increasing delay at higher frequencies. The increase was a factor of 1.3-2.8 times the initial UCF for these events, corresponding to a frequency increase of 0.3-1.4 kHz. The delay between the growth onset at lower frequencies and at higher frequencies was 10-35 sec.

*Narrowband measurements.* The maximum total narrowband growth varied from 12 dB to 29 dB in the seven examples. Defining the growth bandwidth as the frequency

range for which the total growth was within 3 dB of the maximum total growth, the growth bandwidth for the events was 0.4-1.2 kHz. The narrowband growth rates within the growth band were within the range 0.3-2.7 dB/sec and were roughly constant over the 3 dB bandwidth.

In measuring the growth rates, channels showing evidence of discrete emissions were excluded so that the growth rates represent only the growth process for incoherent noise. The two events for which such exclusion were necessary are those shown in Figures 3.23 and 3.28. The growth rate and total growth at a given frequency showed no dependence on the initial wave amplitude. These features are particularly evident in Figure 3.22, for which growth rate and total growth were roughly constant over a bandwidth of 1.2 kHz and an initial dynamic range of 20 dB.

*Total growth.* The total growth integrated over the entire growth band (for this measurement, all frequencies for which growth was observed were included in the filter band) is shown in Figure 3.29 for each of the events. Total integrated growth for the events ranged from 5 dB to 20 dB with growth times of 20-45 sec.

*Multiple station observations.* Figures 3.27 and 3.28 are of particular interest because they show the growth phase for one event recorded at two stations, in this case Byrd and Eights. The time and frequency scales and the choice of narrowband center frequencies is the same for both figures. It can be seen from Figure 3.29 that total growth and growth time were approximately equivalent at both stations. The UCF was approximately 0.3-0.4 kHz higher at Eights than at Byrd both prior to and after the SC. Both stations observed an increase of 1.1-1.2 kHz in the UCF. The onset of the growth phase appears to have occurred at about $55 \pm 10$ sec at each station. The maximum total narrowband growth was the same (13-14 dB) at both stations, although it is somewhat difficult to compare the narrowband growth rates due the presence of discrete emissions in the Eights record. As mentioned previously, the discrete emissions appear to have been an ongoing phenomenon and not a direct result of the SC. Thus the two stations appear to have observed very similar phenomena during this event.

**Table 3.4.** Measured values for growth phase characteristics.

| Event | Initial UCF (kHz) | Final UCF (kHz) | Onset Delay (sec) | WB Growth (dB) | Growth Rate (dB/sec) | Growth Time (sec) | Max. Growth (dB) | 3 dB BW (kHz) | 3 dB CF (kHz) | 3 dB DR (dB) |
|---|---|---|---|---|---|---|---|---|---|---|
| 16 Jul 82 SP | 0.8 | 2.2 | 30 | 10 | 1.3-1.8 | 8-14 | 16 | 1.2 | 1.5 | 20 |
| 13 Jul 68 BY | 0.4 | 1.1 | 35 | 20 | - | - | 29 | 0.4 | 0.8 | 7 |
| 29 May 80 RO | - | 3.3 | 10 | 6 | 1.5-2.5 | 9-14 | 12 | 1.2 | 2.4 | 2 |
| 1 Jun 78 SI | 0.7 | 1.0 | 10 | 6 | 1.3-2.7 | 8-16 | 14 | 0.5 | 0.9 | 17 |
| 28 Jan 64 BY | 1.4 | 1.8 | 35 | 5 | 1.5-1.3 | 10-30 | 14 | 0.5 | 1.5 | 14 |
| 27 Sep 63 BY | 2.4 | 3.5 | 20 | 5 | 0.3-0.4 | 20-30 | 13 | 1.2 | 2.9 | 13 |
| 27 Sep 63 EI | 2.7 | 3.9 | 20 | 5 | 1.3-2.0 | 10-20 | 14 | 1.2 | 3.1 | 13 |

## 3.6 WAVE GROWTH ONSET TIME

Since it is possible to make accurate measurements of the arrival time of both the whistler-mode waves and the magnetic disturbance on the ground as well as the magnetic disturbance at spacecraft locations, the measurements may be used to help identify the wave source region. This technique was first suggested by *Hayashi et al.* [1968], who proposed that the approximately 30 sec delay they observed between the arrival of the waves and the magnetic disturbance represented a propagation time difference between the waves travelling at the whistler-mode group velocity and the magnetic disturbance propagating at the much smaller Alfvén velocity from a source region in the equatorial plane.

### 3.6.1 *DESCRIPTION OF DATA FORMAT*

For this analysis, events were chosen for which both the wave and magnetic perturbation onset could be determined from the University of Maryland digital data to within an estimated accuracy of ±10 sec or better. The GOES magnetometer data were measured to an estimated accuracy of ±5 sec. The errors are in general significantly larger than the sampling period and reflect a subjective determination of the

accuracy with which a particular onset can be identified. The error bars in the data plots refer to these measurement errors.

### 3.6.2 *PARTICULAR RESULTS*

*Wave growth/ground magnetic field delay.* Figure 3.30(a) shows the measured delay between the arrival of the waves and the magnetic perturbation plotted versus the magnetic local time of South Pole. Positive delays indicate that the magnetic perturbation arrived after the wave onset. The delays had a mean value of 30 sec and a standard deviation of 18 sec. Although the delays were almost exclusively within the range 0-60 sec, there was no strong tendency toward any single value nor an obvious dependence on local time. The observed variations are much larger than would be reasonable to expect from the measurement errors. These observations suggest that if the explanation proposed by *Hayashi et al.* [1968] is correct, differences in Alfvén velocity or location of the wave source region for different events add variability in the delay of the order of the measured standard deviation in the data. Such variability precludes the possibility of using delay measurements in individual cases to identify the source region.

*Wave growth/GOES magnetic field delay.* Figure 3.30(b) shows the measured delay between the arrival of the waves on the ground and the onset of the magnetic disturbance at GOES plotted versus the local time at GOES. The figure shows a clear dependence of the delay on local time with apparent minimum and maximum values of 10±20 sec at noon and 100±20 sec at midnight. Such a delay could have a number of causes, but it should be noted that 120 sec is approximately the delay time for the SC disturbance to propagate from noon to midnight at geostationary altitudes, as can be inferred from the results of *Kuwashima and Fukunishi* [1985]. The variation in the delays is again significantly larger than the measurement errors.

The onset time measurements will be discussed in greater detail in Chapter 4 in an effort to determine the location and extent of the wave generation regions associated with SC.

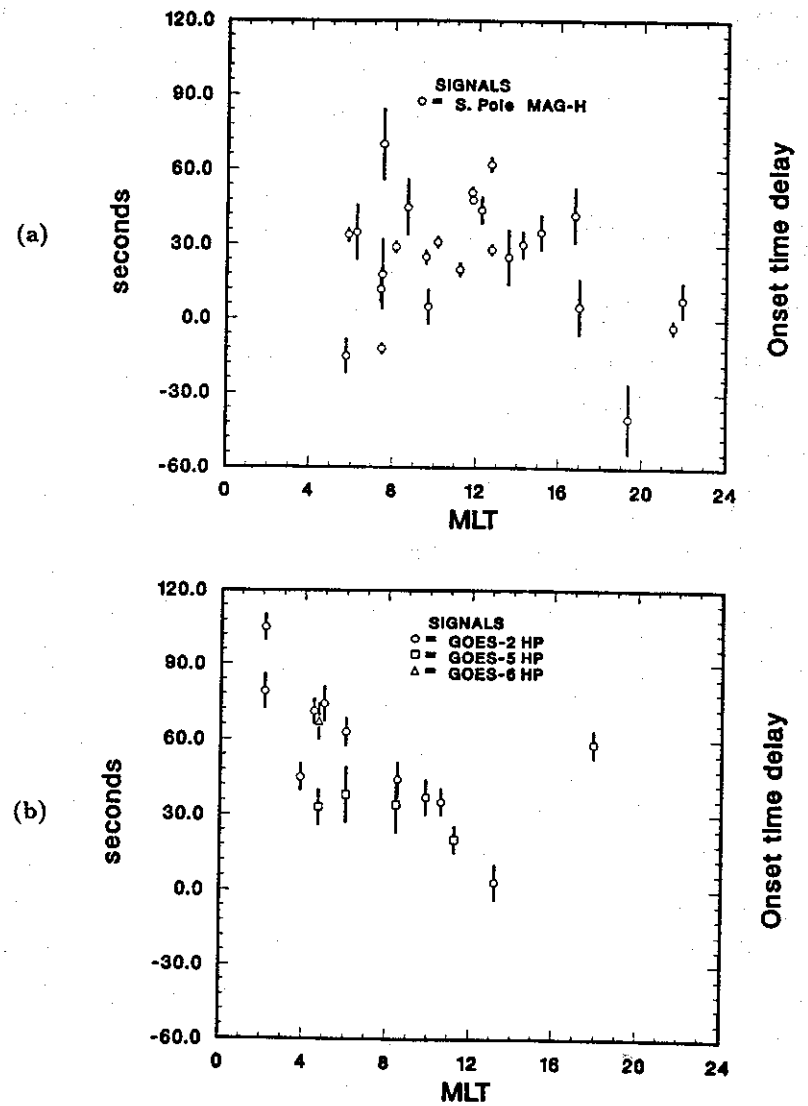


**Figure 3.30.** Measured delay between the onset of wave growth and the magnetic disturbance. (a) The delay between the onset of ELF/VLF wave growth and the arrival of the magnetic disturbance at South Pole. (b) The delay between the onset of wave growth at South Pole and the arrival of the magnetic disturbance at the GOES spececraft.

## 3.7 PARTICLE PRECIPITATION CHARACTERISTICS

Numerous investigators have studied particle precipitation during SC using riometer observations. In this section, riometer data from the University of Maryland riometer systems at South Pole and Siple are presented for the events in the limited data set.

### 3.7.1 *DESCRIPTION OF DATA FORMAT*

The output of the 20.5, 30.0, and 51.4 MHz riometer channels along with the corresponding magnetic field H-component and 0.5-1 kHz amplitude at South Pole are shown for each of the limited data set events in Figures 3.31-3.34. Each channel has been low pass filtered to remove high frequency fluctuations. The details of the filter process are described in Appendix B. Each plot shows a period of 10 min. The dashed line indicates the time when the onset of wave growth was observed.

Measured values of absorption and several related parameters are listed in Table 3.5. The pre-SC absorption level was measured just prior to the decrease in riometer amplitude. The post-SC level was measured at the first distinct maximum in the absorption. In half of the events, the absorption continued to increase after the first distinct maximum and an overall maximum was reached typically several tens of minutes after the absorption onset. The earlier maximum was chosen to best represent the initial absorption due to precipitation associated with the transient wave enhancement and to eliminate possible contributions from subsequent storm effects. The typical measurement error was estimated to be $\pm 0.05$ dB.

### 3.7.2 *PARTICULAR RESULTS*

*Absorption values.* Of the 16 events, 12 showed riometer absorption that was clearly associated with the SC (Figures 3.31(a-d), 3.32(a,c,d), 3.33(a,b), and 3.34(a-c)). In 8 of the 16 events, a background absorption level greater than 0.1 dB at 30 MHz was present prior to the SC. Typical SC absorption values, with the background level subtracted, were 0.2-1.0 dB at 20.5 MHz, 0.1-0.4 dB at 30.0 MHz, and 0.0-0.2 dB at

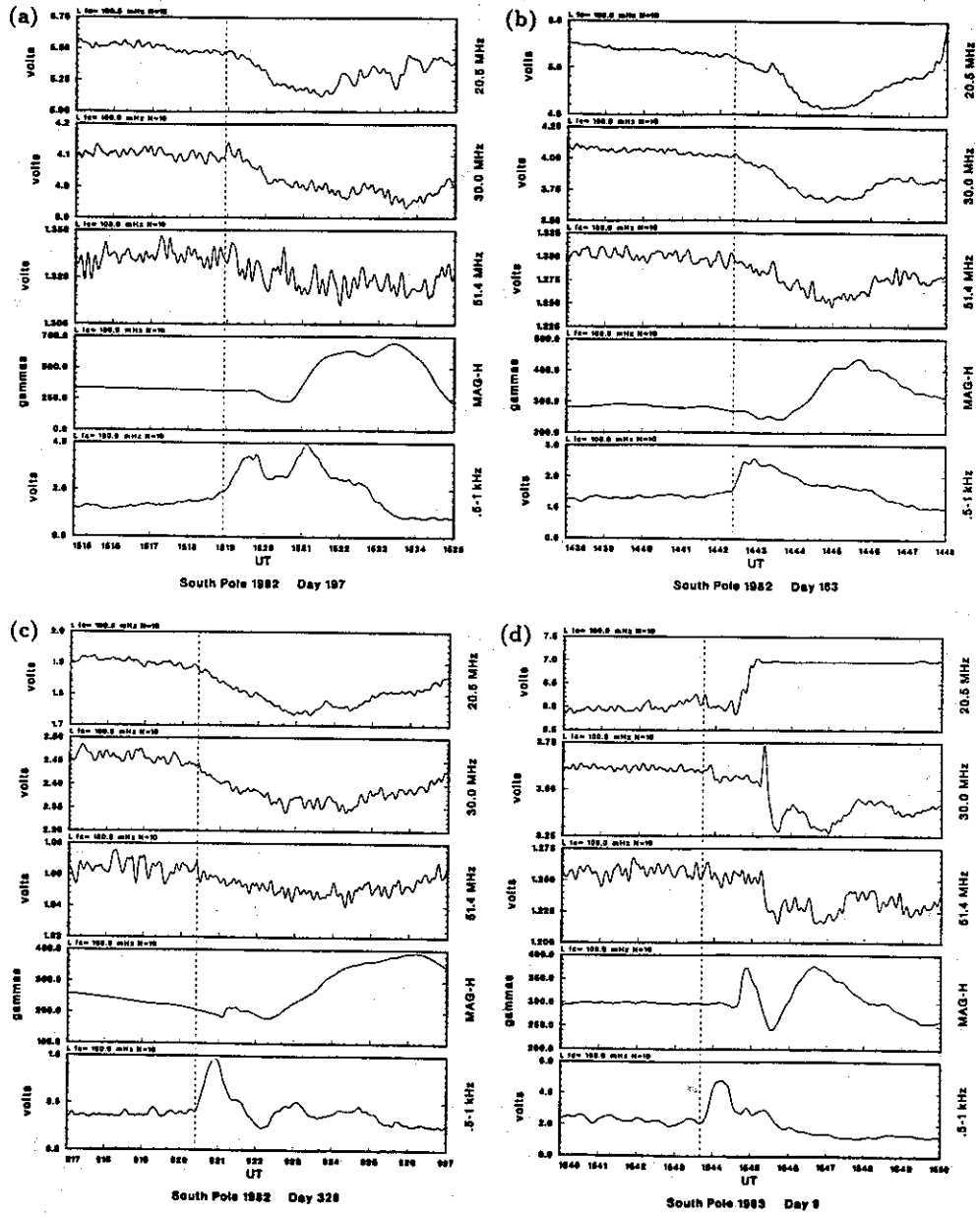


**Figure 3.31.** Riometer data recorded at South Pole for four SC. Each panel shows the output of the 20.5, 30.0, and 51.4 MHz riometer channels as well as the magnetometer H-component and the ELF amplitude in the 0.5-1 kHz channel. The dashed line indicates the wave growth onset.

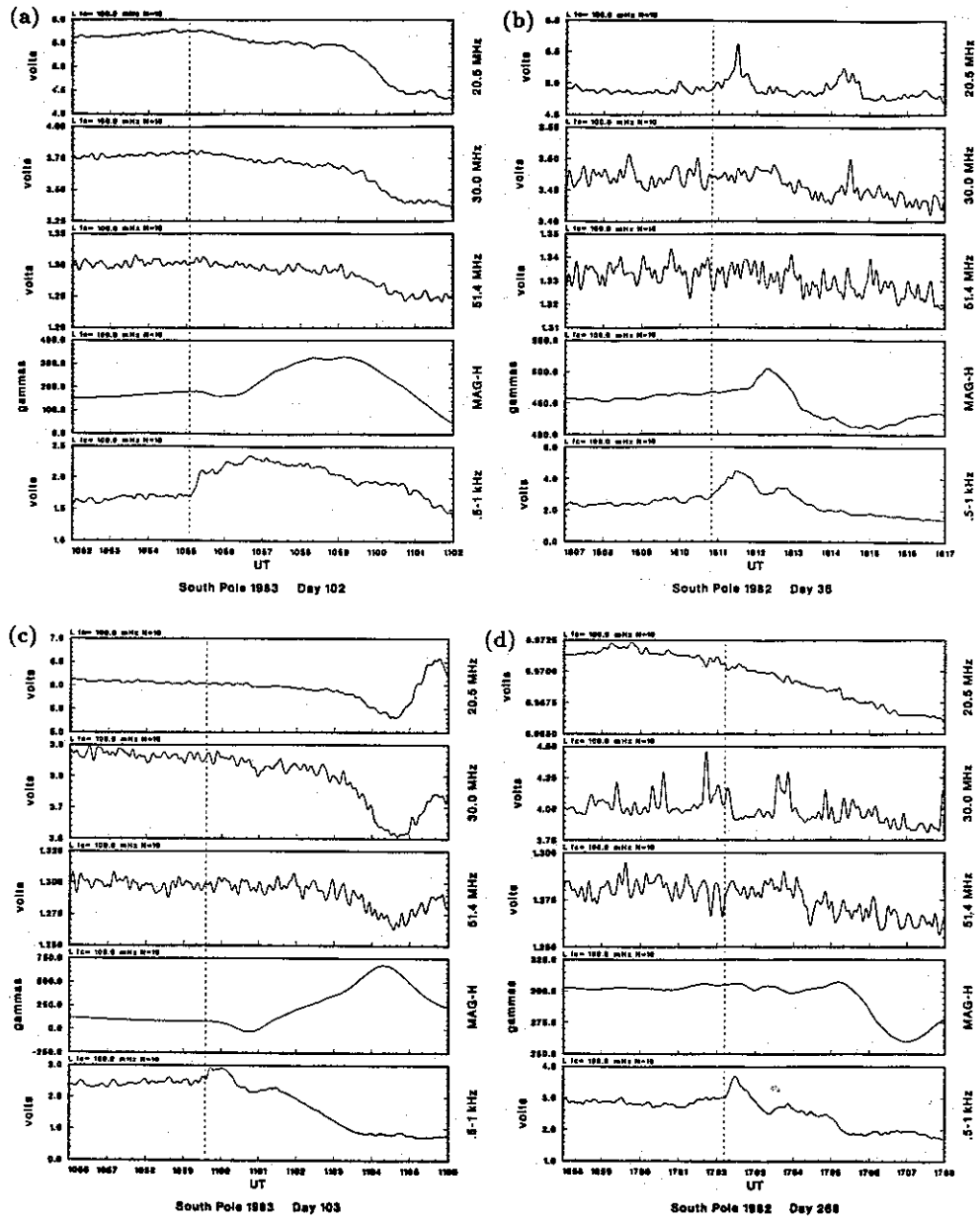


**Figure 3.32.** Riometer data recorded at South Pole for four SC. Each panel shows the output of the 20.5, 30.0, and 51.4 MHz riometer channels as well as the magnetometer H-component and the ELF amplitude in the 0.5-1 kHz channel. The dashed line indicates the wave growth onset.

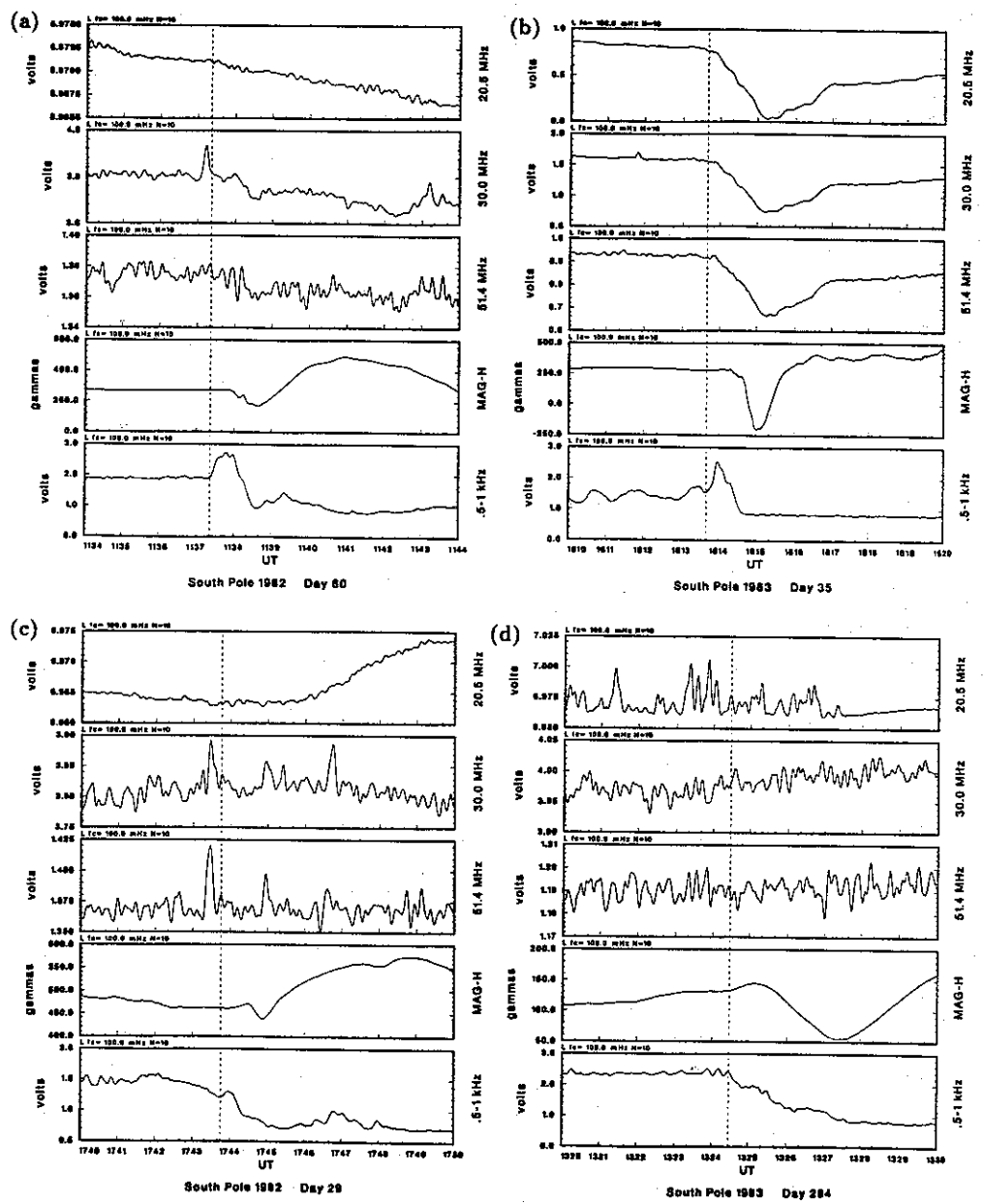


**Figure 3.33.** Riometer data recorded at South Pole for four SC. Each panel shows the output of the 20.5, 30.0, and 51.4 MHz riometer channels as well as the magnetometer H-component and the ELF amplitude in the 0.5-1 kHz channel. The dashed line indicates the wave growth onset.

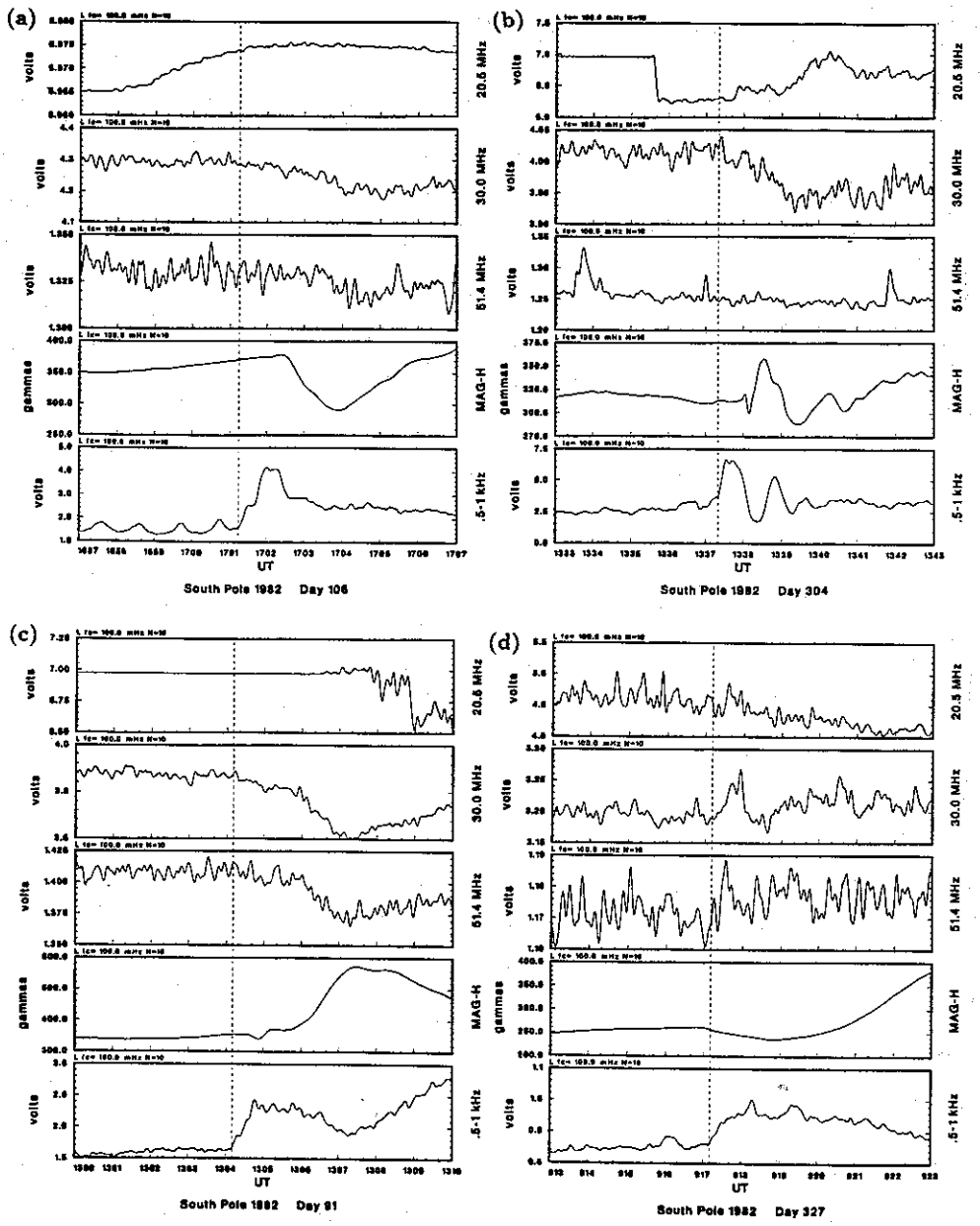


**Figure 3.34.** Riometer data recorded at South Pole for four SC. Each panel shows the output of the 20.5, 30.0, and 51.4 MHz riometer channels as well as the magnetometer H-component and the ELF amplitude in the 0.5-1 kHz channel. The dashed line indicates the wave growth onset.

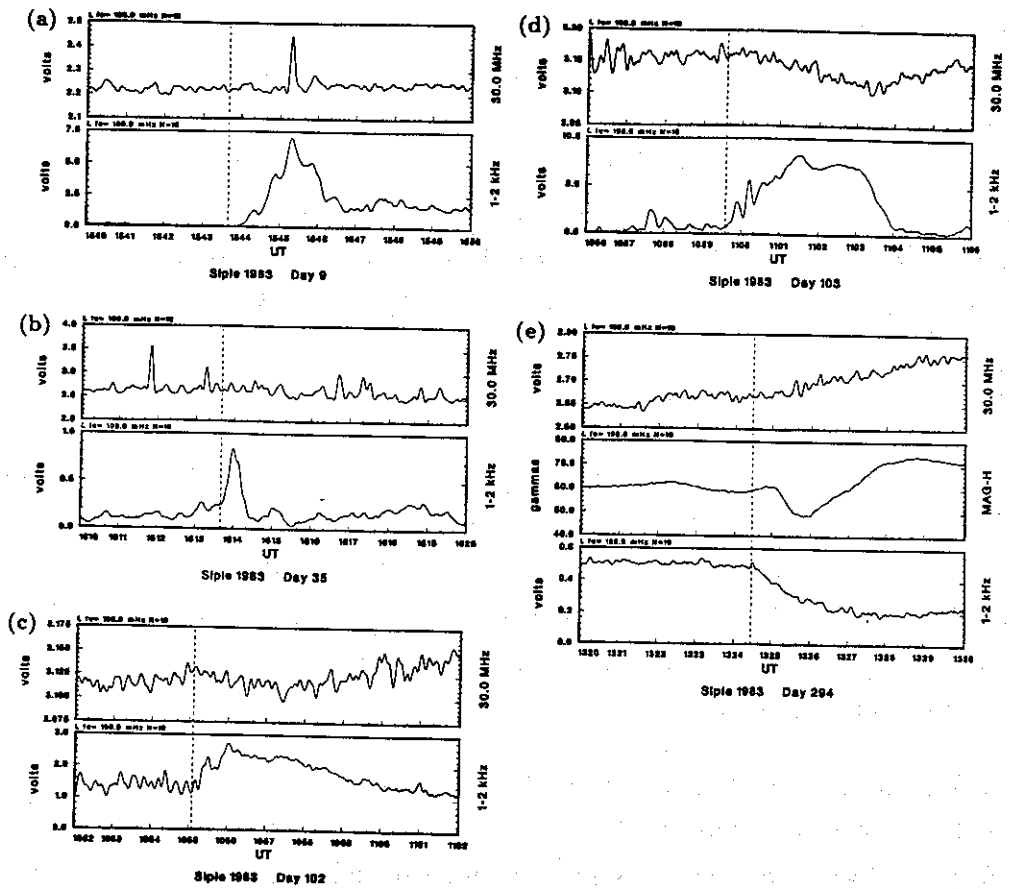


**Figure 3.35.** Riometer data recorded at Siple for five SC. Each panel shows the output of the 30.0 MHz riometer channel as well as the ELF amplitude in the 1-2 kHz channel. The dashed line indicates the wave growth onset at South Pole.

51.4 MHz (the event shown in Figure 3.33(b) was an exception and had much higher absorption levels).

*Absorption onset timing.* In five of the events (Figures 3.31(a-c), 3.33(b), and 3.34(b)), the onset of both the wave growth and the riometer absorption could be identified quite clearly and appeared to be coincident within a measurement error of $\pm 5$ sec. In four other events (Figures 3.31(d), 3.32(a), 3.33(a), and 3.34(c)), there is some indication that riometer absorption may have begun coincident with the wave growth onset, but the signal was too noisy to make a positive identification. In the five best cases, the time delay between the onset of riometer absorption and the arrival of the magnetic perturbation at South Pole was 20-50 sec. The onset of the riometer absorption clearly preceded the arrival of the magnetic perturbation in most of the cases.

*Absorption structure.* The first absorption maximum typically occurred 2-3 min after the absorption onset, as shown in Figures 3.31-3.34. While the 2-3 min period is comparable to the length of the transient wave enhancement, correlations between the duration of the wave enhancement and the structure of the absorption event were not readily evident in the cases shown here. In 10 of the 16 cases, absorption continued for 30 min or longer.

*Comparison of pre- and post-SC absorption.* In four cases (82 163, 82 197, 82 328, 83 035), both the pre- and post-SC absorption levels were significantly larger than the measurement error and it was possible to compare the absorption levels prior to the SC with the levels after the SC. The ratio post-SC/pre-SC was 1.07-2.94. In all four cases, the ratio was the same to $\pm 10\%$ for the three riometer channels. The channel independence indicates that there was no structure in the precipitation pattern on the scale size of the ionospheric viewing area [*T. Rosenberg*, private communication].

*Siple riometer measurements.* Riometer observations from Siple station for several of the events are shown in Figure 3.35. Each panel shows the output of the 30.0 MHz riometer and the ELF amplitude in the 1-2 kHz channel. Two of the events (Figures 3.35(c,d)) showed possible evidence of riometer absorption, with values less than 0.1 dB. Two of the events which did not show evidence of absorption at Siple (Figures

**Table 3.5.** Measured values for riometer absorption.

| Event | | Absorption (dB) | | | | | | | | |
|---|---|---|---|---|---|---|---|---|---|---|
| | | 20.5 MHz | | | 30.0 MHz | | | 51.4 MHz | | |
| Year | Day | Pre SC | Post SC | Post/ Pre | Pre SC | Post SC | Post/ Pre | Pre SC | Post SC | Post/ Pre |
| 1982 | 029 | - | - | - | 0.05 | - | - | 0.01 | - | - |
| | 036 | - | - | - | - | - | - | - | - | - |
| | 060 | - | - | - | 0.12 | 0.21 | 1.75 | 0.02 | 0.06 | - |
| | 091 | - | - | - | 0.04 | 0.36 | - | 0.01 | 0.12 | - |
| | 106 | - | - | - | 0.00 | 0.10 | - | 0.01 | 0.03 | - |
| | 163 | 0.52 | 1.53 | 2.94 | 0.24 | 0.64 | 2.67 | 0.09 | 0.25 | 2.78 |
| | 197 | 0.29 | 0.55 | 1.90 | 0.15 | 0.26 | 1.73 | 0.06 | 0.11 | 1.83 |
| | 268 | - | - | - | 0.22 | 0.35 | 1.59 | 0.10 | 0.14 | 1.40 |
| | 304 | - | - | - | 0.07 | 0.15 | 2.14 | 0.09 | - | - |
| | 327 | 1.32 | - | - | 1.07 | - | - | 0.41 | - | - |
| | 328 | 5.09 | 5.44 | 1.07 | 2.22 | 2.38 | 1.07 | 0.81 | 0.88 | 1.09 |
| 1983 | 009 | 0.00 | - | - | 0.10 | 0.50 | 5.00 | 0.00 | 0.14 | - |
| | 035 | 8.60 | 21.0 | 2.44 | 3.70 | 7.96 | 2.15 | 1.38 | 2.81 | 2.04 |
| | 102 | 0.23 | 0.42 | 1.83 | 0.06 | 0.15 | 2.50 | 0.00 | 0.00 | - |
| | 103 | 0.01 | 0.60 | - | 0.00 | 0.29 | - | 0.01 | 0.08 | - |
| | 294 | - | - | - | 0.08 | - | - | 0.03 | - | - |

3.35(a,b)) exhibited distinct absorption effects at South Pole.

## 3.8 SUMMARY

A number of consistent features of whistler-mode wave activity associated with SC have been presented in this chapter. The observations were described in the context of a small set of sample events but are intended to represent features commonly observed during the analysis of the several hundred events which were studied in the process of developing this thesis. These features will be compared in the next chapters to predictions of gyroresonance interaction theories in an effort to identify restrictions

on the theories and to examine the applicability of theoretical models to dynamic processes.

The observations may be summarized as follows:

*Occurrence statistics:*

Based on the general survey of several hundred events:

1. Approximately 50-60% of reported SC were associated with changes in ELF/VLF wave activity at Siple or South Pole stations. The observation probability on the dayside was 0.6-0.9 at Siple and 0.7-1.0 at South Pole and on the nightside was on the order of 0.0-0.3 at both stations. Approximately 30% of SC were associated with changes in wave amplitude at Palmer.

2. The maximum occurrence rates observed at South Pole and Siple on the dayside suggest that changes in wave activity are associated with at least 80% of reported SC.

The common association of wave activity and SC is consistent with results described in the more limited studies of *Morozumi* [1965] and *Hayashi et al.* [1968], although statistical results for a comprehensive data set have not been presented previously.

*General characterization:*

Based on the general survey of several hundred events:

1. Wave activity associated with SC generally involved amplitude and spectral modification of pre-existing bands of polar chorus or mid-latitude hiss and chorus in the frequency range 0-5 kHz.

2. The typical amplitude response consisted of a 1-8 min transient enhancement after which the amplitude returned to a level different from that prior to the SC. The duration of the transient enhancement was frequency dependent and roughly comparable to the rise time of the magnetic disturbance measured by the GOES satellites.

3. During the transient enhancement, the wave spectrum showed an increase in the upper cutoff frequency (UCF) by a factor of 1.3-2.8 and, in some cases, enhanced

triggering of discrete emissions. Of the 16 events studied in detail, 5 also had an increase in the lower cutoff frequency (LCF).

*Hayashi et al.* [1968] noted that the center frequency of wave emissions increased during the events they studied, although they did not directly relate their observations to an increase in the upper or lower cutoff frequencies. Other investigators [*Tepley and Wentworth*, 1962; *Kokubun and Oguti*, 1968; *Oguti and Kokubun* 1969; *Hirasawa*, 1981] have noted and measured a similar increase in the upper cutoff frequency of ULF emissions during SC. The transient enhancement was reported by *Tepley and Wentworth* [1962] for ULF emissions but has not been previously described for ELF/VLF emissions.

*Wave amplitude oscillations:*

Based on the 16 limited data set events:

1. 3-4 cycles of a damped oscillation with period 60-90 sec were observed in the wave amplitude during the transient enhancement in 12 of 16 events. No clear correlation with oscillations in the magnetic field was evident.

Wave amplitude oscillations during SC have not been reported previously.

*Wave growth characteristics:*

Based on measurements of seven events:

1. Wave growth was generally observed first at lower frequencies and with increasing delay at higher frequencies, with a delay between lowest and highest frequencies of 10-35 sec.

2. Total growth integrated over the wave bandwidth was 5-20 dB.

3. The observed maximum total narrowband growth was 12-29 dB and was independent of frequency over a bandwidth of 0.4-1.2 kHz and initial amplitude over a dynamic range of as much as 20 dB.

4. The observed narrowband growth rate was 0.3-2.7 dB/sec and was independent of frequency over the 3 dB bandwidth.

Quantitative measurements of wave growth associated with SC have not been reported previously.

*Onset timing:*

Based on the general survey of several hundred events:

1. The onset of wave growth preceded the arrival of the magnetic perturbation at ground level. The delay had a mean of 30 sec and a standard deviation of 18 sec with no clear dependence on the local time of the receiver.

2. The onset of wave growth preceded the arrival of the magnetic disturbance at geostationary altitude with a time delay that depended on the local time of the satellite. In the events studied, the delay was $10 \pm 20$ sec near local noon and $100 \pm 20$ sec near local midnight.

*Hayashi et al.* [1968] observed a delay of approximately 30 seconds between the onset of wave growth and the onset of the magnetic perturbation but did not discuss the range of observed values nor the accuracy of their measurements.

*Particle precipitation:*

Based on the 16 limited data set events:

1. Measurable riometer absorption at South Pole was associated with 12 of the 16 events studied. Absorption values were in the range 0.0-4.3 dB at 30.0 MHz with typical values of 0.1-0.4 dB.

2. The onset of riometer absorption was coincident with the onset of wave growth to within the measurement error of $\pm 5$ sec in at least five of the cases.

This is the first reported measurement of simultaneity between the onset of both wave growth and particle precipitation.

# Chapter 4

# DISCUSSION

In this chapter, an overall picture of the time-dependent wave-particle interaction process associated with SC is developed based on the data presented in Chapter 3. The changes in the environmental parameters resulting from the SC are characterized in the first section. The applicability and limitations of the observational results are then discussed and an interpretation of the results is given. The last section provides a general characterization of wave-particle interactions during SC based on these considerations.

## 4.1 CHANGES IN THE ENVIRONMENTAL PARAMETERS

### 4.1.1 *THE INITIAL PERTURBATION*

The environmental changes observed during a SC are driven by a number of physical processes which act over different time scales. During the early part of the SC, the dominant processes are directly linked to the original magnetic disturbance. As the SC progresses, secondary effects such as ionospheric modification, ring current development, and particle injection from the magetotail play increasingly significant roles. In order to minimize the influence of secondary effects, the analysis presented in this thesis is concerned primarily with the early portion of the SC, when the magnetic

disturbance is small compared to the total field and has not begun to saturate. This period typically comprises the first 20-60 sec of the event and will be referred to as the *initial perturbation.*

During the initial perturbation, Alfvén waves generated from the compressional disturbance have not had time to propagate to the ionosphere and back (the minimum time for Alfvén waves to propagate to the ionosphere and return to the equatorial region is on the order of 60 sec at the latitudes and local times of interest [*Singer et al.*, 1981]) and thus field-line resonance processes can be neglected. Drift velocities of energetic electrons (which can be approximated by $15.2R^2$ m sec$^{-1}$ keV$^{-1}$ where $R$ is equatorial distance in $R_e$ [*Lyons and Williams*, 1984]) are sufficiently small that any changes in the energetic particle distribution could not have resulted from acceleration processes more than a few degrees in longitude away from the observing point. Similarly, thermal plasma would not have had time to convect from distant regions. The changes in the environment during the initial perturbation are thus primarily local and can be calculated to a large extent without knowledge about boundary conditions and non-local processes.

### 4.1.2 *CALCULATION OF THE ENVIRONMENTAL CHANGES*

During the initial perturbation, the SC-induced changes in the magnetic field, thermal plasma, and energetic plasma can be related through magnetohydrodynamic (MHD) theory. The compression of the magnetosphere during a SC causes the field lines to move earthward, as shown schematically in Figure 4.1. The thermal plasma is "tied" to magnetic field lines as a result of the frozen-in flux condition of MHD theory. A duct thus remains colocated with a given field line throughout the SC compression and the waves and particles associated with a particular duct prior to the SC will be associated with that duct throughout the SC. For the particle energies of interest, drift velocities are sufficiently small that energetic particles may also be considered "tied" to field lines for most purposes.

The vector magnetic field change associated with a given field line during the SC may be decomposed into changes in the total field strength and changes in the field

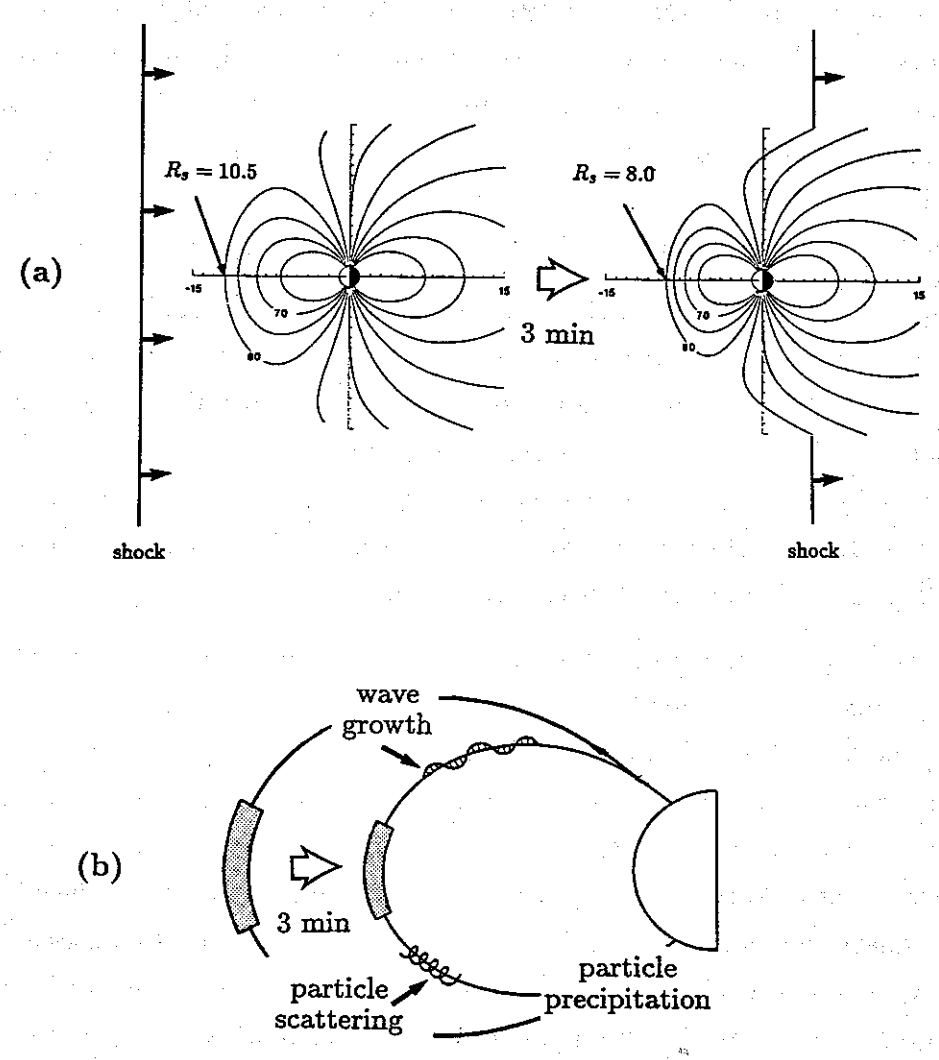


**Figure 4.1.** Schematic diagram showing magnetospheric changes associated with SC. (a) The compression of the magnetosphere caused by the passage of the solar wind shock. The two magnetospheric configurations shown correspond to standoff distances of 10.5 $R_e$ and 8.0 $R_e$. (b) The displacement of a magnetic field line, the motion of the interaction region, and the corresponding consequences for the wave and particle populations.

geometry. The field strength change near the equator (examples of which are shown in Figures 3.7-3.10) may be approximated by a linear function of time acting over the rise time of the disturbance [*Perona*, 1972]. A somewhat more physical approximation [*Baumjohann et al.*, 1982] can be derived by assuming that the magnetopause relaxes exponentially between the old and new standoff distances, resulting in a magnetic field strength increase of the form $B = B_0 + \delta B(1 - e^{-t/\tau})$ throughout the magnetosphere, where $\tau$ is the rise time of the disturbance and $\delta B$ represents the total change in field strength. For times small compared to $\tau$, both approximations are roughly equivalent.

A description of the field geometry changes requires a more sophisticated analysis. Measurements by single spacecraft or ground-based observatories do not provide information on the field geometry and no applicable multiple spacecraft studies have been done. In the absence of such observations, information on field geometry must be obtained by simulating the field changes during a SC with the use of magnetic field models. Results of such simulations and the relative importance of field strength and geometry will be discussed further in Chapter 5.

The changes in thermal and energetic plasma populations resulting from a SC include changes in flux density, velocity space distribution, and drift properties. The changes caused directly by the SC magnetic perturbation conserve the first and second adiabatic invariants but not the third invariant for particles with energies below a few hundred keV [*Wilken et al.*, 1986]. The frozen-in flux condition implies that the thermal plasma density and the energetic particle flux density increase by the same factor as the magnetic field strength. The field strength enhancement also causes an increase in the perpendicular energy of the particles, known as betatron acceleration, resulting in an increase in the particle pitch angle. The field geometry change corresponds to modification of the field line curvature and gradients and thus causes changes in drift velocity for the energetic electrons. The enhanced drift does not affect the energy or pitch angle dependence of the distribution, but does modify the replenishment rate for a duct. Non-adiabatic modifications of the energetic plasma also occur as a result of wave-particle interactions.

The adiabatic changes in the environmental parameters associated with a duct can be calculated explicitly for an arbitrary time-dependent magnetic field perturbation.

As an example, consider a magnetic field of the form

$$B(t) = B_0\,(1 + b(t))\ , \tag{4.1.1}$$

where the subscript 0 indicates the unperturbed or static field and $b(t)$ is the time dependent perturbation. The corresponding thermal plasma density has the form

$$n = n_0\,(1 + b(t)) \tag{4.1.2}$$

and the energetic particle distribution function can be written

$$F(\alpha, E) = F_0(\alpha_0, E_0)\ , \tag{4.1.3}$$

where the pitch angle $\alpha$ and the energy $E$ for a given particle are related to their values in the unperturbed system by

$$\tan^2\alpha = (1 + b(t))\tan^2\alpha_0 \tag{4.1.4}$$

$$E = E_0\left(1 + b(t)\sin^2\alpha_0\right)\ . \tag{4.1.5}$$

A more complete derivation of these and other quantities, which will be used for the comparison between the observations and theoretical models in Chapter 5, is given in Appendix A.

## 4.2 OBSERVATIONAL CONSIDERATIONS

The ground-based observations described in Chapter 3 form the basis for the characterization of wave-particle interactions during SC. In order to interpret the observations, we need to understand how to translate ground-based measurements (e.g.,

growth rate) into parameter values that would be valid within the interaction region. Ground-based wave receivers measure a signal which has undergone an integrated growth process along the length of a duct. The signal may be composed of contributions from several source regions, each of which has been modified by propagation between the source and the receiver. In this section, the importance of both source location and propagation effects is discussed.

### 4.2.1 *LOCATION OF SOURCE REGIONS*

The SC disturbance originates near the subsolar point on the magnetopause and propagates within several minutes throughout the entire inner magnetosphere. Presumably, changes in wave activity occur with some local time and radial dependence as a result of the SC perturbation. It is thus desirable to know the location and extent of wave source regions and their relative contribution to the signal observed on the ground. Ground-based wave receivers suffer, in this instance, from their large viewing area (500-1000 km [*Walker*, 1974; *Tsuruda et al.*, 1982]), which limits the degree to which wave observations can be related to source regions. There are, however, a number of techniques that can be used to address the question of the wave source region.

*Onset time measurements.* A simple estimate of the location of the source region for the earliest wave growth observed on the ground can be made using the onset time measurements described in Section 3.6. The arrival of the magnetic perturbation at geostationary altitudes is known to be strongly local time dependent (corresponding to the azimuthal propagation of the SC disturbance) [*Kuwashima and Fukunishi*,1985], while the ground magnetic onset occurs nearly simultaneously at all local times at high latitudes as a result of sub-ionospheric transmission of the earliest arriving signal [*Kikuchi et al.*, 1978; *Kikuchi*, 1986]. The ground magnetic onset is observed with a mean delay of ~30 sec after the magnetic perturbation is observed at geostationary altitude near local noon (see Figure 2.11).

The results showed no apparent local time dependence for the onset time of wave growth at South Pole when referenced to the arrival of the magnetic perturbation

at the ground (Figure 3.30(a)) but a strong local time dependence when referenced to the magnetic perturbation at GOES (Figure 3.30(b)). The mean delay of 30 sec between the onset of wave growth and the arrival of the ground magnetic perturbation is similar to the value of ~30 sec measured by *Kuwashima and Fukunishi* [1985] for the propagation delay of the magnetic disturbance between GOES near local noon and ground observatories. The results are consistent with the source of the earliest wave growth being near local noon.

Differerences in the propagation path between events provide a possible explanation for the point scatter in Figure 3.30(a) ($\sigma$ =18 sec). Variations in the whistler mode delay (which is on the order of a few seconds) can probably be neglected but significant variations in the propagation delay for Alfvén waves could be caused by differences in either the length of the propagation path or the integrated mass density along the path. A factor of 4 difference in integrated mass density between events would provide a sufficient variation in the propagation delay to account for the observed scatter. Differences in the location of the source region provide an alternate explanation. Using a mean Alfvén speed of 1000 km/sec for the outer magnetosphere [*Wilken et al.*, 1982], a deviation of 18 sec corresponds to variations of $\pm 3$ $R_e$ in radial position or $\pm 2$ hours local time for the location of the earliest source region. It is probable that both effects play some role in determining the point scatter.

*Particle precipitation measurements.* Measurements of particle precipitation associated with SC provide a potentially powerful tool for determining the wave source regions. The 30° half-power beamwidth of the riometers corresponds to a field of view with a radius of about 60 km for absorption occurring at an altitude of 105 km. Assuming that both the waves and particles associated with a given interaction follow the same field-aligned paths from the interaction region to the ionosphere, riometer absorption associated with wave growth should provide a good indicator of the source region.

Previous work [*Ortner et al.*, 1962; *Hartz* 1963] has shown that riometer absorption is associated with SC at all local times and is generally limited to the geomagnetic latitude zone between 57° and 75°. Wave-induced particle precipitation is often assumed to be the cause of the absorption [*Leinbach et al.*, 1970; *Perona*, 1972], implying that

changes in wave activity are triggered by the SC throughout a large portion of the inner magnetosphere. However, the problem has never been carefully studied and other mechanisms (such as particle injection) may be responsible for the some of the observed absorption effects.

The effect of other mechanisms can be minimized by analyzing absorption effects that occur during the initial perturbation. Of the 16 events discussed in Section 3.7, five had well-defined absorption onsets (Figures 3.31(a-c), 3.33(b), 3.34(a)) during the initial perturbation. In all five cases, the absorption onset occurred simultaneous with the onset of wave growth within an error of $\pm 10$ sec. Since the adiabatic changes in particle trajectories can only increase the pitch angle (see Appendix A), adiabatic effects alone can not increase the particle flux within the loss cone and thus can not account for the absorption. With the assumed absence of other scattering mechanisms during the initial perturbation, the increased absorption must result from wave-induced precipitation.

The observation of wave-induced particle precipitation at South Pole implies that South Pole ($\Lambda = 73.8°$) was associated with closed field lines during these events (see *Brown* [1977] for a good discussion of the use of riometer observations during SC to detect the boundary of closed field lines). The local time at South Pole was within two hours of noon in four of the five cases. Since the closed field boundary in the noon region is essentially coincident with the magnetopause, the observation of wave-induced particle precipitation at South Pole suggests an enhancement of wave-particle interactions in the vicinity of the dayside magnetopause.

In the four well-defined cases where South Pole was near local noon, the approximate simultaneity of wave growth and absorption would be expected. The simultaneity in the fifth case (Figure 3-31(c)), for which the local time at South Pole was about 0550, can not be easily explained. The wave growth and absorption onsets were observed at South Pole at 0920:25 UT and the ground magnetic perturbation arrived at 0921:00 UT. The 35 sec delay between the wave growth onset and the arrival of the magnetic perturbation is consistent with previous results, suggesting that the waves propagated sub-ionospherically from a source region near noon. Precipitation effects due to these waves could not have been observed at South Pole (near dawn local time), however.

Wave-induced precipitation should have been observed at South Pole with a delay on the order of 60 sec (the propagation time for the magnetic disturbance between noon and dawn) after the disturbance began in the noon region. The magnetic perturbation arrived at GOES (0220 LT) at 0921:50, indicating that the perturbation could not have reached the dawn meridian prior to about 0921:10 (a time which would be consistent with the disturbance at local noon occurring at about 0920:25, the same time as the wave growth onset).

The absorption observation for this event can not be explained by wave-induced precipitation triggered locally by the SC. An alternate explanation is that waves generated in the noon region propagated in a nonducted mode to the dawn region in advance of the magnetic disturbance where they interacted with and precipitated particles. Such a scheme seems rather unlikely, but raytracing has shown that nonducted waves generated in the noon region can propagate as far away as the dawn meridian [*I. Kimura*, private communication]. The "hybrid mode" [*Rastani et al.*, 1985], in which waves are ducted along some portions of a path and nonducted along others, could also be important in such azimuthal propagation. Although no other similar events were noted, the results suggest the possibility that precipitation could be observed at a given local time significantly in advance of when the SC disturbance reaches overhead field lines.

### 4.2.2 *DISTRIBUTION OF SOURCE REGIONS*

*Duct distribution.* Knowledge regarding the occurrence of ducted propagation at high-latitude stations is limited. *Carpenter* [1981] studied whistlers from Byrd station and concluded that ducted propagation of whistlers at equatorial distances of 6-8 $R_e$ is probably observed on 30-50% of all days and that chorus and hiss propagate at equatorial distances 0.5-1.0 $R_e$ beyond the observed limit of whistler propagation on the dayside. The common occurrence of polar chorus at high-latitudes is also strong, though indirect, evidence that ducts ordinarily exist at equatorial distances greater than 6 $R_e$. These considerations support the results discussed in Section 4.2.1 suggesting that wave growth during SC could originate in ducts near the dayside magnetopause.

The number of ducts contributing to the wave signal observed at ground stations during SC is difficult to determine. The large viewing area of ground-based receivers allows for superposition of wave activity from different ionospheric exit points and thus makes distinction of multiple source regions difficult. Comparison of data from stations separated by distances on the order of the viewing radius (e.g., South Pole and Siple) allows for some resolution of this problem. As shown in Figures 3.16-3.19, spectra at Siple and South Pole appeared similar in many cases (including correlated discrete emissions as in Figures 3.16(b,d) and 3.17(c)), but showed clear differences in other cases. In at least one case (Figure 3.19(b)), similar polar chorus bands with a UCF near 500 Hz were observed at both stations while a hiss band with a UCF above 5 kHz was observed at Siple but not South Pole. In those cases with similar spectra, particularly when similar emissions were identified, it is probable that both stations were viewing the same wave source regions, but the number of such regions can not be determined. In those cases with different spectra, it appears that the stations were viewing at least two different source regions, although some overlap is possible (as in Figure 3.19(b)).

*Sensitivity to source distribution.* While the observations do not resolve the question of the number of source regions, there is a simple argument suggesting that the measured growth values are not very sensitive to the number of contributing source regions or ducts.

Three primary factors affect the contribution of a particular source region to the observed wave growth: the relative wave amplitude, the relative growth rate, and the relative onset time of the growth for a particular source region. Source regions with small relative wave amplitudes compared to other source regions will not be important. Source regions with small relative growth rates will also be insignificant since they will contribute less and less to the total signal amplitude with time. Differences in relative onset time (due, for instance, to different radial positions of the source regions) would result in larger comparative wave amplitudes for those signals with the earliest growth onset and these signals would provide the greatest contribution.

Signals with the highest initial amplitudes and growth rates and the earliest growth onsets thus dominate the observed wave growth process. A given source distribution,

however, may have no one source which dominates all three categories. To investigate this further, a simple computer simulation of the contribution of a number of ducts with different initial wave amplitudes, growth rates, and radial positions was conducted. The results showed that the measured values of growth rate and total growth are only weakly dependent on the number and distribution of source regions. The variation from a wide range of simulated cases was comparable to the observed variation in the measured values.

### 4.2.3 *PROPAGATION EFFECTS*

Since we use relative rather than absolute measurements of wave properties, only those propagation effects which change during the SC are of interest. The effects which must be considered include propagation within the duct, transmission through the ionosphere, and propagation from the ionospheric exit point to the receiver.

The frequency at which waves remain trapped within an enhancement duct is theoretically limited by refractive index effects to $f < f_H/2$ [*Helliwell*, 1965]. During a SC, the frequency range for ducted propagation thus increases in proportion to the gyrofrequency. The range of possible wave normal angles, which is described by the ratio of the electron densities inside and outside the duct [*Helliwell*, 1965], does not change. Scattering losses from the duct are generally considered to be negligible except for frequencies near $f_H/2$ [*Scarabucci and Smith*, 1971; *Karpman and Kaufman*, 1984].

Observations of enhanced riometer absorption during SC suggest that ionospheric absorption losses for ELF/VLF waves should also increase. Additional absorption losses would reduce values for growth rate and total growth measured at ground stations. The spectral distribution would not be significantly modified, however, since absorption losses at the wave frequencies of interest are proportional to $\sqrt{f}$ [*Helliwell*, 1965] and would result in less than 3 dB of differential absorption over the frequency range 0.5-4.0 kHz.

Quantitative absorption values, which depend on both the flux and energy spectrum of the precipitated particles, are very difficult to determine. For the growth period

measurements, made within the first several tens of seconds of the event, the absorption at 30 MHz was in general significantly less than the value measured at the absorption maximum (see Figures 3.31-3.35). It is probably reasonable to assume that measurements made during the growth period are not significantly affected by changes in ionospheric absorption losses or changes in propagation losses between the ionospheric exit point and the receiver.

## 4.3 GENERAL EVENT CHARACTERIZATION

Based on the observations described in Chapter 3 and the considerations discussed in the previous sections, a general characterization of the changes in the properties of the gyroresonance interaction mechanism associated with SC may be developed.

The occurrence statistics suggest that the magnetic field and plasma perturbations associated with SC are sufficient to cause measurable modification of the gyroresonance process for at least 80% of SC. The observed occurrence rate may be limited by the use of a limited number of ground stations and the actual occurrence rate may be somewhat higher.

The amplitude response is characterized by a transient enhancement lasting 1-8 min after which the amplitude is usually reduced to below the pre-SC amplitude but may be significantly higher. Ionospheric absorption losses corresponding to the observed riometer absorption provide a possible explanation for the amplitude reduction, although the continued amplitude reduction in a number of cases following the riometer recovery as well as the clear change in the spectra suggest that ionospheric absorption may not be the primary cause. Damped oscillations with period 60-90 sec are commonly observed during the transient enhancement. The oscillations may be associated with resonant field line oscillations, although the evidence is not clear. An alternate explanation, which will be discussed in Chapter 5, is that they represent an overshoot and subsequent oscillation of the wave amplitude about the new equilibrium value as a result of the step-like magnetic perturbation.

During the growth period, the upper cutoff frequency of the wave activity increases by a factor of 1.3-2.8. In some cases, the lower cutoff frequency increases as well. Growth

is observed first at lower frequencies and with increasing delay (on the order of 10-35 sec) at higher frequencies. The 10-35 sec time delay is significantly shorter than the typical SC rise time (2-6 min), so the increase is probably not simply due to the change in $f_{H_{eq}}$ for a single duct. A possible explanation is that wave growth is triggered in ducts with successively higher values of $f_{H_{eq}}$ as the disturbance propagates radially earthward. An alternate explanation, described in Chapter 5, is that the upper cutoff frequency is not controlled by $f_{H_{eq}}$ but is a function of other medium parameters. The narrowband growth rate (0.3-2.7 dB/sec) and total growth (12-29 dB) are independent of frequency over a bandwidth of 0.4-1.2 kHz and a dynamic range of as much as 20 dB. Triggering of discrete emissions is observed in some cases. Wave measurements during the growth phase correspond to contributions from wave sources in the noon region, probably outside the plasmapause and possibly near the magnetopause. A measurable enhancement of ionospheric absorption due to pitch angle scattering of radiation belt electrons commonly accompanies the growth process.

# Chapter 5
# COMPARISON OF OBSERVATIONS AND THEORY

In this chapter, the observations presented in Chapters 3 and 4 are compared with predictions of the nonlinear and quasi-linear theoretical models of gyroresonance interactions that were described in Chapter 2. Since such models have been developed primarily for static magnetospheres, the appropriate modifications for a dynamic environment are discussed first.

## 5.1 NONLINEAR MODELS

Nonlinear models are commonly used to describe the properties of discrete emissions which are believed to be generated through coherent gyroresonance interactions with electrons [*Helliwell*, 1967]. Nonlinear models are based on explicit calculations of particle trajectories under the influence of wave fields and generally require computationally intensive simulations. Due to the computational requirements, the adaptation of nonlinear computer simulations to a dynamic magnetosphere is beyond the scope of this research.

However, both theoretical [*Helliwell*, 1967; *Inan et al.*, 1978] and experimental [*Inan et al.*, 1983] work has shown that qualitative predictions of discrete emissions properties can be made using several parameters which characterize the nonlinear equations. In this section, the interaction parameters are adapted to a dynamic magnetosphere and used to provide predictions of the occurrence rate for discrete emissions. The results are then compared with the observations of discrete emissions during SC.

### 5.1.1 *THE INTERACTION PARAMETER MODEL*

The theoretical basis of the interaction parameters is described in Chapter 2 and will not be repeated here. The interaction length $L_I$ characterizes the distance over which the resonance condition is satisfied. The trapping threshold $B_T$ is the wave amplitude necessary to trap particles in the potential well of the wave. The bunching efficiency $\Gamma_B$ characterizes the effectiveness of the phase bunching process during the interaction. In order to simulate changes in the interaction parameters that occur during a SC, a dynamic model magnetosphere was developed in which the magnetopause standoff distance could be varied as a function of time. The interaction parameters were then calculated numerically.

*The dynamic model magnetosphere.* The magnetic field that was used is an Olson-Pfitzer static model [*Olson and Pfitzer*, 1974] which was modified to include variations in the magnetopause standoff distance and ring current strength through the use of scaling factors [*Olson and Pfitzer*, 1982] (see Appendix C for a more complete discussion of magnetic field models). The SC was simulated by generating a successive set of field models in which the magnetopause standoff distance was incrementally decreased. The interaction parameters were calculated for each configuration and plotted to illustrate the temporal evolution. The implied quasi-static approximation (i.e., the magnetosphere is static for each incremental calculation) is valid since the interaction time is much smaller than the SC rise time.

The simulation is characterized by a set of twelve parameters which define the magnetic field and plasma configuration, the dynamics of the SC, the properties of the waves and energetic particle distribution, and the location of the interaction. For the purpose of this research, nominal values were chosen for each of the parameters and simulation runs were made in which one parameter was allowed to take on a range of values while the other parameters were held constant. The twelve parameters and their nominal values are listed in Table 5.1.

The nominal magnetic field parameters were chosen to represent a typical SC. Following the theoretical analysis of *Baumjohann et al.* [1983], the temporal evolution of the standoff distance was given the form $R_s = R_{s_f} + (R_{s_i} - R_{s_f})e^{-t/\tau}$, where $R_{s_i}$

Table 5.1. Nominal values for the nonlinear interaction model parameters.

| Parameter | Nominal Value |
|---|---|
| Normalized frequency | $0.35 f_{Heq}$ |
| Pitch angle | 45° |
| Invariant latitude | 68° |
| Local time | 1200 MLT |
| Wave amplitude | 10 pT |
| Initial $R_s$ | 10.5 $R_e$ |
| Final $R_s$ | 8.0 $R_e$ |
| SC risetime | 50 sec |
| $D_{st}$ | 0 |
| Density ref. position | 5.0 $R_e$ |
| Density ref. value | 1 $cm^{-3}$ |
| Density exponent | 0 |

and $R_{s_f}$ are the initial and final standoff distance and $\tau$ is the rise time. The rise time was chosen to be $\tau = 50$ sec. No scaling factor for the ring current was used, since the ring current changes little during the first few minutes of the SC. The ring and tail currents thus represent the quiet-time values used in the basic Olson-Pfitzer model.

The thermal plasma density parameters were chosen to represent a typical plasma configuration well outside the plasmapause. A reference electron density of 1 $cm^{-3}$ was used with no radial dependence. The wave frequency was calculated in multiples of the equatorial gyrofrequency $f_{H_{eq}}$ with a nominal value of $f/f_{H_{eq}} = 0.35$. Waves were assumed to resonate with particles having pitch angles of $\alpha = 45°$. The interaction length was defined as the distance over which the gyrophase varied by $\theta = \pi$ radians. The location of the interaction was defined in terms of the invariant latitude and local time of the particular field line; nominal values were $\Lambda = 68°$ and MLT=1200, corresponding to a region near geostationary orbit on the dayside.

*Interaction parameters during a SC.* The results of the simulations are shown in Figures 5.1-5.7. In each figure, the equatorial gyrofrequency, interaction length, wave

trapping threshold, electron resonant energy, and bunching efficiency are plotted as a function of time during the SC compression.

For the nominal case, the gyrofrequency increased from 2.4 kHz to 4.0 kHz due to the compression and field line displacement, a change of 65%. The interaction length increased from 4900 km to 8000 km, the resonant energy increased from 14 keV to 23 keV, the wave trapping threshold decreased 2.8 dB from the initial value of 9 pT, and the bunching efficiency increased from 2.9 to 4.7.

The results indicate that, for a typical case, the wave amplitude necessary to trap particles decreases by about 3 dB and the importance of phase bunching for a given amplitude wave increases significantly. The importance of such changes is emphasized by the results of *Helliwell et al.* [1980], who showed that the occurrence of triggered emissions from coherent VLF signals was sensitive to differences of input signal power less than 4 dB, and the survey work of *Burtis and Helliwell* [1975] indicating that typical chorus amplitudes in the magnetosphere fall in the range 1-100 pT. Based on their observations, it appears possible that a decrease of 3 dB in the trapping threshold and a corresponding increase in the phase bunching efficiency could result in triggering of coherent emissions.

The various plots indicate a number of interesting parameter dependencies. At higher wave frequencies, the trapping threshold decreases and the bunching efficiency increases. The trapping threshold is lowest and the bunching most efficient for interactions near local noon and at higher ambient electron densities. The latitude plot indicates that the bunching efficiency increases with increasing invariant latitude but that the trapping threshold reaches a minimum between $\Lambda = 65°$ and $\Lambda = 71°$. The magnitude of the changes is generally greater for larger SC compressions, although the response is somewhat complex.

### 5.1.2 *COMPARISON WITH OBSERVATIONS*

The simulation results indicate that the magnetic compression enhances the predisposition of the magnetosphere to the generation of discrete emissions. In Chapter 3,

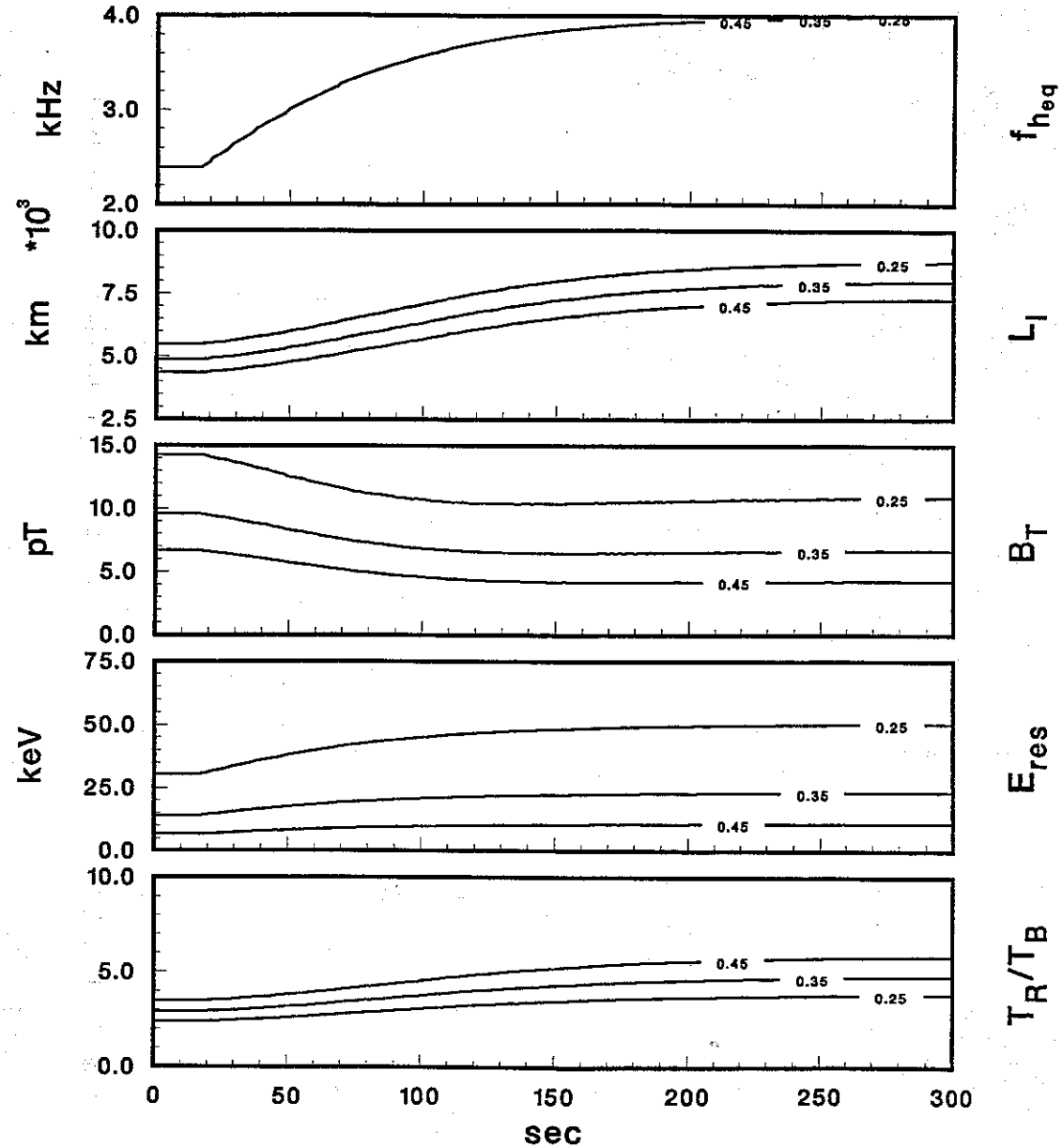


**Figure 5.1.** Simulation of interaction parameters during a SC. The plot shows equatorial gyrofrequency, interaction length, wave trapping threshold, electron resonant energy, and bunching efficiency plotted as a function of time during the SC compression. The curves are plotted parametric in normalized wave frequency $(f/f_H)$.

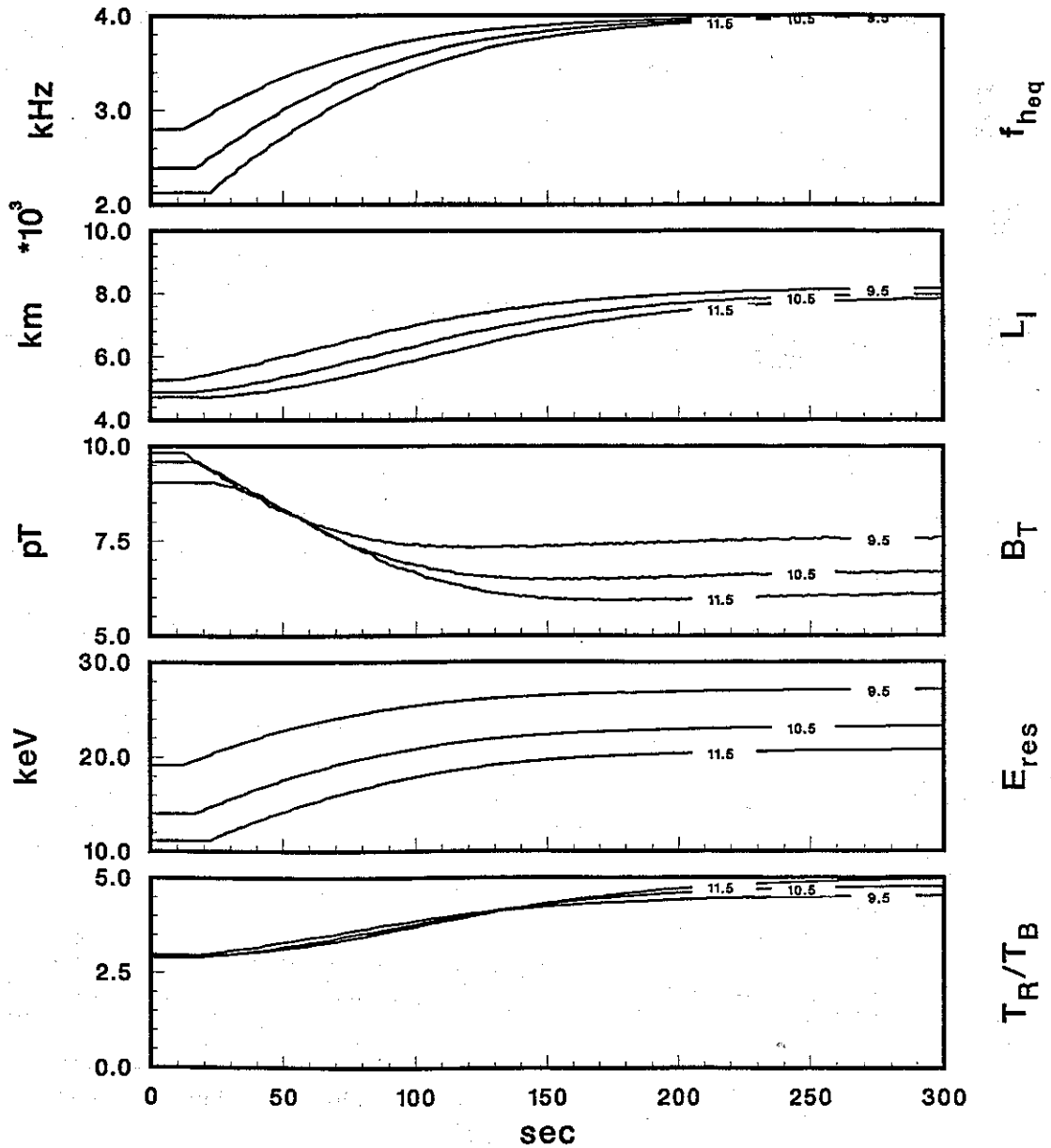


**Figure 5.2.** Simulation of interaction parameters during a SC. The plot shows equatorial gyrofrequency, interaction length, wave trapping threshold, electron resonant energy, and bunching efficiency plotted as a function of time during the SC compression. The curves are plotted parametric in the initial standoff distance ($R_e$).

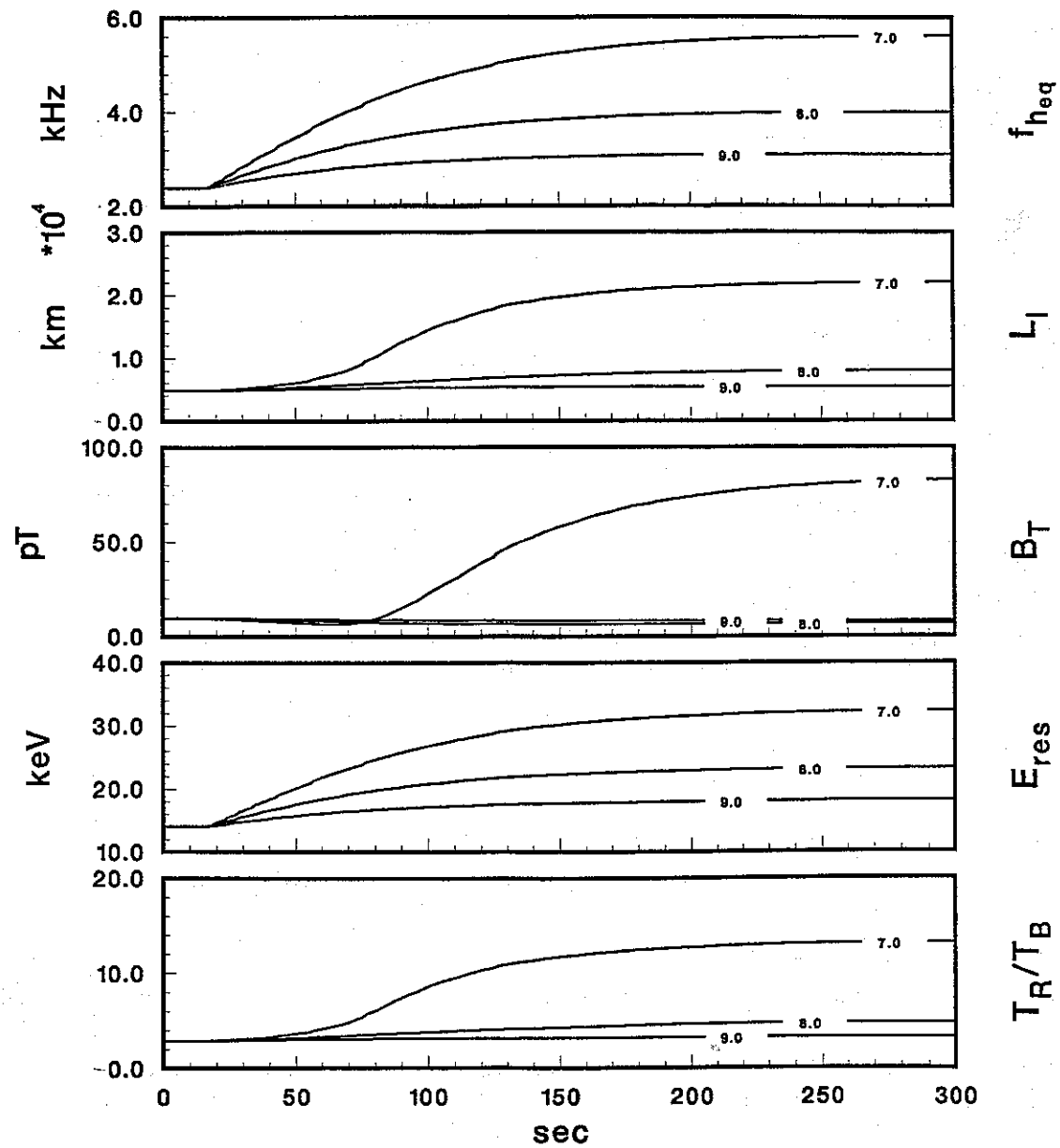


**Figure 5.3.** Simulation of interaction parameters during a SC. The plot shows equatorial gyrofrequency, interaction length, wave trapping threshold, electron resonant energy, and bunching efficiency plotted as a function of time during the SC compression. The curves are plotted parametric in the final standoff distance ($R_e$).

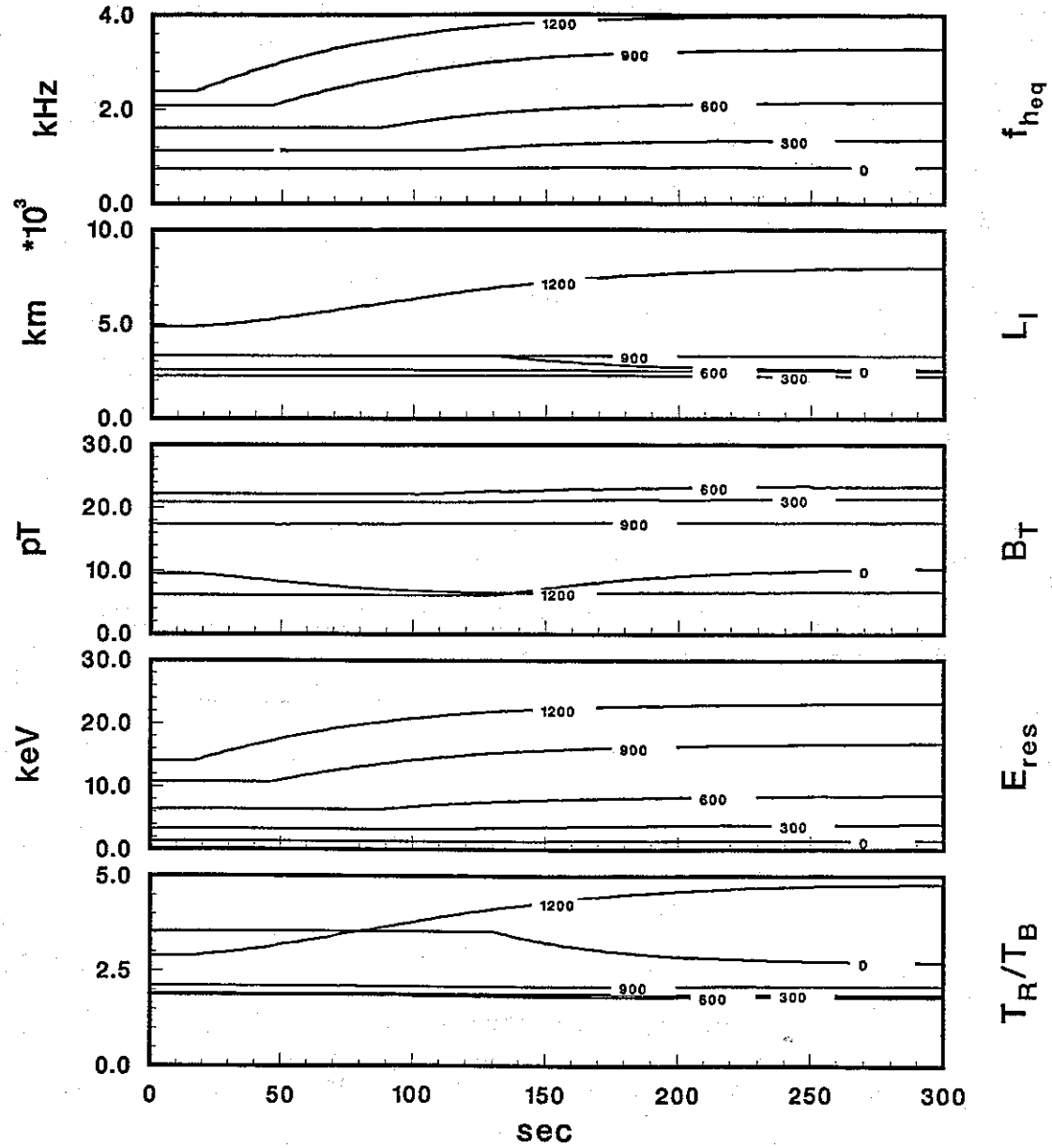


**Figure 5.4.** Simulation of interaction parameters during a SC. The plot shows equatorial gyrofrequency, interaction length, wave trapping threshold, electron resonant energy,and bunching efficiency plotted as a function of time during the SC compression. The curves are plotted parametric in local time (HHMM).

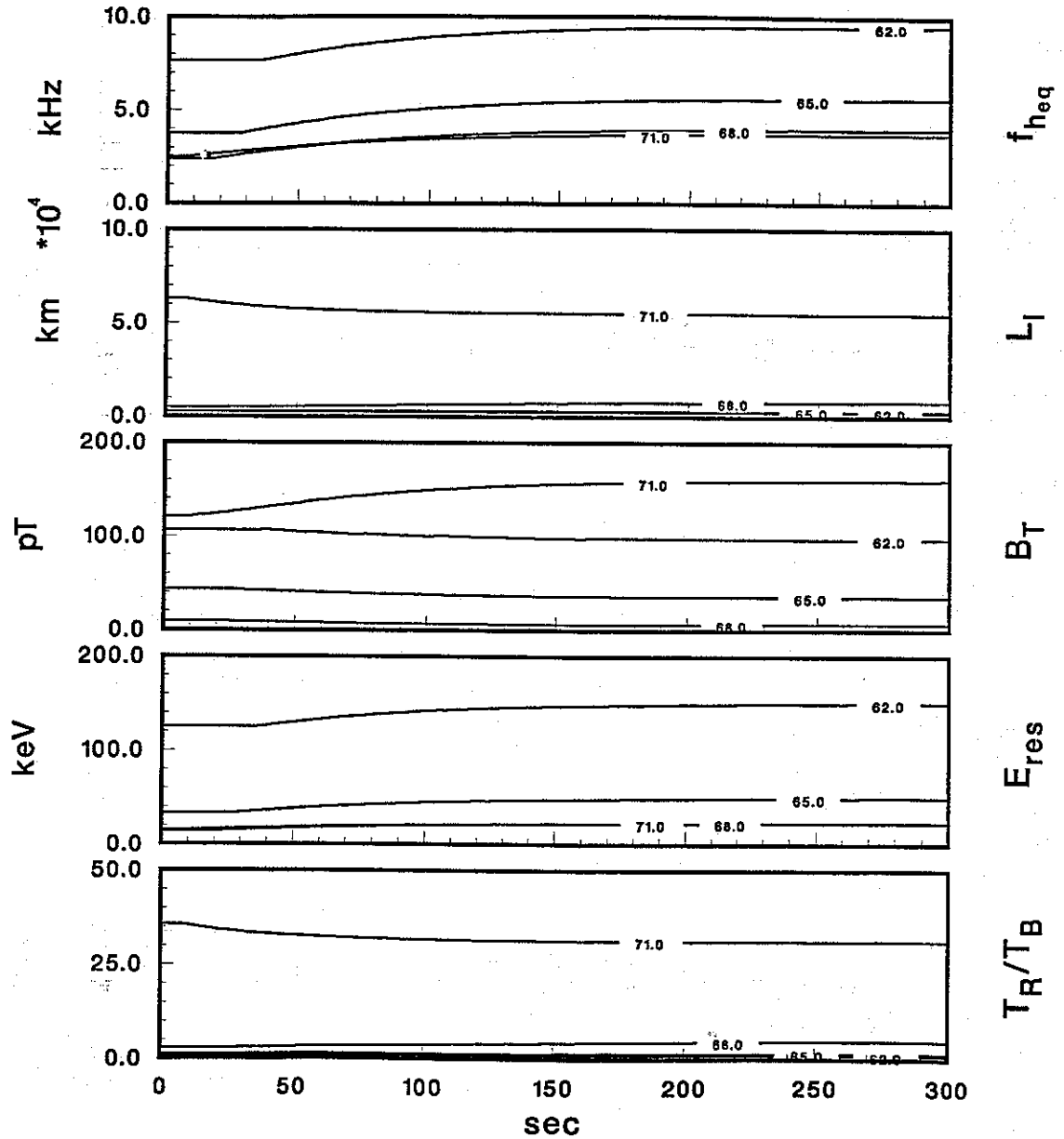


**Figure 5.5.** Simulation of interaction parameters during a SC. The plot shows equatorial gyrofrequency, interaction length, wave trapping threshold, electron resonant energy, and bunching efficiency plotted as a function of time during the SC compression. The curves are plotted parametric in invariant latitude (degrees).

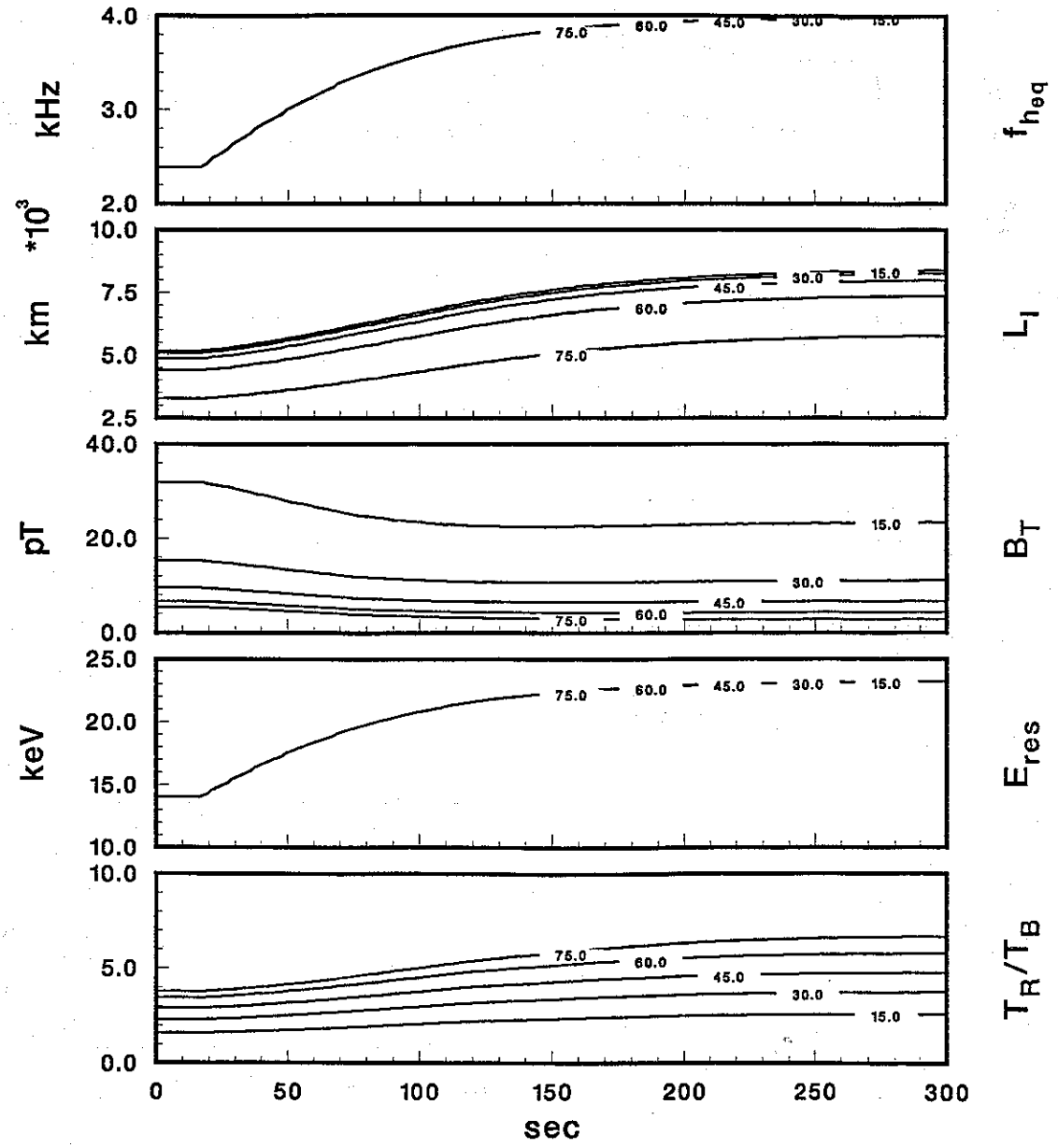


**Figure 5.6** Simulation of interaction parameters during a SC. The plot shows equatorial gyrofrequency, interaction length, wave trapping threshold, electron resonant energy, and bunching efficiency plotted as a function of time during the SC compression. The curves are plotted parametric in pitch angle (degrees).

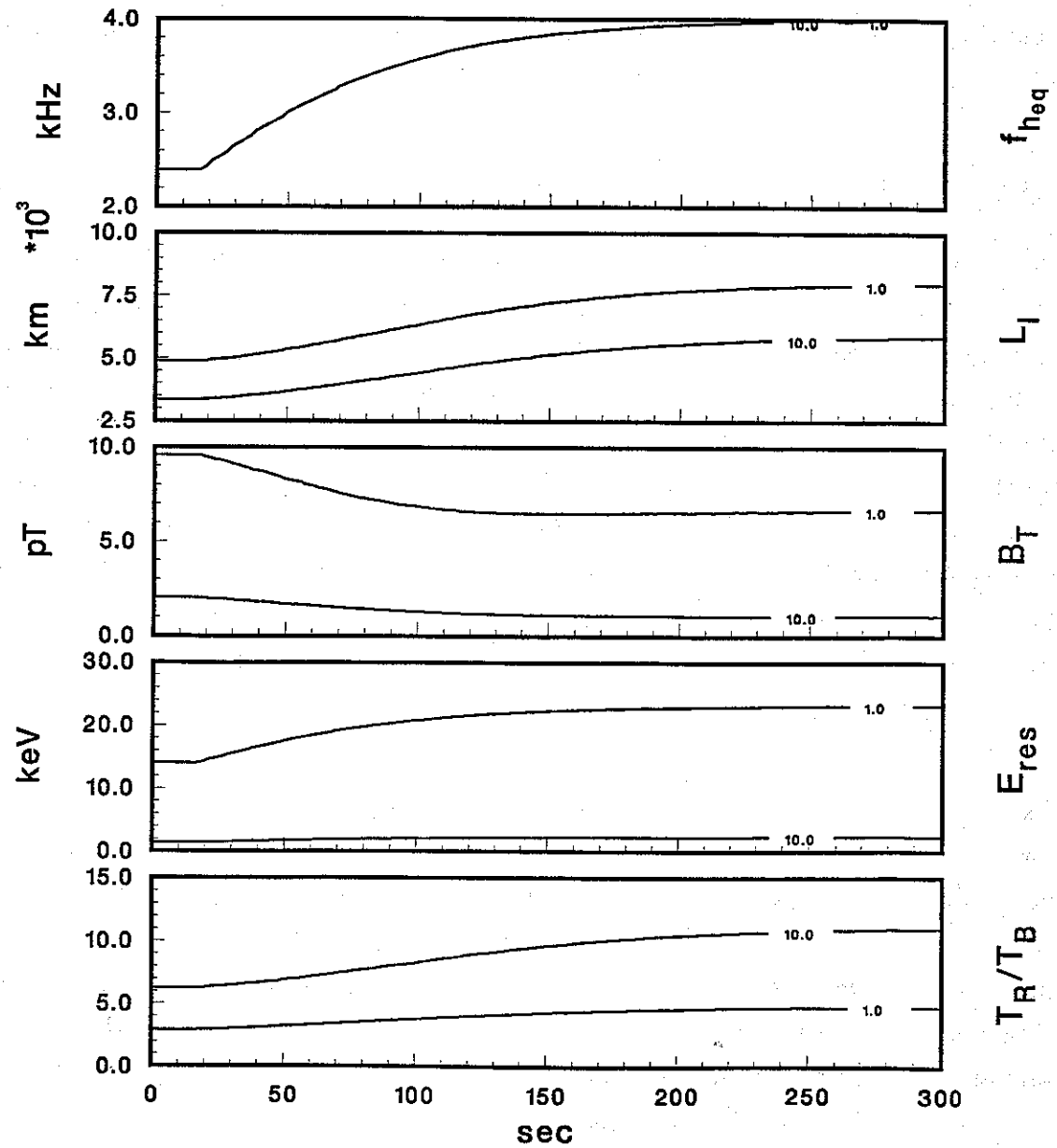


**Figure 5.7.** Simulation of interaction parameters during a SC. The plot shows equatorial gyrofrequency, interaction length, wave trapping threshold, electron resonant energy, and bunching efficiency plotted as a function of time during the SC compression. The curves are plotted parametric in thermal plasma density ($cm^{-3}$).

it was shown (e.g. Figures 3.16(d), 3.23, 3.25) that discrete emissions can be triggered following the SC onset. The observations are thus consistent with the predictions of the dynamic interaction parameter model.

### 5.1.3 *LIMITATIONS*

Nonlinear theories are complete in the sense that they include all of the physics of the wave-particle interaction for basic systems. Limitations arise, however, when applying the theory to the far more complex system defined by the magnetosphere. Those models which include the magnetic field inhomogeneity generally approximate the field within the interaction region by a quadratic or similarly simple analytic function. Boundary conditions imposed by the ionosphere are generally not included. Simulations have been mostly limited to the case of coherent monochromatic waves propagating in a ducted mode, although a theoretical model for nonducted nonlinear interactions has been proposed [*Bell*, 1984]. Computational restrictions generally limit simulations to interactions involving small, carefully chosen portions of the distribution function. It is not clear how these assumptions limit the predictive capabilities of the models.

Experimental studies have yet to conclusively demonstrate the necessary conditions for generation of discrete emissions. Simulations [*Carlson*, 1987] emphasize the importance of phase bunching in the initial growth of a signal to an amplitude where trapping and emission triggering can occur [*Helliwell*, 1967], but the full physical process is not yet understood. The interaction parameters describe the physics of single-particle interactions with waves; the relation between the interaction parameters and triggering of emissions resulting from interactions with a full distribution of particles has not been fully investigated.

## 5.2 QUASI-LINEAR MODELS

Quasi-linear models are commonly used to describe the properties of diffuse emissions. Such models are derived from a stochastic treatment of gyroresonance interactions

and have the important advantage of being primarily analytic models. As described in Chapter 2, quasi-linear models are based on two coupled equations. The first describes the growth rate of the waves caused by the pitch angle anisotropy in the distribution function. The second describes the evolution of the distribution due to scattering by the waves. In this section, modifications of the quasi-linear model developed by *Kennel and Petschek* [1966] are discussed in order to provide predictions for a SC. The predictions are then compared with the observations of diffuse emissions during SC.

### 5.2.1 *QUASI-LINEAR MODELS FOR A SC*

*Modified equations.* The growth rate equation derived by *Kennel and Petschek* [1966] (Equation 2.2.13) provides the starting point for dynamic modifications of quasi-linear theory. Previous dynamic models [*Coroniti and Kennel*, 1970; *Perona*, 1972] have introduced simple time-dependent perturbations in the magnetic field and made a number of approximations to determine the growth rate modification. In order to provide a more reliable assessment of the growth rate in a dynamic environment, a careful derivation of the growth rate under an arbitrary small time-dependent magnetic perturbation is needed. The derivation itself is not discussed here but is given in detail in Appendix A.

The results show that, for a time-dependent magnetic field perturbation of the form

$$B = B_0 \left(1 + b(t)\right), \tag{5.2.1}$$

the growth rate can be written to first order in $b(t)$ as

$$\gamma = \gamma_0 \left(1 + \beta b(t)\right), \tag{5.2.2}$$

where $\gamma_0$ is the growth rate in the static system, $\beta$ is a function of only the static variables, and the time dependence is contained in $b(t)$.

Unfortunately, a similar reformulation of the second of the coupled equations, the diffusion equation, could not be done without the introduction of a number of critical assumptions. The full analysis of the general dynamic quasi-linear problem thus remains for future work. For the comparison with observations, we will use a simpler analysis proposed by *Perona* [1972].

*The Perona model.* *Perona* [1972] set out to provide a theoretical basis for the latitude and local time dependence of electron precipitation observed during SC by *Ortner et al.* [1962] and *Hartz* [1963], who showed that riometer absorption peaks at geomagnetic latitudes between 57° and 75° and local times near noon. Perona started with the quasi-linear formalism of *Kennel and Petschek* [1966] and added a simple time-dependent perturbation to the magnetic field of the form

$$B = B_0(1 + \delta t)\,, \tag{5.2.3}$$

where $\delta$ is chosen such that $B$ reaches its final value at $t = T$. Perona used values of $T = 100$ seconds in the noon sector and $T = 200$ seconds in the midnight sector. By making a number of assumptions (see Section 5.2.3), Perona was able to show that the anisotropy $A$ and the modified diffusion coefficient $D^+$ satisfy the coupled set of differential equations

$$\frac{\partial A}{\partial t} = \frac{1 + A}{B}\frac{dB}{dt} - 2D^+A \tag{5.2.4}$$

$$\frac{dD^+}{dt} = 2\left(\gamma - \nu\right)D^+, \tag{5.2.5}$$

where $\gamma$ is the wave growth rate and $\nu$ is the wave loss rate. The modified diffusion coefficient in this model is directly proportional to the square of the wave amplitude. The wave growth rate was approximated from Equation 2.2.4 as

$$\gamma = \gamma_0(1 + \delta t)\frac{A}{A_0}\,. \tag{5.2.6}$$

The wave loss rate was estimated by taking into account both Landau damping and wave convection out of the source region and has the form

$$\nu = \nu_0(1 + \delta t)^{\frac{1}{2}} . \tag{5.2.7}$$

Using values for $\delta$, $\gamma_0$, and $\nu_0$ which were believed to be typical, Perona found numerical solutions for Equations 5.2.4 and 5.2.5 for field lines at invariant latitudes of 60°, 68°, and 75° for both the noon and midnight sectors.

A plot of Perona's results giving both the diffusion rate and anisotropy as a function of time is shown in Figure 5.8 for the case $\Lambda = 68°$ in the noon sector. The critical value of the diffusion coefficient ($D_C$) represents the transition between weak and strong pitch angle diffusion. The anisotropy $A$ changes by only a factor of 2, but the diffusion coefficient $D$ increases by nearly 3 orders of magnitude. Both $A$ and $D$ exhibit damped oscillations with a period of 35-40 seconds. The wave amplitude, given by the square root of $D$, increases by about 30 dB within a period of 20 seconds (corresponding to a growth rate of 1.5 dB/sec) and then undergoes damped oscillations with a period of 35-40 seconds. For the other cases studied, Perona found that strong diffusion was not attained, although he does not present plots for these cases.

### 5.2.2 *COMPARISON WITH OBSERVATIONS*

Table 5.2 lists the values predicted by Perona and the values obtained in Chapter 3 for a number of important properties of wave activity during SC. The results discussed by Perona are remarkably similar to the observations of diffuse emissions during SC. Perona's predictions for growth rate, growth time, and total growth are all within the range of observed values. The oscillation period is about half the observed value. The oscillations are damped to 3 dB below their initial amplitude within 3-4 cycles, similar to the observed damping rate. Perona's model unfortunately does not include predictions about bandwidth, so no comparison with the observed value is possible.

Predictions about frequency-dependent effects are not explicitly included in Perona's model, but can be inferred to some extent. The increase in the upper cutoff frequency

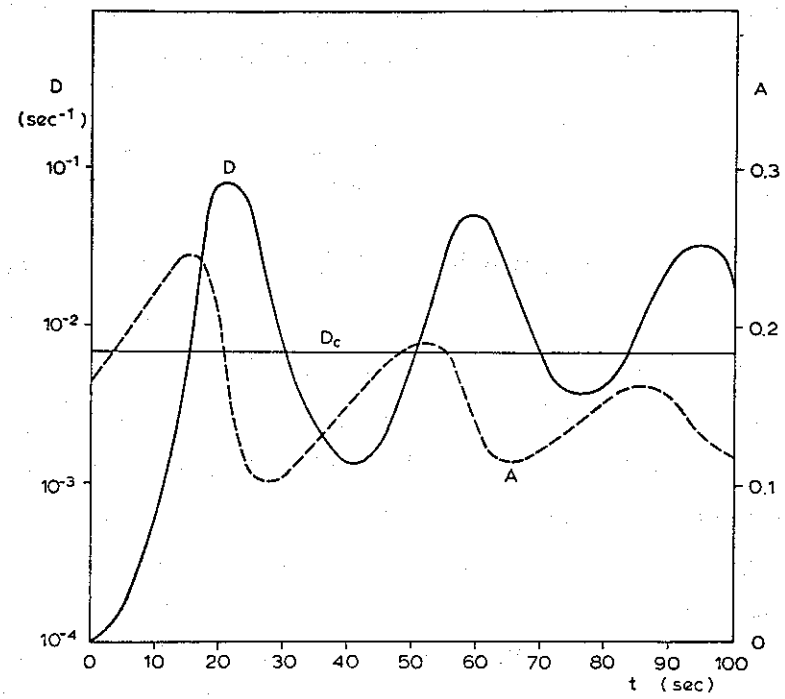


**Figure 5.8.** The anisotropy $A$ and the diffusion coefficient $D$ plotted versus time for a SC. The calculation corresponds to interactions occurring at $\Lambda = 68°$ in the noon sector. $D_c$ is the critical value of the diffusion coefficient [*Perona*, 1972].

(UCF) could result from one of several effects. First, the increase in $f_H/2$ within a given duct increases the highest frequency which can propagate within the duct. Second, the growth rate is a function of the normalized frequency $f/f_H$; a maximum growth rate at some value of $f/f_H$ will occur at a higher absolute frequency after the compression. Third, the compression changes both $A$ and $A_c$ in a manner which could increase the frequency above which the growth rate is negative (defined by $A = A_c$; the effect could occur only if $A$ has a frequency dependence such that $A$ and $A_c$ cross at some frequency).

The third effect would also account for the frequency-dependent onset time of wave growth. Figure 5.9 shows $A_c$ and an arbitrary function $A$ (chosen to satisfy the condition that $A = A_c$ at some arbitrary frequency) plotted versus the pre-SC normalized wave frequency for three values of the time parameter $b$. The point at which $A = A_c$ corresponds to the highest frequency at which the growth rate is positive. As $b$ in-

**Table 5.2.** Comparison between observations and predictions of the Perona theory.

| | | Observations | Perona Predictions |
|---|---|---|---|
| **Frequency increase:** | total | 0.7-1.0 kHz | possible |
| | delay | 10-35 sec | possible |
| **Growth:** | rate | 0.3-3 dB/sec | 1.5 dB/sec |
| | duration | 10-20 sec | 20 sec |
| | total | 12-30 dB | 30 dB |
| | bandwidth | 0.5-1.5 kHz | no prediction |
| **Oscillations:** | period | 60-90 sec | 35-40 sec |
| | damping time | 3-4 cycles | 3-4 cycles |

creases, $A$ increases while $A_c$ decreases; the frequency at which $A = A_c$ thus increases with time. To evaluate the effect properly, the frequency at which the integrated growth rate along the duct becomes positive should really be considered, but the frequency dependence works in the same way. According to this explanation, the rate of change of the upper cutoff frequency during a SC is sensitive to both the rate of change of $b$ and the particular form of $A$.

### 5.2.3 *LIMITATIONS*

All quasi-linear models are fundamentally limited in their applicability by two assumptions: the small wave amplitude limit (hence the term linear) and the gyrophase independence of the interaction. The linearity assumption excludes the effects of particle trapping by the potential well of the wave field. The gyrophase assumption excludes coherent effects due to phase bunching. Quasi-linear models thus can not account for the discrete emissions which are observed throughout much of the inner magnetosphere. Recent experimental work [*Helliwell et al.*, 1986] has suggested the possibility that even diffuse emissions may be generated through coherent interactions. Quasi-linear models also generally assume that $f << f_H$, so the applicability at frequencies near $f = f_H/2$ becomes suspect.

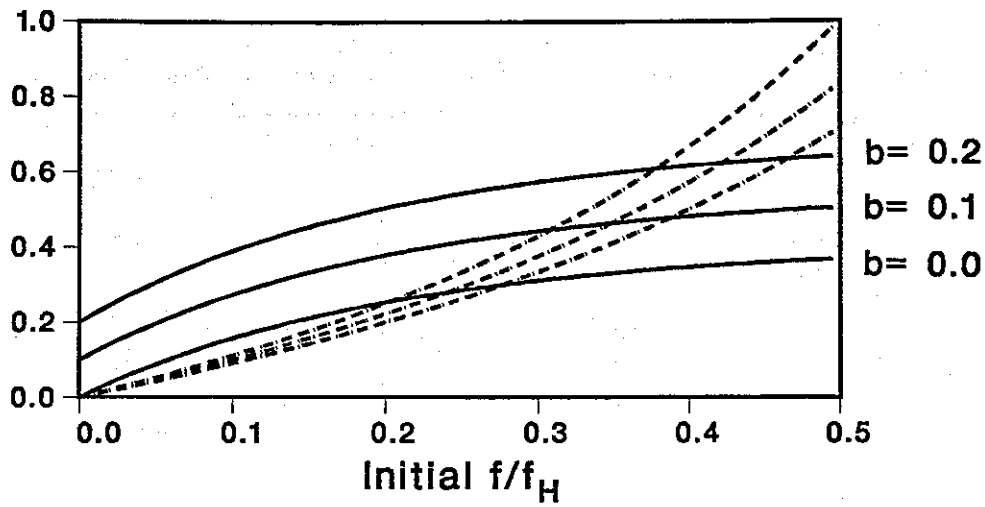


**Figure 5.9.** Possible temporal evolution of $A$ and $A_c$ during a SC. The solid lines represent $A$ and the dashed lines represent $A_c$ for three values of the time parameter $b$. $A$ increases while $A_c$ decreases with time. In this example, the frequency at which $A = A_c$ increases from 0.2 to nearly 0.5 as $b$ goes from 0 to 0.2.

As with nonlinear theories, quasi-linear models also suffer from the assumptions which must be made when adapting the basic theory derived for an infinite plasma to the more complex environment of the magnetosphere. The Perona model incorporates the bounce-averaging procedure used by *Kennel and Petschek* [1966] and *Lyons et al.* [1972], the limitations of which are discussed by *Retterer et al.* [1983]. The models have proven to be particulary sensitive to the choice of ionospheric boundary conditions [*Silevitch and Rothwell*, 1986], wave raypaths [*Huang et al.*, 1983; *Church and Thorne*, 1983], and dynamic effects (see Appendix A).

As noted previously, the Perona model invokes a number of critical assumptions in order to make the problem tenable. Most of the assumptions are stated clearly in the paper. Perona appears to have recognized the resulting limitations for his model, even suggesting that the choice of assumptions could account for the 30-40 sec oscillations in his solution.

Perona's derivation of the time-dependent growth rate is clearly incorrect as is the assumption that $\eta$, the fraction of the distribution in resonance, is constant. The correct values are given by the more complete derivation in Appendix A. However,

for most cases the difference can be effectively eliminated by making a small change in the assumed rise time of the disturbance. Probably more critical are the assumptions about wave propagation, which are used to derive the modification to the wave loss rate. He does not consider the role of ducting or closed nonducted raypaths, one or the other of which appears to be necessary [e.g. *Church and Thorne*, 1983] to provide the wave feedback required to sustain the Kennel-Petschek system. The modified loss rate does not appear correct in this context. Since he does not properly consider the wave bandwidth (such as in the derivation of *Etcheto et al.* [1973]), he limits the ability to predict frequency-dependent effects.

## 5.3 SUMMARY

The ultimate goal of the comparison between theory and observations is to determine to what extent current static models of gyroresonance interactions can be modified to apply to a dynamic magnetosphere. The results presented in this chapter indicate that, despite the extent of the assumptions required to adapt static models to a dynamic environment, simple dynamic models for SC provide predictions which are quite consistent with observations. Nonlinear models predict the observed increased occurrence rate for discrete emissions. Quasi-linear models predict a number of qualitative and quantitative features of diffuse emissions. The models are necessarily primitive and currently valid only for SC, but they indicate the potential for adaptation of static gyroresonance models to a dynamic magnetosphere.

# Chapter 6

# SUMMARY AND RECOMMENDATIONS

## 6.1 SUMMARY

We have developed a new observational method to investigate the effect of dynamic changes in the magnetosphere on gyroresonant wave-particle interactions. The method is based on the analysis of rapid compressions of the magnetosphere known as Sudden Commencements (SC). The SC compression causes a step-like perturbation of the magnetic field and the plasma which in turn modifies wave-particle interactions. By measuring the properties of wave emissions during a SC and comparing them with the properties observed prior to the SC, the corresponding changes in the characteristics of the gyroresonance interaction mechanism caused by the dynamic modification of the environment can be inferred.

The method was applied through development of a data set of wave and particle observations for several hundred SC. The observations were obtained primarily at Antarctic ground stations using wave receivers, magnetometers, and riometers. Supporting data from spacecraft were also used. The wave data were analyzed for both amplitude and spectral modifications associated with the SC and correlated with magnetic field and riometer absorption observations. Changes in both incoherent and coherent wave activity were observed. Particular emphasis was placed on the initial growth period, which allowed for a simplified analysis of the physical processes

which could affect the wave-particle interactions. It was found that the wave response to SC has a number of repeatable quantitative characteristics. Of particular interest is the growth rate for incoherent waves (0.3-2.7 dB/sec), which had not been previously measured and was found to be two orders of magnitude less than growth rates for coherent waves. A summary of the measurements is given at the end of Chapter 3 and a general characterization of ELF/VLF wave phenomena associated with SC is given at the end of Chapter 4.

The strength of the data lies in application as observational constraints for models of gyroresonance interactions in a dynamic magnetosphere. Current models of both nonlinear and quasi-linear theories generally assume that the magnetosphere is static. In an effort to develop a valid dynamic quasi-linear model, the growth rate derived by *Kennel and Petschek* [1966] was modified to include a general time-dependent magnetic perturbation. The derivation is given in Appendix A. The model of *Perona* [1972], which is an adaptation of the Kennel-Petschek theory for SC, was used to obtain predictions which could be compared with the observations. Despite the numerous simplifications introduced in the Perona model, the quantitative predictions of the model generally agree with the measurements we obtained. The results provide the first experimental verification of the Perona theory.

A simple dynamic model of the interaction parameters which characterize nonlinear theories was developed for comparison with the observations of coherent emissions. A realistic magnetic field model in which the magnetopause standoff distance could be varied [*Olson and Pfitzer*, 1974; *Olson and Pfitzer*, 1982] was used to simulate the temporal evolution of the SC. The interaction parameters were then numerically calculated as a function of the SC compression. The results indicate that the occurrence rate of coherent emissions could increase due to the SC, consistent with the observations.

Our observations suggest that dynamic effects may play a significant role in magnetospheric wave-particle interactions. The comparison between observations and models suggests that static models of gyroresonance interactions, when properly modified, can provide quantitative predictions about wave and particle properties in a dynamic magnetosphere. The results emphasize the potential value of carefully developed

gyroresonance models which incorporate dynamic effects.

## 6.2 RECOMMENDATIONS FOR FUTURE WORK

*Spacecraft observations.* As discussed in Chapter 3, ground-based and spacecraft observations provide different information on wave-particle interactions. Ground-based data were used for this study due primarily to data availability restrictions. A similar study of spacecraft observations would complement our results and possibly provide results that could not be obtained using ground-based observations. High resolution (1 sec or better) magnetic field and wave data are essential in order to measure wave growth rates and to correlate wave growth effects with the magnetic disturbance. Broadband data (or narrowband amplitudes in a sufficient number of channels) are important for determining spectral properties and distinguishing between diffuse and discrete emissions. A spacecraft which spends a significant amount of time in the dayside equatorial plane (such as GEOS 2 or AMPTE) would provide the best coverage.

*Analysis of the general class of magnetic perturbations.* A preliminary survey (listed in Appendix E) has shown that SC are a subset of a larger class of events for which correlations are observed between wave activity and magnetic field perturbations. Some investigators [*Hayashi et al.*, 1968; *Kokubun*, 1983] have suggested that a detailed correlation exists between ELF/VLF and magnetic field variations, but the extent of correlated effects is not really known. The results discussed in Chapter 3 indicate that significant wave growth and particle scattering occurs within the first several tens of seconds of the magnetic disturbance when the field strength increase is still small. It is possible that similar effects commonly accompany smaller magnetic perturbations. Small discontinuities in the solar wind are believed to impact the magnetosphere at the rate of several per hour [*Smith*, 1979]. A careful survey of correlated events would indicate the role that dynamic processes play in the magnetosphere.

*Extension of interaction models.* Although the dynamic interaction models used for the analysis in Chapter 5 were based on rather simplistic extensions of current static

models, both qualitative and quantitative predictions were in general agreement with observations. The predictive capabilities of both nonlinear and quasi-linear models were limited, however, by the simplifications used to develop the models.

With the derivation presented in Appendix A, we have initiated an effort to provide a full and complete modification of quasi-linear theory to include dynamic effects. However, since the diffusion equation portion of the theory is not yet reworked, the modification remains incomplete. An extension of the dynamic form of quasi-linear theory and the inclusion of frequency dependence would greatly enhance the applicability of quasi-linear models.

The interaction parameter model presented in Chapter 5 demonstrated that the interaction parameters are significantly modified by SC. *Dowden* [1981] suggested that similar effects caused by resonant field-line oscillations could control the generation of coherent emissions. A full simulation using a realistic magnetosphere with a variety of configurations is necessary to provide a conclusive analysis of the problem.

*Calculation of scattering effects due to dynamic processes.* Recent advances in computer simulations of wave-particle scattering [*Inan*, 1977; *Inan et al.*, 1978; *Chang and Inan*, 1985; *Inan*, 1987] provide the capability to quantitatively calculate both the flux and energy spectrum of particles precipitated by interactions with coherent and incoherent waves. A comparison of scattering simulations incorporating a dynamic magnetosphere with corresponding observations of particle precipitation would provide a further test of models as well as an indication of the importance of dynamic processes in the loss of particles from the radiation belts.

*Application to magnetospheric phenomena.* A number of commonly observed wave phenomena in the magnetosphere have been attributed to the influence of dynamic effects. Particularly interesting is the problem of the origin of quasi-period (QP) emissions. Correlations between QP emissions and magnetic pulsations have been noted by several investigators [e.g., *Ho*, 1974; *Sato and Fukunishi*, 1981; *Lanzerotti et al.*, 1986]. Several explanations have been proposed to explain the observed periodicity and the rising frequency structure, including modulation by particle sources [*Ho*, 1974] and by MHD waves [*Sato and Kokubun*, 1980; *Tixier and Cornilleau-Wehrlin*,

1986]. The 60-90 sec periodicity observed during the transient enhancement of SC (and, in at least one case studied, prior to the transient enhancement) may be controlled by the same mechanism that regulates the periodic structure of QP emissions. The spectral similarity between QP emissions and SC emissions suggests that the results obtained for SC could be applied to understand the QP phenomenon.

# Appendix A

# DERIVATION OF THE WAVE GROWTH RATE

In this appendix, the quasi-linear wave growth rate is modified to include a general small amplitude time-dependent magnetic field perturbation.

## A.1 STATEMENT OF THE PROBLEM

The growth rate for whistler-mode waves in the quasi-linear approximation in a static magnetic field is given by [*Kennel and Petschek*, 1966]

$$\gamma = \pi\omega_H\left(1-\frac{\omega}{\omega_H}\right)^2 \eta(E_R)\left[A(E_R)-A_c\right] \tag{A.1.1}$$

where $\omega_H$ = electron gyrofrequency

$\omega$ = wave frequency

$E_R$ = electron resonant energy

and the functions $\eta(E_R)$, $A(E_R)$, and $A_c$ are

$$\eta(E_R) = 2\pi {v_R}^3 \int_0^{\frac{\pi}{2}} \frac{\sin\alpha}{\cos^3\alpha} F(\alpha, E)d\alpha \tag{A.1.2}$$

$$A(E_R) = \frac{\int_0^{\frac{\pi}{2}} \frac{\sin^2\alpha}{\cos^4\alpha}\frac{\partial F(\alpha,E)}{\partial\alpha}d\alpha}{2\int_0^{\frac{\pi}{2}} \frac{\sin\alpha}{\cos^3\alpha}F(\alpha,E)d\alpha} \tag{A.1.3}$$

$$A_c = \frac{\omega}{\omega_H - \omega} , \tag{A.1.4}$$

where $F$ and $\frac{\partial F(\alpha,E)}{\partial \alpha}$ are evaluated subject to $E_{\|} = E_R$ prior to integration. $A(E_R)$ is the pitch angle anisotropy, $\eta(E_R)$ is the fraction of the distribution in resonance, $Ac$ is the critical anisotropy, and

$$\begin{aligned} v_R &= \text{electron resonant velocity} \\ \alpha &= \text{electron pitch angle} \\ F &= \text{electron distribution function} \end{aligned}$$

We wish to determine the form of $\gamma$ when time-dependence is included in the magnetic field.

## A.2 APPROACH

Consider a dynamic magnetic field of the form

$$B(t) = B_0 \left(1 + b(t)\right) , \tag{A.2.1}$$

where $B_0$ is the static field and $b(t)$ is a dimensionless parameter containing the time dependence. All variables corresponding to the static environment are denoted with a subscript 0. Those variables corresponding to the time-dependent environment have no subscript.

Resonant particles satisfy the resonance condition for longitudinal propagation

$$v_{\|} = v_R = \frac{\omega - \omega_H}{k} , \tag{A.2.2}$$

$$\begin{aligned} \text{where} \quad v_{\|} &= \text{electron parallel velocity} \\ k &= \text{wave number} \end{aligned}$$

For a given wave frequency, the resonance condition is satisfied by different particles in the static and dynamic configurations. Variables corresponding to particles and waves

which satisfy the resonance condition in the static environment are denoted with primes; those which satisfy the resonance condition in the dynamic environment are denoted with double primes. Since we will be mapping particles from the static to the dynamic environment, a variable of the form $\overline{\overline{E_0}}$ is acceptable since it represents the energy of a particle in the static environment which satisfies the resonance condition in the dynamic environment.

In this approach, the entire time dependence of the system is contained in the variable $b(t)$, allowing us to write the growth rate $\gamma$ in terms of the static growth rate $\gamma_0$, the static field parameters, the static field resonance condition, and $b(t)$.

We first show that the terms $\alpha$, $E$, and $F(\alpha, E)$ can be written in terms of $\alpha_0$, $E_0$, $F_0(\alpha_0, E_0)$, and $b(t)$. These relations are then used to describe the particular function $F(\alpha, \overline{\overline{E}})$, which corresponds to resonant particles in the time-dependent formulation, in terms of $F_0(\alpha_0, \overline{\overline{E_0}})$ and $b(t)$. By assuming that $F_0(\alpha_0, \overline{\overline{E_0}}) \simeq F_0(\alpha_0, \overline{E_0})$, $F_0(\alpha_0, \overline{\overline{E_0}})$ can be related to $F_0(\alpha_0, \overline{E_0})$ through a Taylor expansion. A general form of the distribution function is then assumed to facilitate the evaluation of several integrals; the parameters characterizing the function do not appear in the final solution. Finally, an expression for the time-dependent growth rate is obtained which is written as a function of static parameters and the time parameter $b(t)$.

## A.3 TIME-DEPENDENT FORM OF PHYSICAL PARAMETERS

Using the time-dependent magnetic field, the electron gyrofrequency is

$$\omega_H = \omega_{H0} \frac{B(t)}{B_0} = \omega_{H0}(1 + b) \,. \tag{A.3.1}$$

The electron plasma frequency is

$$\omega_p = \omega_{p0}(1 + b)^{\frac{1}{2}} \,, \tag{A.3.2}$$

where we have used the frozen-in flux condition.

A rigorous discussion of the interaction between energetic particles and hydromagnetic waves has been given by *Tamao* [1984]. For this problem, we will consider

only the contribution of betatron acceleration in calculating changes in the particle distribution. Assuming conservation of the first adiabatic invariant and ignoring the change in $v_\parallel$, the particle velocities are

$$v_\parallel{}^2 = v_{\parallel 0}{}^2 \tag{A.3.3}$$

$$v_\perp{}^2 = \frac{2B}{m}\mu = v_{\perp 0}{}^2(1+b)\,. \tag{A.3.4}$$

The pitch angle is

$$\tan^2\alpha = \frac{v_\perp{}^2}{v_\parallel{}^2} = \tan^2\alpha_0(1+b)\,. \tag{A.3.5}$$

The total particle energy is

$$E = \frac{1}{2}m\left(v_{\parallel 0}{}^2 + v_{\perp 0}{}^2(1+b)\right) = E_0(1+b\sin^2\alpha_0)\,. \tag{A.3.6}$$

The refractive index for longitudinal whistler-mode propagation in a cold magnetoplasma is given by [*Helliwell*, 1965]

$$n^2 = 1 - \frac{\frac{\omega_p{}^2}{\omega^2}}{1-\frac{\omega_H}{\omega}} = n_0{}^2\left(1+N(b)\right), \tag{A.3.7}$$

$$\text{where} \quad N(b) = \left[\left(1-\frac{\omega_{H0}}{\omega}\right)\left(1+\frac{\omega\omega_{H0}-\omega^2}{\omega_{p0}{}^2}\right)\right]^{-1}\frac{b}{1-\frac{\omega_{H0}}{\omega-\omega_{H0}}b}\,. \tag{A.3.8}$$

The wave number is

$$k = \frac{\omega n}{c} = k_0(1+N)^{\frac{1}{2}}. \tag{A.3.9}$$

The resonant velocity is

$$\begin{aligned}\overline{\overline{v_R}} &= \frac{\omega-\omega_H}{k} = \frac{\omega-\omega_{H0}(1+b)}{k_0(1+N)^{\frac{1}{2}}} \\ &= \overline{v_{R0}}(1+V)\,,\end{aligned} \tag{A.3.10}$$

$$\text{where} \quad V = \frac{1-(1+N)^{\frac{1}{2}} - \frac{\omega_{H0}}{\omega-\omega_{H0}}b}{(1+N)^{\frac{1}{2}}}. \tag{A.3.11}$$

The resonant energy is

$$\overline{\overline{E_R}} = \overline{E_{R0}}(1+V)^2 \ . \tag{A.3.12}$$

## A.4 TIME-DEPENDENT FORM OF THE DISTRIBUTION FUNCTION

The volume element for the space $(\alpha, E, \phi)$ is

$$dV = -\sqrt{\frac{2}{m^3}}\sqrt{E}\sin\alpha dE d\alpha d\phi \ . \tag{A.4.1}$$

Assuming the distribution functions are independent of $\phi$, we have

$$\int_{\text{space}} F(\alpha, E)\sqrt{E}\sin\alpha d\alpha dE d^3x = \int_{\text{space}} F_0(\alpha_0, E_0)\sqrt{E_0} d\alpha_0 d\phi_0 dE_0 d^3x_0, \tag{A.4.2}$$

where the integrals are over phase space.

Using (A.3.11) and (A.3.12), we have

$$\sqrt{E} = \sqrt{E_0}\left(1 + b\sin^2\alpha_0\right)^{\frac{1}{2}} \tag{A.4.3}$$

$$\sin\alpha = \frac{(1+b)^{\frac{1}{2}}\sin\alpha_0}{(1+b\sin^2\alpha_0)^{\frac{1}{2}}} \tag{A.4.4}$$

$$d\alpha = \frac{(1+b)^{\frac{1}{2}}}{1+b\sin^2\alpha_0} d\alpha_0 \tag{A.4.5}$$

$$dE = \left(1 + b\sin^2\alpha_0\right) dE_0 \tag{A.4.6}$$

$$d^3x = \frac{1}{(1+b)} d^3x_0, \tag{A.4.7}$$

and the left-hand side of (A.4.2) is

$$= \int_{\text{space}} F(\alpha, E)\sqrt{E_0}\sin\alpha_0 d\alpha_0 dE_0 d^3x_0. \tag{A.4.8}$$

The distribution functions are thus related by

$$F(\alpha, E) = F_0(\alpha_0, E_0), \tag{A.4.9}$$

$$\text{where} \quad \tan^2\alpha = (1+b)\tan^2\alpha_0 \tag{A.4.10}$$

$$E = E_0\left(1 + b\sin^2\alpha_0\right). \tag{A.4.11}$$

## A.5 TIME-DEPENDENT DISTRIBUTION FOR RESONANT PARTICLES

The total energy of a particle with resonant energy $E_{R0} = \overline{E_{R0}}$ is

$$\overline{E_0} = \frac{\overline{E_{R0}}}{\cos^2\alpha_0}. \tag{A.5.1}$$

Similarly, for a particle with $E_R = \overline{\overline{E_R}}$

$$\overline{\overline{E}} = \frac{\overline{\overline{E_R}}}{\cos^2\alpha}. \tag{A.5.2}$$

Equation (A.5.2) can be written in terms of static variables using (A.3.5) and (A.3.12) as

$$\overline{\overline{E}} = \frac{\overline{E_{R0}}(1+V)^2}{\cos^2\alpha} = \overline{E_{R0}}(1+V)^2\frac{1+b\sin^2\alpha_0}{\cos^2\alpha_0}. \tag{A.5.3}$$

For resonant particles, the time-dependent distribution function can be written in terms of the static distribution as

$$F(\alpha, \overline{\overline{E}}) = F_0(\alpha_0, \overline{\overline{E_0}}), \tag{A.5.4}$$

$$\text{where} \quad \tan^2\alpha = (1+b)\tan^2\alpha_0 \tag{A.5.5}$$

$$\overline{\overline{E}} = \overline{\overline{E_0}}(1 + b\sin^2\alpha_0). \tag{A.5.6}$$

The total energy of the time-dependent and static particles is related by

$$\overline{\overline{E_0}} = \overline{E_0}(1+V)^2 \tag{A.5.7}$$

$$\overline{\overline{E}} = \overline{E_0}(1+V)^2(1 + b\sin^2\alpha_0). \tag{A.5.8}$$

Note that the equivalent time-dependent particle energy in the static distribution (i.e., $\overline{\overline{E_0}}$) is not equal to the static particle energy (i.e., $\overline{E_0}$) for $b \neq 0$.

## A.6 $\overline{\overline{F_0}}$ IN TERMS OF $\overline{F_0}$

For $V$ small and any reasonably smooth function $F_0$,

$$\overline{\overline{E_0}} \simeq \overline{E_0} \tag{A.6.1}$$

$$F_0(\alpha_0, \overline{\overline{E_0}}) \simeq F_0(\alpha_0, \overline{E_0}) \ . \tag{A.6.2}$$

We can thus do a Taylor expansion of $F_0$ about $E_0 = \overline{E_0}$. Assuming $F_0$ is a separable function,

$$F_0(\alpha_0, E_0) \simeq F_0(\alpha_0, \overline{E_0}) + (E_0 - \overline{E_0}) \frac{\partial F_0}{\partial E_0}\bigg|_{E_0=\overline{E_0}} + \frac{1}{2}(E_0 - \overline{E_0})^2 \frac{\partial^2 F_0}{\partial {E_0}^2}\bigg|_{E_0=\overline{E_0}} \ . \tag{A.6.3}$$

For the resonant particles in the time-dependent formulation, we evaluate this at $E_0 = \overline{\overline{E_0}}$.

## A.7 THE TERMS IN $A(E_R)$

In calculating $A(E_R)$ from (A.1.3), the derivatives are taken with $E$ =CONST and the integrations are done with $E_R$ =CONST.

The various terms in $A(E_R)$ can be written in terms of static quantities as

$$\frac{\partial F}{\partial \alpha} = \left[\frac{\partial F_0}{\partial \alpha_0}\frac{\partial \alpha_0}{\partial \alpha} + \frac{\partial F_0}{\partial E_0}\frac{\partial E_0}{\partial \alpha}\right] \tag{A.7.1}$$

$$d\alpha = \frac{(1+b)^{\frac{1}{2}}}{1 + b\sin^2\alpha_0} d\alpha_0 \tag{A.7.2}$$

$$\frac{\sin^2\alpha}{\cos^4\alpha} = (1+b)(1+b\sin^2\alpha_0)\frac{\sin^2\alpha_0}{\cos^4\alpha_0} \tag{A.7.3}$$

$$\frac{\sin\alpha}{\cos^3\alpha} = (1+b)^{\frac{1}{2}}(1+b\sin^2\alpha_0)\frac{\sin\alpha_0}{\cos^3\alpha_0} \ . \tag{A.7.4}$$

The derivative $\frac{\partial E_0}{\partial \alpha}$ in (A.7.1) can be evaluated, using (A.3.6), as

$$\frac{\partial E_0}{\partial \alpha} = \frac{-2b}{1+b} E \sin\alpha \cos\alpha = \frac{-2b}{(1+b)^{\frac{1}{2}}} E_0 \sin\alpha_0 \cos\alpha_0 \ . \tag{A.7.5}$$

By using (A.7.5) and introducing the Taylor expansion form of $F_0$ from (A.6.3), (A.7.1) is

$$\frac{\partial F}{\partial \alpha} \simeq \frac{1}{(1+b)^{\frac{1}{2}}} \left[ (1 + b\sin^2\alpha_0) \frac{\partial F_0}{\partial \alpha_0} - 2bE_0 \sin\alpha_0 \cos\alpha_0 \frac{\partial F_0}{\partial E_0} \right] \tag{A.7.6}$$

$$\simeq \frac{1}{(1+b)^{\frac{1}{2}}} \left\{ (1 + b\sin^2\alpha_0) \frac{\partial}{\partial \alpha_0} [\text{Taylor expansion}] \right.$$
$$\left. - (2bE_0 \sin\alpha_0 \cos\alpha_0) \frac{\partial}{\partial E_0} [\text{Taylor expansion}] \right\} . \tag{A.7.7}$$

Taking the derivatives, we get

$$\frac{\partial F}{\partial \alpha} \simeq \frac{1}{(1+b)^{\frac{1}{2}}} \left\{ (1 + b\sin^2\alpha_0) \left[ \left. \frac{\partial F_0}{\partial \alpha_0} \right|_{E_0 = \overline{E_0}} + (E_0 - \overline{E_0}) \left. \frac{\partial^2 F_0}{\partial \alpha_0 \partial E_0} \right|_{E_0 = \overline{E_0}} \right] \right.$$
$$\left. - (2bE_0 \sin\alpha_0 \cos\alpha_0) \left[ \left. \frac{\partial F_0}{\partial E_0} \right|_{E_0 = \overline{E_0}} + (E_0 - \overline{E_0}) \left. \frac{\partial^2 F_0}{\partial {E_0}^2} \right|_{E_0 = \overline{E_0}} \right] \right\} . \tag{A.7.8}$$

Evaluation of the energy $E_0$ subject to the resonance condition$E_R = \overline{\overline{E_R}}$, using (A.3.8) and (A.5.1), gives

$$E_0 \Rightarrow \overline{\overline{E_0}} = \overline{E_0}(1+V)^2 \simeq (1+2V) \frac{\overline{E_{R0}}}{\cos^2\alpha_0} \tag{A.7.9}$$

$$(E_0 - \overline{E_0}) \Rightarrow (\overline{\overline{E_0}} - \overline{E_0}) \simeq 2V \frac{\overline{E_{R0}}}{\cos^2\alpha_0}, \tag{A.7.10}$$

where we have kept terms to first order in V. Equation (A.7.8) is now

$$\overline{\overline{\frac{\partial F}{\partial \alpha}}} \simeq \frac{1}{(1+b)^{\frac{1}{2}}} \left\{ (1 + b\sin^2\alpha_0) \left[ \overline{\frac{\partial F_0}{\partial \alpha_0}} + 2V \frac{\overline{E_{R0}}}{\cos^2\alpha_0} \overline{\frac{\partial^2 F_0}{\partial \alpha_0 \partial E_0}} \right] \right.$$
$$\left. - \left( 2b\overline{E_{R0}} \frac{\sin\alpha_0}{\cos\alpha_0} \right) \left[ \overline{\frac{\partial F_0}{\partial E_0}} + 2V \frac{\overline{E_{R0}}}{\cos^2\alpha_0} \overline{\frac{\partial^2 F_0}{\partial {E_0}^2}} \right] \right\} . \tag{A.7.11}$$

## A.8 INITIAL EVALUATION OF $A(\overline{\overline{E_R}})$

The anisotropy function (A.1.3) for particles with resonant energy $E_R = \overline{\overline{E_R}}$ can now be written

$$A(\overline{\overline{E_R}}) = \frac{\int_0^{\frac{\pi}{2}} \frac{\sin^2\alpha}{\cos^4\alpha} \overline{\overline{\frac{\partial F}{\partial \alpha}}} d\alpha}{2\int_0^{\frac{\pi}{2}} \frac{\sin\alpha}{\cos^3\alpha} \overline{\overline{F}} d\alpha} . \tag{A.8.1}$$

Using (A.6.4), (A.7.2), (A.7.3), (A.7.4), and (A.7.11), this is

$$\overline{\overline{A}} = A(\overline{\overline{E_R}}) = \overline{\overline{N}}/\overline{\overline{D}} , \tag{A.8.2}$$

where

$$\begin{aligned}\overline{\overline{N}} \simeq (1+b)\int_0^{\frac{\pi}{2}} \frac{\sin^2\alpha_0}{\cos^4\alpha_0} \Bigg\{ &\left(1 + b\sin^2\alpha_0\right) \left[\overline{\frac{\partial F_0}{\partial \alpha_0}} + 2V \frac{\overline{E_{R0}}}{\cos^2\alpha_0} \overline{\frac{\partial^2 F_0}{\partial\alpha_0 \partial E_0}}\right] \\ &- \left(2b\overline{E_{R0}} \frac{\sin\alpha_0}{\cos\alpha_0}\right) \left[\overline{\frac{\partial F_0}{\partial E_0}} + 2V \frac{\overline{E_{R0}}}{\cos^2\alpha_0} \overline{\frac{\partial^2 F_0}{\partial {E_0}^2}}\right] \Bigg\} d\alpha_0 \end{aligned} \tag{A.8.3}$$

$$\overline{\overline{D}} \simeq 2(1+b)\int_0^{\frac{\pi}{2}} \frac{\sin\alpha_0}{\cos^3\alpha_0} \left[\overline{F_0} + 2V \frac{\overline{E_{R0}}}{\cos^2\alpha_0} \overline{\frac{\partial F_0}{\partial E_0}}\right] d\alpha_0 . \tag{A.8.4}$$

These may be written

$$\begin{aligned}\overline{\overline{N}} \simeq (1+b)\int_0^{\frac{\pi}{2}} \Bigg\{ &\left[\frac{\sin^2\alpha_0}{\cos^4\alpha_0} + b\frac{\sin^4\alpha_0}{\cos^4\alpha_0}\right] \overline{\frac{\partial F_0}{\partial \alpha_0}} \\ &+ \left[-2b\overline{E_{R0}} \frac{\sin^3\alpha_0}{\cos^5\alpha_0}\right] \overline{\frac{\partial F_0}{\partial E_0}} \\ &+ \left[2V\overline{E_{R0}} \frac{\sin^2\alpha_0}{\cos^6\alpha_0} + 2bV\overline{E_{R0}} \frac{\sin^4\alpha_0}{\cos^6\alpha_0}\right] \overline{\frac{\partial^2 F_0}{\partial\alpha_0 \partial E_0}} \\ &+ \left[-4bV\overline{E_{R0}}^2 \frac{\sin^3\alpha_0}{\cos^7\alpha_0}\right] \overline{\frac{\partial^2 F_0}{\partial {E_0}^2}} \Bigg\} d\alpha_0 \end{aligned} \tag{A.8.5}$$

$$\overline{\overline{D}} \simeq 2(1+b)\int_0^{\frac{\pi}{2}} \left\{ \frac{\sin\alpha_0}{\cos^3\alpha_0} \overline{F_0} + 2V\overline{E_{R0}} \frac{\sin\alpha_0}{\cos^5\alpha_0} \overline{\frac{\partial F_0}{\partial E_0}} \right\} d\alpha_0 . \tag{A.8.6}$$

## A.9 INTRODUCTION OF THE DISTRIBUTION FUNCTION

In order to evaluate the integrals (A.8.5) and (A.8.6), we introduce a distribution function of the form

$$F_0(\alpha_0, E_0) = \sum_{i=1}^{I} f_{0i}(E_0)\sin^{a_i}\alpha_0 \ , \tag{A.9.1}$$

where there are an arbitrary number $I$ of terms in the series. The necessary derivatives are

$$\frac{\partial F_0}{\partial \alpha_0} = \sum_{i=1}^{I} a_i f_{0i}\sin^{a_i-1}\alpha_0\cos\alpha_0 \tag{A.9.2}$$

$$\frac{\partial F_0}{\partial E_0} = \sum_{i=1}^{I} \sin^{a_i}\alpha_0 \frac{\partial f_{0i}}{\partial E_0} \tag{A.9.3}$$

$$\frac{\partial^2 F_0}{\partial {E_0}^2} = \sum_{i=1}^{I} \sin^{a_i}\alpha_0 \frac{\partial^2 f_{0i}}{\partial {E_0}^2} \tag{A.9.4}$$

$$\frac{\partial^2 F_0}{\partial \alpha_0 \partial E_0} = \sum_{i=1}^{I} a_i \sin^{a_i-1}\alpha_0\cos\alpha_0 \frac{\partial f_{0i}}{\partial E_0} \ . \tag{A.9.5}$$

Since $f_{0i}$ depends explicitly on only one of the two independent variables $E$ and $\alpha$, we can evaluate $f_{0i}$ at $E_{R0}$ =CONST before taking the derivatives. Thus, using,

$$\frac{df_{0i}}{d\alpha_0} = \frac{\partial f_{0i}}{\partial E_0}\frac{dE_0}{d\alpha_0}, \tag{A.9.6}$$

we have

$$\frac{\partial f_{0i}}{\partial E_0} = \frac{\partial}{\partial E_0}\left[f_{0i}(E_{R0}, \alpha_0)\right] \tag{A.9.7}$$

$$= \left(\frac{dE_0}{d\alpha_0}\right)^{-1}\frac{df_{0i}}{d\alpha_0} = \left(\frac{1}{2E_{R0}}\frac{\cos^3\alpha_0}{\sin\alpha_0}\right)\frac{df_{0i}}{d\alpha_0} \ . \tag{A.9.8}$$

Similarly,

$$\frac{\partial^2 f_{0i}}{\partial {E_0}^2} = \left(\frac{dE_0}{d\alpha_0}\right)^{-1}\frac{d}{d\alpha_0}\left[\frac{1}{2E_{R0}}\frac{\cos^3\alpha_0}{\sin\alpha_0}\frac{df_{0i}}{d\alpha_0}\right]$$

$$= \frac{1}{4{E_{R0}}^2}\left[\left(\frac{\cos^6\alpha_0}{\sin^2\alpha_0}\right)\frac{d^2 f_{0i}}{d{\alpha_0}^2} - \left(3\frac{\cos^5\alpha_0}{\sin\alpha_0} + \frac{\cos^7\alpha_0}{\sin^3\alpha_0}\right)\frac{df_{0i}}{d\alpha_0}\right]. \quad \text{(A.9.9)}$$

The derivatives (A.9.3)-(A.9.5) may now be written for $E_{R0} = \overline{E_{R0}}$ as

$$\overline{\frac{\partial F_0}{\partial E_0}} = \frac{1}{2\overline{E_{R0}}}\sum_{i=1}^{I}\sin^{a_i-1}\alpha_0\cos^3\alpha_0\overline{\frac{df_{0i}}{d\alpha_0}} \quad \text{(A.9.10)}$$

$$\overline{\frac{\partial^2 F_0}{\partial {E_0}^2}} = \frac{1}{4\overline{E_{R0}}^2}\sum_{i=1}^{I}\left[\sin^{a_i-2}\alpha_0\cos^6\alpha_0\overline{\frac{d^2 f_{0i}}{d{\alpha_0}^2}}\right.$$
$$\left. - \left(3\sin^{a_i-1}\alpha_0\cos^5\alpha_0 + \sin^{a_i-3}\alpha_0\cos^7\alpha_0\right)\overline{\frac{df_{0i}}{d\alpha_0}}\right] \quad \text{(A.9.11)}$$

$$\overline{\frac{\partial^2 F_0}{\partial\alpha_0\partial E_0}} = \frac{1}{2\overline{E_{R0}}}\sum_{i=1}^{I}a_i\sin^{a_i-2}\alpha_0\cos^4\alpha_0\overline{\frac{df_{0i}}{d\alpha_0}}. \quad \text{(A.9.12)}$$

## A.10 EVALUATION OF $\overline{\overline{D}}$

Using (A.9.10), equation (A.8.6) is

$$\overline{\overline{D}} \simeq 2(1+b)\int_0^{\frac{\pi}{2}}\left\{\frac{\sin\alpha_0}{\cos^3\alpha_0}\overline{F_0} + V\sum_{i=1}^{I}\frac{\sin^{a_i}\alpha_0}{\cos^2\alpha_0}\overline{\frac{df_{0i}}{d\alpha_0}}\right\}d\alpha_0. \quad \text{(A.10.1)}$$

The second term can be integrated by parts to give

$$=2(1+b)V\sum_{i=1}^{I}\left\{\frac{\sin^{a_i}\alpha_0}{\cos^2\alpha_0}\overline{f_{0i}}\Bigg|_0^{\frac{\pi}{2}} - \int_0^{\frac{\pi}{2}}\left[a_i\frac{\sin^{a_i-1}\alpha_0}{\cos\alpha_0} + 2\frac{\sin^{a_i+1}\alpha_0}{\cos^3\alpha_0}\right]\overline{f_{0i}}d\alpha_0\right\}. \quad \text{(A.10.2)}$$

Using (A.9.1) and (A.9.2), this is

$$= 2(1+b)V\int_0^{\frac{\pi}{2}}\left\{-\frac{1}{\cos^2\alpha_0}\overline{\frac{\partial F_0}{\partial\alpha_0}} - 2\frac{\sin\alpha_0}{\cos^3\alpha_0}\overline{F_0}\right\}d\alpha_0. \quad \text{(A.10.3)}$$

Inserting this in (A.10.1) gives

$$\overline{\overline{D}} \simeq 2(1+b)\int_0^{\frac{\pi}{2}} \left\{(1-2V)\frac{\sin\alpha_0}{\cos^3\alpha_0}\overline{F_0} - \frac{V}{\cos^2\alpha_0}\overline{\frac{\partial F_0}{\partial\alpha_0}}\right\} d\alpha_0 \tag{A.10.4}$$

$$\simeq (1+b)\left[(1-2V)\overline{D} - 2V\int_0^{\frac{\pi}{2}} \frac{1}{\cos^2\alpha_0}\overline{\frac{\partial F_0}{\partial\alpha_0}} d\alpha_0\right] \tag{A.10.5}$$

## A.11 EVALUATION OF $\overline{\overline{N}}$

Using (A.9.10), (A.9.11), and (A.9.12), equation (A.8.5) is

$$\begin{aligned}\overline{\overline{N}} \simeq &(1+b)\int_0^{\frac{\pi}{2}} \left\{\left[\frac{\sin^2\alpha_0}{\cos^4\alpha_0} + b\frac{\sin^4\alpha_0}{\cos^4\alpha_0}\right]\overline{\frac{\partial F_0}{\partial\alpha_0}} - b\sum_{i=1}^{I}\left[\frac{\sin^{a_i+2}\alpha_0}{\cos^2\alpha_0}\right]\overline{\frac{df_{0i}}{d\alpha_0}}\right.\\ &+ V\sum_{i=1}^{I}\left[a_i\frac{\sin^{a_i}\alpha_0}{\cos^2\alpha_0} + a_i b\frac{\sin^{a_i+2}\alpha_0}{\cos^2\alpha_0}\right]\overline{\frac{df_{0i}}{d\alpha_0}} - bV\sum_{i=1}^{I}\left[\frac{\sin^{a_i+1}\alpha_0}{\cos\alpha_0}\right]\overline{\frac{d^2 f_{0i}}{d\alpha_0{}^2}}\\ &\left.+ bV\sum_{i=1}^{I}\left[3\frac{\sin^{a_i+2}\alpha_0}{\cos^2\alpha_0} + \sin^{a_i}\alpha_0\right]\overline{\frac{df_{0i}}{d\alpha_0}}\right\} d\alpha_0 \,.\end{aligned} \tag{A.11.1}$$

Collecting terms gives

$$\begin{aligned}\overline{\overline{N}} \simeq &(1+b)\int_0^{\frac{\pi}{2}} \left\{\left[\frac{\sin^2\alpha_0}{\cos^4\alpha_0} + b\frac{\sin^4\alpha_0}{\cos^4\alpha_0}\right]\overline{\frac{\partial F_0}{\partial\alpha_0}}\right.\\ &+ \sum_{i=1}^{I}\left[(-b)\frac{\sin^{a_i+2}\alpha_0}{\cos^2\alpha_0} + V(a_i+b)\frac{\sin^{a_i}\alpha_0}{\cos^2\alpha_0}\right]\overline{\frac{df_{0i}}{d\alpha_0}}\\ &\left.+ \sum_{i=1}^{I}\left[(-bV)\frac{\sin^{a_i+1}\alpha_0}{\cos\alpha_0}\right]\overline{\frac{d^2 f_{0i}}{d\alpha_0{}^2}}\right\} d\alpha_0 \,.\end{aligned} \tag{A.11.2}$$

The last term is

$$\begin{aligned}= &-bV(1+b)\sum_{i=1}^{I}\left\{\left[\frac{\sin^{a_i+1}\alpha_0}{\cos\alpha_0}\right]\overline{\frac{df_{0i}}{d\alpha_0}}\Bigg|_0^{\frac{\pi}{2}}\right.\\ &\left.- \int_0^{\frac{\pi}{2}}\left[(a_i+1)\sin^{a_i}\alpha_0 + \frac{\sin^{a_i+2}\alpha_0}{\cos^2\alpha_0}\right]\overline{\frac{df_{0i}}{d\alpha_0}} d\alpha_0\right\}.\end{aligned} \tag{A.11.3}$$

Substituting this in (A.11.2) gives

$$\overline{\overline{N}} \simeq (1+b)\int_0^{\frac{\pi}{2}} \left\{ \left[ \frac{\sin^2\alpha_0}{\cos^4\alpha_0} + b\frac{\sin^4\alpha_0}{\cos^4\alpha_0} \right] \overline{\frac{\partial F_0}{\partial \alpha_0}} + \sum_{i=1}^{I} \left[ (a_i V - b)\frac{\sin^{a_i}\alpha_0}{\cos^2\alpha_0} + b\sin^{a_i}\alpha_0 \right] \overline{\frac{df_{0i}}{d\alpha_0}} \right\} d\alpha_0 \,. \tag{A.11.4}$$

The last term can be integrated to give

$$\begin{aligned} =&(1+b)\sum_{i=1}^{I} \left\{ \left[ (a_i V - b)\frac{\sin^{a_i}\alpha_0}{\cos^2\alpha_0} + b\sin^{a_i}\alpha_0 \right] \overline{f_{0i}} \Bigg|_0^{\frac{\pi}{2}} \right. \\ &- \int_0^{\frac{\pi}{2}} \left[ a_i(a_i V - b)\frac{\sin^{a_i-1}\alpha_0}{\cos\alpha_0} \right. \\ &\left. \left. + \; 2(a_i V - b)\frac{\sin^{a_i+1}\alpha_0}{\cos^3\alpha_0} + a_i b\sin^{a_i-1}\alpha_0\cos\alpha_0 \right] \overline{f_{0i}} \right\} d\alpha_0 \,, \end{aligned} \tag{A.11.5}$$

which can be written

$$\begin{aligned} =&(1+b)\sum_{i=1}^{I}\int_0^{\frac{\pi}{2}} \left\{ -Va_i \left[ (a_i-1)\sin^{a_i-2}\alpha_0\cos^2\alpha_0 - \sin^{a_i}\alpha_0 \right] \frac{\sin\alpha_0}{\cos^3\alpha_0} \right. \\ &\left. + \; a_i \left[ (b-V)\frac{\sin^{a_i-1}\alpha_0}{\cos\alpha_0} - 3V\frac{\sin^{a_i+1}\alpha_0}{\cos^3\alpha_0} - b\sin^{a_i-1}\alpha_0\cos\alpha_0 \right] + 2b\frac{\sin^{a_i+1}\alpha_0}{\cos^3\alpha_0} \right\} \overline{f_{0i}} d\alpha_0 \,. \end{aligned} \tag{A.11.6}$$

Using (A.9.1) and (A.9.2), this is

$$\begin{aligned} =&(1+b)\int_0^{\frac{\pi}{2}} \left\{ \left[ -V\frac{\sin\alpha_0}{\cos^3\alpha_0} \right] \overline{\frac{\partial^2 F_0}{\partial {\alpha_0}^2}} \right. \\ &\left. + \left[ (b-V)\frac{1}{\cos^2\alpha_0} - 3V\frac{\sin^2\alpha_0}{\cos^4\alpha_0} - b \right] \overline{\frac{\partial F_0}{\partial \alpha_0}} + \left[ 2b\frac{\sin\alpha_0}{\cos^3\alpha_0} \right] \overline{F_0} \right\} d\alpha_0. \end{aligned} \tag{A.11.7}$$

Inserting (A.11.7) into (A.11.4) gives

$$\begin{aligned} \overline{\overline{N}} \simeq&(1+b)\int_0^{\frac{\pi}{2}} \left\{ \left[ (1-3V)\frac{\sin^2\alpha_0}{\cos^4\alpha_0} + b\frac{\sin^4\alpha_0}{\cos^4\alpha_0} + (b-V)\frac{1}{\cos^2\alpha_0} - b \right] \overline{\frac{\partial F_0}{\partial \alpha_0}} \right. \\ &\left. + \left[ 2b\frac{\sin\alpha_0}{\cos^3\alpha_0} \right] \overline{F_0} - \left[ V\frac{\sin\alpha_0}{\cos^3\alpha_0} \right] \overline{\frac{\partial^2 F_0}{\partial {\alpha_0}^2}} \right\} d\alpha_0 \,, \end{aligned} \tag{A.11.8}$$

which can be written as

$$\overline{\overline{N}} \simeq (1+b)\left[(1+b-3V)\overline{N} + b\overline{D} - V\int_0^{\frac{\pi}{2}} \frac{1}{\cos^2\alpha_0}\overline{\frac{\partial F_0}{\partial \alpha_0}}d\alpha_0 - V\int_0^{\frac{\pi}{2}} \frac{\sin\alpha_0}{\cos^3\alpha_0}\overline{\frac{\partial^2 F_0}{\partial {\alpha_0}^2}}d\alpha_0\right]. \tag{A.11.9}$$

## A.12 EVALUATION OF $A(\overline{\overline{E_R}})$

Using (A.10.5) and (A.11.19) and keeping terms only to first order, $A(\overline{\overline{E_R}})$ is

$$A(\overline{\overline{E_R}}) = \frac{\overline{\overline{N}}}{\overline{\overline{D}}} \simeq \frac{(1+b-3V)\overline{N} + b\overline{D} - V\int_0^{\frac{\pi}{2}} \frac{1}{\cos^2\alpha_0}\overline{\frac{\partial F_0}{\partial \alpha_0}}d\alpha_0 - V\int_0^{\frac{\pi}{2}} \frac{\sin\alpha_0}{\cos^3\alpha_0}\overline{\frac{\partial^2 F_0}{\partial {\alpha_0}^2}}d\alpha_0}{(1-2V)\overline{D} - 2V\int_0^{\frac{\pi}{2}} \frac{1}{\cos^2\alpha_0}\overline{\frac{\partial F_0}{\partial \alpha_0}}d\alpha_0}. \tag{A.12.1}$$

## A.13 EVALUATION OF $\eta(\overline{\overline{E_R}})$

The term $\eta(\overline{\overline{E_R}})$ from (A.1.2) can now be evaluated quite simply. Using (A.3.6), (A.6.4), (A.7.2), and (A.7.4),

$$\eta(\overline{\overline{E_R}}) = 2\pi\overline{v_{R0}}^3(1+V)^3(1+b)\left[(1-2V)\overline{D} - 2V\int_0^{\frac{\pi}{2}} \frac{1}{\cos^2\alpha_0}\overline{\frac{\partial F_0}{\partial \alpha_0}}d\alpha_0\right]. \tag{A.13.1}$$

## A.14 EVALUATION OF $\overline{\overline{A_c}}$

The critical anisotropy $\overline{\overline{A_c}}$ (A.1.4) is

$$\overline{\overline{A_c}} = \frac{\omega}{\omega_{H0}(1+b) - \omega} = (1-\Lambda)\overline{A_{c0}} \tag{A.14.1}$$

$$\text{where} \quad \Lambda = \frac{1}{(1+b) - \frac{\omega}{\omega_{H0}}}b. \tag{A.14.2}$$

## A.15 SMALL FREQUENCY APPROXIMATION

The relations $\omega_H << \omega_p$ and $\omega << \omega_H$ are assumed in the growth rate derivation given by *Kennel and Petschek* [1966] and can thus be used here. Keeping terms to leading order, the terms $N(b)$ (A.3.8), $V$ (A.3.11), and $\Lambda$ (A.14.2) are

$$N(b) \simeq -\frac{\omega}{\omega_{H0}} b \tag{A.15.1}$$

$$V \simeq b \tag{A.15.2}$$

$$\Lambda \simeq b\,. \tag{A.15.3}$$

Using these approximations, the anisotropy (A.14.2), the term $\overline{\overline{\eta}}$ (A.13.1), and the critical anisotropy (A.13.1) reduce to

$$\overline{\overline{A}} \simeq \frac{(1-2b)\overline{N} + b\overline{D} - b\int_0^{\frac{\pi}{2}} \frac{1}{\cos^2\alpha_0}\left[\overline{\frac{\partial F_0}{\partial \alpha_0}} - \frac{\sin\alpha_0}{\cos\alpha_0}\overline{\frac{\partial^2 F_0}{\partial {\alpha_0}^2}}\right] d\alpha_0}{(1-2b)\overline{D} - 2b\int_0^{\frac{\pi}{2}} \frac{1}{\cos^2\alpha_0}\overline{\frac{\partial F_0}{\partial \alpha_0}} d\alpha_0} \tag{A.15.4}$$

$$\overline{\overline{\eta}} \simeq 2\pi \overline{v_{R0}}^3 (1+4b)\left[(1-2b)\overline{D} - 2b\int_0^{\frac{\pi}{2}} \frac{1}{\cos^2\alpha_0}\overline{\frac{\partial F_0}{\partial \alpha_0}} d\alpha_0\right] \tag{A.15.5}$$

$$\overline{\overline{A_c}} \simeq (1-b)\overline{A_{c0}}\,. \tag{A.15.6}$$

The growth rate (A.1.1) can now be written

$$\gamma \simeq \pi\omega_{H0}\left(1 - \frac{\omega}{\omega_{H0}}\right)^2 (1+b)\overline{\overline{\eta}}\left[\overline{\overline{A}} - \overline{\overline{A_c}}\right]\,. \tag{A.15.7}$$

## A.16 SIMPLE EXAMPLE

The properties of the dynamic growth rate given in (A.15.7) are best illustrated by choosing a simple form for the distribution function and calculating the various terms.

For a distribution function of the form

$$F_0(\alpha_0, E_0) = E_0{}^{-m}\sin^a\alpha_0 \,, \tag{A.16.1}$$

the anisotropy (A.15.4) and the term $\overline{\overline{\eta}}$ (A.15.5) are

$$\overline{\overline{A}} \simeq (1+b)\overline{A_0} + b \tag{A.16.2}$$

$$\overline{\overline{\eta}} \simeq (1+b)(1-2mb)\overline{\eta_0} \,. \tag{A.16.2}$$

The growth rate (A.15.7) can thus be written

$$\gamma \simeq \pi\omega_{H0}\left(1-\frac{\omega}{\omega_{H0}}\right)^2 (1+b)^2(1-2mb)\overline{\eta_0}\left[(1+b)\overline{A_0}+b-(1-b)\overline{A_{c0}}\right] \tag{A.16.4}$$

which is

$$\gamma \simeq \gamma_0(1+2b)(1-2mb)\left[1+b\frac{\overline{A_0}+\overline{A_{c0}}+1}{\overline{A_0}-\overline{A_{c0}}}\right] \,, \tag{A.16.5}$$

where $\gamma_0$ is the unperturbed growth rate. For the general case where all the terms involving $b$ are small compared to 1, the growth rate may be written

$$\gamma \simeq \gamma_0(1+\beta b) \tag{A.16.6}$$

$$\text{where} \quad \beta = 2-2m+\frac{\overline{A_0}+\overline{A_{c0}}+1}{\overline{A_0}-\overline{A_{c0}}} \,. \tag{A.16.7}$$

For the particular case where $\overline{A_0} \simeq \overline{A_{c0}}$, the second term in brackets in (A.16.5) dominates the first and the growth rate is (assuming $2mb << 1$)

$$\gamma \simeq \beta b \,, \tag{A.16.8}$$

$$\text{where} \quad \beta = \gamma_0\frac{\overline{A_0}+\overline{A_{c0}}+1}{\overline{A_0}-\overline{A_{c0}}} \,. \tag{A.16.9}$$

Thus, for frequencies at which $\overline{A_0} \simeq \overline{A_{c0}}$, $\gamma$ is directly proportional to $b$.

# Appendix B
# FILTER METHODS

Digital filtering techniques were used to enhance much of the data presented in Chapter 3. The techniques and the effects of filter processing on the data are discussed below.

*Bandpass filters.* The data used for producing the spectral and amplitude plots in Figures 3.22-3.29 were digitized from broadband analog tapes using the Stanford VLF Adelie digitizing system (see Appendix D) and processed using a FFT algorithm on a VAX computer. Bandpass filtering was done in the frequency domain using the FFT data. The frequency resolution of the FFT data used in this study was 5-10 Hz. The bandpass filters utilyze unweighted averages over an integral number of $\Delta f$ pixels in order to provide the 50 Hz bandwidth used for the narrowband plots and the much larger bandwidths used for the total growth plots. The rolloff of the bandpass filters is comparable to the rolloff introduced by the windowing of the FFT data.

*Low/high pass filters.* The low and high pass filters are simple non-recursive filters [e.g., *Hamming*, 1983] incorporating Hamming windows. Frequency response plots for each of the filters are shown in Figure B.1. Low pass filtering was used for smoothing the wave amplitudes shown in Figures 3.22-3.29 and the data in the riometer plots (Figures 3.31-3.35). The filters used for the amplitude plots have a cutoff frequency of 125 mHz and a two-sided width of 16 sec (as indicated at the top corner of each plot). The filters used for the riometer plots have a cutoff frequency of 100 mHz and a two-sided width of 20 sec. High pass filtering was used to emphasize the amplitude

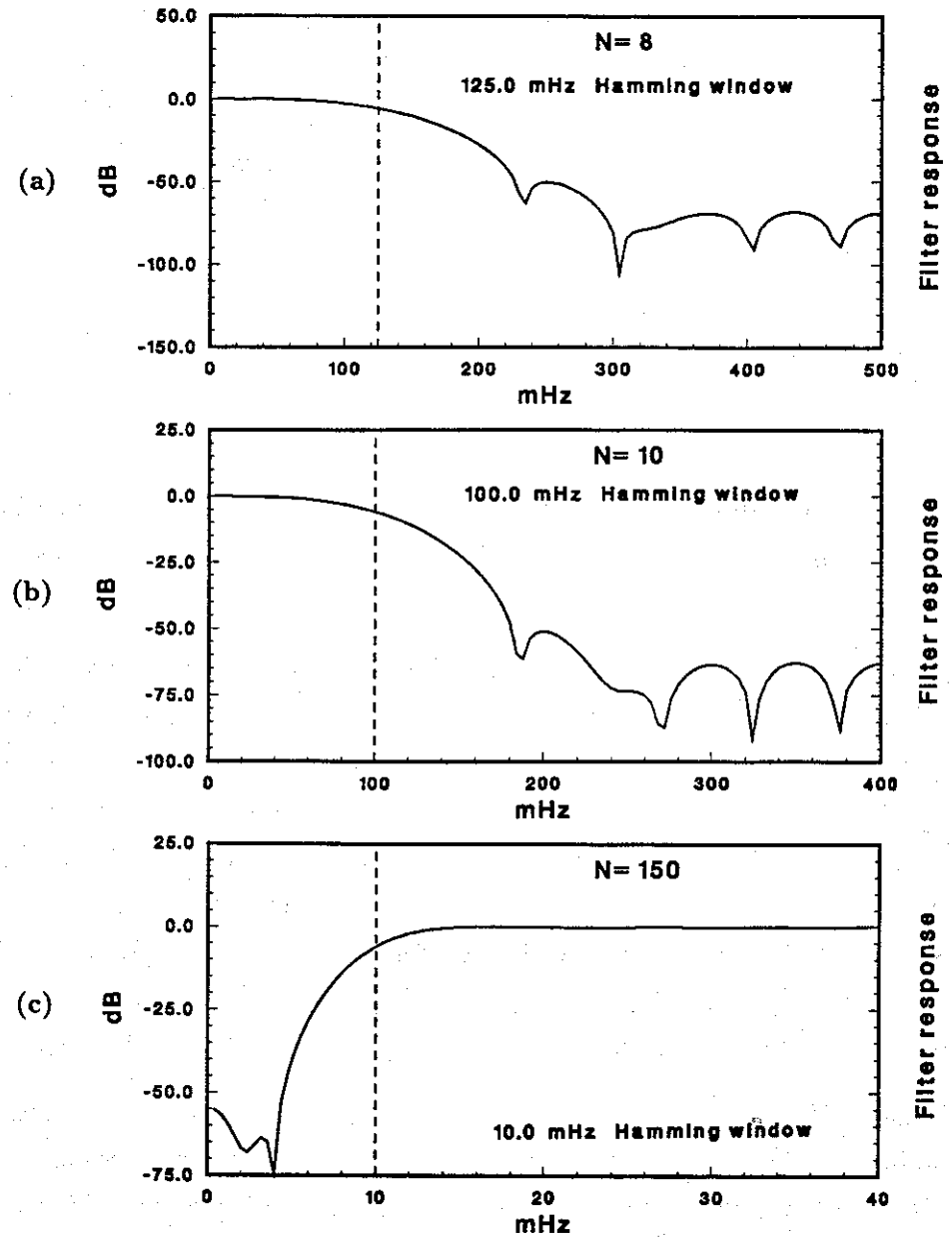


**Figure B.1.** Frequency response of filters used for data analysis. (a) Low pass filter used for smoothing wave amplitudes in Figures 3.22-3.29. (b) Low pass filter used for processing riometer, magnetometer, and ELF/VLF amplitudes in 3.31-3.35 (c) High pass filter used for emphasizing wave amplitude oscillations in Figures 3.11-3.15.

oscillations illustrated in Figures 3.11-3.15. The filters have a cutoff frequency of 10 mHz and and a two-sided width of 300 sec. The large width of the high-pass filters was necessary in order to pass the 60-90 sec oscillations while rejecting the slightly longer periods associated with the transient enhancement. One consequence of the large width is the anomalous amplitude drop that can be seen just prior to the wave growth onset in each figure. The spectral characteristics of the data were not stationary; the amplitude output of the filter is thus suspect during periods where the spectral characteristics change over time scales shorter than the half-width of the filter. The identification of the oscillation period and damping rate is not sensitive to this effect, however.

*Sferic filters.* The sferic filter is a non-standard filter designed to remove the contribution of sferics, which are not of interest in this work, from the total wave amplitude. Sferics cause particular problems when doing low pass filtering of the data, as was done in Figures 3.22-3.29, since their relatively high amplitudes can result in significant contributions to the amplitude at times differing by as much as the half-width of the filter from the occurence time of the sferic. The data used for filtering were the frequency domain data of the FFT output (described above). The filter technique is based on the known properties of the spectrum, namely that sferics are of very short duration and are generally observed over a bandwidth larger than the bandwidth of the magnetospheric wave activity. A band was identified in which sferics were observed but no other wave activity was present. An amplitude plot of this band was generated and a threshold amplitude was identified above which activity indicated the presence of a sferic. Points thus identified as corresponding to sferics were removed and replaced by the arithmetic mean of points at times on either side of the removed point. The threshold level was chosen so that the points removed represented less than a few percent of the total data. The frequency response characteristics of such an interpolation technique are comparable to or better than the characteristics of the low pass filter used subsequently [e.g., *Hamming*, 1983], so the data loss is negligible.

# Appendix C

# MAGNETIC FIELD MODELS

A number of magnetic field models have been developed which attempt to reproduce the field configuration within the magnetosphere. Complete field models include separate descriptions for the internal field of the Earth and the field due to magnetospheric current systems. At geocentric distances greater than a few thousand km the nondipolar contributions of the internal field can be ignored and the magnetic field can be described as a superposition of the internal dipole field and the external fields. Reviews of available external field models are given in *Roederer* [1969], *Walker* [1976], *Olson* [1979], and *Walker* [1983].

*General description.* The most commonly used external field models are *boundary surface models* and *empirical models.* Boundary surface models begin with an initial determination of the magnetopause location based on an evaluation of the pressure balance at the magnetopause boundary [*Beard*, 1960; *Mead and Beard*, 1964; *Olson*, 1969]. The corresponding currents on the magnetopause are determined by requiring that the normal component of the magnetic field vanish at the boundary. The magnetic field at any point is then calculated from the Biot-Savart law by doing a surface integral over the magnetopause [*Mead*, 1964; *Choe and Beard*, 1974a]. Typically, terms to account for a cross-tail current [*Williams and Mead*, 1965; *Choe and Beard*, 1974b] as well as a ring current [*Olson and Pfitzer*, 1974] are also added to the contribution of the surface field. Empirical models [*Mead and Fairfield*, 1975; *Tsyganenko and Usmanov*, 1982] are based on a best fit of a set of parameters, chosen

to describe the physical current systems, to actual spacecraft measurements of the magnetic field.

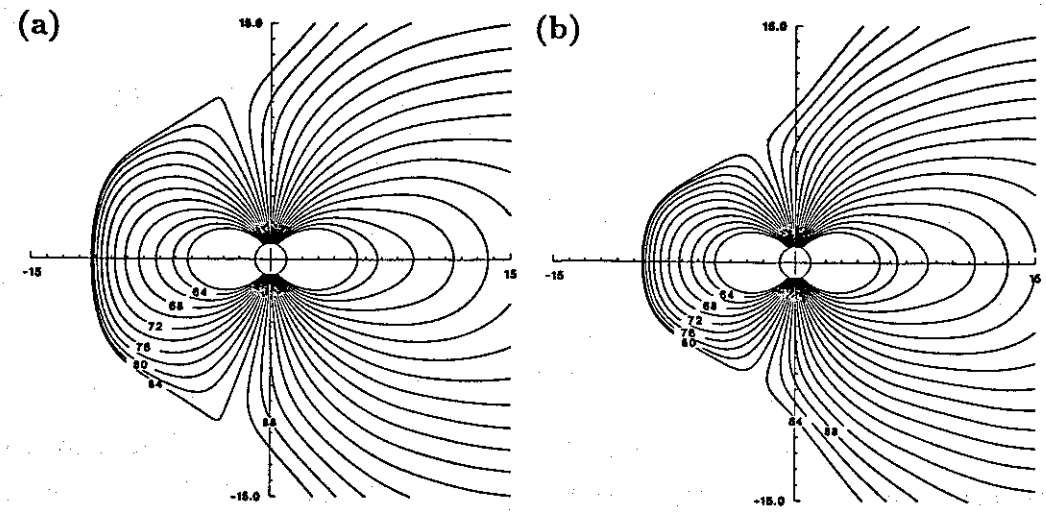


**Figure C.1.** The magnetic field configuration based on the Olson-Pfitzer sixth order field model. (a) $R_s$=10.5 $R_e$ (b) $R_s$=8.0 $R_e$. Field lines that cross the equatorial plane at distances greater than the given values of $R_s$ are not properly modeled. The last closed field line in the standard model is $\Lambda = 77°$.

*The Olson-Pfitzer model.* The Olson-Pfitzer model was used in this thesis for calculations since it is a commonly used model and provides the best means for simulating the magnetic field changes associated with a SC. The model is a boundary surface model which uses an analytic representation of the field in the form of a polynomial series based on an evaluation of the quiet-time current systems developed by *Olson* [1974]. Formulas are given for performing calculations using terms to either second or sixth order. A scaling technique was introduced by *Olson and Pfitzer* [1982] which allows the strengths of the surface, ring, and tail currents to be varied so as to simulate dynamic changes in the magnetosphere. The surface current strength is described in terms of the magnetopause standoff distance ($R_s$) while the ring and tail currents are characterized by the geophysical indices $D_{st}$ and $\epsilon$. The original 1974 model corresponds to values of $R_s$=10.5 $R_e$ and $D_{st}$=0. The field line configuration for $D_{st}$=0 and standoff distances of $R_s$=10.5 and $R_s$=8.0 based on the sixth order model are

shown in Figure C.1.

*Field model for SC.* In order to simulate the inward motion of the magnetopause during a SC, the value of $R_s$ was decreased as a function of time, a technique that Olson and Pfitzer described in their 1982 paper. The ring current strength and the tail current strength were held constant at their quiet-time values. The dynamic model describes the magnetospheric configuration at any given time as a simple scaled version of the quiet-time configuration and does not include boundary distortions corresponding to the propagation of the disturbance along the magnetopause. The finite propagation time of the disturbance was included in our model by using a different value of the standoff distance to calculate the field at each point in the magnetosphere. The standoff distance used corresponded to the value of the standoff distance $t$ seconds prior to the observation, where $t = d/v_A$ ($v_A$ was taken to be 1000 km/sec and $d$ is the distance from the subsolar magnetopause to the observation point). For example, at R=5 $R_e$ near noon, the standoff distance was kept at 10.5 $R_e$ for the first 35 seconds of the SC. The resulting delay of the SC onset at any given location is evident in Figures 5.1-5.7.

# Appendix D
# COMPUTER CODES

Several computer programs were written to facilitate the data analysis and modeling presented in this thesis. All programs were written in FORTRAN and executed on a Digital Equipment Corporation VAX 11/780 computer belonging to STAR Laboratory at Stanford University. Plotting was done using the DISSPLA graphics package.

*UMD data analysis program.* The plotting and analysis routines for the University of Maryland digital data were based on a core program written by Dan Detrick of University of Maryland for reading the UMD data tapes. The program was adapted to run on a VAX using input from disk and modified to provide filtering and plotting capabilities.

*Spectrogram plotting and analysis programs.* Programs for plotting spectrograms and narrowband analysis of wave data were designed to utilyze the Adelie digitizing system developed in the Stanford VLF Group by Bill Burgess. Data were digitized from broadband analog tapes using the Adelie system and processed with a FFT routine on the VAX computer. The spectrogram plotting program provides a direct graphical representation of the FFT output. The narrowband analysis program provides narrowband amplitudes by averaging the amplitude over a band of $\Delta f$ pixels as a function of time. The amplitudes can be filtered to eliminate sferics and the time series output can be either high or low passed. The two programs were intended to complement each other; the plot pairs shown in Chapter 3 were plotted to the same scale and referenced to the same 0 dB level to facilitate comparison.

*Magnetic field modeling program.* A comprehensive magnetic field modeling program was developed in order to provide analysis capabilities in a realistic magnetosphere and to facilitate analysis of the nonlinear parameters during a SC. The program includes options for doing calculations using dipole, Olson-Pfitzer second and sixth order [*Olson and Pfitzer*, 1974; *Olson and Pfitzer*, 1982], and Tsyganenko-Usmanov [*Tsyganenko and Usmanov*, 1982] field models. The code for the Tsyganenko-Usmanov model was written by Dr. David Stern of Goddard Space Flight Center. Standard parameters such as gyrofrequency and field line footprint can be calculated for any location. The nonlinear parameters can be plotted as a function of a number of variables including frequency, radial position, and local time. The simulation of changes in the nonlinear parameters is based on the procedure discussed in Chapter 5.

# Appendix E

# LIST OF EVENTS

| Table Entries | | |
|---|---|---|
| | X | Activity observed |
| | O | Activity not observed |
| | M | Activity observed in magnetometer only |
| | U | Activity observation uncertain |
| | T | Siple transmitter in operation |
| | N | Data not available |
| | A | Magnetic perturbation in AFGL chain |
| | J | Journal or published lists |
| | P | South Pole |
| | S | Siple |

| DATE | | | | | GROUND | | |
|---|---|---|---|---|---|---|---|
| YR | MON | DD | UT | DAY | J | P | S |
| 77 | JAN | 28 | 1840 | 28 | X | N | U |
| 77 | MAR | 27 | 0607 | 86 | X | N | O |
| 77 | APR | 2 | 2158 | 92 | X | N | X |
| 77 | APR | 19 | 0107 | 109 | X | N | N |
| 77 | MAY | 4 | 0417 | 124 | X | N | X |
| 77 | MAY | 28 | 0424 | 148 | X | N | O |
| 77 | JUL | 6 | 1037 | 187 | X | N | U |
| 77 | JUL | 29 | 0027 | 210 | X | N | M |
| 77 | AUG | 9 | 1358 | 221 | X | N | O |
| 77 | SEP | 12 | 2114 | 255 | X | N | X |
| 77 | SEP | 19 | 1144 | 262 | X | N | N |
| 77 | SEP | 21 | 2044 | 264 | X | N | X |
| 77 | OCT | 3 | 1246 | 276 | X | N | X |
| 77 | OCT | 14 | 1151 | 287 | X | N | N |
| 77 | OCT | 26 | 2330 | 299 | X | N | U |
| 77 | NOV | 10 | 1309 | 314 | X | N | O |
| 77 | NOV | 25 | 1226 | 329 | X | N | O |
| 77 | NOV | 26 | 1215 | 330 | X | N | M |
| 77 | NOV | 26 | 1714 | 330 | X | N | X |

| DATE | | | | | GROUND | | |
|---|---|---|---|---|---|---|---|
| YR | MON | DD | UT | DAY | J | P | S |
| 78 | JAN | 3 | 2042 | 3 | X | N | M |
| 78 | JAN | 5 | 1628 | 5 | X | N | X |
| 78 | JAN | 9 | 1625 | 9 | X | N | X |
| 78 | JAN | 25 | 1537 | 25 | X | N | X |
| 78 | JAN | 28 | 1853 | 28 | X | N | O |
| 78 | FEB | 14 | 2147 | 45 | X | N | X |
| 78 | FEB | 25 | 1928 | 56 | X | N | X |
| 78 | MAR | 8 | 1439 | 67 | X | N | X |
| 78 | APR | 10 | 1306 | 100 | X | N | X |
| 78 | APR | 13 | 1925 | 103 | X | N | X |
| 78 | APR | 17 | 2345 | 107 | X | N | M |
| 78 | APR | 30 | 0951 | 120 | X | N | X |
| 78 | MAY | 1 | 0828 | 121 | X | N | M |
| 78 | MAY | 1 | 1835 | 121 | X | N | X |
| 78 | MAY | 2 | 2318 | 122 | X | N | O |
| 78 | MAY | 10 | 2005 | 130 | X | N | U |
| 78 | MAY | 29 | 1831 | 149 | X | N | X |
| 78 | JUN | 1 | 2143 | 152 | X | N | X |
| 78 | JUN | 2 | 0913 | 153 | X | N | X |
| 78 | JUN | 4 | 1211 | 155 | X | N | X |
| 78 | JUN | 10 | 0828 | 161 | X | N | O |
| 78 | JUN | 25 | 0825 | 176 | X | N | X |
| 78 | JUN | 29 | 0951 | 180 | X | N | X |
| 78 | JUL | 3 | 2305 | 184 | X | N | N |
| 78 | JUL | 13 | 0015 | 194 | X | N | U |
| 78 | JUL | 13 | 2328 | 194 | X | N | M |
| 78 | AUG | 18 | 1242 | 230 | X | N | U |
| 78 | AUG | 27 | 0246 | 239 | X | N | X |
| 78 | SEP | 5 | 1859 | 248 | X | N | T |
| 78 | SEP | 9 | 0254 | 252 | X | N | X |
| 78 | SEP | 11 | 0900 | 254 | X | N | X |
| 78 | SEP | 25 | 0718 | 268 | X | N | M |
| 78 | SEP | 29 | 0301 | 272 | X | N | X |
| 78 | OCT | 4 | 0047 | 277 | X | N | X |
| 78 | OCT | 9 | 0322 | 282 | X | N | |
| 78 | OCT | 17 | 0430 | 290 | X | N | |
| 78 | OCT | 29 | 1116 | 302 | X | N | |
| 78 | NOV | 12 | 0100 | 316 | X | N | |
| 78 | NOV | 19 | 2320 | 323 | X | N | |
| 78 | DEC | 14 | 0127 | 348 | X | N | |

| DATE | | | | | GROUND | | |
|---|---|---|---|---|---|---|---|
| YR | MON | DD | UT | DAY | J | P | S |
| 79 | JAN | 4 | 1725 | 4 | X | N | |
| 79 | JAN | 6 | 2331 | 6 | X | N | |
| 79 | JAN | 7 | 13 | 7 | X | N | |
| 79 | JAN | 9 | 0340 | 9 | X | N | |
| 79 | JAN | 25 | 0139 | 25 | X | N | N |
| 79 | FEB | 3 | 1823 | 34 | X | N | N |
| 79 | FEB | 11 | 0148 | 42 | X | N | N |
| 79 | FEB | 18 | 0305 | 49 | X | N | M |
| 79 | FEB | 21 | 0302 | 52 | X | N | M |
| 79 | FEB | 21 | 1551 | 52 | X | N | T |
| 79 | FEB | 22 | 1946 | 53 | O | N | X |
| 79 | FEB | 22 | 2116 | 53 | X | N | X |
| 79 | MAR | 4 | 0446 | 63 | X | N | O |
| 79 | MAR | 6 | 0818 | 65 | X | N | M |
| 79 | MAR | 9 | 0808 | 68 | X | N | M |
| 79 | MAR | 9 | 2318 | 68 | A | N | X |
| 79 | MAR | 15 | 0556 | 74 | X | N | M |
| 79 | MAR | 17 | 0231 | 76 | X | N | M |
| 79 | MAR | 22 | 0826 | 81 | X | N | X |
| 79 | MAR | 25 | 0508 | 84 | A | N | X |
| 79 | MAR | 28 | 0220 | 87 | A | N | X |
| 79 | MAR | 28 | 0827 | 87 | X | N | M |
| 79 | APR | 1 | 2150 | 90 | X | N | X |
| 79 | APR | 3 | 1001 | 93 | X | N | X |
| 79 | APR | 5 | 0156 | 95 | X | N | X |
| 79 | APR | 5 | 13 | 95 | X | N | N |
| 79 | APR | 19 | 0351 | 109 | N | N | T |
| 79 | APR | 24 | 2358 | 114 | X | N | M |
| 79 | APR | 28 | 0333 | 118 | A | N | T |
| 79 | MAY | 26 | 0103 | 146 | A | N | X |
| 79 | MAY | 27 | 0110 | 147 | O | N | X |
| 79 | MAY | 28 | 18 | 148 | X | N | |
| 79 | MAY | 29 | 1850 | 149 | X | N | |
| 79 | MAY | 29 | 2058 | 149 | X | N | X |
| 79 | MAY | 31 | 0930 | 151 | X | N | X |
| 79 | JUN | 6 | 1927 | 157 | X | N | X |
| 79 | JUL | 6 | 1930 | 187 | X | N | X |
| 79 | JUL | 12 | 1240 | 193 | X | N | T |
| 79 | JUL | 26 | 1832 | 207 | X | N | X |
| 79 | JUL | 27 | 0238 | 208 | O | N | T |
| 79 | JUL | 28 | 2101 | 209 | X | N | T |
| 79 | AUG | 1 | 1146 | 213 | X | N | T |
| 79 | AUG | 11 | 1812 | 223 | X | N | M |
| 79 | AUG | 12 | 0502 | 224 | A | N | U |
| 79 | AUG | 13 | 0611 | 225 | X | N | O |
| 79 | AUG | 13 | 0639 | 225 | X | N | M |
| 79 | AUG | 20 | 0625 | 232 | X | N | T |
| 79 | AUG | 23 | 0157 | 235 | O | N | X |
| 79 | AUG | 29 | 0459 | 241 | X | N | |
| 79 | OCT | 6 | 1120 | 279 | X | N | X |
| 79 | NOV | 7 | 1347 | 311 | X | N | M |
| 79 | NOV | 9 | 1203 | 313 | X | N | O |
| 79 | NOV | 11 | 0225 | 315 | X | N | M |
| 79 | NOV | 13 | 0624 | 317 | O | N | X |
| 79 | NOV | 18 | 0210 | 322 | X | N | X |
| 79 | NOV | 29 | 1648 | 333 | X | N | X |
| 79 | NOV | 30 | 0738 | 334 | X | N | O |
| 79 | NOV | 30 | 1617 | 334 | O | N | X |
| 79 | DEC | 30 | 07 | 364 | X | N | |

| DATE | | | | | GROUND | | |
|---|---|---|---|---|---|---|---|
| YR | MON | DD | UT | DAY | J | P | S |
| 80 | JAN | 11 | 0757 | 11 | X | N | M |
| 80 | JAN | 13 | 0510 | 13 | X | N | X |
| 80 | JAN | 17 | 0512 | 17 | X | N | X |
| 80 | JAN | 25 | 1109 | 25 | X | N | M |
| 80 | JAN | 28 | 1543 | 28 | X | N | X |
| 80 | FEB | 6 | 0320 | 37 | X | N | M |
| 80 | FEB | 6 | 0847 | 37 | O | N | X |
| 80 | FEB | 7 | 1218 | 38 | X | N | M |
| 80 | FEB | 14 | 0309 | 45 | X | N | U |
| 80 | FEB | 15 | 1235 | 46 | X | N | M |
| 80 | FEB | 16 | 1120 | 47 | O | N | X |
| 80 | FEB | 25 | 1429 | 56 | X | N | M |
| 80 | MAR | 18 | 0518 | 78 | A | N | X |
| 80 | MAR | 19 | 0617 | 79 | X | N | |
| 80 | MAR | 26 | 1029 | 86 | A | N | X |
| 80 | MAR | 30 | 2354 | 90 | X | N | X |
| 80 | MAR | 31 | 1749 | 91 | X | N | U |
| 80 | APR | 2 | 2112 | 93 | X | N | |
| 80 | APR | 5 | 14 | 96 | X | N | |
| 80 | APR | 6 | 1059 | 97 | X | N | X |
| 80 | APR | 7 | 1212 | 98 | X | N | |
| 80 | APR | 8 | 2336 | 99 | X | N | |
| 80 | APR | 9 | 0508 | 100 | X | N | |
| 80 | APR | 22 | 0037 | 113 | X | N | |
| 80 | MAY | 7 | 0802 | 128 | X | N | |
| 80 | MAY | 29 | 1833 | 150 | X | N | T |
| 80 | MAY | 31 | 2137 | 152 | X | N | |
| 80 | JUN | 6 | 2236 | 158 | X | N | X |
| 80 | JUN | 7 | 1604 | 159 | O | N | X |
| 80 | JUN | 10 | 1627 | 162 | X | N | X |
| 80 | JUN | 24 | 0248 | 176 | X | N | X |
| 80 | JUN | 26 | 0129 | 178 | X | N | |
| 80 | JUL | 8 | 2114 | 190 | O | N | T |
| 80 | JUL | 17 | 1936 | 199 | X | N | |
| 80 | JUL | 18 | 1927 | 200 | X | N | X |
| 80 | JUL | 25 | 1111 | 207 | X | N | X |
| 80 | AUG | 6 | 0010 | 219 | X | N | |
| 80 | AUG | 6 | 0152 | 219 | O | N | T |
| 80 | AUG | 6 | 1332 | 219 | X | N | X |
| 80 | AUG | 11 | 1656 | 224 | X | N | |
| 80 | AUG | 16 | 1240 | 229 | X | N | X |
| 80 | AUG | 17 | 13 | 230 | X | N | |
| 80 | AUG | 19 | 0145 | 232 | A | N | X |
| 80 | AUG | 19 | 1024 | 232 | X | N | X |
| 80 | AUG | 21 | 0316 | 234 | N | N | X |
| 80 | SEP | 20 | 0139 | 264 | X | N | T |
| 80 | OCT | 14 | 1953 | 288 | X | N | X |
| 80 | OCT | 18 | 0114 | 292 | X | N | |
| 80 | OCT | 18 | 1627 | 292 | A | N | X |
| 80 | OCT | 23 | 09 | 297 | X | N | |
| 80 | OCT | 23 | 1750 | 297 | O | N | X |
| 80 | OCT | 23 | 1908 | 297 | A | N | X |
| 80 | OCT | 30 | 1520 | 304 | X | N | |
| 80 | NOV | 9 | 1122 | 314 | X | N | T |
| 80 | NOV | 14 | 1153 | 319 | X | N | |
| 80 | NOV | 19 | 2125 | 324 | X | N | |
| 80 | NOV | 24 | 2258 | 329 | X | N | |
| 80 | NOV | 26 | 0421 | 331 | X | N | |
| 80 | DEC | 11 | 1009 | 346 | X | N | |
| 80 | DEC | 12 | 1820 | 347 | A | N | X |
| 80 | DEC | 12 | 1944 | 347 | A | N | X |
| 80 | DEC | 18 | 0611 | 353 | X | N | |
| 80 | DEC | 19 | 0456 | 354 | X | N | |
| 80 | DEC | 20 | 2026 | 355 | A | N | X |
| 80 | DEC | 25 | 0552 | 360 | X | N | |
| 80 | DEC | 30 | 0738 | 365 | X | N | |

| DATE | | | | | GROUND | | |
|---|---|---|---|---|---|---|---|
| YR | MON | DD | UT | DAY | J | P | S |
| 81 | JAN | 29 | 0646 | 029 | X | X | N |
| 81 | FEB | 6 | 0847 | | X | X | N |
| 81 | FEB | 8 | 1345 | | A | X | N |
| 81 | FEB | 19 | 1705 | | A | X | N |
| 81 | FEB | 23 | 2139 | | X | X | N |
| 81 | MAR | 6 | 0855 | | A | X | N |
| 81 | MAR | 6 | 1229 | | A | X | N |
| 81 | MAR | 25 | 1748 | | A | X | N |
| 81 | MAR | 31 | 1717 | | A | X | N |
| 81 | APR | 4 | 1627 | | A | X | N |
| 81 | APR | 4 | 1637 | | A | X | N |
| 81 | APR | 7 | 1954 | | A | X | N |
| 81 | APR | 15 | 1334 | | A | X | N |
| 81 | APR | 18 | 1502 | | A | X | N |
| 81 | JUN | 6 | 0946 | | X | X | N |
| 81 | JUN | 7 | 0823 | | X | X | N |
| 81 | JUN | 29 | 0610 | | X | O | N |
| 81 | JUL | 17 | 0802 | | X | M | N |
| 81 | JUL | 23 | 0646 | | X | M | N |
| 81 | JUL | 25 | 0514 | | X | O | N |
| 81 | JUL | 25 | 1322 | | X | M | N |
| 81 | AUG | 10 | 0434 | | X | M | N |
| 81 | AUG | 12 | 1602 | | A | X | N |
| 81 | AUG | 14 | 1312 | | A | X | N |
| 81 | AUG | 14 | 1403 | | A | X | N |
| 81 | AUG | 17 | 0045 | | X | X | N |
| 81 | AUG | 23 | 1257 | | X | M | N |
| 81 | AUG | 30 | 2222 | | X | O | N |
| 81 | SEP | 8 | 2146 | | X | X | N |
| 81 | SEP | 18 | 1912 | | X | X | N |
| 81 | SEP | 19 | 0137 | 262 | X | O | N |
| 81 | OCT | 2 | 2021 | 275 | A | X | N |
| 81 | OCT | 10 | 1433 | 283 | A | X | N |
| 81 | OCT | 11 | 2202 | 284 | A | X | N |
| 81 | OCT | 13 | 2240 | 286 | X | O | N |
| 81 | OCT | 22 | 0525 | 295 | X | O | N |
| 81 | NOV | 3 | 1520 | 307 | O | X | N |
| 81 | NOV | 8 | 1618 | 312 | X | X | N |
| 81 | NOV | 11 | 1238 | 315 | A | X | N |
| 81 | NOV | 12 | 1649 | 316 | A | X | N |
| 81 | NOV | 14 | 0535 | 318 | X | O | N |
| 81 | NOV | 16 | 2028 | 320 | A | X | N |
| 81 | NOV | 25 | 0929 | 329 | X | O | N |
| 81 | DEC | 7 | 2126 | 341 | X | X | N |
| 81 | DEC | 12 | 0144 | 346 | X | M | N |
| 81 | DEC | 29 | 0455 | 363 | X | O | M |
| 81 | DEC | 31 | 0207 | 365 | X | M | X |

| DATE | | | | | GROUND | | |
|---|---|---|---|---|---|---|---|
| YR | MON | DD | UT | DAY | J | P | S |
| 82 | JAN | 6 | 1705 | 6 | N | X | X |
| 82 | JAN | 21 | 1402 | 21 | O | X | M |
| 82 | JAN | 21 | 1516 | 21 | X | X | X |
| 82 | JAN | 21 | 1617 | 21 | A | X | X |
| 82 | JAN | 21 | 1731 | 21 | X | O | O |
| 82 | JAN | 29 | 1744 | 29 | X | X | M |
| 82 | JAN | 31 | 0102 | 31 | X | O | X |
| 82 | FEB | 1 | 1100 | 32 | X | X | X |
| 82 | FEB | 3 | 0129 | 34 | X | M | X |
| 82 | FEB | 5 | 1611 | 36 | X | X | X |
| 82 | FEB | 11 | 1313 | 42 | X | X | X |
| 82 | FEB | 11 | 1402 | 42 | O | O | X |
| 82 | FEB | 11 | 1529 | 42 | O | O | X |
| 82 | FEB | 17 | 0604 | 48 | A | O | X |
| 82 | FEB | 21 | 0727 | 52 | X | M | M |
| 82 | FEB | 21 | 2018 | 52 | O | M | X |
| 82 | FEB | 22 | 1545 | 53 | A | M | X |
| 82 | FEB | 22 | 1625 | 53 | O | O | X |
| 82 | FEB | 22 | 1725 | 53 | A | O | X |
| 82 | MAR | 1 | 0447 | 60 | A | O | X |
| 82 | MAR | 1 | 1138 | 60 | X | X | X |
| 82 | MAR | 4 | 0741 | 63 | A | O | X |
| 82 | MAR | 4 | 1442 | 63 | O | X | X |
| 82 | MAR | 4 | 1450 | 63 | O | X | X |
| 82 | MAR | 8 | 0005 | 67 | O | N | X |
| 82 | MAR | 18 | 1325 | 77 | O | X | X |
| 82 | MAR | 22 | 1009 | 81 | O | M | X |
| 82 | APR | 1 | 1305 | 91 | X | X | X |
| 82 | APR | 8 | 0542 | 98 | O | O | X |
| 82 | APR | 11 | 0044 | 101 | A | O | X |
| 82 | APR | 13 | 0108 | 103 | O | X | X |
| 82 | APR | 13 | 0219 | 103 | A | O | X |
| 82 | APR | 16 | 0430 | 106 | O | O | X |
| 82 | APR | 16 | 1702 | 106 | X | X | X |
| 82 | APR | 24 | 2016 | 114 | X | X | X |
| 82 | APR | 28 | 1632 | 118 | O | O | X |
| 82 | MAY | 4 | 0644 | 124 | A | X | X |
| 82 | JUN | 2 | 1500 | 153 | A | X | X |
| 82 | JUN | 2 | 1522 | 153 | N | X | X |
| 82 | JUN | 6 | 0244 | 157 | X | M | M |
| 82 | JUN | 9 | 0040 | 160 | X | M | X |
| 82 | JUN | 12 | 1443 | 163 | X | X | X |
| 82 | JUL | 11 | 0953 | 192 | X | O | X |
| 82 | JUL | 13 | 1617 | 194 | X | M | T |
| 82 | JUL | 16 | 1519 | 197 | X | X | T |
| 82 | JUL | 16 | 2108 | 197 | A | X | T |
| 82 | JUL | 30 | 1422 | 211 | X | X | X |
| 82 | AUG | 1 | 0423 | 213 | N | O | X |
| 82 | AUG | 5 | 2039 | 217 | O | X | X |
| 82 | AUG | 5 | 2047 | 217 | O | | X |
| 82 | AUG | 6 | 1836 | 218 | X | X | X |
| 82 | AUG | 11 | 0214 | 223 | O | O | X |
| 82 | AUG | 23 | 1520 | 235 | O | X | X |
| 82 | AUG | 24 | 1207 | 236 | O | X | X |
| 82 | SEP | 5 | 2250 | 248 | X | X | X |
| 82 | SEP | 6 | 0753 | 249 | X | M | U |
| 82 | SEP | 9 | 0105 | 252 | X | M | U |
| 82 | SEP | 21 | 0339 | 264 | X | M | X |
| 82 | SEP | 24 | 0945 | 267 | X | X | X |
| 82 | SEP | 25 | 1703 | 268 | X | X | X |
| 82 | SEP | 25 | 2030 | 268 | X | M | X |
| 82 | SEP | 26 | 1033 | 269 | O | O | O |
| 82 | OCT | 26 | 0029 | 299 | X | M | X |
| 82 | OCT | 31 | 1338 | 304 | X | X | X |
| 82 | NOV | 17 | 1410 | 321 | O | X | O |
| 82 | NOV | 17 | 1439 | 321 | A | X | O |
| 82 | NOV | 17 | 1513 | 321 | A | X | N |
| 82 | NOV | 17 | 1529 | 321 | N | X | N |
| 82 | NOV | 20 | 1841 | 324 | X | X | U |
| 82 | NOV | 23 | 0917 | 327 | X | X | X |
| 82 | NOV | 24 | 0922 | 328 | X | X | X |
| 82 | NOV | 30 | 1211 | 334 | X | X | U |
| 82 | DEC | 7 | 0329 | 341 | X | X | X |
| 82 | DEC | 7 | 1912 | 341 | A | M | X |
| 82 | DEC | 10 | 0721 | 344 | X | O | M |
| 82 | DEC | 10 | 0822 | 344 | A | M | X |
| 82 | DEC | 10 | 1412 | 344 | A | X | X |
| 82 | DEC | 17 | 0806 | 351 | X | M | U |
| 82 | DEC | 17 | 1837 | 351 | A | N | X |
| 82 | DEC | 17 | 2102 | 351 | O | N | X |
| 82 | DEC | 17 | 2126 | 351 | O | N | X |
| 82 | DEC | 18 | 1341 | 352 | A | M | X |
| 82 | DEC | 18 | 1527 | 352 | A | O | X |
| 82 | DEC | 18 | 1533 | 352 | A | O | X |

| | | | | | | | |
|---|---|---|---|---|---|---|---|
| 82 | DEC | 18 | 1812 | 352 | A | O | X |
| 82 | DEC | 19 | 0254 | 353 | X | X | X |
| 82 | DEC | 19 | 2220 | 353 | N | M | X |
| 82 | DEC | 27 | 0715 | 361 | X | M | M |

| DATE | | | | | GROUND | | |
|---|---|---|---|---|---|---|---|
| YR | MON | DD | UT | DAY | J | P | S |
| 83 | JAN | 1 | 1353 | 1 | O | X | M |
| 83 | JAN | 2 | 2250 | 2 | O | O | X |
| 83 | JAN | 5 | 0730 | 5 | A | O | X |
| 83 | JAN | 9 | 1544 | 9 | X | X | X |
| 83 | JAN | 11 | 1927 | 11 | X | N | X |
| 83 | JAN | 11 | 2309 | 11 | X | N | U |
| 83 | JAN | 16 | 1349 | 16 | O | X | X |
| 83 | JAN | 17 | 1408 | 17 | A | M | U |
| 83 | JAN | 17 | 1506 | 17 | A | X | X |
| 83 | JAN | 17 | 1639 | 17 | O | X | X |
| 83 | JAN | 17 | 1714 | 17 | O | M | X |
| 83 | JAN | 20 | 0257 | 20 | A | M | X |
| 83 | JAN | 23 | 0418 | 23 | A | X | X |
| 83 | JAN | 27 | 0209 | 27 | O | X | M |
| 83 | JAN | 27 | 0228 | 27 | A | X | M |
| 83 | JAN | 28 | 0659 | 28 | O | O | X |
| 83 | JAN | 29 | 2048 | 29 | A | O | X |
| 83 | FEB | 2 | 0320 | 33 | A | X | X |
| 83 | FEB | 4 | 1614 | 35 | X | X | X |
| 83 | FEB | 19 | 0440 | 50 | X | M | N |
| 83 | MAR | 1 | 1154 | 60 | X | X | X |
| 83 | MAR | 1 | 1208 | 60 | O | X | X |
| 83 | MAR | 3 | 1628 | 62 | N | X | X |
| 83 | MAR | 15 | 0342 | 74 | A | X | X |
| 83 | MAR | 16 | 0332 | 75 | A | M | X |
| 83 | MAR | 16 | 0355 | 75 | O | U | X |
| 83 | MAR | 16 | 0407 | 75 | A | M | X |
| 83 | MAR | 25 | 0544 | 84 | X | O | O |
| 83 | MAR | 25 | 2327 | 84 | A | O | X |
| 83 | MAR | 25 | 2358 | 84 | A | O | X |
| 83 | MAR | 28 | 0706 | 87 | X | O | O |
| 83 | APR | 6 | 0222 | 96 | A | X | N |
| 83 | APR | 8 | 0055 | 98 | O | M | X |
| 83 | APR | 12 | 1055 | 102 | X | X | X |
| 83 | APR | 13 | 1005 | 103 | X | X | X |
| 83 | APR | 13 | 1100 | 103 | X | X | X |
| 83 | APR | 13 | 1140 | 103 | A | O | X |
| 83 | APR | 29 | 1456 | 119 | X | O | O |
| 83 | APR | 30 | 0233 | 120 | A | O | X |
| 83 | MAY | 10 | 1855 | 130 | X | X | M |
| 83 | MAY | 11 | 0732 | 131 | X | O | O |
| 83 | MAY | 12 | 0127 | 132 | A | O | X |
| 83 | MAY | 17 | 0021 | 137 | X | M | X |
| 83 | MAY | 17 | 1151 | 137 | X | X | X |
| 83 | MAY | 21 | 0417 | 141 | X | O | O |
| 83 | MAY | 21 | 1226 | 141 | X | X | X |
| 83 | MAY | 24 | 1239 | 144 | X | X | N |
| 83 | JUN | 9 | 1729 | 160 | X | X | M |
| 83 | JUN | 10 | 0308 | 161 | X | O | M |
| 83 | JUN | 12 | 0407 | 163 | A | O | X |
| 83 | JUN | 12 | 0944 | 163 | X | X | X |
| 83 | JUN | 13 | 0118 | 164 | X | M | M |
| 83 | JUN | 19 | 0317 | 170 | A | O | X |
| 83 | JUL | 7 | 0904 | 188 | X | M | O |
| 83 | JUL | 8 | 1634 | 189 | A | M | X |
| 83 | JUL | 10 | 0308 | 191 | A | M | U |
| 83 | JUL | 16 | 1712 | 197 | A | X | X |
| 83 | JUL | 16 | 1802 | 197 | A | X | M |
| 83 | JUL | 17 | 0050 | 198 | O | M | X |
| 83 | JUL | 17 | 0132 | 198 | A | O | X |
| 83 | JUL | 19 | 11 | 200 | X | U | O |
| 83 | JUL | 22 | 0009 | 203 | O | O | X |
| 83 | JUL | 31 | 2014 | 212 | O | X | O |
| 83 | AUG | 7 | 0827 | 219 | X | M | X |
| 83 | AUG | 19 | 1101 | 231 | X | X | X |
| 83 | SEP | 28 | 1301 | 271 | A | X | O |
| 83 | OCT | 2 | 0324 | 275 | A | O | U |
| 83 | OCT | 3 | 0231 | 276 | A | M | U |
| 83 | OCT | 4 | 0541 | 277 | X | O | N |
| 83 | OCT | 6 | 1241 | 279 | X | X | X |
| 83 | OCT | 15 | 0410 | 288 | A | O | U |
| 83 | OCT | 21 | 1324 | 294 | X | X | X |
| 83 | OCT | 24 | 2320 | 297 | A | X | O |
| 83 | NOV | 7 | 1140 | 311 | X | X | O |
| 83 | NOV | 11 | 1110 | 315 | X | X | X |
| 83 | NOV | 11 | 1546 | 315 | A | X | X |
| 83 | NOV | 11 | 1804 | 315 | A | X | X |
| 83 | NOV | 12 | 1438 | 316 | O | U | U |
| 83 | NOV | 20 | 1202 | 324 | A | U | X |
| 83 | NOV | 20 | 1321 | 324 | O | U | X |
| 83 | NOV | 22 | 0307 | 326 | O | M | M |
| 83 | NOV | 28 | 1500 | 332 | X | U | U |
| 83 | DEC | 10 | 0313 | 344 | X | M | X |
| 83 | DEC | 11 | 0853 | 345 | X | U | O |
| 83 | DEC | 30 | 0347 | 364 | X | O | U |

| DATE | | | | | GROUND | | |
|---|---|---|---|---|---|---|---|
| YR | MON | DD | UT | DAY | J | P | S |
| 84 | JAN | 30 | 1500 | 30 | X | | |
| 84 | FEB | 5 | 1208 | 36 | | X | N |
| 84 | FEB | 12 | 1504 | 43 | X | X | N |
| 84 | FEB | 14 | 1330 | 45 | | U | N |
| 84 | FEB | 14 | 1401 | 45 | | X | N |
| 84 | FEB | 20 | 1556 | 51 | X | X | N |
| 84 | FEB | 20 | 1723 | 51 | | X | N |
| 84 | FEB | 23 | 2232 | 54 | | U | N |
| 84 | FEB | 29 | 0338 | 60 | X | O | N |
| 84 | MAR | 6 | 0820 | 66 | X | O | N |
| 84 | MAR | 28 | 2232 | 88 | X | O | N |
| 84 | APR | 17 | 1441 | 108 | X | X | N |
| 84 | APR | 28 | 1912 | 119 | | X | N |
| 84 | MAY | 17 | 1256 | 138 | X | X | N |
| 84 | MAY | 17 | 1623 | 138 | X | X | N |
| 84 | MAY | 17 | 1714 | 138 | | X | N |
| 84 | MAY | 24 | 0845 | 145 | X | X | N |
| 84 | JUN | 15 | 0433 | 167 | X | O | N |
| 84 | JUN | 23 | 2056 | 175 | X | O | N |
| 84 | JUL | 1 | 1252 | 183 | | X | N |
| 84 | JUL | 9 | 1639 | 191 | X | X | N |
| 84 | JUL | 10 | 1227 | 192 | | X | N |
| 84 | JUL | 13 | 0602 | 195 | X | O | N |
| 84 | JUL | 15 | 1940 | 197 | | ? | N |
| 84 | JUL | 21 | 1402 | 203 | | X | N |
| 84 | JUL | 31 | 1451 | 213 | X | X | N |
| 84 | AUG | 17 | 0419 | 230 | | U | N |
| 84 | SEP | 4 | 0746 | 248 | X | O | N |
| 84 | SEP | 6 | 1250 | 250 | | X | N |
| 84 | SEP | 6 | 1256 | 250 | | X | N |
| 84 | SEP | 11 | 1249 | 255 | | X | N |
| 84 | OCT | 18 | 1045 | 292 | X | O | N |
| 84 | OCT | 24 | 0341 | 298 | | X | N |
| 84 | OCT | 30 | 1226 | 304 | | X | N |
| 84 | NOV | 14 | 2355 | 319 | X | | |
| 84 | DEC | 13 | 0102 | 348 | X | | |
| 84 | DEC | 21 | 1721 | 356 | X | | |
| 84 | DEC | 23 | 0939 | 358 | X | | |

| DATE | | | | | GROUND | | |
|---|---|---|---|---|---|---|---|
| YR | MON | DD | UT | DAY | J | P | S |
| 85 | JAN | 8 | 1412 | 8 | X | | N |
| 85 | JAN | 16 | 0220 | 16 | | X | N |
| 85 | JAN | 21 | 1650 | 21 | | X | N |
| 85 | JAN | 23 | 0805 | 23 | X | M | N |
| 85 | FEB | 5 | 0348 | 36 | X | O | N |
| 85 | MAR | 4 | 1454 | 63 | | X | N |
| 85 | MAR | 4 | 1827 | 63 | X | X | N |
| 85 | MAR | 7 | 0955 | 66 | | X | N |
| 85 | MAR | 10 | 0924 | 69 | X | X | N |
| 85 | MAR | 28 | 0521 | 87 | | X | N |
| 85 | APR | 16 | 0344 | 106 | | X | N |
| 85 | APR | 20 | 0311 | 110 | X | O | N |
| 85 | APR | 26 | 1548 | 116 | | X | N |
| 85 | APR | 26 | 1552 | 116 | | X | N |
| 85 | APR | 30 | 0922 | 120 | X | X | N |
| 85 | APR | 30 | 1133 | 120 | | X | N |
| 85 | MAY | 2 | 0144 | 122 | X | O | N |
| 85 | MAY | 6 | 1240 | 126 | | X | N |
| 85 | MAY | 31 | 0219 | 151 | | X | N |
| 85 | MAY | 31 | 0311 | 151 | | X | N |
| 85 | JUN | 6 | 0544 | 157 | X | O | N |
| 85 | JUN | 6 | 1108 | 157 | X | O | N |
| 85 | JUN | 9 | 1715 | 160 | X | X | N |
| 85 | JUN | 20 | 1550 | 171 | | X | N |
| 85 | JUL | 4 | 0401 | 185 | X | O | N |
| 85 | JUL | 22 | 1948 | 203 | X | X | N |
| 85 | AUG | 12 | 1450 | 224 | X | X | N |
| 85 | AUG | 23 | 1807 | 235 | | X | N |
| 85 | AUG | 30 | 1607 | 242 | | X | N |
| 85 | AUG | 30 | 1726 | 242 | | X | N |
| 85 | SEP | 14 | 0342 | 257 | | X | N |
| 85 | SEP | 14 | 0600 | 257 | X | X | N |
| 85 | SEP | 15 | 1445 | 258 | | X | N |
| 85 | SEP | 30 | 0211 | 273 | | X | N |
| 85 | OCT | 31 | 1059 | 304 | X | | N |
| 85 | NOV | 29 | 0806 | 333 | X | | X |
| 85 | DEC | 9 | 2030 | 343 | X | | O |
| 85 | DEC | 10 | 0336 | 344 | X | | |
| 85 | DEC | 12 | 2118 | 346 | X | | O |
| 85 | DEC | 18 | 0645 | 352 | X | | |
| 85 | DEC | 19 | 0045 | 353 | X | | |
| 85 | DEC | 27 | 1834 | 361 | X | | |
| 85 | DEC | 29 | 2248 | 363 | X | | |

# REFERENCES


Araki, T., Global structure of geomagnetic sudden commencements, *Planet. Space Sci., 25*, 373, 1977.

Araki, T., and J. H. Allen, Latitudinal reversal of polarization of the geomagnetic sudden commencement, *J. Geophys. Res., 87*, 5207, 1982.

Arnoldy, R. L., T. E. Moore, and S.-I. Akasofu, Plasma injection events at synchronous orbit related to positive DST, *J. Geophys. Res., 87*, 77, 1982.

Barfield, J. N., and P. J. Coleman, Storm-related wave phenomena observed at the synchronous, equatorial orbit, *J. Geophys. Res., 75*, 1943, 1970.

Baumjohann, W., O. H. Bauer, G. Haerendel, and H. Junginger, Magnetospheric plasma drifts during a sudden impulse, *J. Geophys. Res., 88*, 9287, 1983.

Baumjohann, W., H. Junginger, G. Haerendel, and O. H. Bauer, Resonant Alfvén waves excited by a sudden impulse, *J. Geophys. Res., 89*, 2765, 1984.

Beard, D. B., The interaction of the terrestrial magnetic field with the solar corpuscular radiation, *J. Geophys. Res., 65*, 3559, 1960.

Bell, T. F., The nonlinear gyroresonance interaction between energetic electrons and coherent VLF waves propagating at an arbitrary angle with respect to the Earth's magnetic field, *J. Geophys. Res., 89*, 905, 1984.

Bell, T. F., and U. S. Inan, ISEE-1 observations in the magnetosphere of VLF emissions triggered by nonducted coherent VLF waves during VLF wave-injection experiments, *Adv. Space Res., Vol. 1*, 203, 1981.

Brown, R. R., Sudden commencement absorption events at the edge of the polar cap, *J. Geophys. Res., 82*, 2433, 1977.

Brown, R. R., T. R. Hartz, B. Landmark, H. Leinbach, and J. Ortner, Large-scale electron bombardment of the atmosphere at the sudden commencement of a geomagnetic storm, *J. Geophys. Res., 66*, 1035, 1961.

Burlaga, L. F., and K. W. Ogilvie, Causes of sudden commencements and sudden impulses, *J. Geophys. Res., 74*, 2815, 1969.

Burtis, W. J., and R. A. Helliwell, Magnetospheric chorus: occurrence patterns and normalized frequency, *Planet. Space Sci., 24*, 1007, 1976.

Carlson, C. R., Modeling and simulation of whistler-mode wave growth through cyclotron resonance with energetic electrons in the magnetosphere, *Ph.D. Thesis*, Stanford University, Stanford, Ca., 1987.

Carpenter, D. L., Whistler evidence of a "knee" in the magnetospheric ionization density profile, *J. Geophys. Res., 68*, 1675, 1963.

Carpenter, D. L., A study of the outer limits of ducted whistler propagation in the magnetosphere, *J. Geophys. Res., 86*, 839, 1981.

Carpenter, D. L., F. Walter, R. E. Barrington, and D. J. McEwen, Alouette 1 and 2 observations of abrupt changes in whistler rate and of VLF noise variations at the plasmapause - a satellite-ground study, *J. Geophys. Res., 73*, 2929, 1968.

Carpenter, D. L., and C. G. Park, On what ionospheric workers should know about the plasmapause-plasmasphere, *Rev. Geophys. Space Phys., 11*, 133, 1973.

Carpenter, D. L., K. Stone, J. C. Siren, and T. L. Crystal, Magnetospheric electric fields deduced from drifting whistler paths, *J. Geophys. Res., 77*, 2819, 1972.

Chang, H. C., and U. S. Inan, Test particle modeling of wave-induced energetic electron precipitation, *J. Geophys. Res., 90*, 6409, 1985.

Chang, H. C., U. S. Inan, and T. F. Bell, Energetic electron precipitation due to gyroresonant interactions in the magnetosphere involving coherent VLF waves with slowly varying frequency, *J. Geophys. Res., 88*, 7037, 1983.

Chapman, S., and V. C. A. Ferraro, A new theory of magnetic storms, *Terrest. Magnetism Atmospheric Elec., 36*, 77-97, 171-186, 1931.

Chappell, C. R., K. K. Harris, and G. W. Sharp, The dayside of the plasmasphere, *J. Geophys. Res., 76*, 7632, 1971.

Chen, F. F., *Introduction to Plasma Physics*, Plenum Press, New York, 1974.

Chen, L., and A. Hasegawa, A theory of long-period magnetic pulsations 1. Steady state excitation of field line resonance, *J. Geophys. Res., 79*, 1024, 1974a.

Chen, L., and A. Hasegawa, A theory of long-period magnetic pulsations 2. Impulse excitation of surface eigenmode, *J. Geophys. Res., 79*, 1033, 1974b.

Choe, J. Y., and D. B. Beard, The compressed geomagnetic field as a function of dipole tilt, *Planet. Space Sci., 22*, 595, 1974a.

Choe, J. Y., and D. B. Beard, The near earth magnetic field of the magnetotail current, *Planet. Space Sci., 22*, 609, 1974b.

Church, S. R., and R. M. Thorne, On the origin of plasmaspheric hiss: raypath integrated amplification, *J. Geophys. Res., 88*, 7941, 1983.

Cornilleau-Wehrlin, N., J. Solomon, A. Korth, and G. Kremser, Experimental study of the relationship between energetic electrons and ELF waves observed on board GEOS: A support to quasi-linear theory, *J. Geophys. Res., 90*, 4141, 1985.

Coroniti, F. V., and C. F. Kennel, Electron precipitation pulsations, *J. Geophys. Res., 75*, 1279, 1970.

Davidson, G. T., and Y. T. Chiu, A closed nonlinear model of wave-particle interactions in the outer trapping and morningside auroral regions, *J. Geophys. Res., 91*, 13705, 1986.

Dowden, R. L., The effect of MHD waves on the threshold wave field for initiating VLF nonlinear growth and emissions, *J. Geophys. Res., 86*, 4815, 1981.

Dunckel, N., and R. A. Helliwell, Whistler-mode emissions on the OGO-1 satellite, *J. Geophys. Res., 74*, 6371, 1969.

Dysthe, K. B., Some studies of triggered whistler emissions, *J. Geophys. Res., 76*, 6915, 1971.

Edgar, B. C., The structure of the magnetosphere as deduced from magnetospherically reflected whistlers, *Ph.D. Thesis*, Stanford University, Stanford, Ca., 1972.

Etcheto, J. R. Gendrin, J. Solomon, and A. Roux, A self-consistent theory of magnetospheric hiss, *J. Geophys. Res., 78*, 8150, 1973.

Fairfield, D. H., Average and unusual locations of the earth's magnetopause and bow shock, *J. Geophys. Res., 76*, 6700, 1971.

Fujii, R., N. Sato, and H. Fukunishi, *JARE Data Reports, No. 105*, National Institute of Polar Research, Tokyo, 1985.

Fukunishi, H., Latitude dependence of power spectra of magnetic pulsations near $L = 4$ excited by ssc's and si's, *J. Geophys. Res., 84*, 7191, 1979.

Hamming, R. W., *Digital Filters*, Prentice-Hall, Englewood Cliffs, New Jersey, 1983.

Hartz, T. R., Multi-station riometer observations, in *Radio Astronomical and Satellite Studies of the Atmosphere*, ed. J. Aarons, North-Holland, Amsterdam, 1963.

Hartz, T. R., and N. M. Brice, The general pattern of auroral particle precipitation, *Planet. Space Sci., 15*, 301, 1967.

Hayashi, K., S. Kokubun, and T. Oguti, Polar chorus emission and worldwide geomagnetic variation, *Rep. Ionos. Space Res. Japan, 22*, 149, 1968.

Helliwell, R. A., *Whistlers and Related Ionospheric Phenomena*, Stanford University Press, Stanford, Ca., 1965.

Helliwell, R. A., A theory of discrete VLF emissions from the magnetosphere, *J. Geophys. Res., 72*, 4773, 1967.

Helliwell, R. A., D. L. Carpenter, U. S. Inan, and J. P. Katsufrakis, Generation of band-limited VLF noise using the Siple transmitter: A model for magnetospheric hiss, *J. Geophys. Res., 91*, 4381, 1986.

Helliwell, R. A., D. L. Carpenter, and T. R. Miller, Power threshold for growth of coherent VLF signals in the magnetosphere, *J. Geophys. Res., 85*, 3360, 1980.

Helliwell, R. A., and U. S. Inan, VLF wave growth and discrete emission triggering in the magnetosphere: A feedback model, *J. Geophys. Res., 87*, 4427, 1982.

Helliwell, R. A., and J. P. Katsufrakis, VLF wave injection into the magnetosphere from Siple Station, Antarctica, *J. Geophys. Res., 79*, 2511, 1974.

Hirasawa, T., Effects of magnetospheric compression and expansion on spectral structure of ULF emissions, *Mem. Nat. Inst. Polar Res., spec. issue no. 18*, 127, 1981.

Ho, D., Quasi-periodic (QP) VLF emissions in the magnetosphere, *Ph.D. Thesis*, Stanford University, Stanford, Ca., 1974.

Huang, C. Y., C. K. Goertz, and R. R. Anderson, A theoretical study of plasmaspheric hiss generation, *J. Geophys. Res., 88*, 7927, 1983.

Imhof, W. L., J. B. Reagan, H. D. Voss, E. E. Gaines, D. W. Datlowe, J. Mobilia, R. A. Helliwell, U. S. Inan, and J. P. Katsufrakis, Direct observations of radiation belt electron precipitation by the controlled injection of VLF signals from a ground-based transmitter, *Geophys. Res. Lett., 10*, 361, 1983.

Inan, U. S., Non-linear gyroresonant interactions of energetic particles and coherent VLF waves in the magnetosphere, *Ph.D. Thesis*, Stanford Univ., Stanford, Ca., 1977.

Inan, U. S., Gyroresonant pitch angle scattering by coherent and incoherent whistler mode waves in the magnetosphere, submitted to *J. Geophys, Res., 92*, 127, 1987.

Inan, U. S., T. F. Bell, and R. A. Helliwell, Nonlinear pitch angle scattering of energetic electrons by coherent VLF waves in the magnetosphere, *J. Geophys. Res., 83*, 3235, 1978.

Inan, U. S., R. A. Helliwell, and W. S. Kurth, Terrestrial versus Jovian VLF chorus; a comparative study, *J. Geophys. Res., 88*, 6171, 1983.

Joselyn, J. A., and L. R. Lyons, Ion cyclotron wave growth calculated from satellite observations of the proton ring current during storm recovery, *J. Geophys. Res., 81*, 2275, 1976.

Karpman, V. I., and R. N. Kaufman, Whistler wave propagation in magnetospheric ducts (in the equatorial region), *Planet. Space Sci., 32*, 1505, 1984.

Kaufmann, R. L., and D. M. Walker, Hydromagnetic waves excited during an SC, *J. Geophys. Res., 79*, 5187, 1974.

Kennel, C. F., and H. E. Petschek, Limit on stably trapped particle fluxes, *J. Geophys. Res., 71*, 1, 1966.

Kikuchi, T., Evidence of transmission of polar electric fields to the low latitude at times of geomagnetic sudden commencements, *J. Geophys. Res., 91*, 3101, 1986.

Kikuchi, T., T. Araki, H. Maeda, and K. Maezawa, Transmission of polar electric fields to the equator, *Nature, 273*, 650, 1978.

Kikuchi, T., and T. Araki, Transient response of uniform ionosphere and preliminary reverse impulse of geomagnetic storm sudden commencement, *J. Atmos. Terr. Phys., 41*, 917, 1979a.

Kikuchi, T., and T. Araki, Horizontal transmission of the polar electric field to the equator, *J. Atmos. Terr. Phys., 41*, 927, 1979b.

Kimura, I., H. Matsumoto, T. Mukai, K, Hashimoto, T. F. Bell, U. S. Inan, R. A. Helliwell, and J. P. Katsufrakis, EXOS-B/Siple Station VLF wave-particle interaction experiments: 1. General description and wave-particle correlations, *J. Geophys. Res., 88*, 282, 1983.

Knecht, D. J., *Daily Magnetograms for 1978-83 From the AFGL Network*, AFGL reports: AFGL-TR-85-0027 through -0031 (6 volumes), Air Force Geophysics Laboratory, Hanscom AFB, Ma., 1985.

Knott, K., D. Fairfield, A. Korth, and D. T. Young, Observations near the magnetopause at the onset of the July 29, 1977, sudden storm commencement, *J. Geophys. Res., 87*, 5888, 1982.

Knott, K., A. Pederson, and U. Wedeken, GEOS 2 electric field observations during a sudden commencement and subsequent substorms, *J. Geophys. Res., 90*, 1283, 1985.

Kokubun, S., Characteristics of storm sudden commencement at geostationary orbit, *J. Geophys. Res., 88*, 10025, 1983.

Kokubun, S., and T. Oguti, Hydromagnetic emissions associated with Storm Sudden Commencements, *Rep. Ionos. Space Res. Japan, 22*, 45, 1968.

Korth, A., G. Kremser, N. Cornilleau-Wehrlin, and J. Solomon, Observations of energetic electrons and VLF waves at geostationary orbit during storm sudden commencements (SSC), *Proc. Chapman Conf. on Solar Wind - Magnetosphere Interactions*, 1986.

Kuwashima, M., and H. Fukunishi, Local time asymmetries of the SSC-associated hydromagnetic variations at the geosynchronous altitude, *Planet. Space Sci., 33*, 711, 1985.

Lanzerotti, L. J., C. G. Maclennan, L. V. Medford, and D. L. Carpenter, Study of a QP/GP event at very high latitudes, *J. Geophys. Res., 91*, 375, 1986.

Leinbach, H., R. J. Schmidt, and R. R. Brown, Conjugate observations of an electron precipitation event associated with the sudden commencement of a magnetic storm, *J. Geophys. Res., 75*, 7099, 1970.

Lin, C.-A., D. T. Young, and R. A. Wolf, Magnetospheric plasma motion during a sudden commencement, *Planet. Space Sci., 21*, 1713, 1973.

Lyons, L. R., and R. M. Thorne, Equilibrium structure of radiation belt electrons, *J. Geophys. Res., 78*, 2142, 1973.

Lyons, L. R., R. H. Thorne, and C. F. Kennel, Pitch-angle diffusion of radiation belt electrons within the plasmasphere, *J. Geophys. Res., 77*, 3455, 1972.

Lyons, L. R., and D. J. Williams, *Quantitative Aspects of Magnetospheric Physics*, D. Reidel, Boston, 1984.

Maeda, K., and C. S. Lin, Frequency band broadening of magnetospheric VLF emissions near the equator, *J. Geophys. Res., 86*, 3635, 1981.

Maggs, J. E., Coherent generation of VLF hiss, *J. Geophys. Res., 81*, 1707, 1976.

Matsushita, S., On geomagnetic sudden commencements, sudden impulses, and storm durations, *J. Geophys. Res., 67*, 3753, 1962.

Mayaud, P. N., Analysis of storm sudden commencements for the years 1868-1967, *J. Geophys. Res., 80*, 111, 1975.

McNeill, F. A., VLF radio observations of magnetic impulses in the plasmasphere, *J. Geophys. Res., 75*, 4230, 1970.

Mead, G. D., Deformation of the geomagnetic field by the solar wind, *J. Geophys. Res., 69*, 1181, 1964.

Mead, G. D., and D. B. Beard, Shape of the geomagnetic field solar wind boundary, *J. Geophys. Res., 69*, 1169, 1964.

Mead, G. D., and D. H. Fairfield, A quantitative magnetospheric model derived from spacecraft magnetometer data, *J. Geophys. Res., 80*, 523, 1975.

Morozumi, H. M., Enhancement of VLF chorus and ULF at the time of SC, *Rep. Ionos. Space Res. Japan, 19*, 371, 1965.

Morozumi, H. M., Sudden decrease of VLF chorus intensity at the time of SC, SSC, and SI, unpublished manuscript.

Newton, R. S., D. J. Southwood, and W. J. Hughes, Damping of geomagnetic pulsations by the ionosphere, *Planet. Space Sci., 26*, 201, 1978.

Nishida, A., Ionospheric screening effect and storm sudden commencement, *J. Geophys. Res., 69*, 1861, 1964.

Nishida, A., *Geomagnetic Diagnosis of the Magnetosphere*, Springer-Verlag, New York, 1978.

Nishida, A., and L. J. Cahill, Sudden impulses in the magnetosphere observed by Explorer 12, *J. Geophys Res., 69*, 2243, 1964.

Nopper, R. W., W. J. Hughes, C. G. Maclennan, and R. L. McPherron, Impulse excited pulsations during the July 29, 1977 event, *J. Geophys. Res., 87*, 5911, 1982.

Nunn, D., A self-consistent theory of triggered VLF emissions, *Planet. Space Sci., 22*, 349, 1974.

Oguti, T., and S. Kokubun, Hydromagnetic emissions in high latitudes associated with storm sudden commencements-II, *Rep. Ionos. Space Res. Japan, 23*, 162, 1969.

Oliven, M. N., and D. A. Gurnett, Microburst phenomena: 3. An association between microbursts and VLF chorus, *J. Geophys. Res., 73*, 2355, 1968.

Olson, J. V., and L. C. Lee, Pc1 wave generation by sudden impulses, *Planet. Space Sci., 31*, 295, 1983.

Olson, W. P., The shape of the tilted magnetopause, *J. Geophys. Res., 74*, 5642, 1969.

Olson, W. P., A model of the distributed magnetospheric currents, *J. Geophys. Res., 79*, 3731, 1974.

Olson, W. P., ed., *Quantitative Modeling of Magnetospheric Processes*, American Geophysical Union, Washington, D. C., 1979.

Olson, W. P., and K. A. Pfitzer, A quantitative model of the magnetospheric magnetic field, *J. Geophys. Res., 79*, 3739, 1974.

Olson, W. P., and K. A. Pfitzer, A dynamic model of the magnetospheric magnetic and electric fields for July 29, 1977, *J. Geophys. Res., 87*, 5943, 1982.

Omura, Y., and H. Matsumoto, Computer simulation of basic processes of coherent whistler wave-particle interactions in the magnetosphere, *J. Geophys. Res., 87*, 4435, 1982.

Ondoh, T., Hydromagnetic interpretation of high latitude sudden impulse, *J. Radio Res. Labs.*, *18*, 19, 1971.

Ortner, J., B. Hultqvist, R. R. Brown, T. R. Hartz, O. Holt, B. Landmark, J. L. Hook, and H. Leinbach, Cosmic noise absorption accompanying geomagnetic storm sudden commencements, *J. Geophys. Res.*, *67*, 4169, 1962.

Park, C. G., Whistler observations during a magnetospheric sudden impulse, *J. Geophys. Res.*, *80*, 4738, 1975.

Park, C. G., C. S. Lin, and G. K. Parks, A ground-satellite study of wave-particle correlations, *J. Geophys. Res.*, *86*, 37, 1981.

Patel, V. L., and L. J. Cahill, Magnetic field variations of the SI in the magnetosphere and correlated effects in interplanetary space, *Planet. Space Sci.*, *22*, 1117, 1974.

Patel, V. L., and P. J. Coleman, Sudden impulses in the magnetosphere observed at synchronous orbit, *J. Geophys. Res.*, *75*, 7255, 1970.

Paulikas, G. A., and J. B. Blake, Effects of sudden commencements on solar protons at the synchronous orbit, *J. Geophys. Res.*, *75*, 734, 1970.

Perona, G. E., Theory on the precipitation of magnetospheric electrons at the time of a sudden commencement, *J. Geophys. Res.*, *77*, 101, 1972.

Rastani, K., U. S. Inan, and R. A. Helliwell, DE-1 observations of Siple transmitter signals and associated sidebands, *J. Geophys. Res.*, *90*, 4128, 1985.

Ratcliffe, J. A., *The Magneto-Ionic Theory and its Application to the Ionosphere*, Cambridge University Press, Cambridge, England, 1959.

Retterer, J. H., J. R. Jasperse, and T. S. Chang, A new approach to pitch andgle scattering in the magnetosphere, *J. Geophys. Res.*, *88*, 201, 1983.

Roederer, J. G., Quantitative models of the magnetosphere, *Rev. Geophys.*, *7*, 77, 1969.

Rosenberg, T. J., R. A. Helliwell, and J. P. Katsufrakis, Electron precipitation associated with discrete very-low-frequency emissions, *J. Geophys. Res.*, *76*, 8445, 1971.

Rosenberg, T. J., J. C. Siren, D. L. Matthews, K. Marthinsen, J. A. Holtet, A. Egeland, D. L. Carpenter, and R. A. Helliwell, Conjugacy of electron microbursts and VLF chorus, *J. Geophys. Res.*, *86*, 5819, 1981.

Rosenberg, T. J., R. Wei, D. L. Detrick, and U. S. Inan, Observations and modeling of wave-induced microburst electron precipitation, submitted to *J. Geophys. Res.*, 1987.

Sakurai, T., Y. Tonegawa, K. Tomomura, and Y. Kato, A multi-satellite study of magnetic pulsations associated with a storm sudden commencement (SSC) as observed at synchronous orbit, *Mem. Nat. Inst. Polar Res., spec. issue no. 31*, 1, 1984.

Sato, N., and H. Fukunishi, Interaction between ELF-VLF emissions and magnetic pulsations: Classification of quasi-periodic ELF-VLF emissions based on frequency-time spectra, *J. Geophys Res.*, *86*, 19, 1981.

Sato, N., and S. Kokubun, Interaction between ELF-VLF emissions and magnetic pulsations: Quasi-periodic ELF-VLF emissions associated with Pc 3-4 magnetic pulsations and their geomagnetic conjugacy, *J. Geophys. Res., 85*, 101, 1980.

Scarabucci, R. R., and R. L. Smith, Study of magnetospheric field oriented irregularities - the mode theory of bell-shaped ducts, *Radio Sci., 6*, 65, 1971.

Schulz, M, and L. J. Lanzerotti, *Particle Diffusion in the Radiation Belts*, Springer-Verlag, New York, 1974.

Schutz, S., G. J. Adams, and F. S. Mozer, Electric and magnetic fields measured during a sudden impulse, *J. Geophys. Res., 79*, 2002, 1974.

Silevitch, M. B., and P. L. Rothwell, Nonlinear particle precipitation events - theory, *EOS Transactions, 67*, 1165, 1986.

Singer, H. J., D. J. Southwood, R. J. Walker, and M. J. Kivelson, Alfven wave resonances in a realistic magnetospheric magnetic field geometry, *J. Geophys. Res., 86*, 4589, 1981.

Smith, E. J., Interplanetary magnetic fields, *Rev. Geophys. Space Phys., 17*, 610, 1979.

Tamao, T., Hydromagnetic coupling oscillations and drift wave instabilities in nonuniform, collisionless plasma, *Phys. Fluids, 12*, 1458, 1969.

Tamao, T., Unsteady interactions of solar wind disturbances with the magnetosphere, *J. Geophys. Res., 80*, 4230, 1975.

Tamao, T., Interaction of energetic particles with HM-waves in the magnetosphere, *Planet. Space Sci., 32*, 1371, 1984.

Tepley, L. R., and R. C. Wentworth, Hydromagnetic emissions, X-ray bursts, and electron bunches, Part I: Experimental results, *J. Geophys. Res., 67*, 3317, 1962.

Thorne, R. M., E. J. Smith, R. K. Burton, and R. E. Holzer, Plasmaspheric hiss, *J. Geophys. Res., 78*, 1581, 1973.

Tixier, M., and N. Cornilleau-Wehrlin, How are the VLF quasi-periodic emissions controlled by harmonics of field line oscillations? The results of a comparison between ground and GEOS satellites measurements, *J. Geophys. Res., 91*, 6899, 1986.

Tkalcevic, S., U. S. Inan, and R. A. Helliwell, Nonlinear pitch-angle scattering and trapping of energetic particles during Landau resonance interactions with whistler mode waves, *J. Geophys. Res., 89*, 10813, 1984.

Tsunomura, S., and M. Kuwashima, On the nature of flux variations of trapped particles associated with sudden commencement and sudden impulse at synchronous orbit, *Mem. Nat. Inst. Polar Res., spec. issue no. 31*, 27, 1984.

Tsuruda, K., S. Machida, T. Terasawa, A. Nishida, and K. Maezawa, High spatial attenuation of the Siple transmitter signal and natural VLF chorus observed at ground-based chain stations near Roberval, Quebec, *J. Geophys. Res., 87*, 742, 1982.

Tsyganenko, N. A., and A. V. Usmanov, Determination of the magnetic current system parameters and development of experimental geomagnetic field models based on data from IMP and HEOS satellites, *Planet. Space Sci., 30*, 985, 1982.

Ullaland, S. L., K. Wilhelm, J. Kangas, and W. Riedler, Electron precipitation associated with a sudden commencement of a geomagnetic storm, *J. Atmos. Terr. Phys., 32*, 1545, 1970.

Vomvoridis, J. L., T. L. Crystal, and J. Denavit, Theory and computer simulations of magnetospheric very low frequency emissions, *J. Geophys. Res., 87*, 1473, 1982.

Voss, H. D., W. L. Imhof, M. Walt, J. Mobilia, E. E. Gaines, J. B. Reagan, U. S. Inan, R. A. Helliwell, D. L. Carpenter, J. P. Katsufrakis, and H. C. Chang, Lightning-induced electron precipitation, *Nature, 312*, 740, 1985.

Walker, A. D. M., Excitation of the earth-ionosphere waveguide by downgoing whistlers, II, Propagation in the magnetic meridian, *Proc. Royal Soc. London, Ser. A., 340*, 1974.

Walker, R. J., An evaluation of recent quantitative magnetospheric magnetic field models, *Rev. Geophys. Space Phys., 14*, 411, 1976.

Wedeken, U., H. Voelker, K. Knott, and M. Lester, SSC-excited pulsations recorded near noon on GEOS 2 and on the ground (CDAW 6), *J. Geophys. Res., 91*, 3089, 1986.

Wilken, B., D. N. Baker, P. R. Higbie, T. A. Fritz, W. P. Olson, and K. A. Pfitzer, Magnetospheric configuration and energetic particle effects associated with a SSC: A case study of the CDAW 6 event on March 22, 1979, *J. Geophys. Res., 91*, 1459, 1986.

Wilken, B., C. K. Goertz, D. N. Baker, P. R. Higbie, and T. A. Fritz, The SSC on July 29, 1977 and its propagation within the magnetosphere, *J. Geophys. Res., 87*, 5901, 1982.

Williams, D. J., and G. D. Mead, Night side magnetosphere configuration as obtained from trapped electrons at 1100 kilometers, *J. Geophys. Res., 70*, 3017, 1965.

Wilson, C. R., and M Sugiura, Hydromagnetic interpretation of sudden commencements of magnetic storms, *J. Geophys. Res., 66*, 4097, 1961.